Soft Chemical Routes to Ferroelectric and Multiferroic Materials

---

Tong Zhu

New College

March 2020



A thesis submitted to the
Board of the Faculty of Physical Sciences
in partial fulfilment of the requirements
for the degree of Doctor of Philosophy

Soft Chemical Routes to Ferroelectric and Multiferroic Materials

This work is focussed on the synthesis and characterisation of ferroelectric and multiferroic materials which adopt $n = 2$ Dion-Jacobson or Ruddlesden-Popper structures.

A series of $n = 2$ Dion-Jacobson phases, $RbNdM_2O_7$ and $CsNdM_2O_7$ (M = Nb/Ta), were investigated and it was observed that they adopt polar crystal structures, confirmed by both second-harmonic generation and neutron diffraction experiments. Their polar structures are driven by several tilting distortions and cation displacement modes. The different polar structures adopted by the caesium and rubidium phases are attributed to the different sizes of Rb^+ and Cs^+ cations.

To extend our understanding on the size effect of interlayer cations, the metastable Ruddlesden-Popper phases $NaNdM_2O_7$ and $LiNdM_2O_7$ were prepared from $RbNdM_2O_7$ via cation exchange reactions. The lithium phases adopt a polar crystal structure, with lithium cations ordered as stripes. In contrast, the sodium phases are non-polar and the sodium cations adopt a checkerboard order pattern. Their different structures are again explained by the size differences between lithium and sodium cations.

A temperature dependant phase transition study of polar $RbNdM_2O_7$ and $CsNdM_2O_7$ reveals that upon heating, both rubidium and caesium phases undergo first-order phase transitions to anti-polar structures before reaching the highest symmetry aristotype structures. A complex competition between many distortion modes was observed during their phase transitions.

An $n = 2$ Ruddlesden-Popper phase, $Li_2SrTa_2O_7$, was prepared by a ceramic synthesis and it adopts a polar crystal structure. A further cation exchange reaction using $MnCl_2$ leads to a polar and magnetically ordered phase $MnSrTa_2O_7$. This manganese phase adopts an incommensurate crystal structure with an unambiguous modulation of the ordering pattern of manganese cations. The superstructure is explained by a competition between minimising Mn-Mn repulsion and optimising metal-oxide bonding. The unusual magneto-lattice coupling behaviour observed from variable temperature neutron diffraction data indicates a magnetoelectric effect in $MnSrTa_2O_7$.

Similar cation exchange reactions performed on $Li_2SrTa_2O_7$ using $CoCl_2$ or $CuCl_2$ produce partially exchanged phases $Co_xLi_{2-2x}SrTa_2O_7$ and $Cu_xLi_{2-2x}SrTa_2O_7$ with different structures with respect to their manganese analogue. Complex cation order is expected in these two phases.

A polar oxynitride phase, $Na_{1+x}NdTa_2O_{7-x}N_x$, was prepared by a low temperature ammonolysis from non-polar $NaNdTa_2O_7$, suggesting layered perovskite oxynitrides can be a new family of polar materials. In addition, a series of transition metal oxynitrides, $M_xLi_yNdTa_2O_{7-z}N_z$ (M = Mn/Fe/Co/Ni/Cu) were made from a four-step synthesis. Among these materials, the nickel phase adopts a polar crystal structure and exhibit a magnetic order below 20 K.

Declaration

The work described in this thesis was carried out at the Inorganic Chemistry Laboratory at the University of Oxford between October 2016 and March 2020 under the supervision of Professor Michael A. Hayward. All the work presented in this thesis is my own expect where I have either acknowledged help from a named person of given reference to a published source. None of the work has been submitted by the author for any degree at any other university.

Tong Zhu



March 2020

To my family.

Acknowledgements

First of all, I would like to thank my supervisor Professor Michael Hayward for offering me the opportunity to work in this group. Thanks for your passion and knowledge, which guided me to the completion of this exciting project.

I would like to thank Dr. Nicole Benedek for the DFT calculation, Prof. Shiv Halasyamani and Dr. Weiguo Zhang for collecting SHG data, Dr. Alex Gibbs and Dr. Pascal Manuel for the assistance in collecting neutron diffraction data, and Dr. Simon Cassidy for the magnetic measurements and the instruction in FullProf. I would like to specially thank Dr. Fabio Orlandi for the help in characterisation of incommensurate structures. Also, thank you to Great Britain China Centre and New College for the funding.

I want to thank all members in my research group whom I had a great time with. I hope all of you have a brilliant future. I also want to thank people from Clarke group, Goodwin group and Battle group; it is a great pleasure to work with all of you.

Thank you to my parents and my uncle. Without your support and encouragement, I would never be able to travel such a long distance and pursue my dream at Oxford. Finally, thank you Prof. John Kuo, who made me taste the beauty of chemistry and show me how to behave as a great man. I hope you enjoy the sunshine in California.

Table of Contents

Soft Chemical Routes to Ferroelectric and Multiferroic Materials.....I
Declaration.....III
Acknowledgements.....VII
Chapter 1 – Introduction.....1
1.1 Perovskite and related structures.....1
1.1.1 Perovskite structure and tolerance factor….....1
1.1.2 Ruddlesden-Popper and Dion-Jacobson structures….....2
1.2 Octahedral tilting distortions and Glazer notation system….....4
1.3 Ferroelectric and magnetoelectric multiferroic materials….....7
1.3.1 Ferroelectric materials….....7
1.3.2 Magnetoelectric multiferroic materials.....9
1.4 Trilinear coupling mechanism….....10
1.5 Topochemical reactions….....14
1.5.1 Traditional synthesis of crystalline solids….....14
1.5.2 Topochemical cation exchange reactions 15
Chapter 2 - Experimental Methods and Techniques.....17
2.1 Synthesis methods.....17
2.1.1 Ceramic synthesis.....17
2.1.2 Cation exchange reactions.....17
2.1.2.1 Open-ended tubes.....17
2.1.2.2 Sealed glass ampules.....18
2.1.2.3 Venting system.....19
2.1.3 Reactions under flowing NH_3.....20
2.1.4 Drying hygroscopic products.....21
2.2 Powder diffraction.....22
2.2.1 X-ray powder diffraction.....23
2.2.1.1 Panalytical Empyrean and X'Pert diffractometers.....24
2.2.1.2 Synchrotron X-ray powder diffraction.....25
2.2.2 Neutron powder diffraction.....26
2.2.2.1 HRPD, GEM and WISH.....28
2.3 Rietveld refinement.....29
2.3.1 Peak broadening.....31

2.4 SQUID magnetometry.....32
2.5 Curie-Weiss law.....33
2.6 Bond valence sum (BVS).....34
2.7 Second-harmonic generation (SHG) 35
2.8 Incommensurate structure.....36
Chapter 3 - The Synthesis and Characterisation of Polar Dion-Jacobson Phases A'NdM_2O_7 (A' = Rb/Cs， M = Nb/Ta).....37
3.1 Introduction.....37
3.2 Synthesis.....38
3.3 Results.....39
3.3.1 Optical SHG measurements.....39
3.3.2 Structure characterisation of $CsNdTa_2O_7$.....40
3.3.2.1 Room temperature synchrotron X-ray powder diffraction.....40
3.3.2.2 Room temperature neutron powder diffraction.....40
3.3.3 Structure characterisation of $RbNdNb_2O_7$.....42
3.3.3.1 Room temperature synchrotron X-ray powder diffraction.....42
3.3.3.2 Room temperature neutron powder diffraction.....43
3.3.4 Structure characterisation of $RbNdTa_2O_7$.....46
3.3.4.1 Room temperature synchrotron X-ray powder diffraction.....46
3.3.4.2 Room temperature neutron powder diffraction.....48
3.4 Discussion.....50
3.4.1 Justification of using neutrons.....50
3.4.2 Theory revised.....56
3.4.3 Structural differences in Rb$Nd M_2O_7$ and Cs$Nd M_2O_7$.....57
3.5 Conclusions.....62
Chapter 4 – Topochemical Cation Exchange of Rb$Nd M_2O_7$ to Li$Nd M_2O_7$ and Na$Nd M_2O_7$ (M = Nb/Ta).....64
4.1 Introduction.....64
4.2 Synthesis.....66
4.3 Results.....66
4.3.1 Optical SHG measurements.....66
4.3.2 Symmetry analysis of n = 2 Ruddlesden-Popper phases.....67
4.3.3 Structure characterisation of $LiNdNb_2O_7$.....70

4.3.3.1 Room temperature synchrotron X-ray powder diffraction.....70
4.3.3.2 Room temperature neutron powder diffraction.....71
4.3.4 Structure characterisation of $LiNdTa_2O_7$.....76
4.3.4.1 Room temperature synchrotron X-ray powder diffraction.....76
4.3.4.2 Room temperature neutron powder diffraction.....77
4.3.5 Structure characterisation of $NaNdNb_2O_7$.....79
4.3.5.1 Room temperature synchrotron X-ray powder diffraction.....79
4.3.5.2 Room temperature neutron powder diffraction.....81
4.3.6 Structure characterisation of $NaNdTa_2O_7$.....87
4.3.6.1 Room temperature synchrotron X-ray powder diffraction.....87
4.3.6.2 Room temperature neutron powder diffraction.....89
4.4 Discussion.....92
4.4.1 Structure differences between $LiNdM_2O_7$ and $NaNdM_2O_7$.....92
4.4.2 DFT – A useful supplementary tool for crystal structure characterisation.....96
4.5 Conclusion.....98
Chapter 5 – Phase Transition Behaviours of Polar Dion-Jacobson Phases A'NdM_2O_7 (A' = Rb/Cs, *M* = Nb/Ta).....100
5.1 Introduction.....100
5.2 Synthesis and Measurements.....102
5.3 Results.....103
5.3.1 Symmetry analysis of $n = 2$ Dion-Jacobson phases.....103
5.3.2 Phase transition behaviours of $RbNdTa_2O_7$.....105
5.3.2.1 The 1st phase transition of $RbNdTa_2O_7$– ferroelectric (P1) to paraelectric (P2)..105
5.3.2.2 The 2nd phase transition of $RbNdTa_2O_7$ – Loss of the a^- tilts (P2 to P3).....111
5.3.2.3 Final phase transition of $RbNdTa_2O_7$ (P3 to P4).....114
5.3.2.4 Summary of the phase transition behaviours of $RbNdTa_2O_7$.....116
5.3.3 Phase transition behaviours of $RbNdNb_2O_7$.....118
5.3.4 Phase transition behaviours of $CsNdTa_2O_7$.....123
5.3.4.1 The 1st phase transition – ferroelectric (R1) to paraelectric (R2).....123
5.3.4.2 The 2nd phase transition of $CsNdTa_2O_7$ – Simultaneous loss of a^- and c^- tilts...128
5.3.4.3 Summary of the phase transition behaviours of $CsNdTa_2O_7$….....130
5.3.5 Phase transition behaviours of $CsNdNb_2O_7$.....131
5.4 Discussion.....138
5.4.1 Comparison of the phase transition behaviours of $RbNdM_2O_7$ and $CsNdM_2O_7$….138

5.4.2 Phase transition temperatures....140
5.5 Conclusions....143
Chapter 6 – $Li_2SrTa_2O_7$: A Polar Ruddlesden-Popper Phase with a Non-Trivial Crystal Structure....145
6.1 Introduction....145
6.2 Synthesis....145
6.3 Results....146
6.3.1 Optical SHG measurements....146
6.3.2 Room temperature synchrotron X-ray powder diffraction....146
6.3.3 Room temperature neutron diffraction....147
6.3.4 Low temperature neutron diffraction....150
6.4 Discussion....154
6.4.1 Oxygen lattice....154
6.4.2 Cation lattice....156
6.5 Conclusions....159
Chapter 7 – $MnSrTa_2O_7$: Retrosynthesis towards Multiferroic Materials....160
7.1 Introduction....160
7.2 Synthesis....161
7.3 Results....162
7.3.1 Optical SHG measurements....162
7.3.2 Room temperature synchrotron X-ray powder diffraction....162
7.3.3 Room temperature neutron powder diffraction....163
7.3.3.1 Commensurate structure....163
7.3.3.2 Incommensurate structure....165
7.3.4 Magnetic characterisation of $MnSrTa_2O_7$....169
7.3.4.1 SQUID Magnetometry of $MnSrTa_2O_7$....169
7.3.4.2 Low temperature neutron powder diffraction (1 K)....171
7.3.4.3 Variable temperature neutron powder diffraction....175
7.4 Discussion....179
7.4.1 From $Li_2SrTa_2O_7$ to $MnSrTa_2O_7$: introducing magnetism into a polar phase....179
7.4.2 Structural modulation in $MnSrTa_2O_7$....180
7.5 Conclusions....181
Chapter 8 – Topochemical Cation Exchange of $Li_2SrTa_2O_7$ Using Other Divalent 3*d* Transition Metal Cations....182

8.1 Introduction....182
8.2 Synthesis....182
8.3 Results....183
8.3.1 Structural characterisation of $Cu_xLi_{2x-2}SrTa_2O_7$....183
8.3.1.1 Optical SHG measurements and complexometric titration....183
8.3.1.2 Room temperature synchrotron X-ray powder diffraction....184
8.3.1.3 Neutron powder diffraction (HRPD)....188
8.3.1.4 Neutron powder diffraction (GEM)....190
8.3.1.5 Combining the synchrotron X-ray and neutron diffraction data....193
8.3.2 Magnetic characterisation of $Cu_xLi_{2-2x}SrTa_2O_7$....193
8.3.2.1 SQUID Magnetometry of $Cu_xLi_{2-2x}SrTa_2O_7$....193
8.3.3 Structural characterisation of $CoSrTa_2O_7$....195
8.3.3.1 Optical SHG measurements and titration....195
8.3.3.2 Room temperature synchrotron X-ray powder diffraction....195
8.3.3.3 Neutron powder diffraction (HRPD)....196
8.3.4 Magnetic characterisation of $CoSrTa_2O_7$....198
8.3.4.1 SQUID Magnetometry of $CoSrTa_2O_7$....198
8.3.4.2 Low temperature neutron powder diffraction....199
8.4 Discussion....199
8.4.1 Structural comment on $CuSrTa_2O_7$ and $CoSrTa_2O_7$....199
8.4.2 Incomplete exchange of lithium....200
8.5 Conclusions....201
Chapter 9 – More Diffraction and More Than Diffraction: Synthesis and Characterisation of Some Layered Oxynitrides....203
9.1 Introduction....203
9.2 Synthesis....204
9.3 $Na_{1+x}NdTa_2O_{7-x}N_x$ and $Na_{1+x}NdNb_2O_{7-x}N_x$....205
9.3.1 Results....205
9.3.1.1 Optical SHG measurements....205
9.3.1.2 Structural characterisation of $Na_{1+x}NdTa_2O_{7-x}N_x$....206
9.3.1.2.1 Room temperature synchrotron X-ray powder diffraction....206
9.3.1.2.2 Room temperature neutron powder diffraction....207
9.3.1.3 Structural characterisation of $Na_{1+x}NdNb_2O_{7-x}N_x$....210
9.3.2 Discussion....211

9.4 $Li_{1+x}NdTa_2O_{7-x}N_x$ and $M_xLi_yNdTa_2O_{7-z}N_z$ (M = Mn/Fe/Co/Ni/Cu).....212
9.4.1 Results.....212
9.4.1.1 Optical SHG measurements.....212
9.4.1.2 Structural characterisation of $Li_{1+x}NdTa_2O_{7-x}N_x$.....212
9.4.1.3 Cation exchange reactions of $Li_{1+x}NdTa_2O_{7-x}N_x$.....213
9.4.1.4 Structural characterisation of $M_xLi_yNdTa_2O_{7-z}N_z$ (M = Mn/Fe/Co/Ni/Cu).....214
9.4.1.4.1 Structural characterisation of $Co_xLi_yNdTa_2O_{7-z}N_z$.....214
9.4.1.4.2 Structural characterisation of $Ni_xLi_yNdTa_2O_{7-z}N_z$.....218
9.4.1.5 Magnetic characterisation of $M_xLi_yNdTa_2O_{7-z}N_z$ (M = Mn/Fe/Co/Ni/Cu).....219
9.4.2 Discussion.....222
9.5 Conclusions.....223
Chapter 10 – Conclusions.....224
Appendix 1 – Index of Figures.....228
Appendix 2 – Additional Data for Chapter 5.....237
Bibliography.....240

Chapter 1 – Introduction

1.1 Perovskite and related structures

1.1.1 Perovskite structure and tolerance factor

Perovskite was named for a mineral composed of $CaTiO_3$ discovered in the 19th century. The name has later been used to describe a class of compounds with a general formula close or derived from the chemical composition ABX_3, where A and B are cations and X is an anion[1]. Since the majority of the compounds with perovskite structures are complex oxides, X will be considered as O in the following contexts. The basic perovskite structure is regarded as a 3D array of corner-sharing BO_6 octahedra, in which the A-site cations sit in the twelve coordinate sites. The 'idealised' perovskite structure is cubic, described in space group *Pm*-3*m*, one example of the aristotype structure is the room temperature structure adopted by $SrTiO_3$[2], shown in Figure 1.1. In this structure, Ti^{4+} cations sit in the center of the perfect octahedra surrounded by six O^{2-} ions and large Sr^{2+} cations lie in the cavity inside the octahedral array, surrounded by twelve O^{2-} ions.

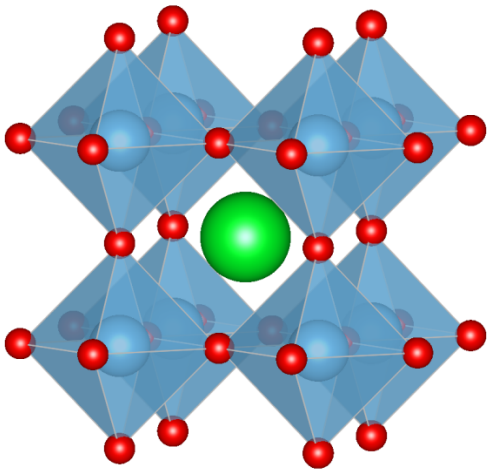


Figure 1.1. The simple cubic perovskite structure adopted by $SrTiO_3$. The green and red spheres are the Sr^{2+} and O^{2-} ions respectively. The Ti^{4+} cations are inside the polyhedra.

The BO_6 octahedra are free to tilt, distort and expand in the perovskite structure, meaning the structure is highly flexible and a large variety of cations can be accommodated in the

structure. The 'perfect' cubic perovskite is considered as an 'ideal' case and it requires a strict relationship between the ionic radii. This relationship can be parameterized by the Goldschmidt tolerance factor[3]:

$$t = \frac{< A - O >}{\sqrt{2} < B - O >} = \frac{r_A + r_O}{\sqrt{2}(r_B + r_O)}$$

where t is the tolerance factor, r_A , r_B and r_O are the ionic radii of A, B and O^{2-} ions respectively. A perovskite structure would form if t is close to one and for a 'perfect' cubic perovskite, t is equal to one. A smaller tolerance factor indicates that A cations are too small and consequently BO_6 octahedra in a perovskite structure tend to distort to compensate for the A-O bonding, leading to a low symmetry crystal structure. A detailed introduction of the octahedral tilting distortions is given in Section 1.2.

1.1.2 Ruddlesden-Popper and Dion-Jacobson structures

The Ruddlesden-Popper structure is one of the 'successors' of the 3D perovskite structure. The general formula of the Ruddlesden-Popper phases can be expressed as $(AO)(ABO_3)_n$, or $A'_2A_{n-1}B_nO_{3n+1}$ when interlayer cations (A') and conventional 12-coordinated A-site cations are different chemical species[4]. The structure can be viewed as a layered structure with 2D perovskite arrays separated by A'O rock salt layers. n is the number of slabs in each perovskite array and a 3D perovskite can be considered as a special case where $n = \infty$. In a typical Ruddlesden-Popper structure, A' cations sit in the nine-coordinate sites, A cations are located in the twelve-coordinate sites and B cations reside in the octahedral sites (Figure 1.2). The aristotype Ruddlesden-Popper phase adopts a tetragonal structure described in space group *I*4/*mmm* and adjacent perovskite units are related by translational symmetry (½, ½, ½). Depending on the cation sizes, A' cations may also alternatively sit in small pseudo-tetrahedral sites between perovskite layers. One example is $Li_2La_2Ti_3O_{10}$ in which Li^+ cations are located in pseudo-tetrahedral sites (Figure 2)[5].

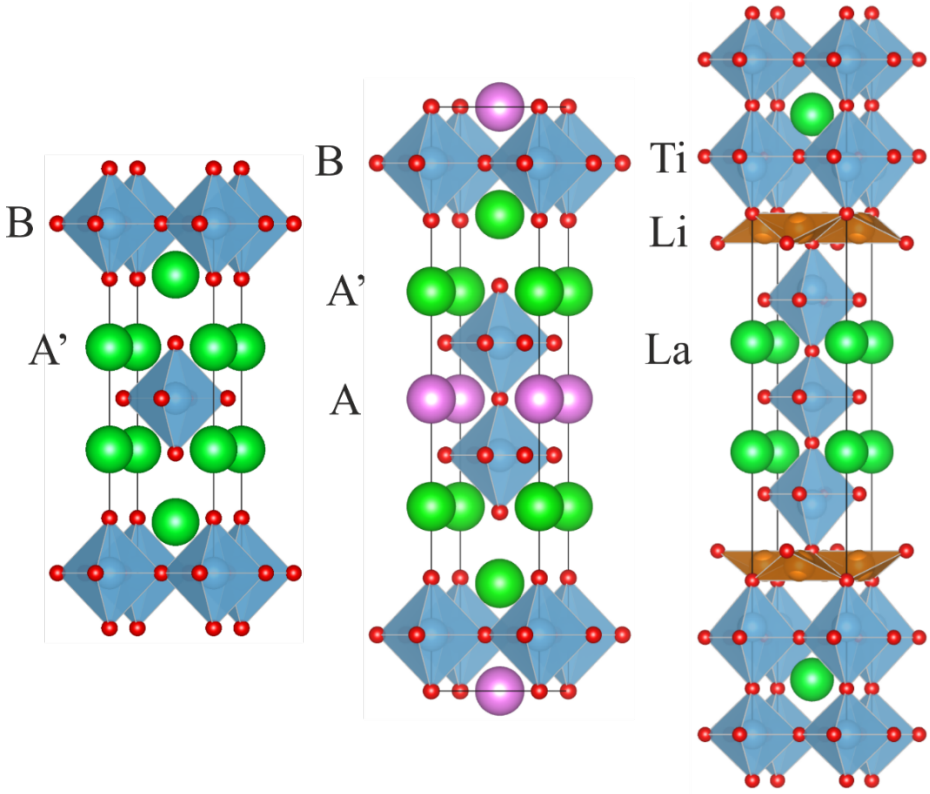


Figure 1.2. The Ruddlesden-Popper structures with molecular formula A'_2BO_4 (left), $A'_2AB_2O_7$ (middle) and $Li_2La_2Ti_3O_{10}$ (right).

Another layered 'successor' of the 3D perovskite structure is the Dion-Jacobson structure. The general formula of the Dion-Jacobson phase can be described as $A'A_{n-1}B_nO_{3n+1}$ where n is the number of slabs in the perovskite units[6, 7]. The main difference between the Dion-Jacobson phase and the Ruddlesden-Popper phase is how adjacent perovskite layers are stacked. In the aristotype Dion-Jacobson structure, adjacent perovskite layers have a primitive stacking arrangement along the stacking axis and the structure can be described in space group *P*4/*mmm* (Figure 1.3). The Dion-Jacobson structure forms for large A' cations such as Cs^+ and Rb^+ and the interlayer cations sit in the eight-coordinate sites. The large monovalent interlayer A' cations in the Dion-Jacobson phases are very mobile due to the low charge density and the small lattice energy, making the Dion-Jacobson phases suitable precursors for redox-neutral cation exchange reactions.

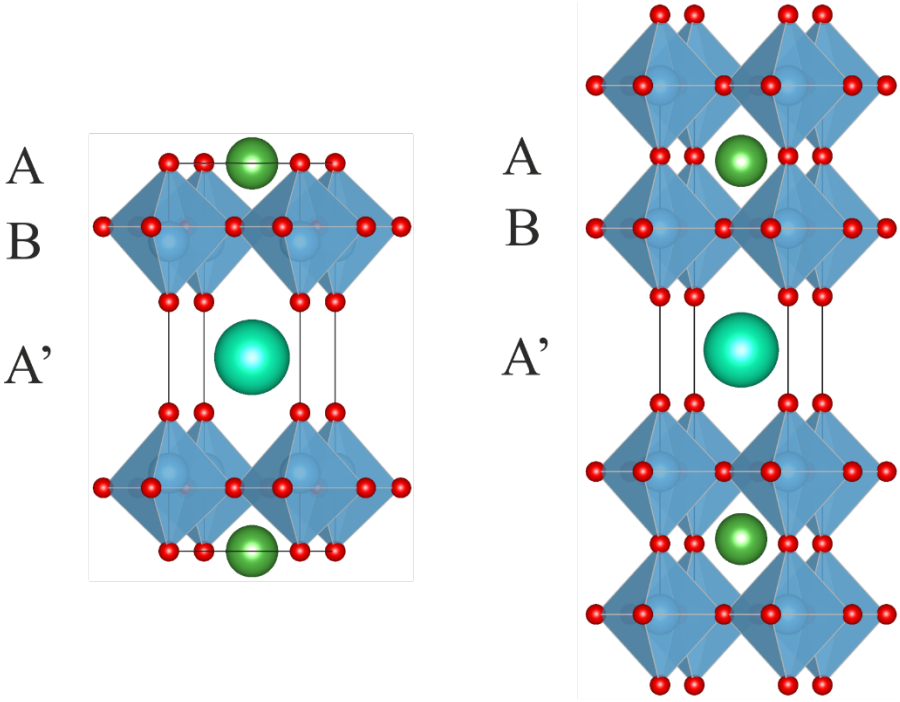


Figure 1.3. The n = 2 (left) and n = 3 (right) Dion-Jacobson structures.

1.2 Octahedral tilting distortions and Glazer notation system

The tilting distortions of the BO_6 octahedra in the perovskite structure occur due to the small sizes of A cations and the need to compensate for the A-site bonding. These tilting distortions can be described using the Glazer notation system[8, 9]. In a 3D perovskite structure, the BO_6 octahedra can rotate around all three Cartesian axes. Figure 1.4 shows two types of tilting distortions the BO_6 octahedra can adopt along the *z*-axis. It can be seen that due to the corner-sharing nature of the structure, the octahedral tilting distortions in a single *xy* plane are collective, and the adjacent octahedra tilt cooperatively, meaning if a selected octahedron has a clockwise tilting distortion, its neighbouring four octahedra in the *xy* plane must have an anti-clockwise tilting distortion. However, the adjacent octahedra along the *z* direction are not constrained and they can tilt either clockwise or anti-clockwise. In the Glazer notation system, if the adjacent octahedra tilt in opposite directions along a Cartesian axis (left-hand-side structure in Figure 1.4), it is described as an out-of-phase tilting distortion along this direction; if they tilt in the same direction, it is described as an

in-phase tilting distortion (right-hand-side structure in Figure 1.4). The out-of-phase tilting and the in-phase tilting distortions are described by a negative (-) and a positive (+) superscript respectively. The magnitude of the tilting distortion is described by letters *a*, *b*, or *c*. Different letters mean different magnitudes of tilting distortions. For example, an $a^-a^-a^-$ notation means the tilting distortions along all three Cartesian axes are out-of-phase with the same magnitude. An $a^-b^-c^-$ notation means the tilting distortions along all three Cartesian axes are out-of-phase but with three different magnitudes. A superscript '0' is used when there is no tilting distortion therefore under Glazer notation system, an undistorted, aristotype perovskite structure is described as $a^0a^0a^0$. The most commonly found tilting distortion in 3D perovskites is $a^-a^-c^+$, suggesting there are out-of-phase tilting distortions along both the *x* and *y* directions with the same magnitude and an in-phase tilting distortion along the *z* direction with a different magnitude.

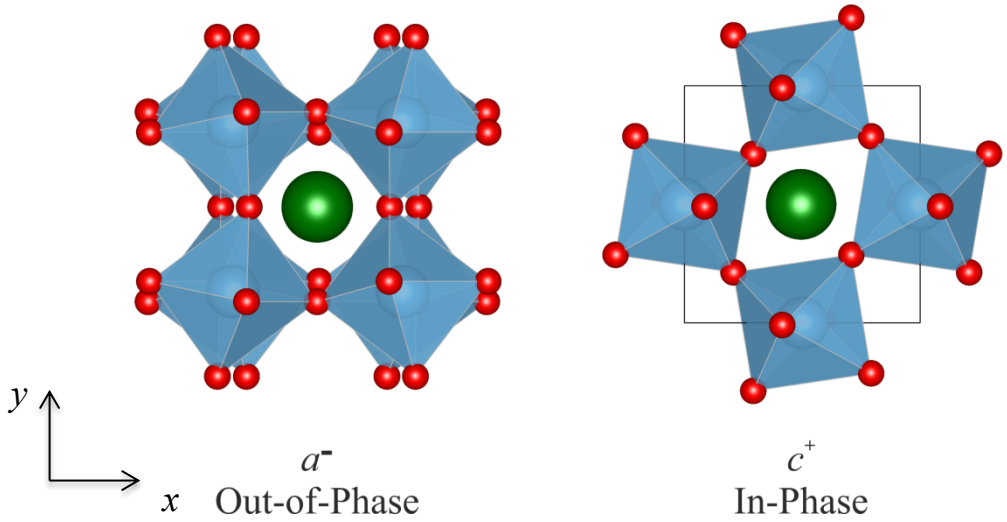


Figure 1.4. Out-of-phase (left) and in-phase (right) tilting distortions along the *z* axis.

In the Ruddlesden-Popper and Dion-Jacobson phases, the tilting distortions in each perovskite layer can be described in the same way as in the 3D perovskites. However, there is an extra complexity: it is not necessary for the adjacent perovskite layers to adopt exactly the same tilting distortion. Figure 1.5 shows the ambient temperature crystal structure of $RbNdNb_2O_7$[10] (Chapters 3 and 5) described in space group *I*2*cm*. The tilting distortions in

adjacent layers are not exactly the same and the structure does not have a primitive stacking arrangement. The NbO_6 octahedra in sheet 1 and sheet 3 tilt in the opposite directions, so do sheet 2 and sheet 4, despite the same type of local tilting distortion ($a^-a^-c^+$) in the two layers. As a consequence, $RbNdNb_2O_7$ is deemed to have an $a^-a^-c^+/-(a^-a^-c^+)$ tilting distortion, the negative sign before the second ($a^-a^-c^+$) indicates that the tilting distortions in layer II are in the opposite direction with respect to layer I along all three Cartesian axes.

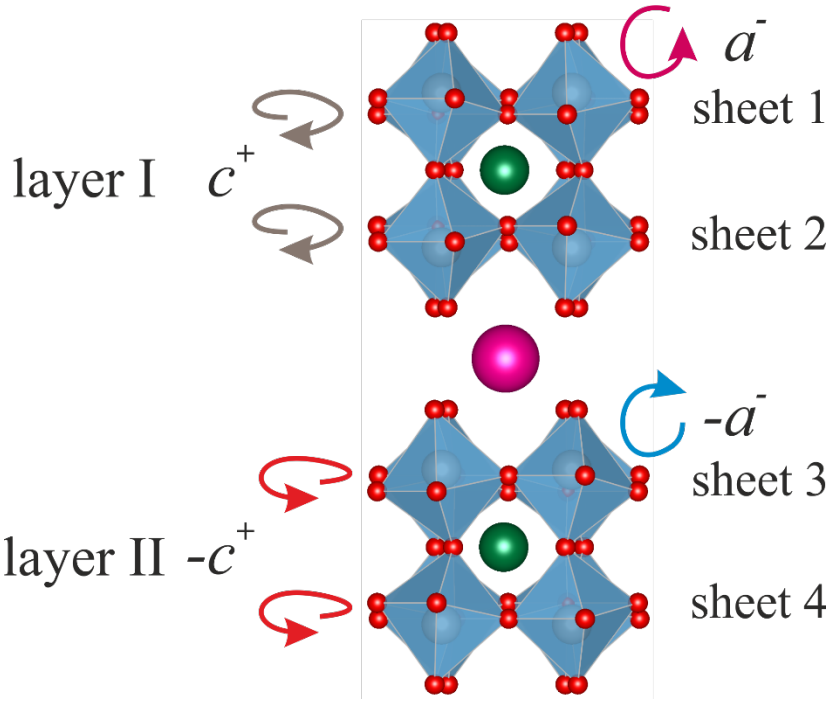


Figure 1.5. The $a^-a^-c^+/-(a^-a^-c^+)$ tilting distortion adopted by $RbNdNb_2O_7$.

Another alternative descriptor for the octahedral tilting distortion is the Aleksandrov and Bartolome system[11]. In this system, the out-of-phase tilt and the in-phase tilt are described as Φ and Ψ respectively. Therefore in the Aleksandrov and Bartolome system, $a^-a^-c^+$ is expressed as ΦΦΨ and $a^-b^-c^+$ is written as $\Phi_1\Phi_2\Psi$. Both the Glazer notation system and the Aleksandrov and Bartolome system will be used throughout this thesis.

It can be very challenging to directly deduce the structural symmetry of the Ruddlesden-Popper and Dion-Jacobson phases from the octahedral tilting distortions because the distortions involve the displacements of many oxide ions and their displacements can be very complex. Symmetry analysis is therefore performed using the ISODISTORT

software[12] to relate the tilting distortions to their corresponding space groups. Detailed analysis will be given in Chapters 4 and 5.

1.3 Ferroelectric and magnetoelectric multiferroic materials

1.3.1 Ferroelectric materials

Ferroelectric materials exhibit a spontaneous electric polarization, which can be reversed by an external electric field. Ferroelectric materials have a high electric permittivity, which makes them good materials for capacitors. The switchable polarization means they can also be used in memory storage devices[13].

It is obvious that in order to have a spontaneous electric polarization, ferroelectric materials are required to adopt non-centrosymmetric (NCS) crystal structures[14]. In a centrosymmetric compound, the existence of inversion symmetry means that even if local electric dipoles exist, they are present in pairs, which cancel each other out, hence centrosymmetric phases have zero macroscopic polarization. Therefore the primary structural requirement of a ferroelectric compound is that it cannot have inversion symmetry. However, lacking inversion symmetry does not mean a phase is polar. For example, a methane molecule has a perfect tetrahedral geometry, which is non-centrosymmetric, but it is not polar. It is summarized that only a small group of non-centrosymmetric crystal classes are polar, therefore in order to be polar, a compound needs to crystallize in some specific crystal classes (Figure 1.6)[14, 15].

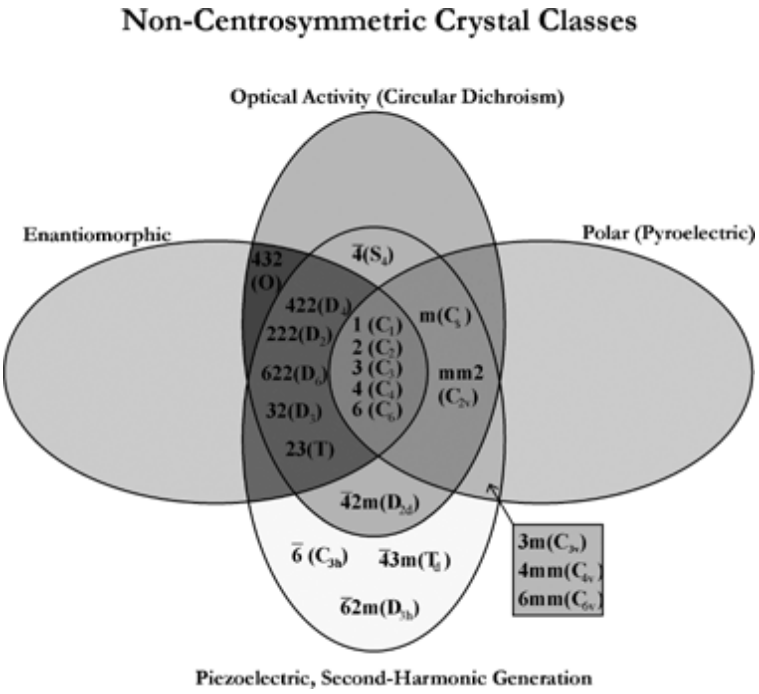
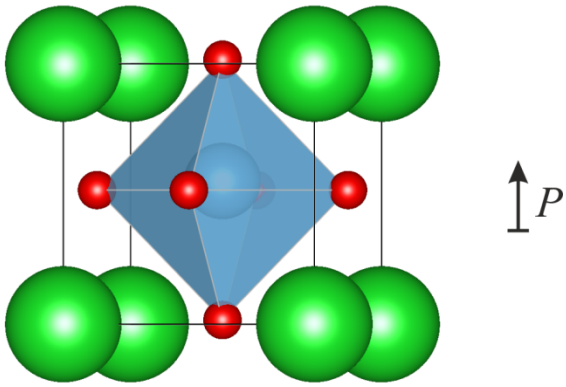


Figure 1.6. Relationships between different physical properties in non-centrosymmetric crystal classes[15].

Preparing solids with non-centrosymmetric crystal structures is very challenging because crystalline solids tend to form centrosymmetric structures which are in general more stable than asymmetric analogues. In order to overcome this problem, it is necessary to introduce other interactions which favour non-centrosymmetric structures. The most common approach to break the inversion symmetry in a solid is the use of a second order Jahn-Teller distortion[16]. It is observed that if a transition metal possessing a d^0 electronic configuration resides in a perfect octahedron of oxide ions, it tends to displace away from the center of the octahedron due to an energetic benefit of a hybridisation of the empty transition metal *d* orbitals and the filled oxygen *p* orbitals[17]. One typical example which exhibits such a second order Jahn-Teller distortion is $BaTiO_3$. At room temperature, the Ti^{4+} cation distorts towards one of the oxide ions, lifting the symmetry to a non-centrosymmetric *P*4*mm* structure[18] (Figure 1.7).



$BaTiO_3$
P4mm

Figure 1.7. Room temperature *P4mm* structure of $BaTiO_3$. Green and red spheres are the Ba^{2+} and O^{2-} ions respectively. The Ti^{4+} cation is in the octahedron and slightly displaced away from the center, generating a net polarisation.

An alternative but equivalent approach is to use *p* block metal cations with 'stereo-active' lone pairs. The hybridisation of the metal *s* and *p* orbitals with the oxide *p* orbitals stabilizes the structure and breaks the inversion symmetry[17]. One example of this 'lone-pair' method is $PbTiO_3$[19].

1.3.2 Magnetoelectric multiferroic materials

Magnetoelectric multiferroics are materials which are simultaneously ferroelectric and ferromagnetic (or antiferromagnetic)[20]. In addition, multiferroic materials require some coupling between the two properties, namely the magnetoelectric effect: an external electric field induces a proportional magnetization, and vice versa. Multiferroic materials can be used in multiple-state memory devices, spintronic devices and magnetic sensors[13]. One typical example of multiferroic compounds is $BiFeO_3$, in which ferroelectricity is induced by the stereo-active Bi^{3+} cations and the antiferromagnetic order is due to the Fe^{3+} cations[21, 22].

As discussed in the previous section, a primary requirement for ferroelectricity is the lack of inversion symmetry. The second order Jahn-Teller approach, which requires d^0 or ns^2 electronic configurations, is incompatible with magnetism which requires unpaired *d*

electrons. The contraindicated requirements of ferroelectricity and magnetism, as well as the difficulty of making non-centrosymmetric solids, mean preparing multiferroic materials is extremely challenging. There has therefore been a great effort to find alternative ways to prepare solids with non-centrosymmetric structures, especially the ones without special electronic requirements. One of the most promising approaches is the use of the trilinear coupling mechanism, which involves a combination of lattice distortions and cation displacements to break inversion symmetry in the perovskite structure and generate macroscopic polarization[13, 23].

1.4 Trilinear coupling mechanism

The definition of trilinear coupling mechanism can be described as: two non-polar lattice distortion modes couple to a polar distortion mode to generate a polar structure[23-25]. In a perovskite structure, these non-polar lattice distortions can be the octahedral tilting distortions and the polar mode is a cation displacement, therefore it is also called the octahedral tilting approach. It is considered as an attractive approach to prepare polar layered perovskites because there is no specific electronic requirement on the cations in the material. In order to better explain how this approach leads to a polar structure, an example of $CsNdTa_2O_7$ is given below[10].

$CsNdTa_2O_7$ is an n = 2 Dion-Jacobson phase and was previously reported to adopt an aristotype $P4/mmm$ structure at ambient temperature[26] (Figure 1.8). However, it is actually polar due to the trilinear coupling mechanism[10] and the mechanism can be understood as follows**:** The Goldschmidt tolerance factor t is equal to 0.925 for the $NdTa_2O_7$ perovskite double layers, indicating the perovskite units tend to have tilting distortions. The tilting distortion is described as $a^-a^-c^+$ under the Glazer notation system, which is a linear combination of an $a^-a^-c^0$ tilting mode and an $a^0a^0c^+$ mode. Although these two tilting

modes are non-polar individually, with the $a^-a^-c^0$ tilting mode leading to a centrosymmetric *Pmam* structure and the $a^0a^0c^+$ tilting distortion mode leading to a centrosymmetric *P*4/*mbm* structure, their combination leads to a structure with an $a^-a^-c^+$ tilting distortion which can only be described by a polar space group $P2_1am$. The coupling between the two non-polar modes allows a third, polar mode (cation displacement mode) to appear, which leads to the bulk polarization in the material (Figure 1.8). It should be noticed that without the third, polar mode, even though the structure is described by a polar space group, the material itself is not polar.

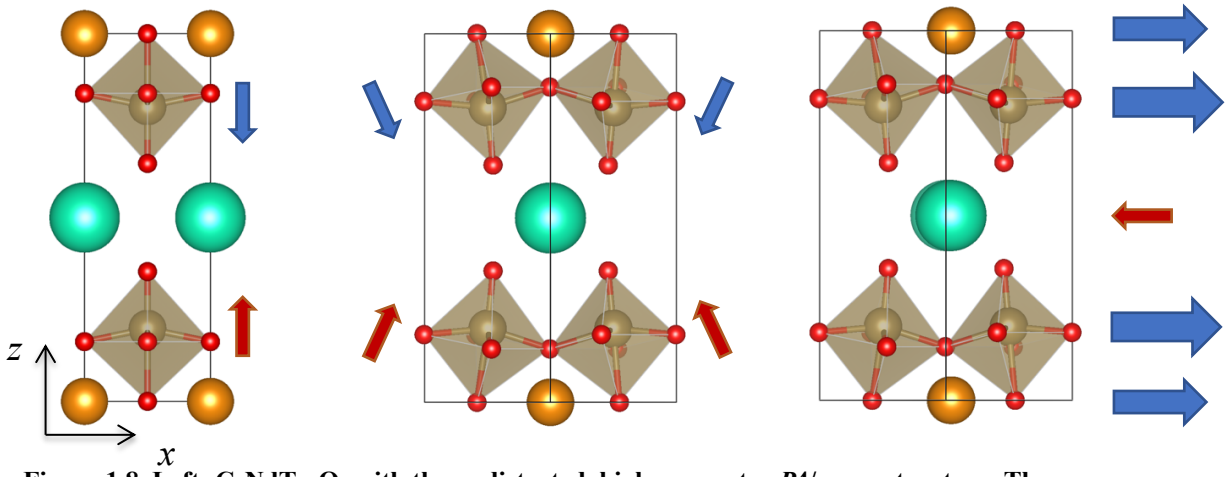


Figure 1.8. Left: $CsNdTa_2O_7$ with the undistorted, high-symmetry *P*4/*mmm* structure. The arrows indicate the local dipoles as a result of the displacement of Ta^{5+} cations along the *z*-axis due to the second order Jahn-Teller effect. These two dipoles are the same in magnitudes but opposite in directions, hence no net macroscopic polarization.
Middle: $CsNdTa_2O_7$ with a distorted, low-symmetry $P2_1am$ structure. Although the tilting distortions of the TaO_6 octahedra lead to a structure described by a polar space group, the bulk phase is still non-polar in absence of the polar mode.
Right: $CsNdTa_2O_7$ with a distorted, low-symmetry $P2_1am$ structure with extra cation displacements. This is the 'real' room temperature structure. The macroscopic polarization is non-zero, thus polar.

It can be seen from the example of $CsNdTa_2O_7$ that the driving force for the symmetry breaking is the octahedral tilting distortions. This is a pure geometrical rather than electronic consideration and there is no restriction for using transition metal cations with partially filled *d* orbitals.

The trilinear coupling mechanism is more plausible for layered perovskites, especially n = 2 layered perovskites. It is very challenging to prepare polar 3D perovskites utilizing the

trilinear coupling mechanism because it requires an extra cation order. Collective tilting distortions in a simple 3D perovskite with formula ABO_3 lower the structural symmetry and the potential A-site cation movement can generate local electric dipoles but the reciprocal nature of the octahedral tilting distortions means these local dipoles cancel across the material. Using $SrSnO_3$ as an example, it adopts a low-symmetry structure in space group *Pnam* with an $a^-a^-c^+$ tilting distortion[27] (Figure 1.9). The polarisation in alternative layers is the same in magnitude but opposite in directions, hence there is no macroscopic polarisation. One obvious solution is to make distorted $AA'B_2O_6$ perovskites with ordered AO/A'O layers so that electric dipoles in alternative layers no longer cancel exactly. One theoretically proposed polar compound is $Sr_{0.5}Ba_{0.5}SnO_3$ with ordered Ba and Sr layers[28] (Figure 1.9). Since the magnitudes of the polarization induced in the Sr-O and Ba-O layers are not identical, the cancellation is incomplete and there is a residual polarization. However, making cation-ordered perovskites is very challenging and hence the octahedral tilting approach is not very suitable for making polar 3D perovskites.

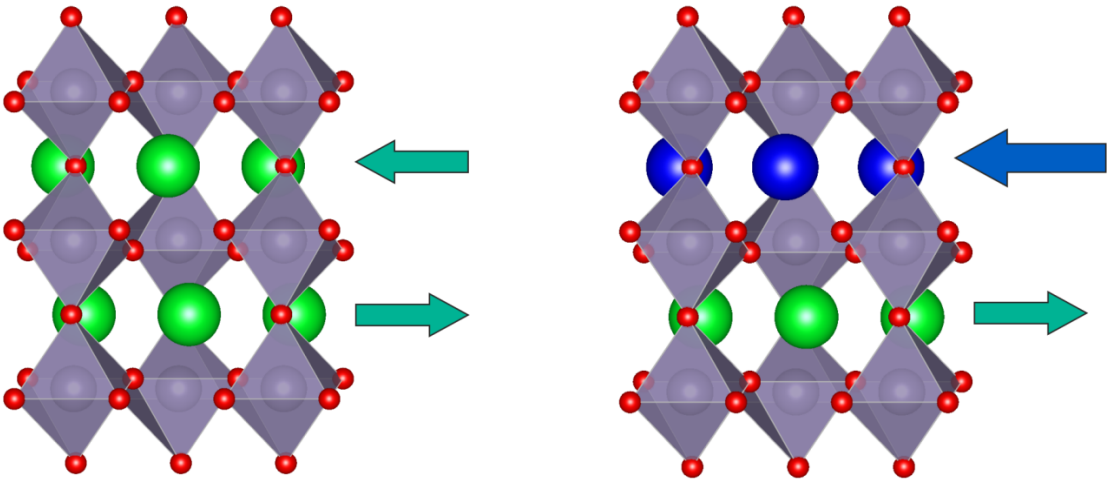


Figure 1.9. Left: Local electric dipoles in $SrSnO_3$ in space group *Pnam*; Right: Local electric dipoles in theoretically proposed $Ba_{0.5}Sr_{0.5}SnO_3$ in space group $P2_1am$. Both structures have the same $a^-a^-c^+$ tilting distortion.

In contrast to 3D perovskites, the two dimensional connectivity in $n = 2$ layered perovskites means the local electric dipoles do not necessarily cancel out, even without a complex cation order. One typical example is the polar $n = 2$ Ruddlesden-Popper phase $Ca_3Mn_2O_7$.

It adopts a polar $A2_1am$ structure at room temperature with an $a^-a^-c^+/a^-a^-c^+$ tilting distortion[29] (Figure 1.10). Each perovskite block has three CaO sheets, which means although the Ca^{2+} cations are displaced in a reciprocal manner, they do not cancel in a single perovskite slab and there is a residual polarisation in each perovskite slab. If the adjacent perovskite slab has the same 'sign' of the tilting distortion, as in the $Ca_3Mn_2O_7$ case, the same residual polarisation is generated and the bulk phase is polar. It should be noticed that the adjacent perovskite slab can generate a residual polarization with the same magnitude but an opposite direction, meaning the local polarisation cancels across the material and the bulk phase is anti-polar (non-polar). One example of an anti-polar compound is $La_3Ni_2O_{5.5}F_{3.5}$ (Figure 1.9) in space group *Pnam* with an $a^-a^-c^+/a^-a^--c^+$ tilting distortion[30]. It can be seen that statistically there is a 50% chance that local polarisation induced in adjacent perovskite layers do not cancel and result in a macroscopic polarization. There must be chemical reasons for cancelling/not cancelling local polarization across layers. This is one of the topics this thesis is focused on. In addition, anti-polar perovskite compounds themselves are found also to be technologically useful[31].

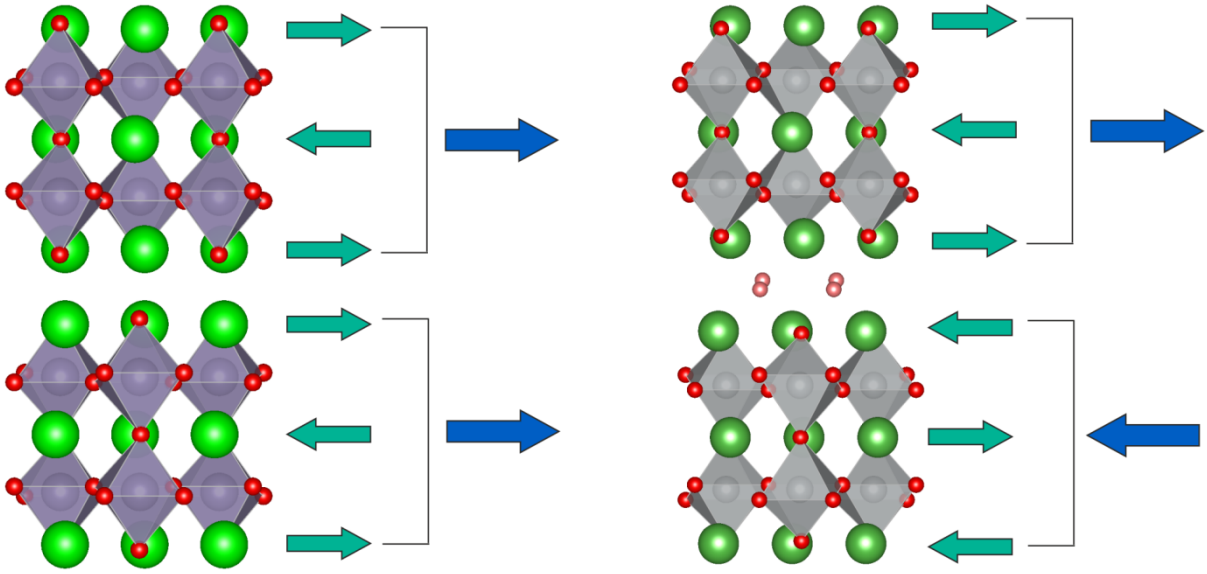


Figure 1.10. Left: Polar $Ca_3Mn_2O_7$ in space group $A2_1am$ with an $a^-a^-c^+/a^-a^-c^+$ tilting distortion; Right: Anti-polar (non-polar) $La_3Ni_2O_{5.5}F_{3.5}$ in space group *Pnam* with an $a^-a^-c^+/a^-a^--c^+$ tilting distortion. Green arrows show the electric dipoles generated in each metal-oxide layer; Blue arrows show the electric dipoles generated in each perovskite layer.

The octahedral tilting distortion approach is more suitable for n = 2 layered perovskite phases than their n = 1 and n = 3 analogues. As shown in Figure 1.2, there is no 12-coordinate site in the structure to accommodate the A cations in n = 1 layered perovskites. Therefore the size-mismatch argument between the A-site and B-site cations is no longer reproducible and the structure does not tend to tilt like in the n = 2 case. The n = 3 phases have even numbers of A-O layers in each perovskite block and hence local polarization cancel in each perovskite block. However, there are examples of polar n = 1 and n = 3 layered perovskite phases but more complex mechanisms are involved to explain their macroscopic polarization[32-34].

1.5 Topochemical reactions

1.5.1 Traditional synthesis of crystalline solids

A characteristic feature of solids, compared to liquids and gases, is the low mobility of the chemical species of which they are made, due to the strong bonding interactions between ions. Consequently traditional synthesis of complex oxides requires very high reaction temperatures (normally more than 1000 °C) to overcome these diffusion barriers. Although the traditional ceramic synthesis has been demonstrated to be extremely useful and has produced countless functional materials, there are at least two drawbacks: 1. High temperature reactions only lead to the formation of the thermodynamically stable products and metastable phases, which may have interesting properties, are not seen. This severely limits the range of materials solid-state chemists can make. 2. Researchers have very little ability to predict the reaction products of thermodynamically controlled synthesis because there is generally no structural relation between the reactants and the products. It is therefore difficult to have a rational design of the reaction products via traditional ceramic synthesis. In response to these undesired features, several ‘soft’ reaction techniques have

been developed. These 'soft' reactions require lower reaction temperatures and allow the synthesis of metastable phases which are inaccessible using the high-temperature ceramic synthesis. The low-temperature methods are normally 'topochemical' as they exploit the high mobility of particular ions in a solid and only modify parts of the existing structure, meaning many of the structural features of the parent solids are retained. The topochemical approaches give solid-state chemists more opportunities to have a rational design of the products with desired properties.

1.5.2 Topochemical cation exchange reactions

Topochemical cation exchange reactions are one of the most common low-temperature solid state reactions[35]. It is a redox-neutral reaction as there is no change in the oxidation states of the ions in the host lattices. This topochemical reaction has several requirements[36]: 1. The cations to be intercalated and extracted must have the highest mobility in the solid and are mobile enough to overcome the diffusion barrier at the reaction temperature; 2. The product must be a kinetically stable phase so that it can survive at the reaction temperature; 3. The cation exchange reaction must be spontaneous. For example, the reaction can be driven by the formation of stable by-products such as water. These requirements make layered Dion-Jacobson and Ruddlesden-Popper phases excellent candidates for topochemical cation exchange reactions. The open layers between perovskite slabs mean it is easier for the interlayer cations to diffuse. Consequently, the interlayer cations are more exchangeable compared to the more tightly-bonded cations in the perovskite slabs. Cation exchange reactions of Dion-Jacobson phases and Ruddlesden-Popper phases are usually accompanied by an increase in lattice energy by substituting large cations with small cations, for example substituting Rb^+ with Li^+ cations[37]. In addition to simple cation substitution reactions, it is also possible to intercalate charged layers of metal salts into the layered framework via topochemical cation exchange reactions. Figure 1.11 shows a

reaction from an n = 2 Dion-Jacobson phase $RbLaNb_2O_7$ to $(CuCl)LaNb_2O_7$ and the product contains sheets of $(CuCl)^+$ between perovskite slabs[38].

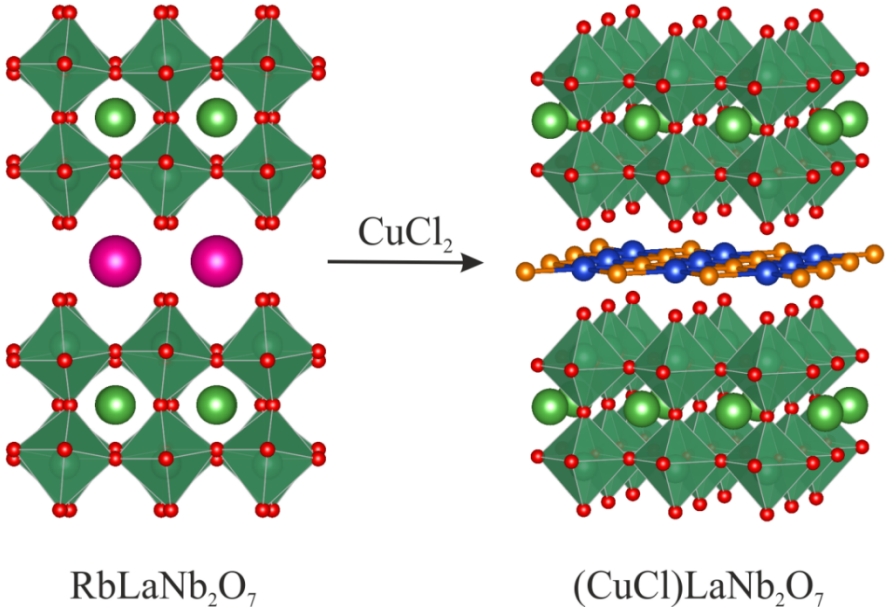


Figure 1.11. A cation exchange reaction from $RbLaNb_2O_7$ to $(CuCl)LaNb_2O_7$. The Rb^+ cations are substituted by $(CuCl)^+$ sheets.

The core of this project is to investigate how cation exchange reactions can be utilized to make novel ferroelectric and multiferroic materials. In addition, it is interesting to study if substituting one cation with another would lead to any local and/or bulk structure change.

Chapter 2 – Experimental Methods and Techniques

2.1 Synthesis methods

2.1.1 Ceramic synthesis

Traditionally complex oxides are synthesised using a high-temperature ceramic synthesis, which involves heating a mixture of metal oxides and/or metal salts at a high temperature (typically more than 1000 °C). In this approach, ions need to diffuse relatively large distances (typically several microns) to reach the grain boundary in order for a reaction to occur. The low mobility of the ions in solids means the ceramic synthesis is very slow and reactions normally takes days even weeks to reach completion. A high reaction temperature is required to overcome the large energy barriers to diffusion, and even then ionic mobility is low. Multiple grindings and pellet pressing are required in order to achieve good sample homogeneity and to increase the reaction speed. If a reactant has a high vapour pressure at the reaction temperature, additional quantities of the reactant (typically 5% to 20% extra) are added at the beginning of the reaction in order to compensate for the loss at high temperatures.

2.1.2 Cation exchange reactions

Cation exchange reactions are performed by mixing the precursors with metal nitrates or halides. Depending on the properties of the reactants, cation exchange reactions demonstrated in this thesis were carried out in either open-ended tubes, sealed glass ampules or using the venting system, under an inert atmosphere.

2.1.2.1 Open-ended tubes

Open-ended tubes are suitable for reactants which melt and are air-stable at the reaction temperature. Ground reagents were placed in an open-ended tube which was placed vertically in a low temperature furnace, as shown in Figure 2.1. In this thesis, this setup is

used for the cation exchange reactions using $LiNO_3$ or $NaNO_3$. Both nitrates have low melting points (255 °C for $LiNO_3$ and 308°C for $NaNO_3$)[39] and the cation exchange reactions using these two nitrates were carried out at temperatures higher than their melting points, with fused silica tubes. Since both nitrates are hygroscopic, the tube needs to have one open end so that water vapour can be safely expelled.

As the nitrates are both liquids at the reaction temperature, the diffusion rates of the Na^+ and Li^+ cations are much faster than the conventional solid-solid reaction. Consequently, the cation exchange reactions involving melted salts are normally very quick, typically completing in hours rather than days. After the reaction, the cation-exchanged products were washed with distilled water to remove the remaining nitrates.

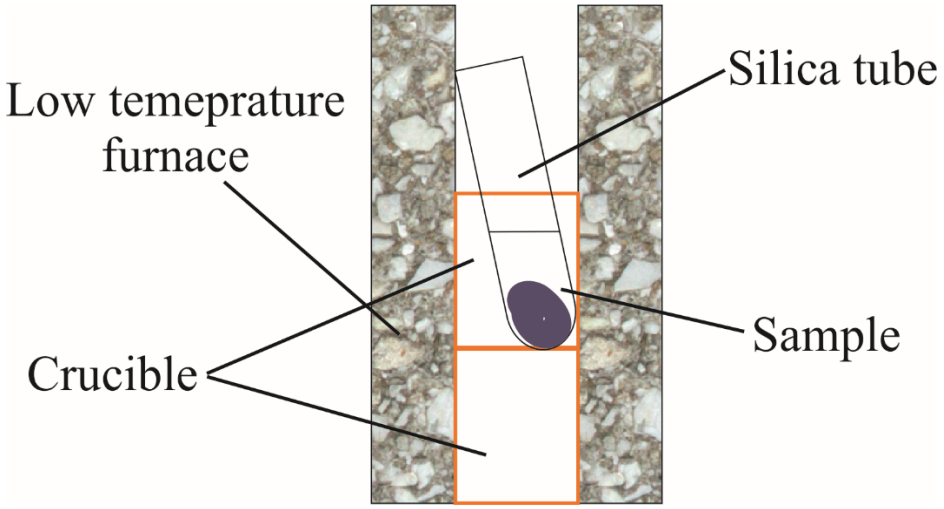


Figure 2.1. Setup for a cation exchange reaction using open-ended silica tubes.

2.1.2.2 Sealed glass ampules

Sealed glass ampules were used for cation exchange reactions using metal halides as these reagents react with oxygen to form metal oxides at elevated temperatures. The perovskite precursors and 5 molar equivalents of an anhydrous 3*d* transition metal halide were ground and mixed using an agate pestle and mortar in an argon-filled glovebox. The mixture was then loaded into a 9 mm silica tube and sealed with a Young's tap. The tube was then evacuated to 1.0×10^{-2} mbar and sealed using a blowtorch to form a glass ampule. The

ampule was then placed in a low temperature furnace, heated to the reaction temperature (typically between 300 °C and 400 °C) with a ramping rate 4 °C/min and kept at the reaction temperature for several days before being cooled to room temperature. After each heating cycle, the glass ampule was broken in the glovebox, reground and the reaction progress was analysed by performing an X-ray diffraction measurement. If the reaction was deemed to have reached completion, the mixture was thoroughly washed with distilled water to remove the remaining metal halides and dried at 140 °C for 12 hours.

2.1.2.3 Venting system

Metal halides used for the cation exchange reactions usually contain small amounts of water. The water vapour can be problematic in a sealed ampoule and cause an explosion. This is especially true when a synthesis of a large-scale sample (~4 g) is needed. Consequently, a venting system was established to remove the water vapour as well as to prevent the material from reacting with air. Figure 2.2 shows a setup of a venting system. Samples were prepared as described in Section 2.1.2.2 and loaded into a 12 mm Pyrex tube. The tube was sealed with a Young's tap inside the glove box, connected to flowing argon and horizontally placed in a low temperature furnace. The system was purged for 30 minutes, heated to the reaction temperature (typically between 300 °C and 400 °C) with a ramping rate 3 °C/min and maintained at the reaction temperature for several days before being cooled to room temperature. After each heating cycle, the tube was evacuated and transferred into the glovebox. The mixture was reground and the reaction progress was monitored by X-ray diffraction. If the reaction was deemed to have reached completion, the mixture was washed with distilled water to remove remaining metal halides and dried at 140 °C for 12 hours.

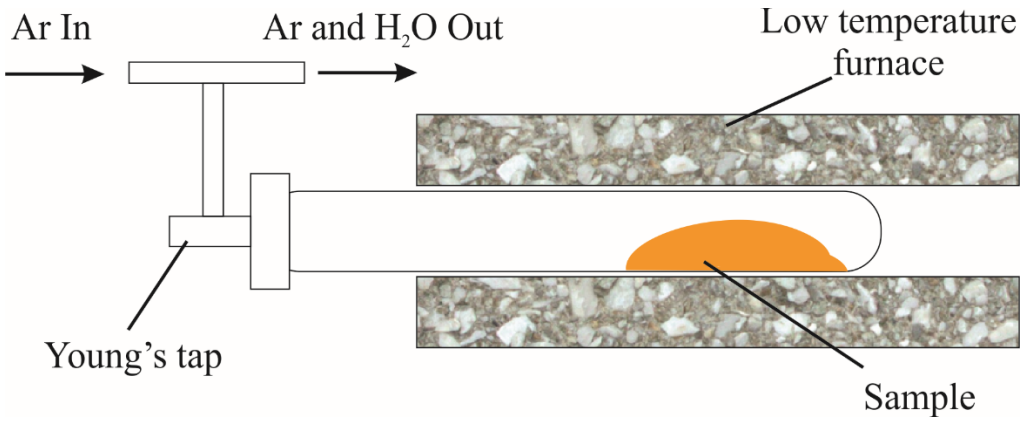


Figure 2.2. Setup for the cation exchange reaction using a venting system.

2.1.3 Reactions under flowing NH_3

Perovskites with mixed oxides and nitrides in the anion sites, namely oxynitrides, can be prepared by heating the oxide precursors with the corresponding metal carbonates under flowing NH_3 at moderate temperatures. For example, $Na_{1+x}NdTaO_{7-x}N_x$ can be synthesized by heating a mixture of $NaNdTa_2O_7$ and Na_2CO_3 at 450 °C under flowing NH_3. The reaction setup is shown in Figure 2.3. Samples were placed in an alumina boat crucible and sealed in a silica tube with both ends caped with T-junction taps. The tube was then placed in a clamshell furnace with NH_3 gas flowing apparatus attached to the T-junction taps. The gas flowing rate was controlled by a gas flow meter connected to the inlet T-junction tap. The reaction was carried out in a fume hood due to the toxicity of NH_3. The system was purged with NH_3 for 30 minutes and then heated to the reaction temperature with a ramping rate 3 °C/min. After each heating cycle, the mixture was reground and the reaction progress was monitored by X-ray diffraction. Once the reaction was deemed to have reached completion, the mixture was thoroughly washed with distilled water and dried at 140 °C for 12 hours.

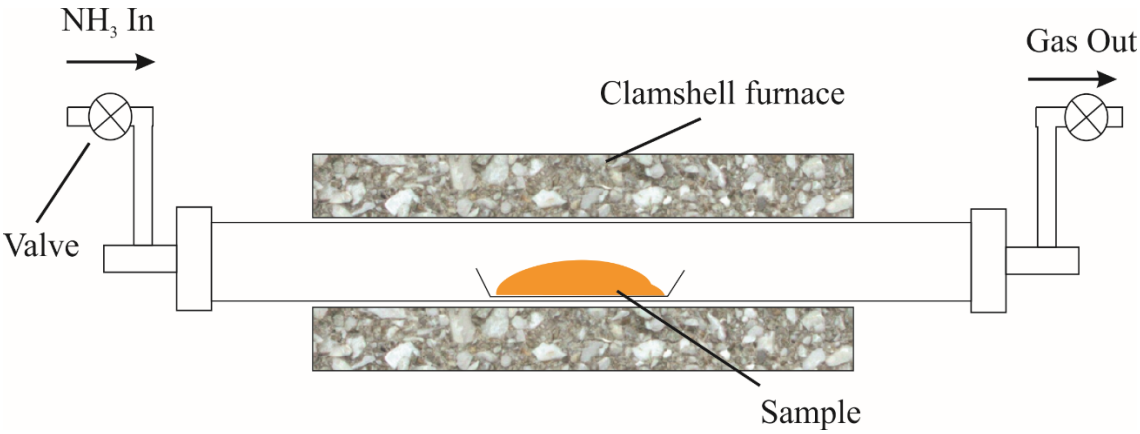


Figure 2.3. Horizontal flow system used to prepare oxynitrides.

2.1.4 Drying hygroscopic products

Some products in this thesis are hygroscopic and they cannot be fully dried at 140 °C in the drying oven. The absorbed water is problematic in two aspects: 1. The crystal structure of the hydrated products might be different to the anhydrous version. In this case water molecules sit between perovskite double layers, leading to an expanded *c* lattice (assuming *z* is the stacking axis) and a different crystal structure; 2. The strong incoherent and inelastic scattering from the hydrogen atom means the quality of the neutron diffraction data collected from the hydrated sample will be poor, making the structural characterisation more difficult. Therefore for these hydrated compounds, a further drying process is necessary.

The drying system has the same setup as Figure 2.3. The only difference is that the flowing gas is argon rather than NH_3. After the normal washing and drying process, the hydrated product was heated to 300 °C at 3 °C/min, kept at this temperature for 12 hours under flowing argon and then cooled to room temperature. The tube was evacuated and transferred into the glovebox. The anhydrous product was stored in the glovebox to avoid any further hydration.

2.2 Powder diffraction

Powder diffraction is undoubtedly the most important technique in solid-state chemistry. X-ray and neutron powder diffraction techniques are essential for the structural identification of a crystalline solid.

Diffraction of X-ray and neutron radiation arises from the periodic arrangement of atoms in a crystal. The periodically arranged atoms generate an array of crystal planes. Each set of the lattice plane has an equal distance, *d*, from its neighbouring planes. A beam of incident radiation with a wavelength similar to *d* can be diffracted by the crystal planes according to Bragg's Law[40]:

$$n\lambda = 2d_{hkl}\sin\theta$$

where λ is the wavelength of the incident beam, d_{hkl} is the inter-planar distance, θ is the angle between the incident (or diffracted) beam and the lattice plane, *n* is an integer. A cartoon illustration of the derivation of Bragg's Law is shown in Figure 2.4.

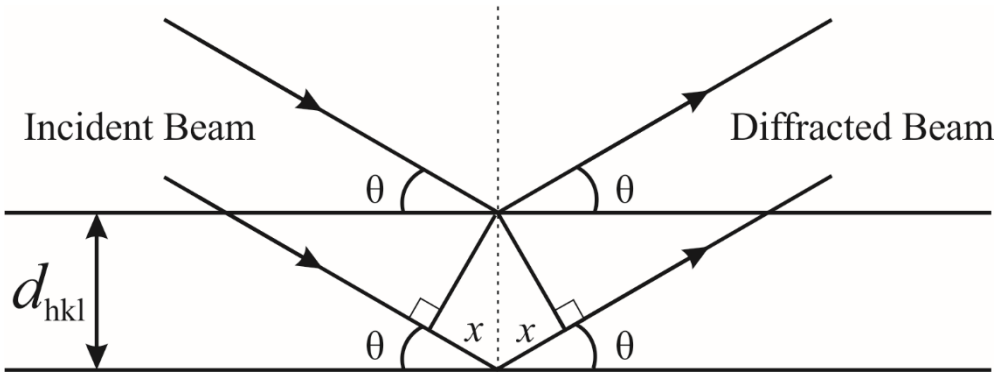


Figure 2.4. A cartoon illustration of the Bragg's Law.

The assignment of the hkl indices of a given set of lattice plane is defined by the size and shape of the unit cell. Therefore different choices of the unit cells lead to different hkl values. The intensity of a reflection is given by:

$$I_{hkl} \propto mPLAF_{hkl}^2$$

where m is the reflection multiplicity, P is the polarisation factor, L is the Lorentz factor, A is the absorption factor and F_{hkl} is the structure factor. The structure factor contains the information of how atoms are arranged in the unit cell and it can be described as[41]:

$$\boldsymbol{F_{hkl} = \sum_{n} f_n \exp[2\pi i(hx_n + ky_n + lz_n)] \exp\left(\frac{-8\pi^2 U_{iso_n} \sin^2\theta_{hkl}}{\lambda^2}\right)}$$

where f_n is the scattering factor of the nth atom, x_n, y_n and z_n are the atomic fraction coordinates of the nth atom in the unit cell and U_{iso_n} is the atomic isotropic thermal displacement factor of the nth atom. The second exponential term suggests that there is a decrease in intensity as a function of increased scattering angle.

2.2.1 X-ray powder diffraction

X-rays have a similar wavelength to the spacing of lattice planes in a crystal, which makes X-ray diffraction a suitable tool to study the crystal structure of a crystalline solid. X-ray powder diffraction is a readily available technique, and is used for routine crystal structural characterisation and to monitor the progress of a reaction. Since the incident X-rays interact with the electron densities of the atoms, the X-ray scattering factor (f_n) of a given atom is related to its atomic number. The X-ray scattering factor of a given atom also depends on the scattering angle and it decreases rapidly with increased scattering angle[42]. Consequently, X-ray diffraction is insensitive to light elements especially when heavy metals are also present. In addition, the weak peak intensity at high scattering angles (small d-spacing) means X-ray diffraction is not an optimal tool to study local structural distortions. Therefore, X-ray powder diffraction is not able to unambiguously determine the crystal structures of distorted layered perovskite oxides discussed in this thesis, in which both heavy metals and oxides are present and the structural distortions mainly arise from small displacements of the oxide ions.

2.2.1.1 Panalytical Empyrean and X'Pert diffractometers

Panalytical Empyrean and X'Pert diffractometers were used to collect X-ray diffraction data from compounds discussed in this thesis. Both diffractometers use the Bragg-Brentano geometry and generate monochromatic Cu $K_{\alpha 1}$ radiation. The Cu K_{β} radiation is eliminated by incorporating a Ni filter, which strongly absorbs the Cu K_{β} radiation. A crystal monochromator is used to further eliminate the Cu $K_{\alpha 2}$ radiation. Both incident and diffracted beams are collimated by the Söller slits. The Panalytical Empyrean diffractometer yields data with higher intensity with respect to the X'Pert diffractometer therefore the Empyrean diffractometer is used to monitor the reaction progress. The X'Pert diffractometer yields higher resolution data, hence data collected from the X'Pert diffractometer are more suitable for the Rietveld refinements.

Sample preparations are the same for both instruments. Non air-sensitive samples were ground and dispersed on a silicon wafer which was coated with a thin layer of Dow-Corning high vacuum grease. The silicon wafer was deliberately cleaved along the [110] plane which is systematically absent and hence this sample holder does not yield any diffraction peak. The wafer was then mounted in a spinning sample stage and was rotating during the measurement to minimise the effect of non-uniform sample distribution. Air-sensitive samples were prepared in the argon-filled glovebox. Samples were ground and sprinkled on a glass slide which was coated with a thin layer of Dow-Corning high vacuum grease. The slide was then inserted and sealed in an air-sensitive X-ray sample holder (Figure 2.5). The sample holder was mounted into a flat sample stage for a measurement.

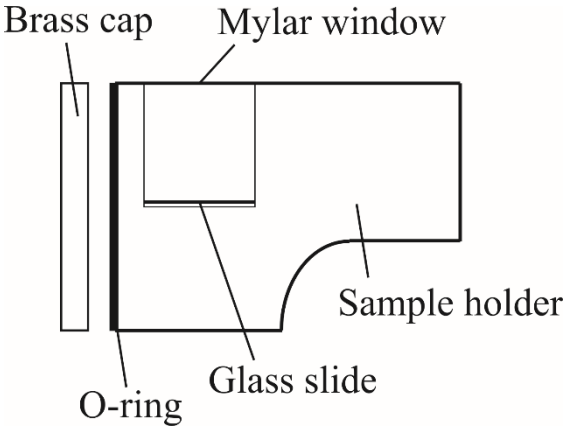


Figure 2.5. Air-sensitive sample holder used for Panalytical Empyrean and X'Pert diffractometers.

2.2.1.2 Synchrotron X-ray powder diffraction

The acceleration of charged particles such as electrons gives electromagnetic radiation. In a synchrotron facility, electrons are accelerated to a speed close to light. A wide spectrum of electromagnetic radiation is produced by the high-speed electrons which are travelling in a storage ring and the X-ray portion can be used for the powder diffraction experiments. Compared to the conventional laboratory X-ray powder diffraction, synchrotron X-ray provides exceptionally bright X-ray beams, meaning the measurement takes much shorter time (typically in minutes, even seconds) and reaches much better signal-to-noise ratio. Additionally, its extreme brightness means that the monochromator can be designed as highly wavelength selective and the beam can be very well collimated: although most of the incoming beam is sacrificed during this process in order to reach superior resolution, the resultant monochromatic beam is still sufficiently intense.

Synchrotron X-ray powder diffraction data shown in this thesis were collected in the I11 beamline at the Diamond Light Source in Oxfordshire. I11 is a dedicated instrument for high-resolution powder diffraction[43]. Monochromatic X-ray beams are selected by the double-crystal-monochromator which is comprised of two liquid nitrogen cooled Si (111) crystals. Samples are ground and loaded in glass capillaries. The capillary is sealed by a blowtorch and mounted into a brass sample base which has an internal magnetic body. The

sample holder is mounted at the center of the diffractometer and the capillary spins during the measurement. There are two different detectors in I11. The wide-angle position sensitive detector (PSD) is made by Mythen-2 modules[44] and is optimized for a rapid measurement (typically in seconds). The other type of detector is the multi-analysing crystal (MAC) detector[45] in which 45 Si (111) crystals are deployed in five identical MAC-arms. The MAC detector is optimized for diffraction experiments which require extremely high resolution. The sacrifice in intensity means a measurement using the MAC detector takes longer time (typically 30 minutes).

Different sample environment options are available in I11. An Oxford Cryostream is used to control the sample temperature in a range of $80 \leq T/K \leq 500$. A Cyberstar hot air blower is deployed if a measurement at high temperatures ($300 \leq T/K \leq 1273$) is required.

2.2.2 Neutron powder diffraction

The principle of wave-particle duality means neutrons also have a wavelength and hence can be used for diffraction experiments if appropriate wavelengths are achieved. In contrast to X-rays which interact with the electron clouds, neutrons are diffracted by the nuclei of atoms. This fundamental difference means the neutron powder diffraction has several different features compared to the X-ray powder diffraction: 1. The neutron scattering length, *b*, is different to the X-ray scattering factor *f* for a given atom. Unlike the X-ray scattering factor, the neutron scattering lengths do not vary systematically with the atomic number and light atoms which poorly scatter X-rays, scatter neutrons similarly to heavy atoms, meaning light elements can be located precisely in the presence of heavy metals by using neutron diffraction[46]. 2. In contrast to the electron cloud, the atomic nucleus is a point scatterer with a finite size. This implies the neutron scattering length is independent of the scattering angle whereas in the X-ray case the scattering form factor decreases rapidly with increased scattering angle. Consequently, diffraction peaks at high angles (low *d*-spacing)

are more intense and hence more structural information can be extracted from neutron diffraction. 3. Neutrons are spin-half particles and have a magnetic moment so they can interact with the magnetic moments carried by solids. This feature allows for the characterisation of the magnetic structure of a solid with a long-range magnetic order. 4. Neutrons are very penetrating therefore complex sample environments, such as cryostats, furnaces and high-pressure apparatus can be deployed, enabling diffraction experiments under broader conditions. 5. The interaction between neutrons and the nuclei of atoms is weak. Therefore the neutron diffraction experiment usually requires large sample sizes. For the neutron diffraction measurements listed in this thesis, samples with sizes from 3 g to 5 g were used.

The intensity of a reflection from the crystal structure in the neutron powder diffraction is calculated by a similar expression with the X-ray powder diffraction in Section 2.2 with only one exception: the X-ray scattering factor *f* is replaced by the neutron scattering length *b*. The magnetic structure factor $F_{hkl,mag}$ of an unpolarised neutron source can be expressed as follows[47]:

$$\boldsymbol{F_{hkl,mag} = \sum_j q_j p_j e^{2\pi i h x_j}}$$

where q_j is the magnetic interaction vector, p_j is the magnetic scattering length, h is the magnetic scattering vector and x_j is the position vector of the magnetic atom in the unit cell. The intensity of a magnetic reflection is calculated from the magnetic structure factor and the projection of the magnetic factor onto the lattice plane by the following equation:

$$\boldsymbol{I_{hkl,mag} = \left|F_{hkl,mag}\right|^2 cos^2 \alpha}$$

where α is the angle between the magnetic structure and the corresponding lattice plane.

For neutron powder diffraction measurements, samples were loaded into vanadium cans and sealed with lids and screws. Vanadium is chosen as the container material due to its

low neutron coherent scattering length (-0.3824 fm)[46], meaning the Bragg scattering from the vanadium container is weak.

Neutron powder diffraction data shown in this thesis were collected using HRPD[48], GEM[49] and WISH[50] instruments at the ISIS Neutron and Muon Source in Oxfordshire.

2.2.2.1 HRPD, GEM and WISH

Neutrons in the ISIS Neutron and Muon source are produced by a spallation process. Protons are accelerated to 800 MeV in a synchrotron and guided to the heavy metal target made by tantalum metal, triggering an intranuclear cascade which releases a pulse of neutrons. Neutrons produced by this process have very high energy and are slowed down by hydrogenous moderators to reach suitable wavelengths for diffraction experiments. This process produces polychromatic neutron beams with suitable wavelengths for time-of-flight measurements. The time-of-flight technique can be explained by combining the de Broglie relationship and Bragg's law as shown by the following equation:

$$\boldsymbol{\lambda = \frac{h}{mv} = \frac{h}{m} \times \frac{t}{L} = 2d\sin\theta}$$

where h is Plank's constant, m is the mass of the neutron, v is the velocity of the travelling neutron which can be calculated from the travelling distance L and the time-of-flight t. The time-of-flight technique uses fixed-angle detectors so θ is a known parameter. As the path length L is pre-determined and the time-of-flight t can be measured, consequently the neutron wavelengths λ can be calculated and the diffraction pattern can be considered as a function of neutron wavelengths.

The High Resolution Powder Diffractometer (HRPD) is optimized for high-resolution measurements with three banks of detectors. Its high resolution (especially the back-scattering bank) enables scientists to measure peak splitting to very high precision and

study subtle structural distortions. Therefore HRPD was used as the primary instrument for the structural characterisation in this thesis. The HRPD setup is shown in Figure 2.6.

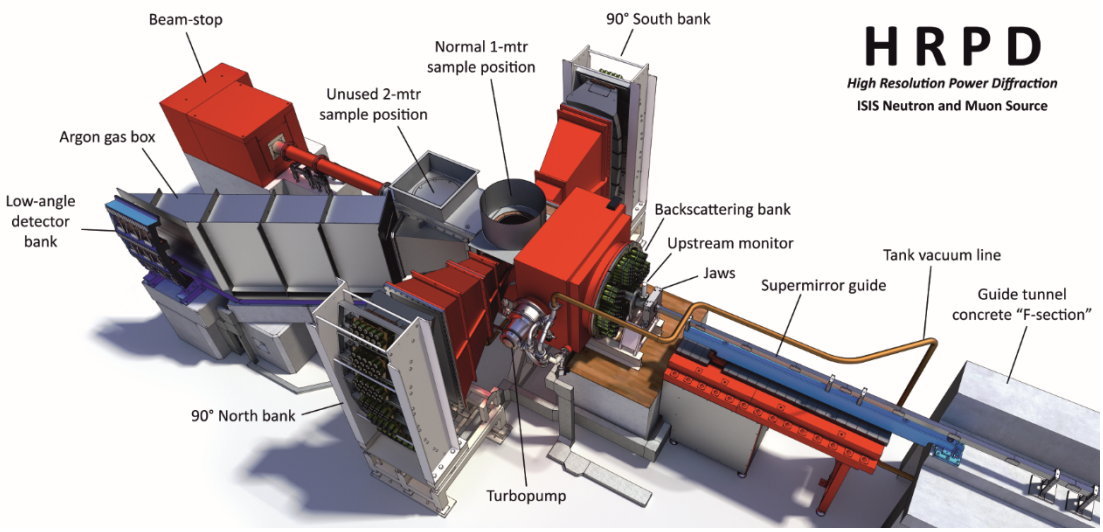


Figure 2.6. HRPD instrument at the ISIS Neutron and Muon Source[51].

The General Materials Diffractometer (GEM) is an instrument designed to give the best compromise of both high resolution and high intensity. Diffraction data are collected using 6 fixed-angle detector banks ranging from 9° to 154°. Its high resolution in the high *d*-spacing region means the GEM instrument provides a good opportunity for the observation of magnetic reflections and the characterisation of the magnetic structures.

The WISH instrument is a long-wavelength diffractometer which has a *d*-spacing range of 0.7 – 50 Å. Its broad *d*-spacing range and high resolution at high *d*-spacings make it a good candidate for studying complex magnetic structures and large unit cell systems (especially incommensurate structures).

2.3 Rietveld refinement

Structural refinement is essential for the crystal structural characterisation. For a structural refinement, a diffraction pattern is calculated from an approximated structural model and compared to the observed diffraction data. Both the observed data and the calculated pattern

consist of the individual integrated *hkl* intensities. The model is then refined and an updated diffraction pattern is generated and again compared to the observed diffraction data. This process is repeated until the refined structure has the best intensity fit to the observed data. However, the peak overlapping problem in the powder diffraction data usually leads to the loss of some structural information contained in the composite peaks and the individual *hkl* intensity is hard to determine. The Rietveld method overcomes this limitation by calculating the intensity at each point and comparing it to the observed intensity in an experimental diffraction pattern[52]. The total difference between the calculated pattern and the experimental data is given by the following expression:

$$\boldsymbol{S = \sum_i w_i[y_i(obs) - y_i(cal)]^2}$$

Where *S* is the difference between the calculated and experimental intensities, w_i is the weighting factor and $y_i(obs)$ and $y_i(cal)$ are the observed and calculated intensities at a given point *i*. The structural model is refined to minimise *S*. The quality of the fit is assessed by three parameters: the profile factor *Rp*, the weighted profile factor *wRp* and χ^2, defined as follows:

$$\boldsymbol{Rp = \frac{\sum|y_i(obs) - y_i(cal)|}{\sum y_i(obs)}}$$

$$\boldsymbol{wRp = \sqrt{\frac{\sum_i w_i[y_i(obs) - y_i(cal)]^2}{\sum_i w_i[y_i(obs)]^2}} = \sqrt{\frac{S}{\sum_i w_i[y_i(obs)]^2}}}$$

$$\boldsymbol{\chi^2 = \frac{\sum_i w_i[y_i(obs) - y_i(cal)]^2}{N - V + C} = \frac{S}{N - V + C}}$$

where *N* is the total number of observations, *V* is the number of variables and *C* is the number of constraints used in the least square refinements. From a Rietveld refinement, structural information such as lattice parameters, atomic positions, atomic thermal displacements and site occupancies, as well as the extra profile parameters, can be obtained.

The Rietveld refinement shown in this thesis was performed using the GSAS suite of programs[53].

2.3.1 Peak broadening

In an ideal case where both the sample and the instrument are perfect, the diffraction peaks should be extremely sharp. However, in practice diffraction peaks exhibit some broadening due to both instrumental and sample contributions.

In practise, there is always a peak broadening contribution from the imperfect instrument setup. For example, the X-ray radiation used in the laboratory diffractometers is not perfectly monochromatic and consist a small range of wavelengths. Combining this effect with Bragg's law, it is deduced that for a given reflection d_{hkl}, there is a corresponding range of θ. In addition, there is a finite volume of the sample and therefore the diffraction is not always occurring in the center of the diffractometer, leading to some peak broadening. Other factors such as the beam divergence and any misalignment of the diffractometer can also lead to the broadening of the Bragg peaks in a diffraction pattern.

In addition to the imperfect instrument setup, it is also not realistic to have a perfect sample for a powder diffraction measurement and there are always broadening contributions from imperfect samples. There are two main sources known as particle size and strain. It is suggested that the broadening is reciprocally related to the particle size, the bigger the particle size, the narrower the diffraction peak. It is obvious that the particle size is defined by its shape therefore an irregular crystallite shape can lead to an anisotropic peak broadening, suggesting that diffraction peaks along different crystallite dimensions can have different broadening effects. The strain broadening can be understood by the displacements of the lattice planes. A homogeneous strain will lead to the shift of diffraction peaks but no broadening. If the strain is inhomogeneous, the shifts in 2θ will be arbitrary and it will lead to the peak broadening. The broadening effects from both

instrumental and sample contributions are modelled during a Rietveld refinement. In general, instrumental peak broadening is modelled with Gaussian function parameters while sample contribution to peak broadening is modelled with Lorentzian function parameters.

2.4 SQUID magnetometry

A Quantum Design MPMS XL SQUID (Direct-Current Superconducting Quantum Interference Device) magnetometry was used to measure the magnetic properties of samples shown in this thesis. SQUIDs are able to detect small magnetization changes of a sample in magnetic field by using the Josephson effect[54]. A SQUID consists of two pieces superconducting rings separated by a thin layer of insulating materials which are called Josephson junctions. For a SQUID measurement, samples are moved through the superconducting rings and the magnetic field generated by the sample induces an 'opposing' current in the rings. The voltage which arises from the induced current is proportional to the magnetic moment of the sample moving through the superconducting rings and hence the magnetic property can be measured.

For the measurements in this thesis, samples of approximately 40 mg were precisely weighed and loaded into a gelatine capsule. The capsule was then inserted into a plastic straw, stabilized by another 8 capsules (4 above and 4 below the sample capsule). The top and the bottom capsules were wrapped with a layer of diamagnetic tape to ensure the sample capsule did not move in the straw during the measurement. All empty capsules were pierced with a needle so they could be properly evacuated. The prepared straw was then connected and taped to the end of a steel rod and loaded into the SQUID for a measurement. Magnetization data were collected either as a function of field at a constant temperature or as a function of temperature at a constant field. The magnetization-field isotherms were

collected over the field range -5 ≤ H/T ≤ 5 at 5 K and 300 K. The zero-field cooling (ZFC) and field cooling (FC) measurements were conducted from 5 K to 300 K under a constant field of 100 Oe, with the ZFC measurement cooling in the absence of a magnetic field but the FC measurement cooling at 100 Oe.

2.5 Curie-Weiss law

The paramagnetic susceptibility of a material, χ, describes how responsive a material is to an applied field. The Curie law describes a relationship between the paramagnetic susceptibility and the temperature:

$$\boldsymbol{\chi = \frac{C}{T}}$$

Where *C* is a constant called the Curie constant and *T* is the temperature in Kelvin. The Curie Law is based on an assumption that there is no interaction between the localized atomic magnetic moments and they are reoriented by the external field. This is not the case in many solids, which have internal interactions between localized moments. Consequently a modified and more accurate expression, called the Curie-Weiss law, is given:

$$\boldsymbol{\chi = \frac{C}{T - \theta}}$$

Where θ is called the Weiss temperature. The Curie constant can be related to the effective magnetic moments as follows:

$$\boldsymbol{C = \frac{N_A \mu_B {\mu_{eff}}^2}{3k_B} \approx \frac{1}{8}{\mu_{eff}}^2}$$

where N_A is the Avogadro's constant, μ_B is the Bohn magneton, k_B is the Boltzmann's constant and μ_{eff} is the effective magnetic moment.

If there is only spin contribution to the moment from the sample, a further relationship can be expressed as:

$$\boldsymbol{\mu_{eff} = g\sqrt{S(S+1)}}$$

where g is the gyromagnetic factor and S is the spin quantum number.

Since μ_{eff} can be calculated from the Curie constant extracted from a magnetisation measurement and $g = 2$, the spin quantum number S can be calculated and the number of unpaired d electrons in the sample can be deduced if the orbital contribution is believed to be negligible[55].

2.6 Bond valence sum (BVS)

The bond valence model allows the estimation of the valence of ions by considering the bond length and the identity of atoms which form the bond[56]. The bond valence sum of an ion can be expressed as:

$$\boldsymbol{V_i = \sum_j s_{ij}}$$

where V_i is the total bond valence of ion i and s_{ij} is the valence of a bond between ion i and j, which can be calculated as following:

$$\boldsymbol{s_{ij} = e^{(R_0 - R)/b}}$$

where R is the observed bond length between ion i and j, R_0 and b are bond valance parameters. Bond valence sum calculations performed in this thesis use bond valence parameters reported by Brese and O'Keeffe[57]. The bond valence sum calculations in this thesis were performed to help validate the refined crystal structures and explain the structural differences adopted by different compounds.

2.7 Second-harmonic generation (SHG)

Structural characterisation of crystalline solids with distorted structures from powder diffraction data can be challenging and hence an optical technique, called second-harmonic generation (SHG), was used to assist the characterisation. SHG can be defined as an optical process in which two photons with the same wavelength combine to produce a single photon with a half wavelength (so twice the energy)[15]. It is found that most non-centrosymmetric crystal classes exhibit SHG activities and all polar classes are SHG active. By performing a SHG measurement, it can be determined very quickly and accurately if the material adopts a non-centrosymmetric crystal structure and hence a considerable number of space groups can be eliminated before analysing the diffraction data. A setup of the measurement is illustrated in Figure 2.7[15].

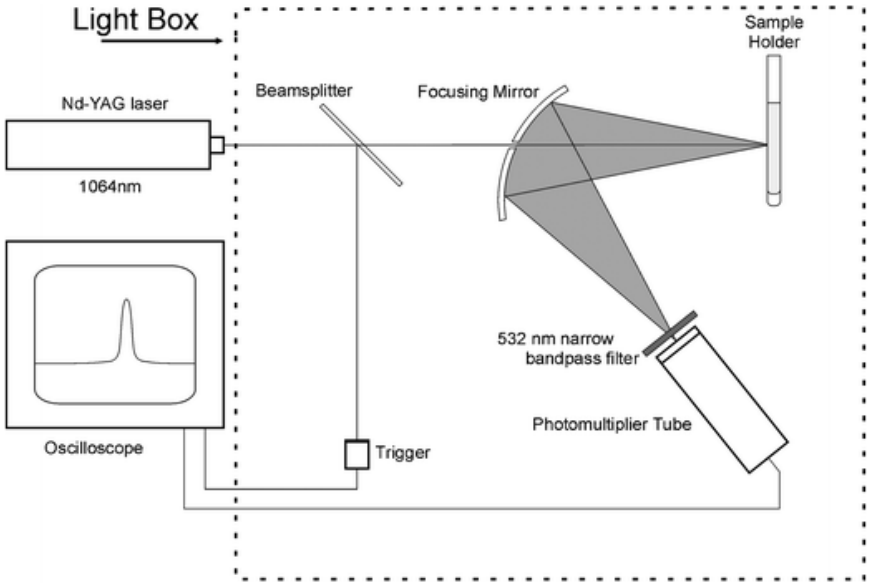


Figure 2.7. A schematic diagram of a Kurtz-Powder Laser System for SHG test[15].

For the SHG measurements described in this thesis, samples of hundreds milligrams were loaded into a sample holder and placed in the SHG device. If the compound adopts a non-centrosymmetric crystal structure, an incident laser beam with a wavelength 1064 nm (IR) would be converted to a green light with a wavelength of 532 nm and detected by the monitor. For a particle-size dependent measurement, a dense pellet was ground and sieved

into particle sizes in a range from 20 μm to 125 μm and the SHG intensity was measured as a function of particle size. All SHG data mentioned in this thesis were collected by Dr. Weiguo Zhang and Prof. Shiv Halasyamani from University of Houston.

2.8 Incommensurate structure

An incommensurate structure can be considered as a perturbation of a periodic structure[58]. Unlike the normal crystal phases, which have lattice periodicities in three dimensions, the translational symmetry is lost along at least one crystallographic axis in an incommensurate structure and the lattice periodicities are deemed no longer three dimensional. However, the modulation of an incommensurate structure with respect to the basic lattice is periodic and a solid with an incommensurate structure is still deemed to possess a long-range order.

An incommensurate structure gives some Bragg peaks which cannot be indexed by three integer indices, suggesting it is not possible to use the traditional three-dimensional space groups to describe an incommensurate structure. However, the long-range order in an incommensurate structure is as perfect as in the ordinary periodic structure and hence it can be described with higher-dimensional crystallography. In general, an incommensurate structure is considered as a basic structure plus one or more modulation wave-vectors along the three traditional crystallographic axes and is described by a superspace group. The details of the high-dimensional crystallography are beyond the scope of this thesis thus not discussed here.

Chapter 3 – The Synthesis and Characterisation of Polar Dion-Jacobson Phases A'NdM_2O_7 (A' = Rb/Cs， M = Nb/Ta)

3.1 Introduction

Prior studies have suggested that n = 2 Dion-Jacobson phases adopt undistorted crystal structures in space group $P4/mmm$[26, 59]. In contrast, recent theoretical and experimental works show that a series of n = 2 Dion-Jacobson phases in fact crystallise in distorted crystal structures and some of them are even polar[24, 60-64]. For example, First-principles DFT calculations predicted that Rb$A$$Nb_2O_7$ and Cs$A$$Nb_2O_7$ (A = Y, Nd, La or Bi) all adopt polar, $P2_1am$ structures[24]. Subsequent experimental studies utilizing synchrotron X-ray diffraction and optical SHG measurements proved that $RbLaNb_2O_7$ and $RbLaTa_2O_7$ are polar[63]. High-resolution neutron diffraction study shows that $CsNdNb_2O_7$ indeed adopts a polar, $P2_1am$ structure (Figure 3.1)[60]. $RbBiNb_2O_7$ and $CsBiNb_2O_7$ were also proved to be polar from experiments, with switchable electric dipoles demonstrated for $RbBiNb_2O_7$[62].

In order to test if the theory prediction is universally correct, we examined the structures and properties of $RbNdNb_2O_7$, $RbNdTa_2O_7$ and $CsNdTa_2O_7$ using synchrotron X-ray diffraction and neutron diffraction techniques, supported by the optical SHG measurements and the first-principles DFT calculations, to see if these phases are indeed polar.

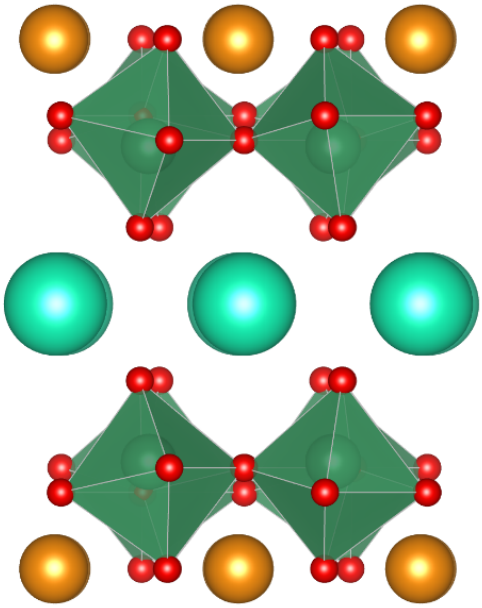


Figure 3.1. The structure of $CsNdNb_2O_7$ in space group $P2_1am$, with an $a^-a^-c^+$ tilting distortion in the Glazer notation. The cyanic and gold spheres are Cs and Nd respective. Nb is inside the polyhedra.

3.2 Synthesis

Powder samples of $RbNdNb_2O_7$, $RbNdTa_2O_7$ and $CsNdTa_2O_7$ were prepared via a ceramic synthesis method from Rb_2CO_3 (99.8%), Cs_2CO_3 (99.994%), Nd_2O_3 (99.99%) and Nb_2O_5 (99.9985%) or Ta_2O_5 (99.993%). Nd_2O_3, Nb_2O_5 and Ta_2O_5 were dried at 900 °C before being used. Suitable stoichiometric ratios of the oxides were ground together in an agate pestle and mortar and then combined with a 50% excess of Rb_2CO_3 or Cs_2CO_3 (to compensate for metal loss due to the volatility of these reagents at high temperature). These mixtures were then heated at 850 °C in air for 12 hours, reground, pressed into pellets. Samples of $RbNdNb_2O_7$ were then heated in air for four periods of 48 hours at 1000 °C and a further 48 hours at 1050 °C. Samples of $RbNdTa_2O_7$ and $CsNdTa_2O_7$ were heated in air for four periods of 48 hours at 1050 °C. All samples were washed in distilled water as a final step, to remove any remaining Rb or Cs oxides, and then dried for 12 hours at 140 °C in air. Reaction progress and final sample purity were assessed by X-ray powder diffraction

data collected using a PANalytical X'pert diffractometer incorporating an X'celerator position sensitive detector (monochromatic Cu Kα1 radiation).

3.3 Results

3.3.1 Optical SHG measurements

Particle-size dependent SHG measurements show that $CsNdTa_2O_7$, $RbNdNb_2O_7$ and $RbNdTa_2O_7$ are SHG active and their SHG activity increases with an increase in particle size (Figure 3.2). This indicates that all three phases adopt non-centrosymmetric crystal structures.

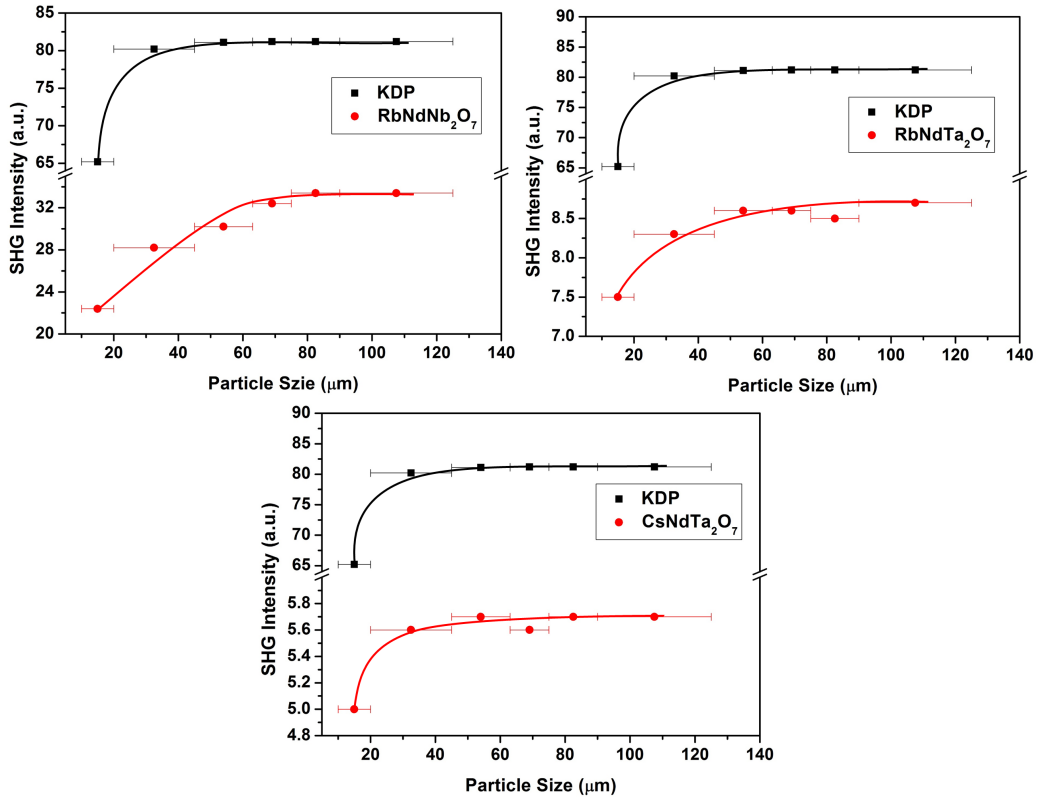


Figure 3.2. Plots of SHG activity of $RbNdNb_2O_7$ (top left), $RbNdTa_2O_7$ (top right) and $CsNdTa_2O_7$ (bottom) as a function of particle size, compared to KH_2PO_4 (KDP) standard.

3.3.2 Structure characterisation of $CsNdTa_2O_7$

3.3.2.1 Room temperature synchrotron X-ray powder diffraction

High-resolution synchrotron X-ray diffraction data from $CsNdTa_2O_7$ collected at ambient temperature can be indexed using an orthorhombic unit cell with an approximate $\sqrt{2} \times \sqrt{2} \times 1$ geometric expansion of the aristotype *P*4/*mmm* unit cell, (a = 5.458 Å, b = 5.448 Å, c = 11.273 Å). This unit cell expansion is consistent with the reported structure of $CsNdNb_2O_7$, in a polar space group $P2_1am$[60]. In terms of the octahedral tilting distortion, this structure can be described in $a^-a^-c^+$ using the Glazer notation system. SHG activity indicates that $CsNdTa_2O_7$ adopts a non-centrosymmetric crystal structure, therefore a model in space group $P2_1am$ was constructed and refined against the synchrotron X-ray diffraction data, which yielded a statistically good fit. The observed, calculated and difference plots in space group $P2_1am$ are shown in Figure 3.3.

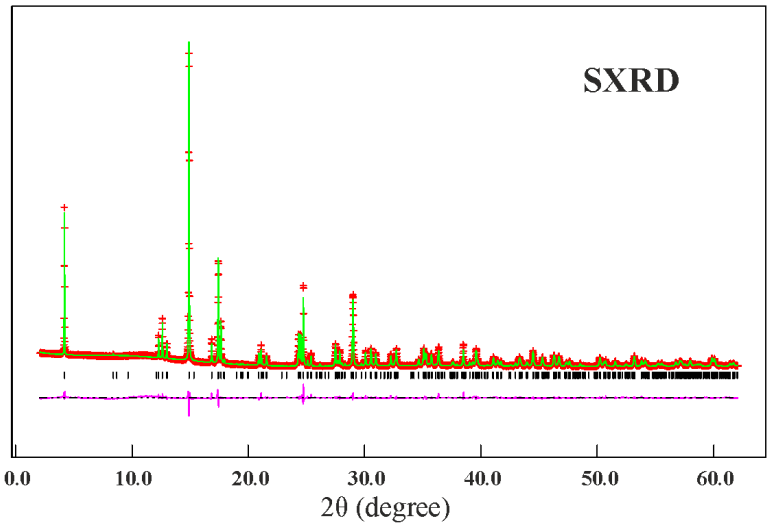


Figure 3.3. Observed, calculated and difference plots from the refinement of the $P2_1am$ model against the synchrotron X-ray diffraction data collected from $CsNdTa_2O_7$ at ambient temperature.

3.3.2.2 Room temperature neutron powder diffraction

Neutron powder diffraction data were collected from a sample of approximately 4.5 g $CsNdTa_2O_7$ at ambient temperature using the HRPD instrument at ISIS. A primitive, orthorhombic unit cell with a $\sqrt{2} \times \sqrt{2} \times 1$ geometric expansion of the aristotype unit cell

is needed to index the diffraction data. The refinement of the $P2_1am$ model against the neutron diffraction data gives a statistical good fit, confirming that $CsNdTa_2O_7$ and $CsNdNb_2O_7$ are isostructural. The observed, calculated and difference plots in space group $P2_1am$ are shown in Figure 3.4 and full details of the parameters from the refinements are shown in Table 3.1. Selected bond lengths from the refined structure of $CsNdTa_2O_7$ are shown in Table 3.2.

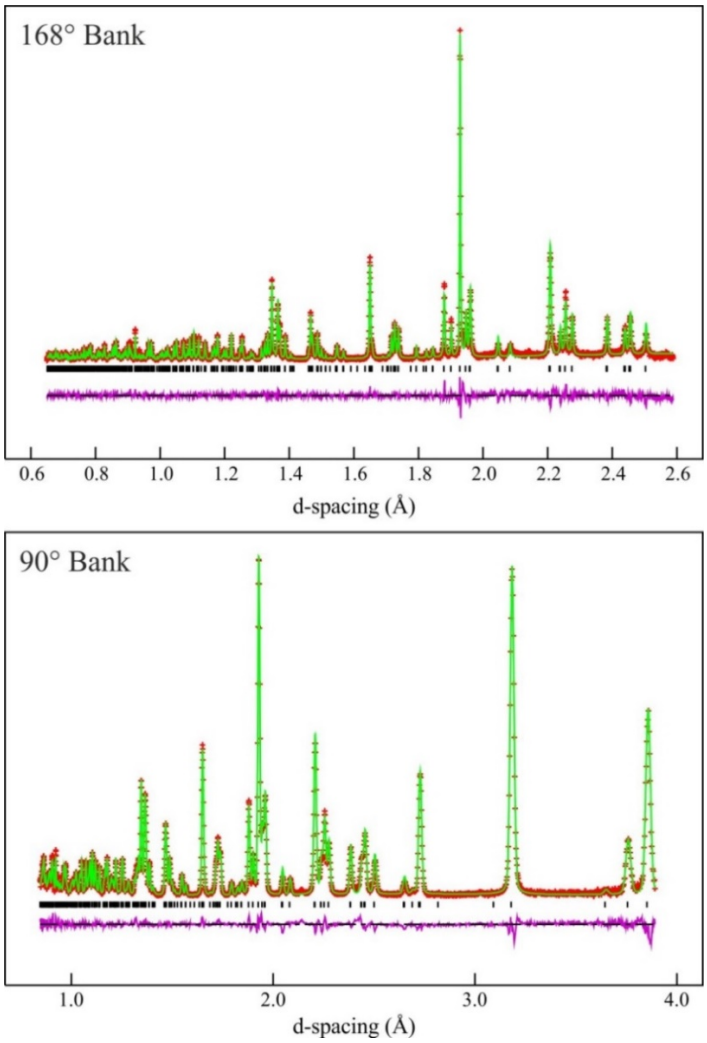


Figure 3.4. Observed, calculated and difference plots from the refinement of the $P2_1am$ model against the high-resolution neutron diffraction data collected from $CsNdTa_2O_7$ at ambient temperature.

Atom	site	*x*	*y*	*z*	U_{iso} (Å^3)
Cs(1)	2*b*	0.2556(9)	0.2358(6)	½	0.0136(3)
Nd(1)	2*a*	0.2740(5)	0.2456(3)	0	0.0033(3)
Ta(1)	4*c*	0.7493(4)	0.2521(3)	0.1997(1)	0.0050(3)
O(1)	4*c*	0.5128(6)	0.5184(6)	0.1447(1)	0.0126(4)
O(2)	4*c*	0.9509(5)	0.9551(5)	0.1835(1)	0.0140(5)
O(3)	4*c*	0.7511(6)	0.2926(3)	0.3563(1)	0.0118(4)
O(4)	2*a*	0.7318(9)	0.1841(4)	0	0.0095(6)
$CsNdTa_2O_7$ – space group $P2_1am$ (#26) a = 5.4588(1) Å, b = 5.4494(1) Å, c = 11.2754(2) Å, volume = 335.41(1) Å^3 Formula weight: 751.03 g mol^{-1}, Z = 2 Radiation source: Neutron Time of flight Temperature: 298 K χ^2 = 5.63, wRp = 4.8%, Rp = 5.2%					

Table 3.1. Parameters from the structural refinement of $CsNdTa_2O_7$ against neutron powder diffraction data collected at 298 K.

Cation	Anion	length (Å)	BVS
Cs(1)	O(3) × 2	3.038(4)	Cs +1.06
	O(3) × 2	3.168(5)	
	O(3) × 2	3.210(5)	
	O(3) × 2	3.304(4)	
Nd(1)	O(1) × 2	2.520(4)	Nb +3.07
	O(1) × 2	2.533(2)	
	O(2) × 2	2.564(4)	
	O(2) × 2	3.147(3)	
	O(4)	2.354(4)	
	O(4)	2.521(6)	
	O(4)	2.979(6)	
	O(4)	3.115(3)	
Ta(1)	O(1)	2.004(4)	Ta +5.06
	O(1)	2.039(4)	
	O(2)	1.966(4)	
	O(2)	1.990(3)	
	O(3)	1.779(2)	
	O(4)	2.285(1)	

Table 3.2. Selected bond lengths from the refined structure of $CsNdTa_2O_7$.

3.3.3 Structure characterisation of $RbNdNb_2O_7$

3.3.3.1 Room temperature synchrotron X-ray powder diffraction

High-resolution synchrotron X-ray diffraction data collected from $RbNdNb_2O_7$ at ambient temperature can be indexed using an orthorhombic unit cell with an approximate $\sqrt{2} \times \sqrt{2}$

× 2 geometric expansion of the aristotype *P*4/*mmm* unit cell, (a = 5.458 Å, b = 5.448 Å, c = 22.546 Å). The extinction conditions suggested a body-centred space group. The unit cell expansion and the extinction conditions are consistent with a reported structure of $RbLaNb_2O_7$ in space group *Imam*, described in an $a^-a^-c^0$/-($a^-a^-c^0$) tilt[65]. However, this centrosymmetric space group is not compatible with the observed SHG activity of $RbNdNb_2O_7$. Given that $CsNdTa_2O_7$ and $CsNdNb_2O_7$ both adopt a polar $P2_1am$ structure with an $a^-a^-c^+$ tilt, an in-phase rotation of the NbO_6 octahedra along the z-axis was added to the *Imam* structure, to form a polar structure in space group *I*2*cm*, with an $a^-a^-c^+$/-($a^-a^-c^+$) tilt. Refining this model against the synchrotron X-ray diffraction data yielded a good fit. The observed, calculated and difference plots against the synchrotron X-ray data in space group *I*2*cm* are shown in Figure 3.5. The weak peak at approximate 20.6° can only be indexed when the c lattice is doubled.

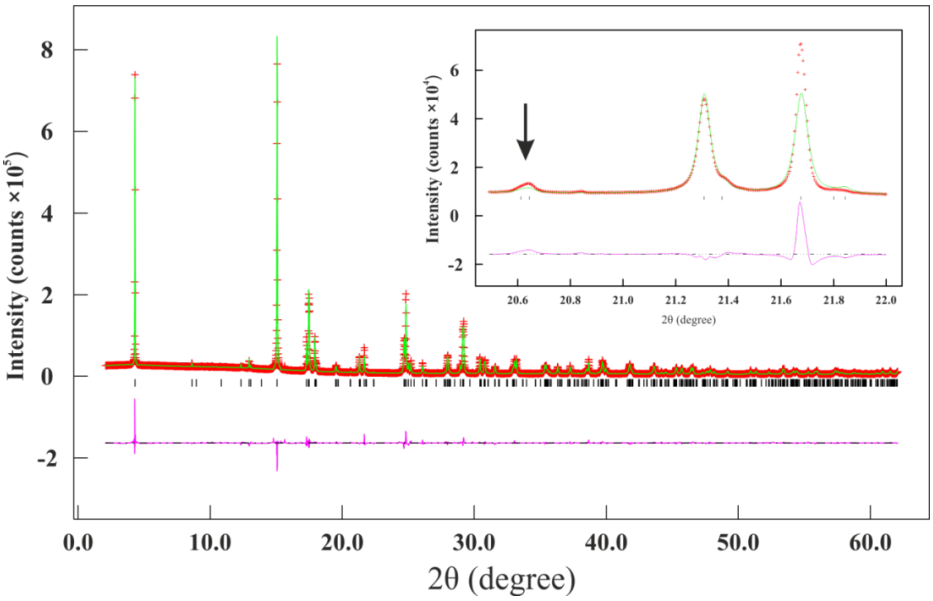


Figure 3.5. Observed, calculated and difference plots from the refinement of the *I*2*cm* model against the synchrotron X-ray diffraction data collected from $RbNdNb_2O_7$ at 298 K.

3.3.3.2 Room temperature neutron powder diffraction

Neutron powder diffraction data were collected from a sample of approximately 4.5 g $RbNdNb_2O_7$ at ambient temperature using the HRPD instrument at ISIS. The diffraction

data can be indexed with an expanded unit cell with a $\sqrt{2} \times \sqrt{2} \times 2$ geometric expansion on the aristotype *P*4/*mmm* unit cell. The extinction conditions are consistent with a body-centred space group. An *I*2*cm* model was then refined against the neutron diffraction data and gave good statistical and visual fits. The observed, calculated and difference plots in space group *I*2*cm* are shown in Figure 3.6 and full details of the parameters from the refinements are shown in Table 3.3. Selected bond lengths from the refined structure of $RbNdNb_2O_7$ are shown in Table 3.4. The refined structure is shown in Figure 3.7.

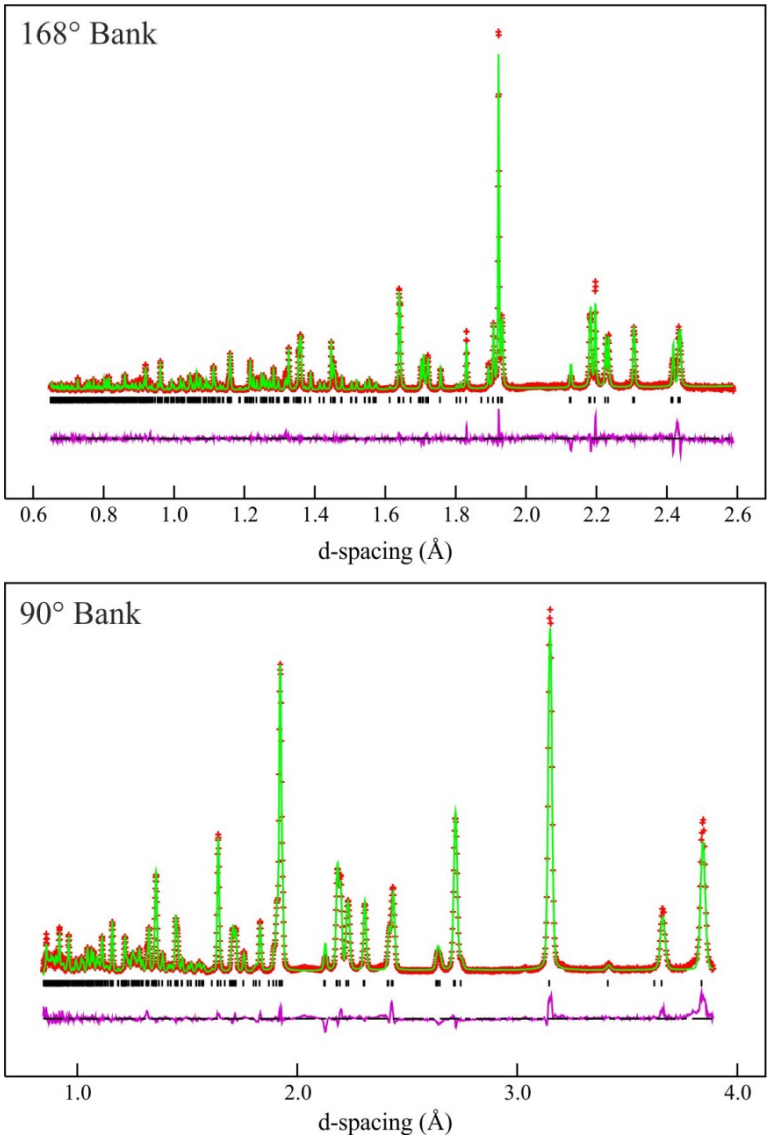


Figure 3.6. Observed, calculated and difference plots from the refinement of the *I*2*cm* model against the high-resolution neutron diffraction data collected from $RbNdNb_2O_7$ at ambient temperature.

Atom	site	*x*	*y*	*z*	U_{iso} (Å^3)
Rb(1)	4*a*	0.7521(12)	0	0	0.0364(4)
Nd(1)	4*b*	0.7541(10)	0.9995(4)	¼	0.0105(3)
Nb(1)	8*c*	0.2454(6)	0.0009(3)	0.3532(5)	0.0124(3)
O(1)	8*c*	0.9943(7)	0.7597(8)	0.3244(8)	0.0197(4)
O(2)	8*c*	0.0700(5)	0.2975(5)	0.3491(10)	0.0238(5)
O(3)	8*c*	0.7447(9)	0.5527(4)	0.4322(8)	0.0218(5)
O(4)	4*b*	0.7192(8)	0.4269(5)	¼	0.0176(9)
$RbNdNb_2O_7$ – space group *I*2*cm* (#46) *a* = 5.4414(1) Å, *b* = 5.4278(1) Å, *c* = 21.9625(4) Å, volume = 648.65(4) Å^3 Formula weight: 527.51 g mol^{-1}, Z = 4 Radiation source: Neutron Time of flight Temperature: 298 K χ^2 = 8.23, wRp = 6.31%, Rp = 6.25%					

Table 3.3. Parameters from the structural refinement of $RbNdNb_2O_7$ against neutron powder diffraction data collected at 298 K.

Cation	Anion	length (Å)	BVS
Rb(1)	O(3) × 2	2.848(2)	Rb +0.912
	O(3) × 2	3.079(8)	
	O(3) × 2	3.150(8)	
	O(3) × 2	3.349(2)	
Nd(1)	O(1) × 2	2.464(5)	Nd +2.99
	O(1) × 2	2.578(5)	
	O(2) × 2	2.637(3)	
	O(2) × 2	3.210(4)	
	O(4)	2.328(4)	
	O(4)	2.562(7)	
	O(4)	2.938(7)	
	O(4)	3.114(3)	
Nb(1)	O(1)	1.996(5)	Nb +5.05
	O(1)	2.058(5)	
	O(2)	1.874(4)	
	O(2)	2.080(4)	
	O(3)	1.759(2)	
	O(4)	2.305(1)	

Table 3.4. Selected bond lengths from the refined structure of $RbNdNb_2O_7$.

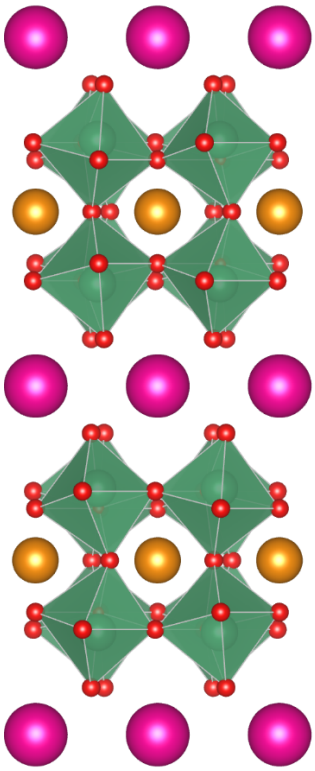


Figure 3.7. The structure of $RbNdNb_2O_7$ in space group *I*2*cm*, with an $a^-a^-c^+/-(a^-a^-c^+)$ distortion. The purple and gold spheres are Rb and Nd respective. Nb is inside the polyhedra.

3.3.4 Structure characterisation of $RbNdTa_2O_7$

3.3.4.1 Room temperature synchrotron X-ray powder diffraction

High-resolution synchrotron X-ray diffraction data collected from $RbNdTa_2O_7$ at ambient temperature can be indexed using an orthorhombic unit cell with a $\sqrt{2} \times \sqrt{2} \times 2$ geometric expansion on the aristotype *P*4/*mmm* unit cell (a = 5.430 Å, b = 5.425 Å, c = 22.163 Å). The extinction condition is consistent with a body-centred space group. The unit cell expansion, the extinction condition and the observed SHG activity from $RbNdTa_2O_7$ together suggest that it is likely to be isostructural to $RbNdNb_2O_7$, which has *I*2*cm* space symmetry with an $a^-a^-c^+/-(a^-a^-c^+)$ tilting distortion. Refining the *I*2*cm* model against the synchrotron X-ray diffraction data gave good fits (wRp = 3.75%, Rp = 2.31%). The observed, calculated and difference plots in space group *I*2*cm* are shown in Figure 3.8. Weak peaks at 19.7° and 20.6° (shown with solid arrows) can only be indexed when the c

lattice is doubled. Figure 3.9 shows the refinement plots using a $P2_1am$ model, in which the c lattice is not doubled. It can be clearly observed that weak diffraction peaks at 19.7° and 20.6° (shown with solid arrows) are not indexed and additional peaks are simulated.

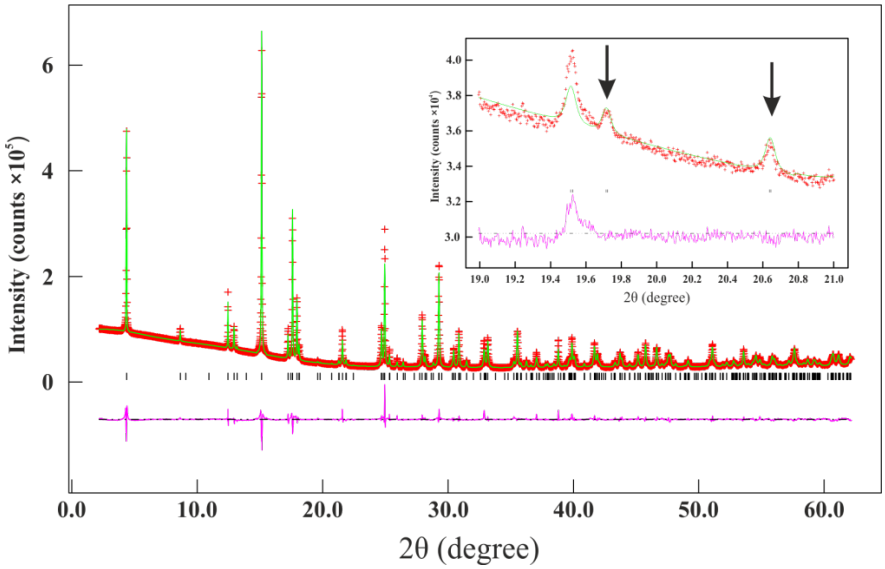


Figure 3.8. Observed, calculated and difference plots from the refinement of the *I*2*cm* model against the synchrotron X-ray diffraction data collected from $RbNdTa_2O_7$ at 298 K. Diffraction peaks in the regime between 19° and 21° are well simulated.

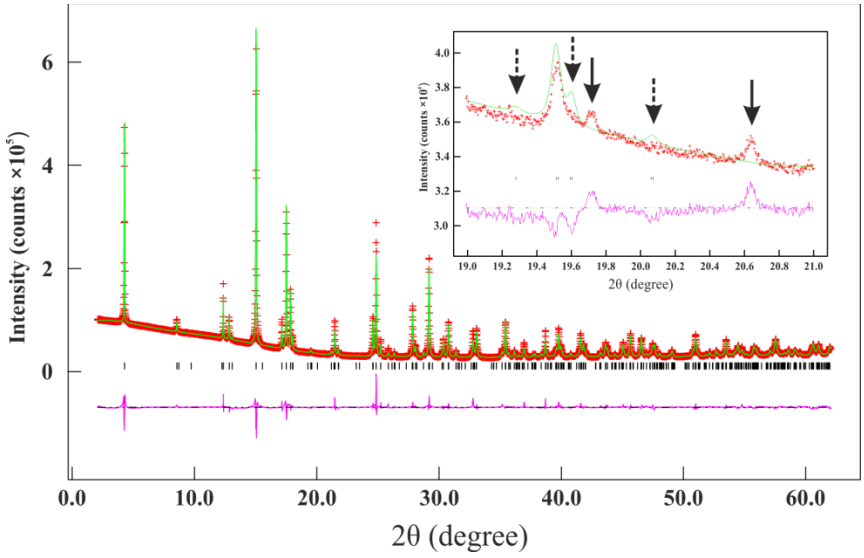


Figure 3.9. Observed, calculated and difference plots from the refinement of the $P2_1am$ model against the synchrotron X-ray diffraction data collected from $RbNdTa_2O_7$ at 298 K. There are two peaks (labelled with solid arrows) this model cannot account for in the region between 19° and 21°. In addition, the model gives additional peaks (labelled with dashed arrows) which are not observed from the diffraction data.

3.3.4.2 Room temperature neutron powder diffraction

Neutron powder diffraction data were collected from a sample of approximately 4.5 g $RbNdTa_2O_7$. The diffraction data can only be indexed using an expanded unit cell with a $\sqrt{2} \times \sqrt{2} \times 2$ expansion of the undistorted cell, which is consistent with the analysis on the synchrotron diffraction data. Refinement of the *I*2*cm* model against the neutron diffraction data gives a statistically good fit, confirming that $RbNdTa_2O_7$ is isostructural to $RbNdNb_2O_7$. The observed, calculated and difference plots in space group *I*2*cm* are shown in Figure 3.10 and full details of the parameters from the refinements are shown in Table 3.5. Selected bond lengths from the refined structure are shown in Table 3.6.

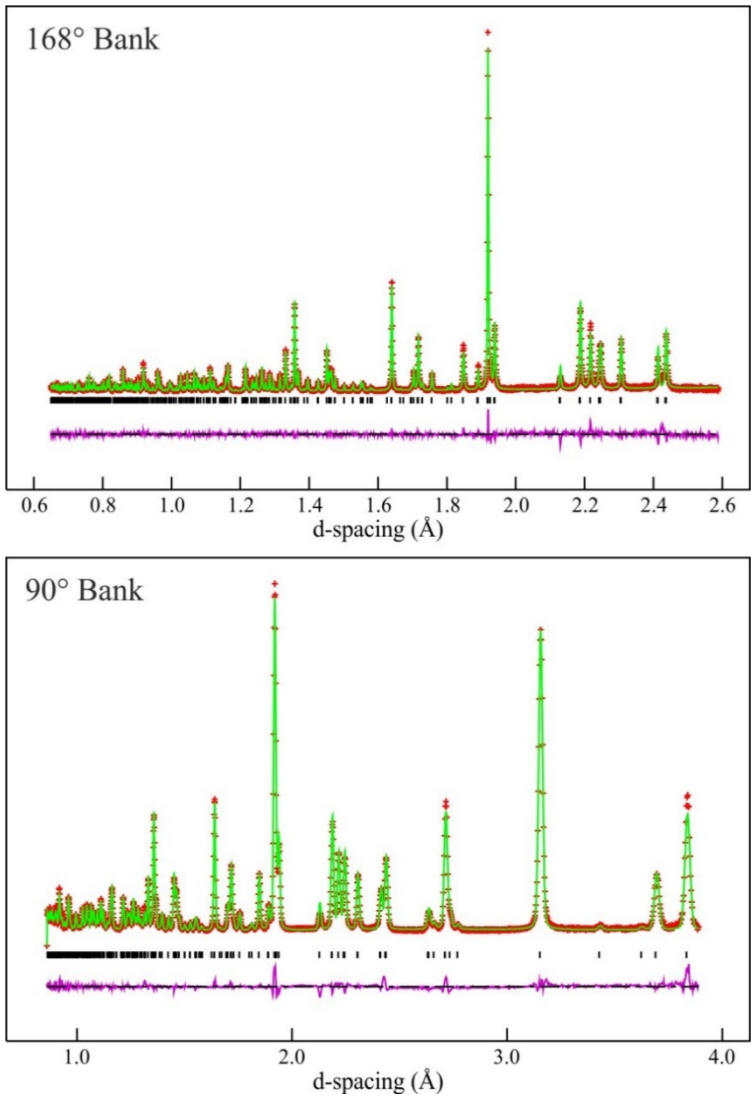


Figure 3.10. Observed, calculated and difference plots from the refinement of the *I*2*cm* model against the high-resolution neutron diffraction data collected from $RbNdTa_2O_7$ at ambient temperature.

Atom	site	*x*	*y*	*z*	U_{iso} (Å^3)
Rb(1)	4*a*	0.7387(7)	0	0	0.0318(3)
Nd(1)	4*b*	0.7279(5)	0.0034(3)	¼	0.0071(3)
Ta(1)	8*c*	0.2491(4)	0.9993(3)	0.35261(3)	0.0044(2)
O(1)	8*c*	0.9851(5)	0.7710(5)	0.32396(6)	0.0142(3)
O(2)	8*c*	0.0590(4)	0.2938(5)	0.34500(7)	0.0175(4)
O(3)	8*c*	0.7457(6)	0.5492(3)	0.43198(5)	0.0163(3)
O(4)	4*b*	0.7697(8)	0.4318(4)	¼	0.0144(6)
$RbNdTa_2O_7$ – space group *I*2*cm* (#46) *a* = 5.4305(1) Å, *b* = 5.4241(1) Å, *c* = 22.1683(3) Å, volume = 652.98(3) Å^3 Formula weight: 703.59 g mol^{-1}, Z = 4 Radiation source: Neutron Time of flight Temperature: 298 K χ^2 = 8.33, wRp = 4.85%, Rp = 4.96%					

Table 3.5. Parameters from the structural refinement of $RbNdTa_2O_7$ against neutron powder diffraction data collected at 298 K.

Cation	Anion	length (Å)	BVS
Rb(1)	O(3) × 2	2.873(2)	Rb +0.88
	O(3) × 2	3.084(5)	
	O(3) × 2	3.150(5)	
	O(3) × 2	3.339(2)	
Nd(1)	O(1) × 2	2.496(3)	Nd +3.09
	O(1) × 2	2.577(3)	
	O(2) × 2	2.547(2)	
	O(2) × 2	3.186(3)	
	O(4)	2.335(3)	
	O(4)	2.513(5)	
	O(4)	2.963(4)	
	O(4)	3.109(3)	
Ta(1)	O(1)	1.998(3)	Ta +5.10
	O(1)	2.048(3)	
	O(2)	1.909(3)	
	O(2)	2.030(3)	
	O(3)	1.779(1)	
	O(4)	2.308(1)	

Table 3.6. Selected bond lengths from the refined structure of $RbNdTa_2O_7$.

3.4 Discussion

3.4.1 Justification of using neutrons

X-ray diffraction, even using synchrotron X-ray source, is not a very sensitive probe of the distorted crystal structures of $CsNdTa_2O_7$, $RbNdNb_2O_7$ and $RbNdTa_2O_7$. The octahedral tilts arise from the small displacement of oxide ions from their high-symmetry positions. Due to the low X-ray scattering factor of oxygen compared to heavy metals, the intensity contribution from oxide ions is weak especially considering we are studying very subtle displacements of oxide ions. As demonstrated in Figure 3.8 and 3.9, superlattice peaks at 19.7° and 20.6° indicate that the $P2_1am$ structural model, with unexpanded c lattice with respect to the aristotype structure, is incorrect for $RbNdTa_2O_7$ but the intensity for these two peaks is too weak for us to deduce oxygen positions precisely. On the other hand, oxygen has a similar neutron scattering length to the heavy metals (Table 3.7), which means the displacements of oxide ions result in much stronger contributions to peak intensities in the neutron diffraction pattern. Therefore high-resolution neutron diffraction data gives us a much better chance to determine the crystal structures of these polar Dion-Jacobson phases.

Element	Rb	Cs	Nd	Nb	Ta	O
Neutron Scattering Length (fm)	7.09	5.42	7.69	7.054	6.91	5.803

Table 3.7. Neutron coherent scattering lengths for selected elements[46].

In order to test the argument that neutron diffraction data is necessary to study the distorted crystal structures of $CsNdTa_2O_7$, $RbNdNb_2O_7$ and $RbNdTa_2O_7$, three different structural models, $P2_1am$ with an $a^-a^-c^+$ tilt ($\sqrt{2} \times \sqrt{2} \times 1$ geometric expansion), $Imam$ with an $a^-a^-c^0$/-($a^-a^-c^0$) tilt ($\sqrt{2} \times \sqrt{2} \times 2$ geometric expansion), and $I2cm$ with an $a^-a^-c^+$/-($a^-a^-c^+$) tilt ($\sqrt{2} \times \sqrt{2} \times 2$ geometric expansion), were constructed and refined against both synchrotron X-ray diffraction and neutron diffraction data collected from $CsNdTa_2O_7$, $RbNdNb_2O_7$ and $RbNdTa_2O_7$. Table 3.8 shows the refinement statistics and it can be seen

that refinements of three models against synchrotron X-ray diffraction data gave equally good fits in all three cases. Therefore, it can be concluded that it is not possible to pick up the 'winner' from synchrotron X-ray diffraction data. In contrast, refinements against the neutron powder diffraction data unambiguously show that the $P2_1am$ model gives much superior fit for $CsNdTa_2O_7$ while the $I2cm$ model gives much better statistical fits for both $RbNdNb_2O_7$ and $RbNdTa_2O_7$.

Figures 3.11, 3.12 and 3.13 show the observed, calculated and difference plots in models of $P2_1am$, $Imam$ and $I2cm$ against high-resolution neutron diffraction data collected from $CsNdTa_2O_7$, $RbNdNb_2O_7$ and $RbNdTa_2O_7$, respectively. Plots between 1.2 Å and 1.8 Å are zoomed in to emphasize different qualities of fits using different models. It is dramatic to see how sensitive neutron diffraction is to subtle structural distortions. For example, superlattice peaks at 1.76 Å, corresponding to doubling the *c* lattice, are clearly observed in Figure 3.12 and Figure 3.13. It can be visualized from Figure 3.11, Figure 3.12 and Figure 3.13 that the $P2_1am$ model gives a much superior visual fit for $CsNdTa_2O_7$ while the $I2cm$ model gives better visual fits for both $RbNdNb_2O_7$ and $RbNdTa_2O_7$. This is a direct contrast to Figure 3.8 and Figure 3.9, in which $I2cm$ and $P2_1am$ models give equally good visual fits for $RbNdTa_2O_7$ against the synchrotron X-ray diffraction data.

$CsNdTa_2O_7$						
	Synchrotron X-ray			Neutron		
Space group	χ^2	wRp (%)	Rp (%)	χ^2	wRp(%)	Rp (%)
*P*2$_1$*am* (#26)	4.29	3.06	1.84	5.63	4.80	5.21
Imam (#74)	4.36	3.10	1.89	48.74	14.11	11.75
*I*2*cm* (#46)	4.33	3.07	1.87	47.53	13.95	11.43
$RbNdNb_2O_7$						
	Synchrotron X-ray			Neutron		
Space group	χ^2	wRp (%)	Rp (%)	χ^2	wRp(%)	Rp (%)
*P*2$_1$*am* (#26)	5.05	5.79	3.81	103.10	16.31	12.12
Imam (#74)	5.12	5.85	3.84	68.07	13.22	11.10
*I*2*cm* (#46)	4.97	5.76	3.78	8.23	6.31	6.25
$RbNdTa_2O_7$						
	Synchrotron X-ray			Neutron		
Space group	χ^2	wRp (%)	Rp (%)	χ^2	wRp(%)	Rp (%)
*P*2$_1$*am* (#26)	6.81	3.78	2.33	86.69	15.63	11.63
Imam (#74)	6.87	3.81	2.36	40.59	10.70	9.56
*I*2*cm* (#46)	6.76	3.75	2.31	8.33	4.85	4.96

Table 3.8. Fitting statistics from the structural refinements of $CsNdTa_2O_7$, $RbNdNb_2O_7$ and $RbNdTa_2O_7$ against both synchrotron X-ray and neutron powder diffraction data.

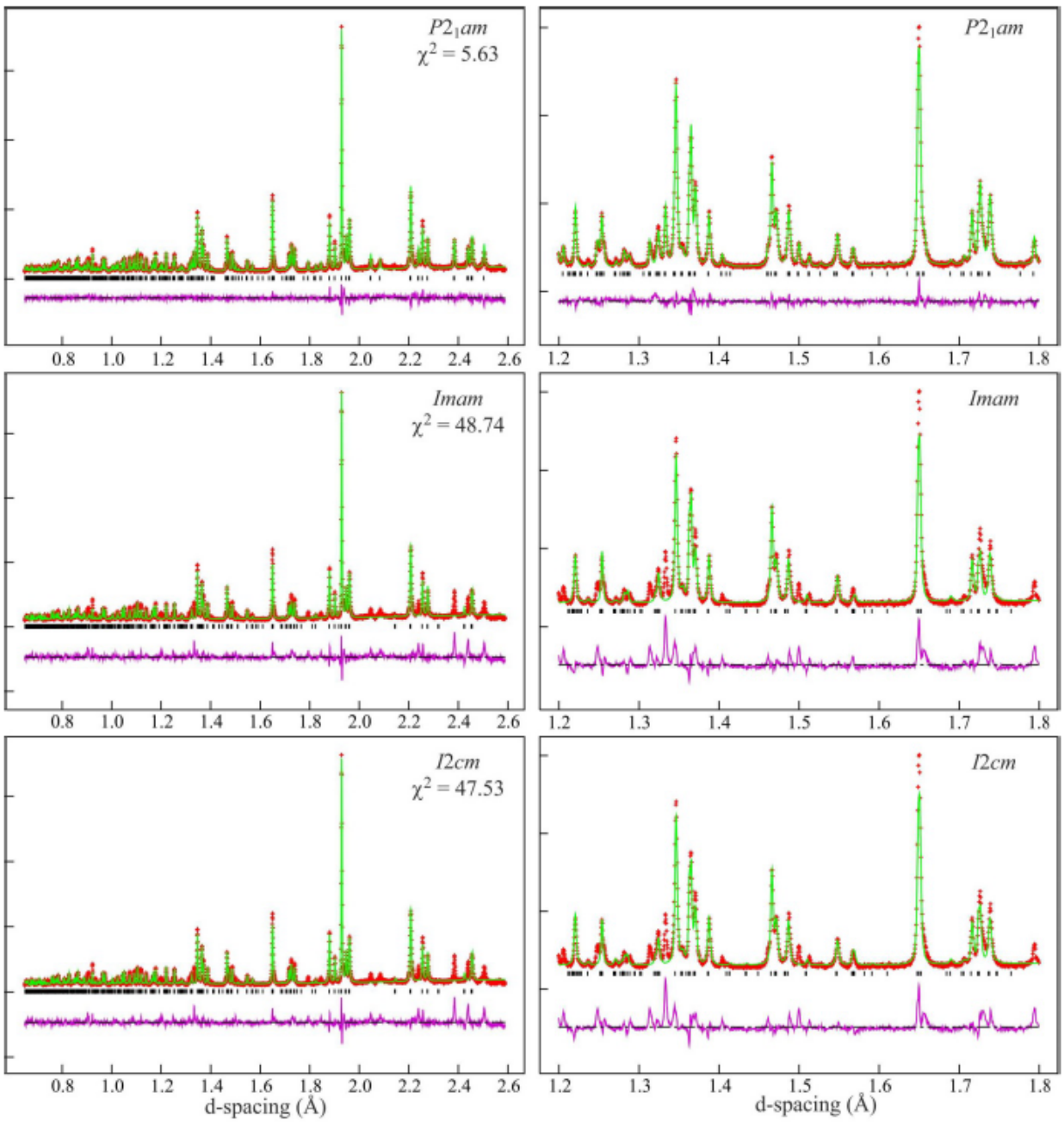


Figure 3.11. Observed, calculated and difference plots from the refinement against the high-resolution neutron diffraction data collected from $CsNdTa_2O_7$ at ambient temperature, of structural models of *P*2₁*am*, *Imam* and *I*2*cm*. Panels on the right show the expanded regions from 1.2 Å to 1.8 Å, which highlight the difference in the quality of the fits with different models.

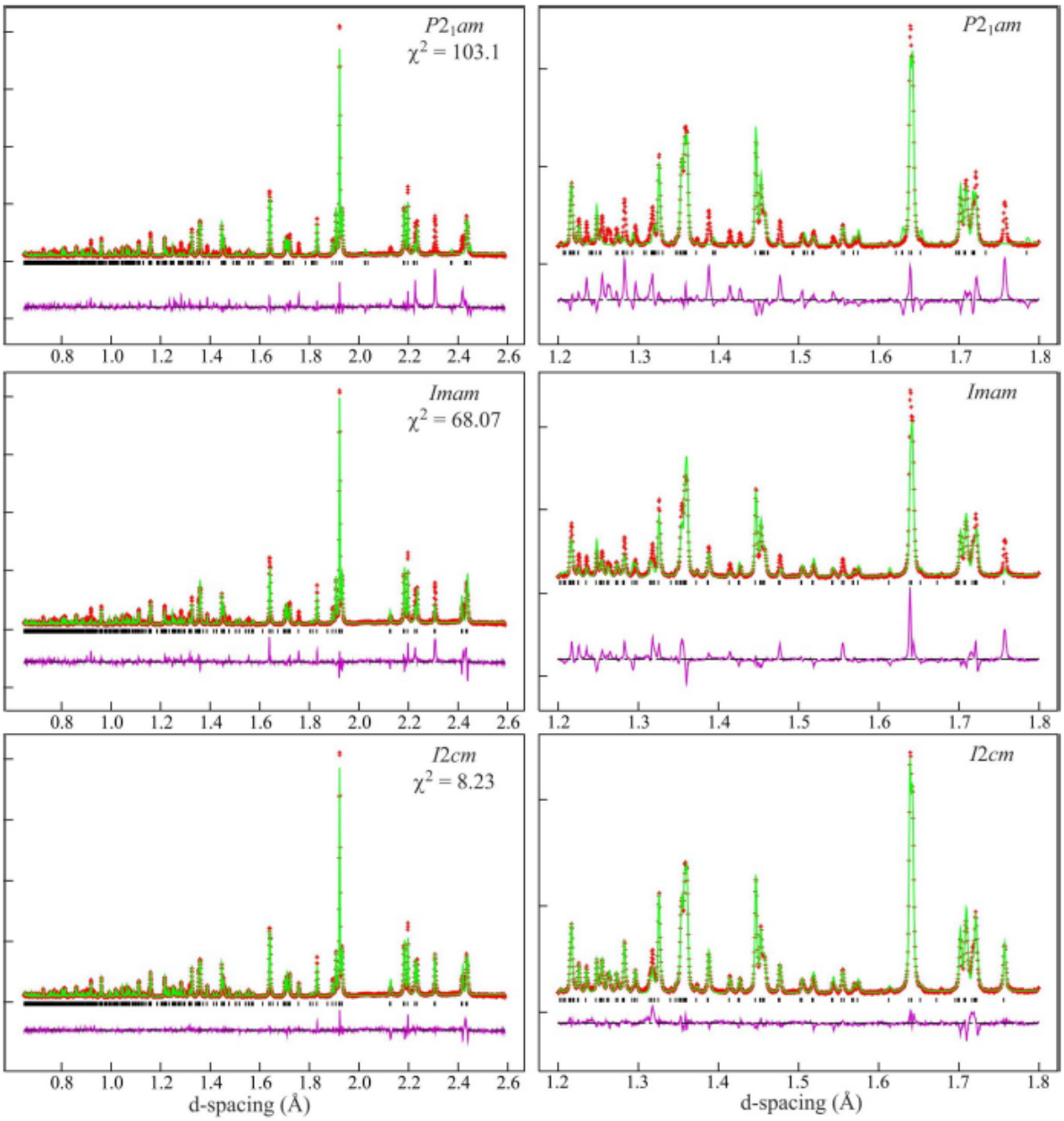


Figure 3.12. Observed, calculated and difference plots from the refinement against the high-resolution neutron diffraction data collected from $RbNdNb_2O_7$ at room temperature, of structural models of *P*2₁*am*, *Imam* and *I*2*cm*. Panels on the right show the expanded regions from 1.2 Å to 1.8 Å, which highlight the difference in the quality of the fits with different models.

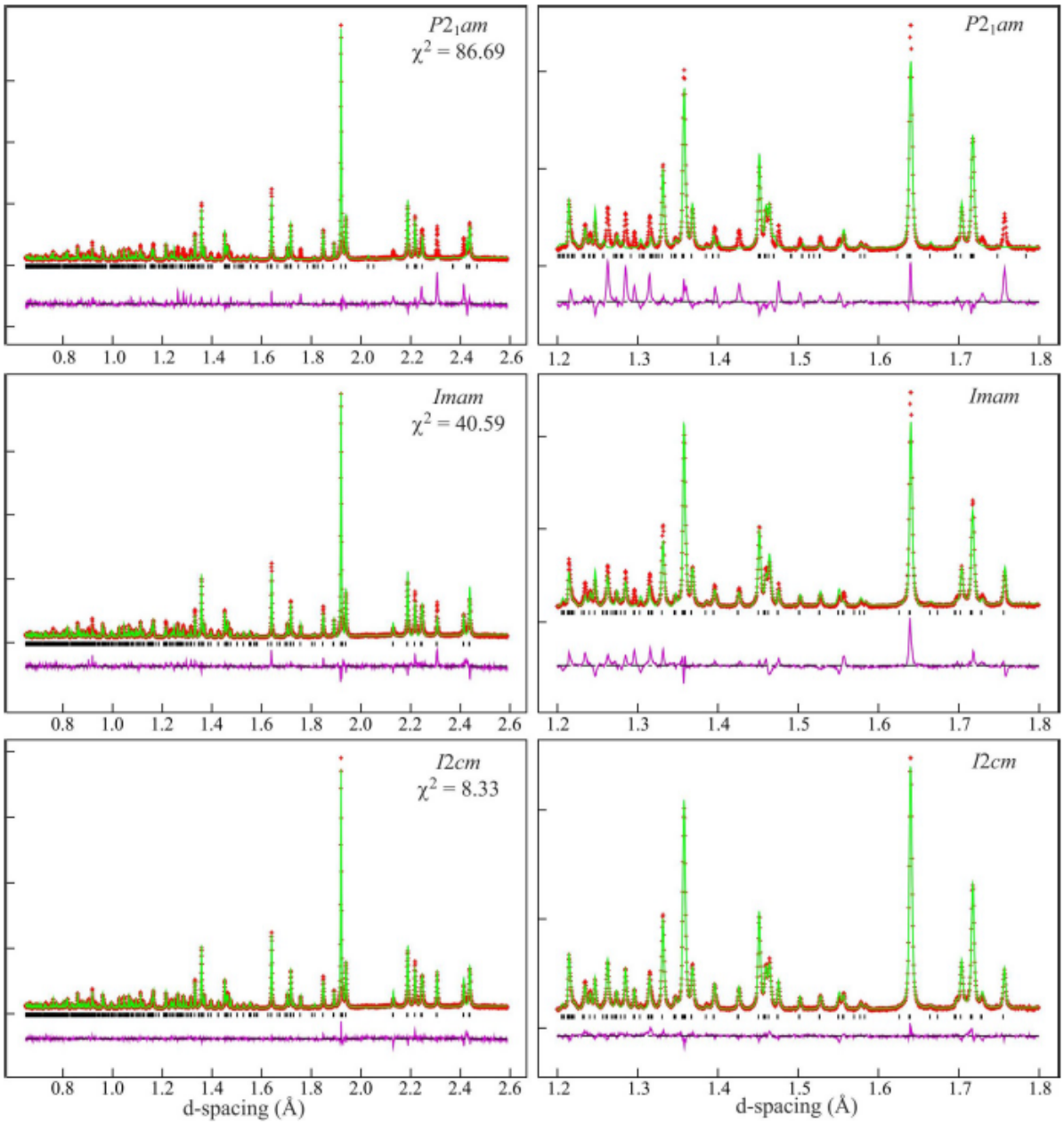


Figure 3.13. Observed, calculated and difference plots from the refinement against the high-resolution neutron diffraction data collected from $RbNdTa_2O_7$ at room temperature, of structural models of *P*2₁*am*, *Imam* and *I*2*cm*. Panels on the right show the expanded regions from 1.2 Å to 1.8 Å, which highlight the difference in the quality of the fits with different models.

3.4.2 Theory revised

As mentioned in Section 3.1, prior theoretical works predicted that both $RbNdNb_2O_7$ and $CsNdNb_2O_7$ adopt polar $P2_1am$ structures[24]. Our analysis of neutron diffraction data shows that $CsNdNb_2O_7$ indeed adopts a $P2_1am$ structure but $RbNdNb_2O_7$ adopts an $I2cm$ structure in which the c lattice is doubled with respect to the $P2_1am$ structure. The reason for the wrong structural assignment from DFT calculation is that crystal structures with expanded c lattice (parallel to the stacking axis) were not considered for $n = 2$ Dion-Jacobson phases in previous works.

Table 3.9 shows the calculated energy of the $P2_1am$ and $I2cm$ structures for $RbNdNb_2O_7$, $RbNdTa_2O_7$, $CsNdNb_2O_7$ and $CsNdTa_2O_7$[10]. Calculations show that the energy of the $I2cm$ phase is lower than that of the $P2_1am$ phase in both cases of $RbNdNb_2O_7$ and $RbNdTa_2O_7$, whereas the energy of the $P2_1am$ phase is lower for $CsNdNb_2O_7$ and $CsNdTa_2O_7$. The revised theoretical calculations are consistent with our experimental observations.

The theory revision case shows that, although first principle DFT calculation is a powerful tool for searching new polar materials and predicting their crystal structures, it is necessary to combine computational predictions with experimental data to generate accurate results. The calculations have to test the right set of models in order to find the correct structure.

	ΔE (meV/formula unit)	
	$P2_1am$	$I2cm$
$RbNdNb_2O_7$	-349	-360
$RbNdTa_2O_7$	-297	-307
$CsNdNb_2O_7$	-320	-309
$CsNdTa_2O_7$	-267	-258

Table 3.9. Energy differences between the aristotype $P4/mmm$ and $P2_1am$/$I2cm$ structures of $RbNdNb_2O_7$, $RbNdTa_2O_7$, $CsNdNb_2O_7$ and $CsNdTa_2O_7$[10].

3.4.3 Structural differences in RbNdM_2O_7 and CsNdM_2O_7

As RbNdM_2O_7 and CsNdM_2O_7 (M = Nb/Ta) are confirmed to have different crystal structures (*I*2*cm* for RbNdM_2O_7 with a Glazer tilt of $a^-a^-c^+$/-($a^-a^-c^+$) and $P2_1am$ for CsNdM_2O_7 with an $a^-a^-c^+$ tilt), it is reasonable to ask where their structural differences come from. Before discussing the differences, it is worth looking at the similarities first. Despite the differences in the bulk structures, the local perovskite distortions in RbNdM_2O_7 and CsNdM_2O_7 are the same, both in the Glazer tilt $a^-a^-c^+$. This indicates that both A-site (Nd^{3+}) and B-site (Nb^{5+}/Ta^{5+}) cations must have similar bonding environments in RbNdM_2O_7 and CsNdM_2O_7. The bonding similarity can be demonstrated by the corresponding bond lengths and BVS values in the refined structures. Using RbNdTa_2O_7 and CsNdTa_2O_7 as examples, the refined TaO_6 polyhedra have an average bond length of 2.012 Å (BVS = 5.10) and 2.011 Å (BVS = 5.06) for RbNdTa_2O_7 and CsNdTa_2O_7, respectively. The average Nd-O bond lengths are 2.711 Å (BVS = 3.09) for RbNdTa_2O_7 and 2.708 Å (BVS = 3.07) for CsNdTa_2O_7. Therefore, it is safe to conclude that the bulk structural differences in RbNdM_2O_7 and CsNdM_2O_7 have no obvious bonding effect on A-site or B-site cations.

Since the perovskite double sheets are effectively the same in RbNdM_2O_7 and CsNdM_2O_7, it must be the A'-O layer which results in the structural differences. This is not surprising given the only 'variables' in these two types of polar Dion-Jacobson phases are the interlayer A' cations (Rb^+ and Cs^+). Therefore we want to have a close inspection of the RbO_8 and CsO_8 layers. One question to ask then is 'what would happen to the RbO_8 polyhedra if RbNdM_2O_7 adopted the $P2_1am$ structural symmetry and what about the CsO_8 polyhedra if CsNdM_2O_7 adopted the *I*2*cm* structural symmetry'. It is obvious that, in order to answer this question and have a direct comparison, a hypothetical '$P2_1am$' structure for RbNdM_2O_7 and a hypothetical '*I*2*cm*' structure for CsNdM_2O_7 are required. One important

point to notice here is that the hypothetical structures are not extracted from the refined structures with wrong models. For example, the refined $P2_1am$ structural model against the neutron diffraction data collected from $RbNdNb_2O_7$ cannot be used for the comparison because the refined structure based on the wrong model gives wrong atomic positions therefore it would not be able to describe the desired octahedral distortions or the RbO_8 polyhedra. A proper principle is needed to 'design' the theoretical structures. $RbNdNb_2O_7$ and $CsNdNb_2O_7$ will be used as examples to illustrate the 'designing principle'.

In the $P2_1am$ structure adopted by $CsNdNb_2O_7$ (Figure 3.1), perovskite double layers are related by a translational symmetry along the stacking axis in a simple primitive (0, 0, ½) stacking pattern. '½' is used so that it can be directly compared with $RbNdNb_2O_7$, in which the '*c*' lattice parameter is doubled with respect to the $P2_1am$ cell. In contrast, in the *I*2*cm* structure adopted by $RbNdNb_2O_7$ (Figure 3.7), perovskite double layers are stacked in a (½, 0, ½) configuration (Figure 3.14). The hypothetical $P2_1am$-type structure on $RbNdNb_2O_7$ can be constructed by shifting the top perovskite double layer (-½, 0, 0) from the 'real' *I*2*cm* structure. Similarly, the hypothetical *I*2*cm*-type structure for $CsNdNb_2O_7$ can be built by shifting the top perovskite double layer (½, 0, 0) from the 'real' $P2_1am$ structure. This designing principle means the $NdNb_2O_7$ perovskite double sheets remain the same in the 'real' and 'hypothetical' structures, so do the local distortions. The structural transformation is illustrated in Figure 3.14. One additional point to notice is that the hypothetical structure is not exactly *I*2*cm* for $CsNdNb_2O_7$ due the different site symmetry of Rb/Cs in the two structural models, which will be explained later.

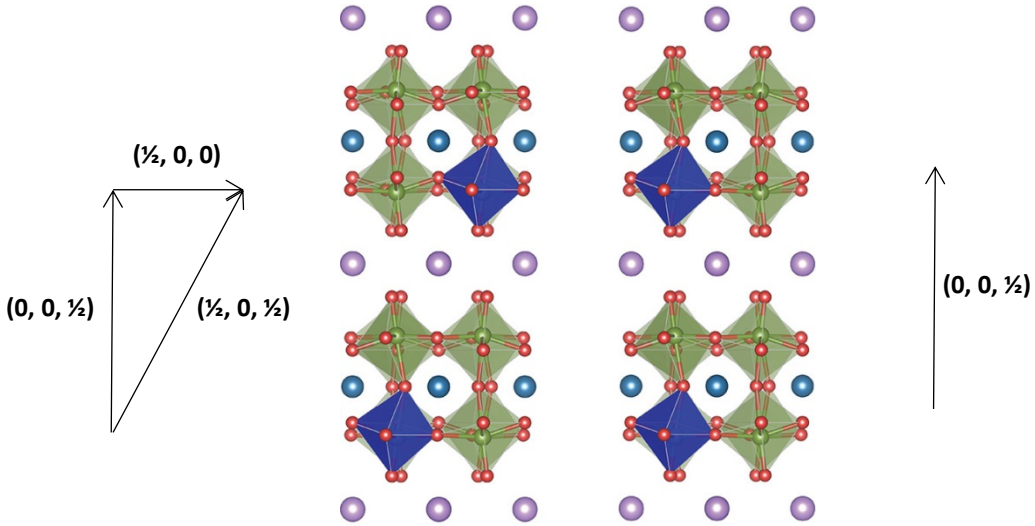


Figure 3.14. Left: Refined structure of $RbNdNb_2O_7$ in space group *I*2*cm* with an $a^-a^-c^+/-(a^-a^-c^+)$ distortion. Equivalent NbO_6 polyhedra are coloured in blue to illustrate the (½, 0, ½) stacking. Right: Hypothetical structure of $RbNdNb_2O_7$ with an $a^-a^-c^+$ distortion. Equivalent NbO_6 polyhedra are coloured in blue to illustrate the (0, 0, ½) stacking. The two polymorphs can be inter-converted by an additional ±(½, 0, 0) translation of the top layer. $CsNdNb_2O_7$ can be considered as an exactly opposite case where the right-hand side structure is the refined structure while the left structure is the hypothetical structure with an additional (½, 0, 0) shift of the top layer.

RbO_8 polyhedra in the refined *I*2*cm* structure of $RbNdNb_2O_7$ and in the hypothetical, primitive stacking structure are shown in Figure 3.15. It can be seen that RbO_8 polyhedra in the two structures have the same Rb-O bond lengths. However, a (½, 0, ½) stacking pattern of perovskite double sheets means the 'opposite' O atoms are displaced in opposite directions (Figure 3.14 and 3.15). The consequence is that the interlayer O-O bond length is longer in the refined *I*2*cm* structure, which suggests that the interlayer O-O repulsion is weaker in the refined *I*2*cm* structure, a clear advantage of adopting the *I*2*cm* structure rather than the hypothetical, primitive-stacking $P2_1am$ structure.

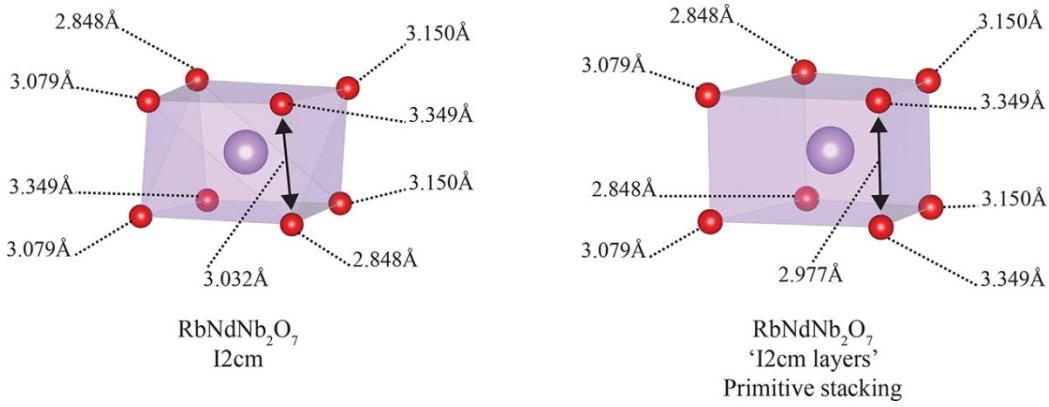


Figure 3.15. Left: A RbO_8 polyhedron in the refined *I2cm* structure. Right: A RbO_8 polyhedron in the hypothetical, primitive stacking structure. Values on the oxide ions (red spheres) represent the corresponding Rb-O bond lengths; Values on the double-arrow lines are the corresponding O-O bond lengths. RbO_8 bond lengths are the same in the two polyhedra while the interlayer O-O bond is longer in the *I2cm* structure.

Given the clear advantage of adopting the *I*2*cm* structure, one obvious question to ask is why $CsNdM_2O_7$ adopts a *P*2$_1$*am* structure. CsO_8 polyhedra in the refined *P*2$_1$*am* structure and the hypothetical *I*2*cm*-type structure, both from $CsNdNb_2O_7$, are shown in Figure 3.16. The hypothetical structure is not exactly '*I*2*cm*' because *P*2$_1$*am* and *I*2*cm* structural models have different site symmetry for Cs^+ cations. To be more specific, there are two free parameters, *x* and *y* (Table 3.1), for Cs^+ cations in the *P*2$_1$*am* structural symmetry but only one free parameter, *x* (Table 3.2 and 3.3), in the *I*2*cm* structural symmetry. Therefore there are more degrees of freedom for Cs^+ cations in the *P*2$_1$*am* structure. The additional displacement for Cs^+ cations in the *P*2$_1$*am* structure symmetry means that the bond lengths in the hypothetical, *I*2*cm*-type structure are different from the refined *P*2$_1$*am* structure. There is a very short Cs-O bond (2.857 Å) in the *I*2*cm*-type structure and it is too short for Cs to adopt this configuration (Figure 3.16). This short Cs-O bond means $CsNdNb_2O_7$ chooses to adopt the *P*2$_1$*am* structure and the additional degree of freedom for Cs^+ cations can release the bond strain, despite a weaker interlayer O-O repulsion in the hypothetical *I*2*cm*-type structure.

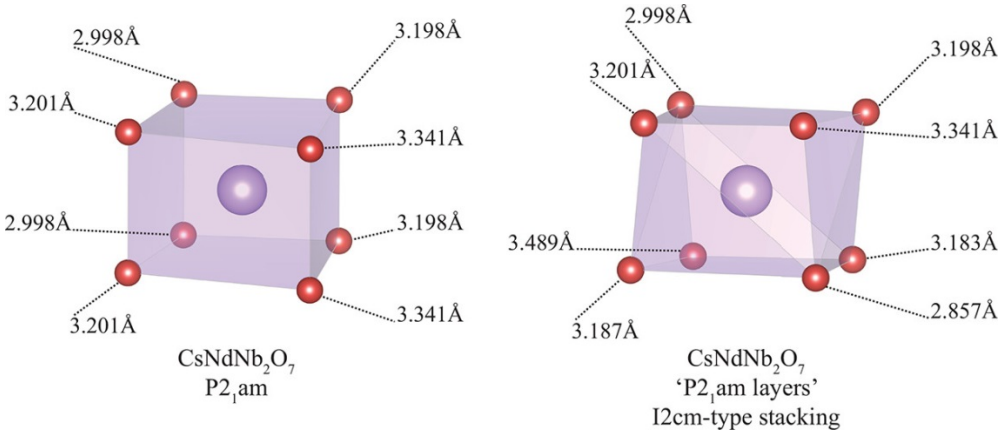


Figure 3.16. Left: A CsO_8 polyhedron in the refined *P*2₁*am* structure. Right: A CsO_8 polyhedron in the hypothetical, *I*2*cm*-type structure. Values on oxide ions (red spheres) represent the corresponding Cs-O bond lengths. There is a very short Cs-O bond in the *I*2*cm*-type structure. This short Cs-O bond is not observed in the *P*2₁*am* structure due to the extra degree of freedom Cs^+ cations have in the *P*2₁*am* structural symmetry.

In summary, the structural choice for $RbNdM_2O_7$ and $CsNdM_2O_7$ is a compromise. The NdM_2O_7 perovskite double layers are remarkably similar in $RbNdM_2O_7$ and $CsNdM_2O_7$. $RbNdM_2O_7$ adopts an *I*2*cm* structure with a (½, 0, ½) stacking pattern because this structural configuration minimizes the interlayer O-O repulsion although Rb^+ cations are locked in a relatively high-symmetry site. $CsNdM_2O_7$ adopts a *P*2₁*am* structure with a (0, 0, ½) stacking configuration because this structural symmetry gives Cs^+ cations more degrees of freedom to avoid the formation of a very short Cs-O bond although this structural configuration may lead to slightly stronger interlayer O-O repulsion. BVS values for Rb^+ cations are 0.91 in $RbNdNb_2O_7$ and 0.88 in $RbNdTa_2O_7$, which indicate Rb^+ cations are well bonded and the extra degree of freedom in the primitive stacking structure is not really necessary for Rb^+ cations so the structure tends to minimize the interlayer O-O repulsion as its priority. Another simple way to understand the structural differences is to refer to the ionic radii of Rb^+ and Cs^+ cations[66]. Rb^+ (1.61 Å) is smaller so does the RbO_8 polyhedra. The interlayer O-O repulsion 'issue' hence is critical and $RbNdM_2O_7$ tend to minimize the O-O repulsion by adopting the *I*2*cm* structure. Cs^+ (1.74 Å) is larger so are the CsO_8

polyhedra, therefore the interlayer O-O repulsion is not as strong as in $RbNdM_2O_7$ case so optimizing Cs-O bonding is the priority.

3.5 Conclusion

Our characterisation reveals that a series of n = 2 Dion-Jacobson phases adopt polar structures. Among these polar phases, $CsNdTa_2O_7$ is isostructural to previously reported $CsNdNb_2O_7$ and adopts a polar $P2_1am$ structure with an $a^-a^-c^+$ tilt. $RbNdNb_2O_7$ and $RbNdTa_2O_7$ adopt a different polar structure in space group $I2cm$ with an $a^-a^-c^+$/-($a^-a^-c^+$) tilt. The structural differences arise from the size difference between Rb^+ and Cs^+ cations. $RbNdNb_2O_7$ and $RbNdTa_2O_7$ adopt an $I2cm$ structure with a (½, 0, ½) stacking configuration of the perovskite double sheets to minimise the interlayer O-O repulsion. $CsNdTa_2O_7$ adopts a $P2_1am$ structure in a primitive stacking of the perovskite layers so that a short Cs-O bond can be avoided and Cs-O bonding can be optimized.

Octahedral tilting distortions in $RbNdNb_2O_7$, $RbNdTa_2O_7$ and $CsNdTa_2O_7$ arise from the subtle displacements of oxide ions from their high symmetry positions, therefore high-resolution neutron diffraction technique is essential for the crystal structure characterisation due to the similar neutron scattering lengths of oxygen compared to heavy metals. This conclusion is also true for other perovskite materials with distorted structures.

Our findings, combined with recent theoretical studies, suggest that other similar n = 2 Dion-Jacobson phases should also be revised to investigate if other polar phases can be discovered.

Two additional questions can be asked based on our findings: 1. Since the difference in interlayer cations, especially their ionic radii, results in different distorted structures, what would happen if Rb^+/Cs^+ cations are replaced by other Group I metal cations? 2. What is

the phase transition behaviour of $RbNdNb_2O_7$, $RbNdTa_2O_7$ and $CsNdTa_2O_7$? Both questions will be answered in the following chapters.

Chapter 4 – Topochemical Cation Exchange of $RbNdM_2O_7$ to $LiNdM_2O_7$ and $NaNdM_2O_7$ (M = Nb/Ta)

4.1 Introduction

Dion-Jacobson phases are very suitable starting materials for low temperature cation exchange reactions. In Dion-Jacobson phases, large, monovalent interlayer cations have high mobility due to their open coordination environments and low charge density. Therefore they can be easily exchanged by smaller cations to often form metastable phases. For example, the metastable phases $LiNdNb_2O_7$ and $NaNdNb_2O_7$ can be prepared by treating $RbNdNb_2O_7$ with the corresponding metal nitrates[37, 67]. $HNdNb_2O_7$ can be made by proton exchange from $RbNdNb_2O_7$ with diluted nitric acid[67]. During the cation exchange reactions from $RbNdNb_2O_7$ to $LiNdNb_2O_7$ and $NaNdNb_2O_7$, there is a change in the stacking arrangements of the perovskite sheets, from a primitive stacking pattern in the Dion-Jacobson framework to a body-centred stacking pattern in the Ruddlesden-Popper framework (Figure 4.1). This structural change is driven by the decrease in interlayer cation sizes from Rb^+ to Li^+/Na^+. The change in the stacking arrangements forms small interlayer tetrahedral sites in the exchanged phases to accommodate Li^+ and Na^+ cations.

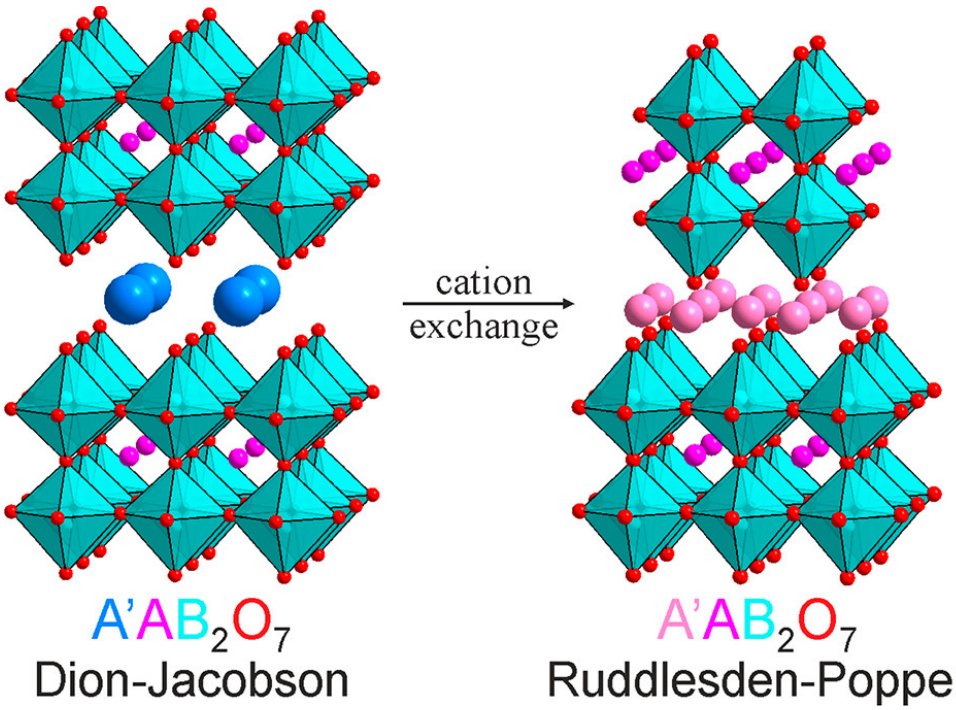


Figure 4.1. Structural transformation from the *n* = 2 Dion-Jacobson framework to the *n* = 2 Ruddlesden-Popper framework[68]. The pink A' cations are half occupied.

Both $LiNdNb_2O_7$ and $NaNdNb_2O_7$ were previously reported to have an undistorted structure in space group $I4/mmm$[67]. In this undistorted structure, Li^+ and Na^+ cations adopt a disordered arrangement in the interlayer tetrahedral sites with half occupancy and there is no octahedral tilt in the $NdNb_2O_7$ perovskite layer (Figure 4.1). However, as described in Chapter 3, both $RbNdNb_2O_7$ and $CsNdNb_2O_7$ adopt distorted structures and the $NdNb_2O_7$ perovskite double layers have an $a^-a^-c^+$ tilting distortion in both $RbNdNb_2O_7$ and $CsNdNb_2O_7$. It is therefore interesting to see if $LiNdNb_2O_7$ and $NaNdNb_2O_7$ indeed have undistorted structures. Another reason to suspect the previous report may be incorrect is that the crystal structures of $LiNdNb_2O_7$ and $NaNdNb_2O_7$ were both established from X-ray diffraction experiments and X-ray diffraction is not sensitive to either O displacement or Li/Na order.

4.2 Synthesis

Powder samples of $RbNdNb_2O_7$ and $RbNdTa_2O_7$ were prepared by a ceramic synthesis method, as described in Chapter 3. Lithium and sodium exchange reactions were performed by reacting $RbNdNb_2O_7$ and $RbNdTa_2O_7$ with 10 molar equivalents of either $LiNO_3$ (99.8%) or $NaNO_3$ (99%). The mixtures were ground and loaded into an open-ended silica tube. Lithium exchange reactions were heated at 300 °C in air for two periods of 48 hours. Sodium exchange reactions were heated at 400 °C in air for two periods of 48 hours. The silica tubes were kept in a vertical orientation during the heating cycles as both lithium and sodium nitrates melt at the reaction temperatures. Between heating cycles, samples were washed with distilled water to remove the remaining lithium or sodium nitrates, dried for 12 hours at 140 °C in air, and mixed with fresh 10 molar equivalents of lithium or sodium nitrates. After the final heating step, all samples were washed with distilled water to remove remaining nitrates, and dried for 12 hours at 140 °C in air. Samples of $NaNdNb_2O_7$ and $NaNdTa_2O_7$ were then dried under flowing argon for 12 hours at 300 °C to eliminate all absorbed water and were then transferred into an argon-filled glovebox for storage. Reaction progress and final sample purity were assessed by X-ray powder diffraction data collected using a PANalytical X'pert diffractometer incorporating an X'celerator position sensitive detector (monochromatic Cu Kα1 radiation).

4.3 Results

4.3.1 Optical SHG measurements

Particle-size dependent SHG measurements show that both $LiNdNb_2O_7$ and $LiNdTa_2O_7$ are SHG active therefore they adopt non-centrosymmetric structures (Figure 4.2). In contrast,

both $NaNdNb_2O_7$ and $NaNdTa_2O_7$ show no detectable SHG intensity, indicating they adopt centrosymmetric crystal structures.

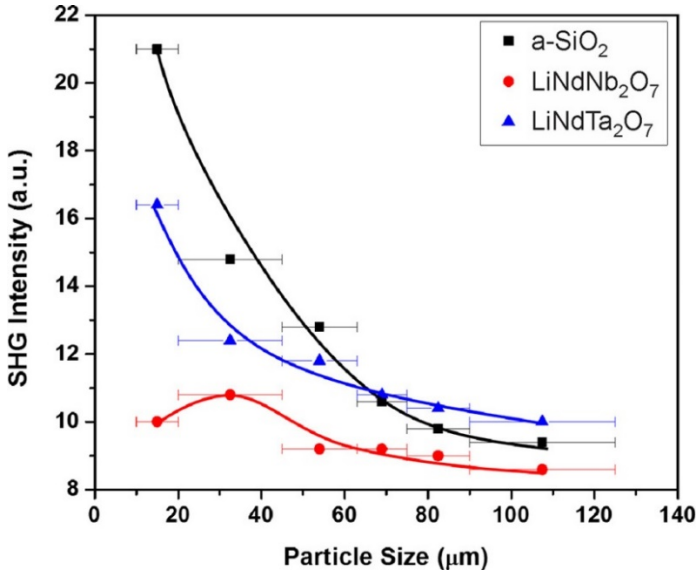


Figure 4.2. Plots of SHG activity of $LiNdNb_2O_7$ and $LiNdTa_2O_7$ as a function of particle size, compared to an α-SiO_2 standard.

4.3.2 Symmetry analysis of $n = 2$ Ruddlesden-Popper phases

Synchrotron X-ray and neutron powder diffraction data indicate that $LiNdM_2O_7$ and $NaNdM_2O_7$ adopt distorted structures with expanded unit cells (detailed characterisation will be given later in this chapter). Direct crystallographic analysis of the distorted structures adopted by $n = 2$ Ruddlesden-Popper phases can be challenging. Therefore a symmetry analysis was performed by referring to a previous crystallography study[11] and using the ISODISTORT software[12] to generate a series of 'chemically plausible' distorted crystal structures of $n = 2$ Ruddlesden-Popper phases (Table 4.1).

Using $CsNdTa_2O_7$ as an example, in Chapter 3, it is demonstrated $CsNdTa_2O_7$ adopts a $P2_1am$ structure with an $a^-a^-c^+$ tilting distortion. This polar structure can be considered as an undistorted $P4/mmm$ space symmetry 'plus' two irreducible representations, A and B. Irreducible representation A leads to the out-of-phase rotation of the TaO_6 octahedra along both x and y directions, resulting in a structure with an $a^-a^-c^0$ tilting distortion. Irreducible

representation B leads to the in-phase rotation of the TaO_6 octahedra along the *z* direction, resulting in a structure with an $a^0a^0c^+$ tilting distortion. These two irreducible representations are independent of each other and the final non-centrosymmetric structure arises from a combination of these two irreducible representations. Alternatively, the polar $P2_1am$ structure can be viewed as a low symmetry structure by freezing two phonon modes with respect to the aristotype, $P4/mmm$ structure. By applying possible irreducible representations on the aristotype structure, we can relate distortions with their corresponding structure symmetries.

Twist	Glazer Tilts	Space Group (standard setting)	Stacking axis	Space Group (c-stacking)	Irrep	Centrosymmetric?
000/000	$a^0b^0c^0/a^0b^0c^0$	*I*4/*mmm* (139)	c	*I*4/*mmm*		Yes
$00\Psi_z/00\Psi_z$	$a^0a^0c^+/a^0a^0c^+$	*Cmca* (64)	a' = c	*Bbcm*	X_2^+ (0,a)	Yes
$00\Phi_z/00\Phi_z$	$a^0a^0c^-/a^0a^0c^-$	*Ccca* (68)	a' = c	*Bbcb*	X_1^- (0,a)	Yes
$\Phi00/0\Phi0$	$a^-b^0c^0/b^0a^-c^0$	$P4_2/mnm$ (136)	c' = c	$P4_2/mnm$	X_3^- (a,a)	Yes
$\Phi\Phi0/\Phi\Phi0$	$a^-a^-c^0/a^-a^-c^0$	*Cmcm* (63)	a' = c	*Bbmm*	X_3^- (0,a)	Yes
$\Phi_1\Phi_20/\Phi_2\Phi_10$	$a^-b^-c^0/b^-a^-c^0$	*Pnnm* (58)	c' = c	*Pnnm*	X_3^- (a,b)	Yes
$\Phi00/0\text{-}\Phi0$	$a^-b^0c^0/b^0\text{-}a^-c^0$	$P4_2/mcm$ (132)	c' = c	$P4_2/mcm$	X_4^- (a,a)	Yes
$\Phi\Phi0/\text{-}(\Phi\Phi)0$	$a^-a^-c^0/\text{-}(a^-a^-)c^0$	*Cmma* (67)	a' = c	*Bmcm*	X_4^- (0,a)	Yes
$\Phi_1\Phi_20/\text{-}(\Phi_2\Phi_1)0$	$a^-b^-c^0/\text{-}(b^-a^-)c^0$	*Pccm* (49)	c' = c	*Pccm*	X_4^- (a,b)	Yes
$\Phi\Phi\Psi_z/\Phi\Phi\Psi_z$	$a^-a^-c^+/a^-a^-c^+$	$Cmc2_1$ (36)	a' = c	$A2_1am$	$X_2^+ \bullet X_3^-$ (0,a; 0,b)	No
$\Phi\Phi\Psi_z/\Phi\Phi\text{-}\Psi_z$	$a^-a^-c^+/a^-a^-\text{-}c^+$	*Pnma* (62)	b' = c	*Pnam*	$X_2^+ \bullet X_3^-$ (0,a; b,0)	Yes
$\Phi_1\Phi_2\Psi_z/\Phi_2\Phi_1\Psi_z$	$a^-b^-c^+/b^-a^-c^+$	$Pmn2_1$ (31)	a' = c	$P2_1nm$	$X_2^+ \bullet X_3^-$ (0,a; b,c)	No
$\Phi\Phi\Psi_z/\text{-}(\Phi\Phi\Psi_z)$	$a^-a^-c^+/\text{-}(a^-a^-c^+)$	*Abm*2 (39)	b' = c	*B*2*cm*	$X_2^+ \bullet X_4^-$ (0,a; 0,b)	No
$\Phi\Phi\Psi_z/\text{-}(\Phi\Phi)\Psi_z$	$a^-a^-c^+/\text{-}(a^-a^-)c^+$	*Pbcm* (57)	c' = c	*Pbcm*	$X_2^+ \bullet X_4^-$ (0,a; b,0)	Yes
$\Phi_1\Phi_2\Psi_z/\text{-}(\Phi_1\Phi_2)\Psi_z$	$a^-b^-c^+/\text{-}(a^-b^-)c^+$	*Pma*2 (28)	a' = c	*P*2*cm*	$X_2^+ \bullet X_4^-$ (0,a; b,c)	No
$\Phi\Phi\Phi_z/\Phi\Phi\Phi_z$	$a^-a^-c^-/a^-a^-c^-$	*C*2/*c* (15)	a' = c	*A*2/*a*	$X_1^- \bullet X_3^-$ (0,a; 0,b)	Yes
$\Phi\Phi\Phi_z/\Phi\Phi\text{-}\Phi_z$	$a^-a^-c^-/a^-a^-\text{-}c^-$	*Pbcn* (60)	a' = c	*Pnab*	$X_1^- \bullet X_3^-$ (0,a; b,0)	Yes
$\Phi_1\Phi_2\Phi_z/\Phi_2\Phi_1\Phi_z$	$a^-b^-c^-/b^-a^-c^-$	$P2_1/c$ (14)	c' = c	$P2_1/c$	$X_1^- \bullet X_3^-$ (0,a; b,c)	Yes
$\Phi\Phi\Phi_z/\text{-}(\Phi\Phi)\Phi_z$	$a^-a^-c^-/\text{-}(a^-a^-)c^-$	*Pcca* (54)	a' = c	*Pbcb*	$X_1^- \bullet X_4^-$ (0,a; b,0)	Yes
$\Phi_1\Phi_2\Phi_z/\text{-}(\Phi_1\Phi_2)\Phi_z$	$a^-b^-c^-/\text{-}(a^-b^-)c^-$	*P*2/*c* (13)	c' = c	*P*2/*c*	$X_1^- \bullet X_4^-$ (0,a; b,c)	Yes
$\Phi\Phi\Phi_z$	$a^-a^-c^-$	*P*2/*c* (13)	a' = ½ c	*P*2/*a*	$X_1^- \bullet X_4^-$ (0,a; 0,b)	Yes

Table 4.1. 'Chemically plausible' distortions of *n* = 2 Ruddlesden-Popper structures. All these distorted structures have the same *c* lattice except the last one.

Undistorted n = 2 Ruddlesden-Popper phases have an $I4/mmm$ space symmetry. 8 chemically-plausible distorted structures can be generated by applying a single irreducible representation on the undistorted structure and they are labelled in orange in Table 4.1. These structures only contain tilting distortions along x/y or z directions. The remaining 12 distorted structures (labelled in green or grey) are generated by applying two independent irreducible representations on the $I4/mmm$ structure. Therefore they have distortions along both x/y and z directions. The first two columns describe the distortions using the notations of Aleksandrov and Bartolome or Glazer. The third column lists the space groups of the distorted structures in their standard space group settings, after applying the irreducible representations, with the fourth column listing the stacking axes in the standard settings. The fifth column lists the space groups oriented with z-axes as the stacking axes. The sixth column shows the corresponding irreducible representations with their direction parameters. The table lists all chemically plausible tilting distortions of n = 2 Ruddlesden-Popper phases. Structures with 'chemically plausible' distortions are defined as retaining equivalence of BO_6 octahedra in all perovskite double layers. This means all perovskite layers must be able to be related by symmetry and there must be some relation between distortions in adjacent perovskite layers. For examples, structures with $a^-a^-c^+/\text{-}(a^-a^-)c^+$, $a^-b^-c^+/\ b^-a^-c^+$ or $a^-a^-c^+/\ a^-a^-\text{-}c^+$ are chemically plausible because topologically equivalent cations have the same local environments in these distorted structures. In contrast, structures with $a^-a^-c^+/a^-a^-c^0$ or $a^-a^-c^+/b^-b^-c^+$ are chemically implausible because topologically equivalent cations now have different local environments in different perovskite double layers and adjacent layers are not able to be related by symmetry.

One obvious advantage of the symmetry analysis is that although Table 4.1 is not mathematically comprehensive, it provides limited structural candidates for n = 2

Ruddlesden-Popper phases. $LiNdM_2O_7$ and $NaNdM_2O_7$ are assumed to adopt one of the structures with 'chemically plausible' distortions.

4.3.3 Structure characterisation of $LiNdNb_2O_7$

4.3.3.1 Room temperature synchrotron X-ray powder diffraction

Synchrotron X-ray diffraction data collected from $LiNdNb_2O_7$ at ambient temperature can be indexed using an orthorhombic unit cell with an approximate $\sqrt{2} \times \sqrt{2} \times 1$ geometric expansion of the aristotype *I*4/*mmm* unit cell, (a = 5.450 Å, b = 5.397 Å, c = 20.456 Å). The SHG activity suggests that it adopts a non-centrosymmetric structure (Figure 4.2). Therefore all space groups describing centrosymmetric structures in Table 4.1 can be eliminated, leaving only four structural candidates: *P*2*cm* (#28), *P*2_1*nm* (#31), *Bb*2_1*m* (#36, transformed from *A*2_1*am* in order to be consistent with other space groups in both lattice parameters and peak indexes) and *B*2*em* (#39). Further examination of the low angle region of the diffraction data reveals that the *Bb*2_1*m* model can also be eliminated as the observations of [010] and [012] peaks are inconsistent with the *b* glide plane in the *Bb*2_1*m* space symmetry, as shown in Figure 4.3. Refining the remaining models against the synchrotron X-ray diffraction data gives equally good fits for all three models. As an example, the observed, calculated and difference plots against the synchrotron X-ray data in space group *B*2*em* are shown in Figure 4.4.

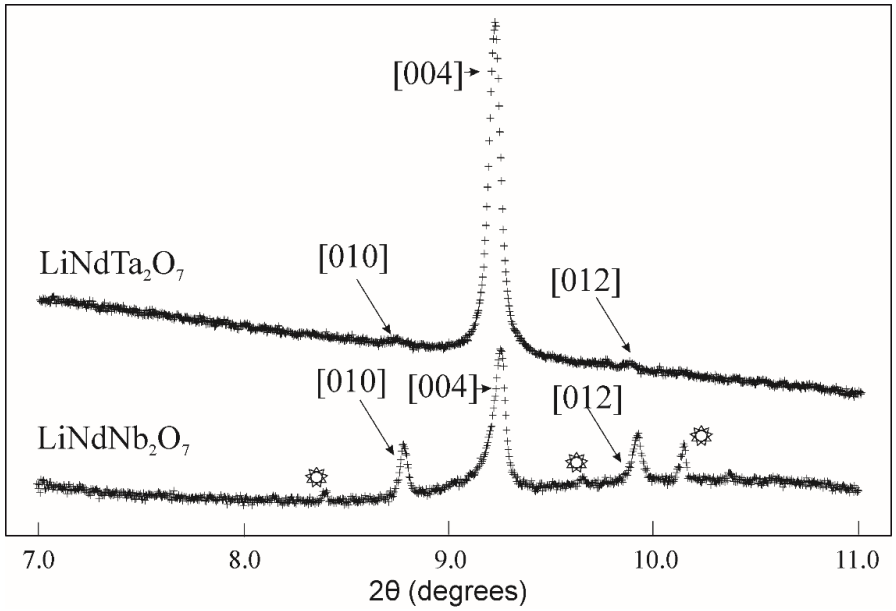


Figure 4.3. Synchrotron X-ray powder diffraction data collected from $LiNdNb_2O_7$ and $LiNdTa_2O_7$ in the range of $7 < 2\theta/° < 11$. Observation of [010] and [012] peaks rule out the *Bb*2$_1$*m* symmetry models. Peaks marked with stars are attributed to $NdNbO_4$ secondary phase.

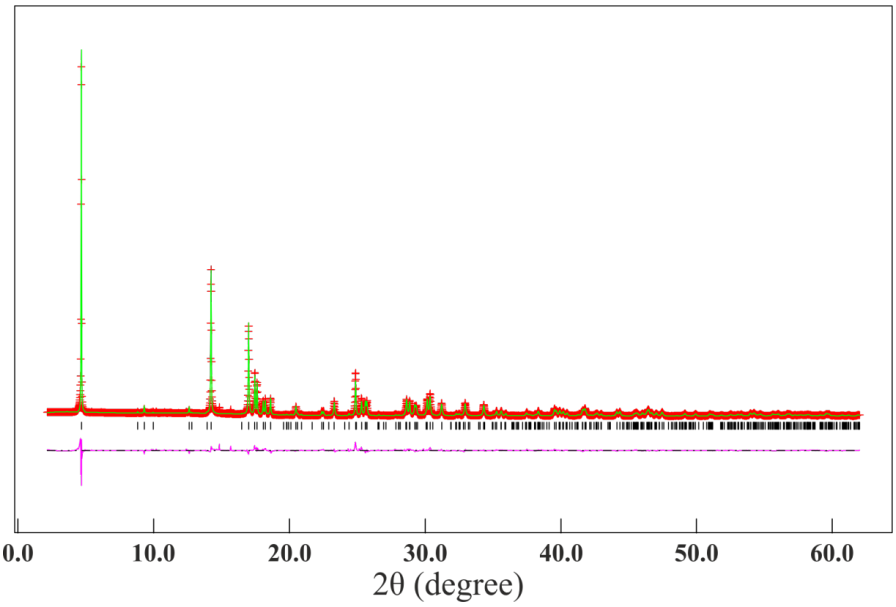


Figure 4.4. Observed, calculated and difference plots from the refinement of the *B*2*em* model against the synchrotron X-ray diffraction data collected from $LiNdNb_2O_7$ at 298 K.

4.3.3.2 Room temperature neutron powder diffraction

Neutron powder diffraction data were collected from a sample of approximately 4 g $LiNdNb_2O_7$ at ambient temperature using the HRPD instrument at ISIS. The diffraction data can be indexed using an expanded unit cell with a $\sqrt{2} \times \sqrt{2} \times 1$ geometric expansion of the undistorted cell. The extinction conditions suggested a *B*-centred or a primitive space

group. Structural models were constructed for $LiNdNb_2O_7$ in space groups *P*2*cm*, *P*2_1*nm* and *B*2*em*. The Li^+ cations within $LiNdNb_2O_7$ sit in the pseudo-tetrahedral sites located between the perovskite double layers. As the number of pseudo-tetrahedral sites is twice the number of the Li^+ cations, they can adopt either an ordered or a disordered arrangement. The *P*2*cm* symmetry model has two 2*a* and two 2*b* crystallographic sites to accommodate Li^+ cations, while in the *P*2_1*nm* symmetry model, the Li^+ cations can reside in two separate 4*b* sites. In the *B*2*em* symmetry model, the Li^+ cations can be arranged in one 4*a* and one 4*b* site. Therefore, Li^+ cations can have ordered or disordered configurations in all three models.

Refinements of these three models against the neutron diffraction data reveal that ordered Li^+ arrangements give the best fits for both *P*2*cm* and *B*2*em* models while a disordered arrangement gives the best fits for the *P*2_1*nm* model. Fitting statistics show that the *P*2*cm* and *B*2*em* models give far superior fits to the *P*2_1*nm* model (Table 4.2). However, the fitting difference between the *P*2*cm* and *B*2*em* models is too small to unambiguously pick a 'correct' structural solution.

space group	tilt system	Glazer tilt	χ^2	wRp (%)	Rp (%)
P2_1*nm*	$\Phi_1\Phi_2\Psi_z/\Phi_2\Phi_1\Psi_z$	$a^-b^-c^+/b^-a^-c^+$	111.3	16.18	13.35
*P*2*cm*	$\Phi_1\Phi_2\Psi_z/-(\Phi_1\Phi_2)\Psi_z$	$a^-b^-c^+/-(a^-b^-)c^+$	10.10	4.88	5.61
*P*2*cm* (constrained)	$\Phi_1\Phi_2\Psi_z/-(\Phi_1\Phi_2)\Psi_z$	$a^-b^-c^+/-(a^-b^-)c^+$	17.79	6.48	6.52
*B*2*em*	$\Phi\Phi\Psi_z/-(\Phi\Phi\Psi_z)$	$a^-a^-c^+/-(a^-a^-c^+)$	13.05	5.55	6.07

Table 4.2. Fitting statistics from the structural refinements of different symmetry models against neutron powder diffraction data collected from $LiNdNb_2O_7$

A close inspection of the *P*2*cm* model reveals that it has lower symmetry with respect to the *B*2*em* model. There are 2 Li, 2 Nd, 2 Nb and 8 O ions in the asymmetric unit in the *P*2*cm* model while there are only half the numbers of the corresponding ions in the asymmetric unit in the *B*2*em* model. The lower symmetry of the *P*2*cm* model means chemically equivalent cations can reside in crystallographically different sites, hence

different local environments. Table 4.3 shows that BVS values for chemically equivalent cations are very uneven in the refined *P*2*cm* structure. Constraints can be added to the *P*2*cm* model to make chemically equivalent cations crystallographically more equivalent. This constrained model was refined against the neutron diffraction data and it can be seen from Table 4.2 that the constrained model gives much worse fits to the diffraction data, indicating the *P*2*cm* space symmetry is incorrect. As a result, we conclude that $LiNdNb_2O_7$ adopts a *B*2*em* symmetry model with an $a^-a^-c^+/-(a^-a^-c^+)$ tilting distortion with the Li^+ cations adopting an ordered arrangement. The observed, calculated and difference plots in space group *B*2*em* are shown in Figure 4.5 and full details of the parameters from the refinements are shown in Table 4.4. Selected bond lengths from the refined structure of $LiNdNb_2O_7$ are shown in Table 4.5. The refined structure is shown in Figure 4.6.

	*P*2*cm*	*P*2*cm* (constrained)	*B*2*em*
Li1	0.88	0.86	0.99
Li2	1.12	1.10	
Nd1	3.61	3.63	3.07
Nd2	2.79	3.02	
Nb1	4.76	5.02	5.09
Nb2	5.42	5.07	

Table 4.3. Bond valence sums (in valence units) calculated from the *P*2*cm*, constrained *P*2*cm* and *B*2*em* symmetry models of $LiNdNb_2O_7$.

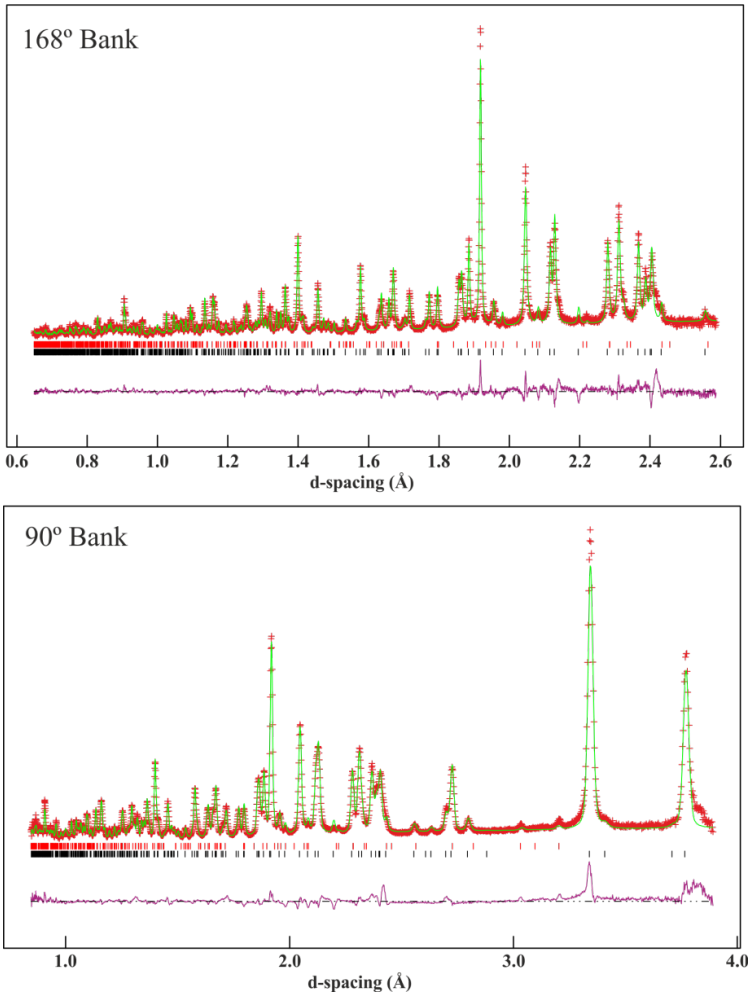


Figure 4.5. Observed, calculated and difference plots from the refinement of the *B*2*em* model against high-resolution neutron diffraction data collected from $LiNdNb_2O_7$ at ambient temperature. $NdNbO_4$ was added as the secondary phase with red tick-marks.

Atom	site	*x*	*y*	*z*	U_{iso} (Å^3)
Li(1)	4*a*	0.5820(20)	0	½	0.0294(22)
Nd(1)	4*c*	0.2957(8)	0.2520(5)	¼	0.0161(6)
Nb(1)	8*d*	0.3136(7)	0.7518(4)	0.1390(1)	0.0162(4)
O(1)	8*d*	0.3101(8)	0.8386(3)	0.0566(1)	0.0172(5)
O(2)	8*d*	0.1225(5)	0.4556(5)	0.1443(1)	0.0216(6)
O(3)	8*d*	0.5598(6)	0.0154(7)	0.1719(1)	0.0227(6)
O(4)	4*c*	0.3195(10)	0.6819(5)	¼	0.0201(8)
$LiNdNb_2O_7$ – space group *B*2*em* (#39) *a* = 5.4498(2) Å, *b* = 5.3974(2) Å, *c* = 20.4556(8) Å, volume = 601.70(7) Å^3 Formula weight: 448.99 g mol^{-1}, Z = 4 Radiation source: Neutron Time of flight Temperature: 298 K χ^2 = 12.78, wRp = 5.49%, Rp = 6.04%					

Table 4.4. Parameters from the structural refinement of $LiNdNb_2O_7$ against neutron powder diffraction data collected at 298 K.

Cation	Anion	length (Å)	BVS
Li(1)	O(1) × 2	1.909(12)	Li +0.99
	O(1) × 2	2.072(13)	
Nd(1)	O(2) × 2	2.602(4)	Nd +3.07
	O(2) × 2	3.215(4)	
	O(3) × 2	2.501(5)	
	O(3) × 2	2.507(5)	
	O(4)	2.324(4)	
	O(4)	2.620(8)	
	O(4)	2.877(8)	
	O(4)	3.080(4)	
Nb(1)	O(1)	1.751(3)	Nb +5.09
	O(2)	1.911(5)	
	O(2)	2.025(5)	
	O(3)	1.986(6)	
	O(3)	2.068(5)	
	O(4)	2.302(2)	

Table 4.5. Selected bond lengths from the refined structure of $LiNdNb_2O_7$.

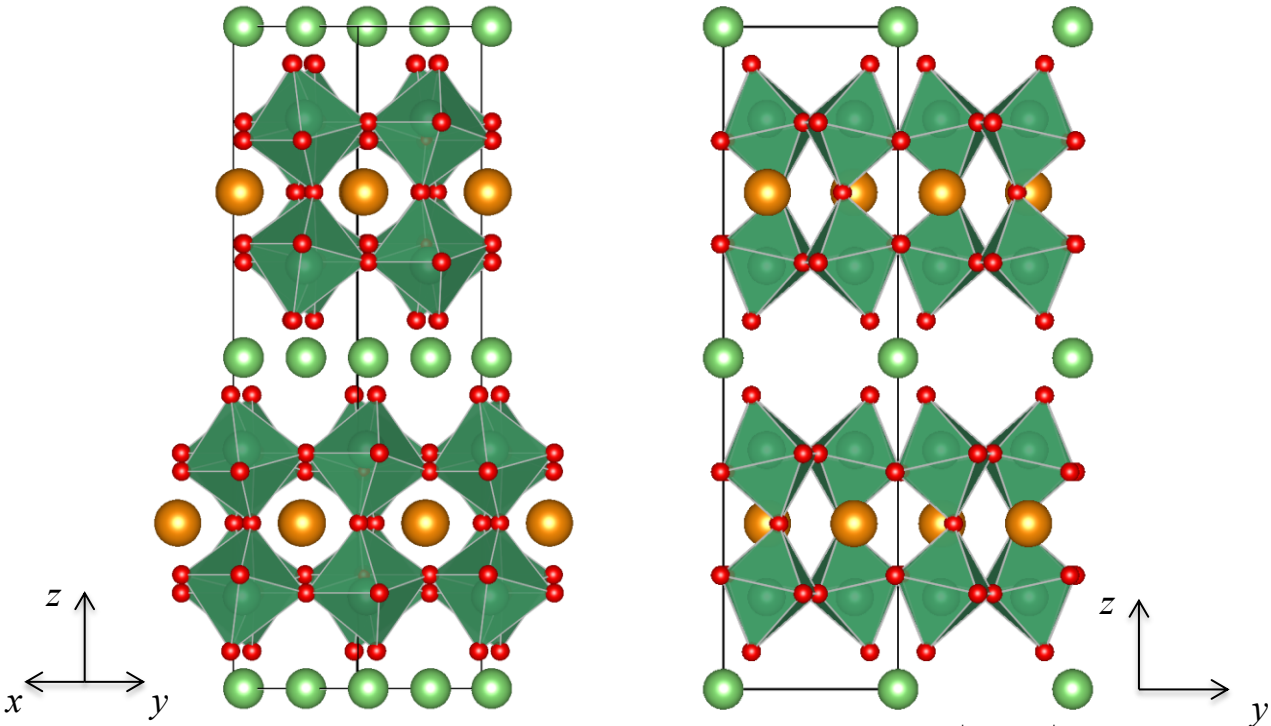


Figure 4.6. The structure of $LiNdNb_2O_7$ in space group *B2em*, with an $a^-a^-c^+$/-($a^-a^-c^+$) tilting distortion. The green and yellow spheres are Li^+ and Nd^{3+} respectively. Nb^{5+} is inside the polyhedra.

4.3.4 Structure characterisation of $LiNdTa_2O_7$

4.3.4.1 Room temperature synchrotron X-ray powder diffraction

Synchrotron X-ray diffraction data collected from $LiNdTa_2O_7$ at ambient temperature can be indexed using an orthorhombic unit cell with an approximate $\sqrt{2} \times \sqrt{2} \times 1$ geometric expansion of the aristotype *I*4/*mmm* unit cell, (a = 5.443 Å, b = 5.409 Å, c = 20.501 Å). The observed SHG activity suggests that it adopts a non-centrosymmetric crystal structure (Figure 4.2). Similar to $LiNdNb_2O_7$, the systematic absence analysis (Figure 4.3) reveals that there are only three structural candidates for $LiNdTa_2O_7$: *P*2*cm* (#28), $P2_1nm$ (#31) and *B*2*em* (#39). Refining these three models against the synchrotron X-ray diffraction data gives equivalently good fits to all three models. As an example, the observed, calculated and difference plots against the synchrotron X-ray data in space group *B*2*em* are shown in Figure 4.7.

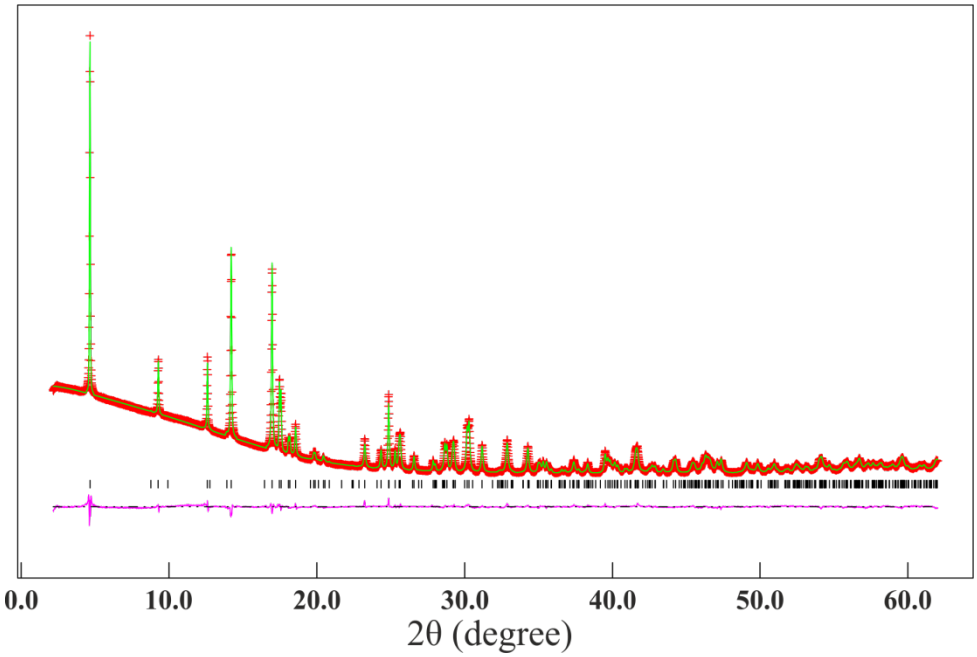


Figure 4.7. Observed, calculated and difference plots from the refinement of the *B*2*em* model against the synchrotron X-ray diffraction data collected from $LiNdTa_2O_7$ at 298 K.

4.3.4.2 Room temperature neutron powder diffraction

Neutron powder diffraction data were collected from a sample of approximately 4 g $LiNdTa_2O_7$ at ambient temperature using the HRPD instrument at ISIS. The diffraction data can be indexed using an expanded unit cell with a $\sqrt{2} \times \sqrt{2} \times 1$ geometric expansion of the undistorted cell. The extinction conditions suggested a *B*-centred or a primitive space group. As a direct analogue to $LiNdNb_2O_7$, Li^+ cations can have a variety of ordered or disordered arrangements in the symmetry models of $P2_1nm$, $P2cm$ and $B2em$. Refinements of these three models against the neutron diffraction data reveal that the $P2cm$ and $B2em$ models give much better fits to the $P2_1nm$ model (Table 4.6). However, the fitting difference between the $P2cm$ and $B2em$ models are generally too small to be significant.

space group	tilt system	Glazer tilt	χ^2	wRp (%)	Rp (%)
$P2_1nm$	$\Phi_1\Phi_2\Psi_z/\Phi_2\Phi_1\Psi_z$	$a^-b^-c^+/b^-a^-c^+$	83.51	14.41	13.66
$P2cm$	$\Phi_1\Phi_2\Psi_z/-(\Phi_1\Phi_2)\Psi_z$	$a^-b^-c^+/-(a^-b^-)c^+$	4.57	3.37	4.02
$P2cm$ (constrained)	$\Phi_1\Phi_2\Psi_z/-(\Phi_1\Phi_2)\Psi_z$	$a^-b^-c^+/-(a^-b^-)c^+$	8.52	4.61	4.73
$B2em$	$\Phi\Phi\Psi_z/-(\Phi\Phi\Psi_z)$	$a^-a^-c^+/-(a^-a^-c^+)$	5.76	3.79	4.38

Table 4.6. Fitting statistics from the structural refinements of different symmetry models against neutron powder diffraction data collected from $LiNdTa_2O_7$.

Following a similar principle to $LiNdNb_2O_7$, a constrained $P2cm$ symmetry model of $LiNdTa_2O_7$ was constructed and refined against the neutron diffraction data. It can be observed from Table 4.6 that the constrained $P2cm$ model gives much worse fits to the diffraction data, indicating the $P2cm$ structure symmetry is incorrect. As a result, we conclude that $LiNdTa_2O_7$ is isostructural to $LiNdNb_2O_7$ and adopts a $B2em$ structure symmetry with an $a^-a^-c^+/-(a^-a^-c^+)$ tilting distortion, in which the Li^+ cations adopt an ordered configuration between perovskite double layers. The observed, calculated and difference plots in space group $B2em$ are shown in Figure 4.8 and full details of the parameters from the refinements are shown in Table 4.8. Selected bond lengths from the refined structure of $LiNdTa_2O_7$ are shown in Table 4.9. The refined structure is a direct analogue to $LiNdNb_2O_7$ in Figure 4.6.

	*P*2*cm*	*P*2*cm* (constrained)	*B*2*em*
Li1	1.33	1.10	0.98
Li2	0.84	0.85	
Nd1	3.57	3.55	3.03
Nd2	2.81	3.00	
Ta1	5.05	5.12	5.18
Ta2	5.25	5.17	

Table 4.7. Bond valence sums (in valence units) calculated from the *P*2*cm*, constrained *P*2*cm* and *B*2*em* symmetry models of $LiNdTa_2O_7$.

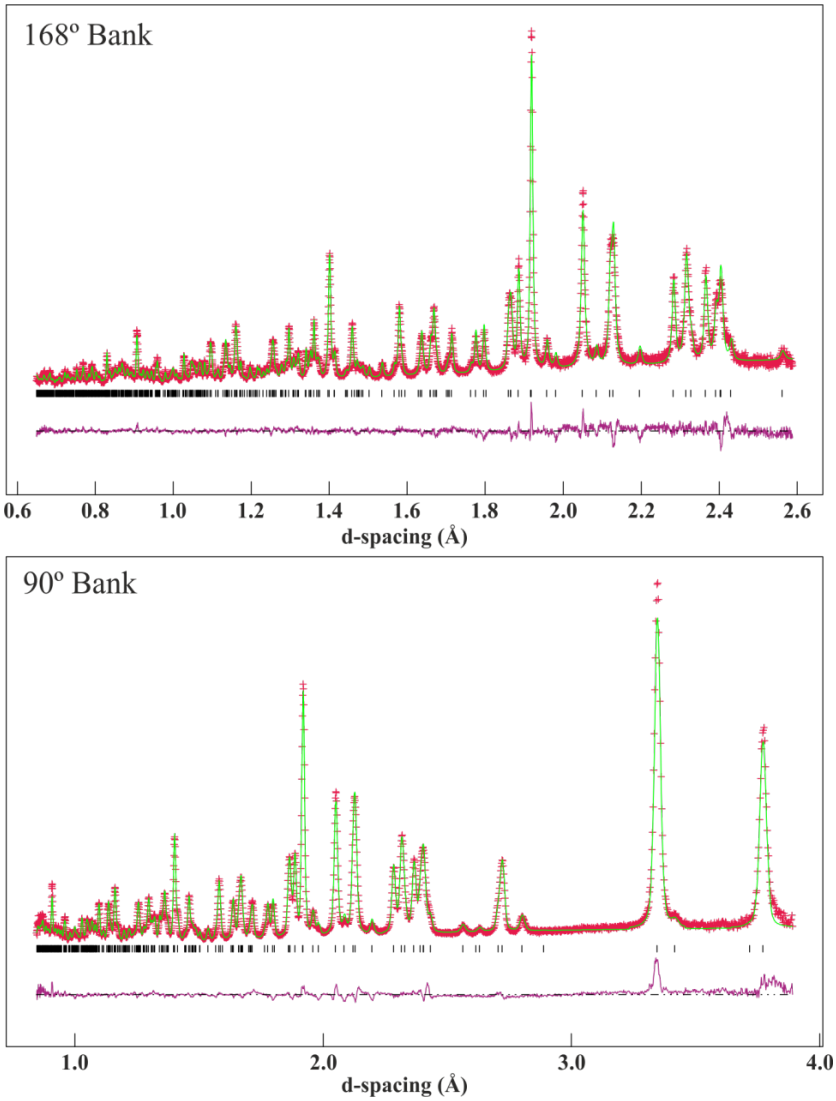


Figure 4.8. Observed, calculated and difference plots from the refinement of the *B*2*em* model against high-resolution neutron diffraction data collected from $LiNdTa_2O_7$ at ambient temperature.

Atom	site	*x*	*y*	*z*	U_{iso} (Å^3)
Li(1)	4*a*	0.5782(16)	0	0	0.0235(15)
Nd(1)	4*c*	0.2994(7)	0.2547(4)	¼	0.0132(4)
Ta(1)	8*d*	0.3178(6)	0.7540(3)	0.1397(1)	0.0108(3)
O(1)	8*d*	0.3115(7)	0.8374(2)	0.0564(1)	0.0158(4)
O(2)	8*d*	0.1170(4)	0.4611(4)	0.1457(1)	0.0195(5)
O(3)	8*d*	0.5563(5)	0.0182(5)	0.1721(1)	0.0155(4)
O(4)	4*c*	0.3232(8)	0.6833(3)	¼	0.0174(6)
$LiNdTa_2O_7$ – space group *B*2*em* (#39) *a* = 5.4427(2) Å, *b* = 5.4092(2) Å, *c* = 20.5011(7) Å, volume = 603.57(6) Å^3 Formula weight: 625.07 g mol^{-1}, Z = 4 Radiation source: Neutron Time of flight Temperature: 298 K χ^2 = 5.76, wRp = 3.79%, Rp = 4.38%					

Table 4.8. Parameters from the structural refinement of $LiNdTa_2O_7$ against neutron powder diffraction data collected at 298 K.

Cation	Anion	length (Å)	BVS
Li(1)	O(1) × 2	1.930(7)	Li +0.98
	O(1) × 2	2.054(8)	
Nd(1)	O(2) × 2	2.609(3)	Nd +3.03
	O(2) × 2	3.150(4)	
	O(3) × 2	2.479(4)	
	O(3) × 2	2.546(4)	
	O(4)	2.322(4)	
	O(4)	2.613(7)	
	O(4)	2.871(7)	
	O(4)	3.094(4)	
Ta(1)	O(1)	1.767(3)	Ta +5.18
	O(2)	1.929(4)	
	O(2)	2.005(4)	
	O(3)	1.996(4)	
	O(3)	2.042(4)	
	O(4)	2.294(2)	

Table 4.9. Selected bond lengths from the refined structure of $LiNdTa_2O_7$.

4.3.5 Structure characterisation of $NaNdNb_2O_7$

4.3.5.1 Room temperature synchrotron X-ray powder diffraction

Synchrotron X-ray diffraction data collected from $NaNdNb_2O_7$ at ambient temperature can be indexed using a tetragonal unit cell with an approximately $\sqrt{2} \times \sqrt{2} \times 1$ geometric

expansion of the undistorted cell ($a \sim b = 5.483$ Å, $c = 20.911$ Å). This contrasts previous reports in which $NaNdNb_2O_7$ was characterised to adopt an undistorted, *I*4/*mmm* structure[37, 67]. Lacking SHG activity suggests that it adopts a centrosymmetric structure. Therefore all space groups describing non-centrosymmetric structures in Table 4.1 can be eliminated. As $NaNdNb_2O_7$ can be metrically tetragonal but described in an orthorhombic symmetry model, twelve centrosymmetric space groups with orthorhombic or tetragonal structures (except *I*4/*mmm*) in Table 4.1 were initially considered as possible candidates: $P4_2/mcm$ #132, $P4_2/mnm$ #136, *Pccm* #49, *Pbcb* #54, *Pbcm* #57, *Pnnm* #58, *Pnab* #60, *Pnam* #62, *Bbmm* #63, *Bbcm* #64, *Bmcm* #67 and *Bbcb* #68. The space group settings are described with their stacking axes being parallel to *z*.

Further examination of the synchrotron X-ray diffraction data reveals that most structural candidates can be eliminated based on the systematic absence analysis. Figure 4.9 shows the synchrotron X-ray diffraction data at low angles. The observations of the [011], [110] and [111] reflections indicate that all centred space groups, as well as $P4_2/mcm$, *Pccm* and *Pbcm*, can be eliminated, leaving only three structural models for $NaNdNb_2O_7$ ($P4_2/mnm$, *Pnnm* and *Pnam*). These three structural models were constructed for $NaNdNb_2O_7$. As a direct analogue to $LiNdM_2O_7$, the Na^+ cations sit in the pseudo-tetrahedral sites located between perovskite double layers. The *Pnam* symmetry model has a single 8*d* crystallographic site to accommodate the Na^+ cations therefore it must be half-occupied to follow the stoichiometry. As a result, the Na^+ cations have a disordered arrangement in the *Pnam* structure. In contrast, the $P4_2/mnm$ symmetry model has one 4*d* and one 4*e* site. In the *Pnnm* model, the Na^+ cations can be arranged in one 4*e* and one 4*f* site. Therefore in these two symmetry models, the Na^+ cations can have either an ordered or a disordered arrangement. Refining these three models against the synchrotron X-ray diffraction data

gives equally good fits for all models. As an example, the observed, calculated and difference plots in space group $P4_2/mnm$ are shown in Figure 4.10.

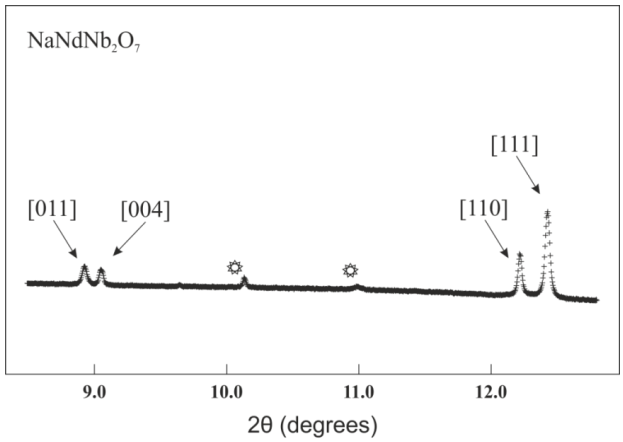


Figure 4.9. Synchrotron X-ray diffraction data collected from $NaNdNb_2O_7$. The observation of [011], [110] and [111] peaks rules out all centred models as well as $P4_2/mcm$, $Pccm$ and $Pbcm$. Peaks marked with stars are attributed to $NdNbO_4$ secondary phase.

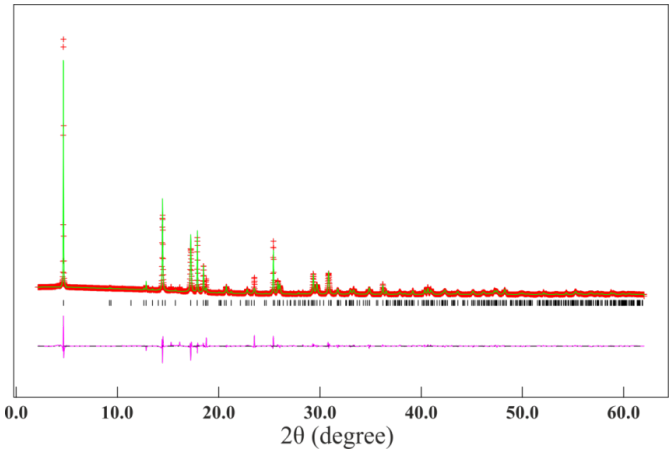


Figure 4.10. Observed, calculated and difference plots from the refinement of the $P4_2/mnm$ model against the synchrotron X-ray diffraction data collected from $NaNdNb_2O_7$ at 298 K.

4.3.5.2 Room temperature neutron powder diffraction

Neutron powder diffraction data were collected from a sample of approximately 4 g $NaNdNb_2O_7$ at ambient temperature using the HRPD instrument at ISIS. The diffraction data can be indexed using an expanded unit cell with a $\sqrt{2} \times \sqrt{2} \times 1$ geometric expansion of the undistorted cell. Models of $P4_2/mnm$, $Pnnm$ and $Pnam$ space groups were refined against the neutron diffraction data. Refinements proceeded smoothly and Na^+ cations were initially set to be disordered with half occupancy in all pseudo-tetrahedral sites. The sodium occupancy was refined as the last step. Fitting statistics show that all three models achieved

good fits (Table 4.10) and the fitting differences are too small to be significant. The refinements suggest that the Na^+ cations adopt ordered arrangements in both *Pnnm* and $P4_2/mnm$ structures but a disordered arrangement in the *Pnam* structure.

space group	tilt system	Glazer tilt	χ^2	wRp (%)	Rp (%)
Pnnm	$\Phi_1\Phi_2 0/\Phi_2\Phi_1 0$	$a^-b^-c^0/b^-a^-c^0$	8.40	4.67	4.68
Pnam	$\Phi\Phi\Psi_z/\Phi\Phi\text{-}\Psi_z$	$a^-a^-c^+/a^-a^-\text{-}c^+$	9.97	5.08	5.20
$P4_2/mnm$	$\Phi 00/0\Phi 0$	$a^-b^0c^0/b^0a^-c^0$	8.86	4.79	4.82

Table 4.10. Fitting statistics from the structural refinements of different models against neutron powder diffraction data collected from $NaNdNb_2O_7$.

Close inspection of the refinements reveals that the *Pnam* model cannot account for some peaks at high *d*-spacing regions. Figure 4.11 shows that [114] and [112] reflections, at 3.12 Å and 3.63 Å respectively, are properly fitted with the *Pnnm* and $P4_2/mnm$ models but not the *Pnam* model. This indicates the *Pnam* model is incorrect.

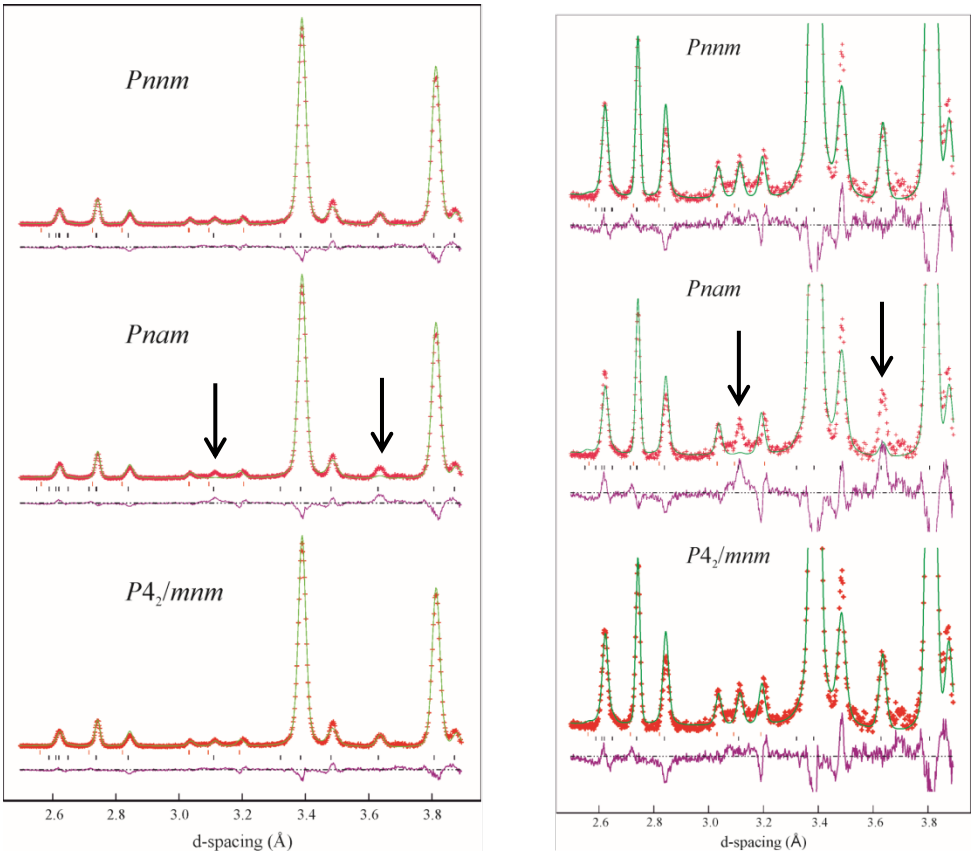


Figure 4.11. Observed, calculated and difference plots from the refinement of the *Pnnm*, *Pnam* and $P4_2/mnm$ models against neutron powder diffraction data collected from $NaNdNb_2O_7$ at 298 K. $NdNbO_4$ was added as the secondary phase with the red tick-marks. Peaks labelled with arrows show that the *Pnam* space group is incorrect.

The remaining two models, $P4_2/mnm$ ($a^-b^0c^0/b^0a^-c^0$) and *Pnnm* ($a^-b^-c^0/b^-a^-c^0$), are very similar in terms of octahedral tilting distortions. The $P4_2/mnm$ model can be considered as a special case of *Pnnm* in which the magnitude of the '*b*' tilt is zero. The refined *Pnnm* structure is shown in Figure 4.12 and it can be visualized that the magnitude of the '*a*' tilt is significantly greater than '*b*' which is close to zero. There are different approaches to quantify octahedral tilting distortions and in this case O-O-O bond angles are used to evaluate how tilted the perovskite framework is along a particular direction (Figure 4.13). If the MO_6 octahedra are not tilted, the Ou-Ov-Ow bond angle would be 180 °. The larger the bond angle is deviated from 180 °, the more tilted the perovskite framework is along a particular direction. Corresponding bond angles were measured to quantify *a* and *b* tilting distortions in the refined *Pnnm* structure of $NaNdNb_2O_7$ (Table 4.11).

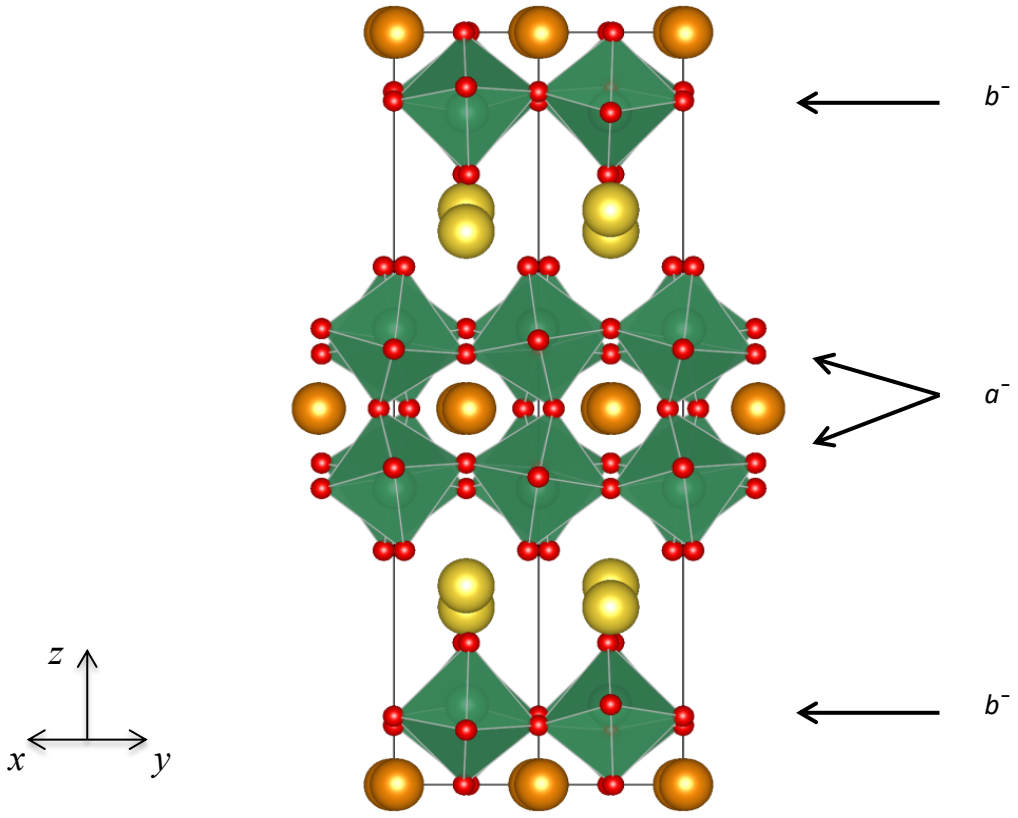


Figure 4.12. The refined structure of $NaNdNb_2O_7$ in space group $P4_2/mnm$, with an $a^-b^-c^0$/ $b^-a^-c^0$ distortion. The yellow and orange spheres are Na^+ and Nd^{3+} cations respectively. Nb^{5+} cations are inside the polyhedra.

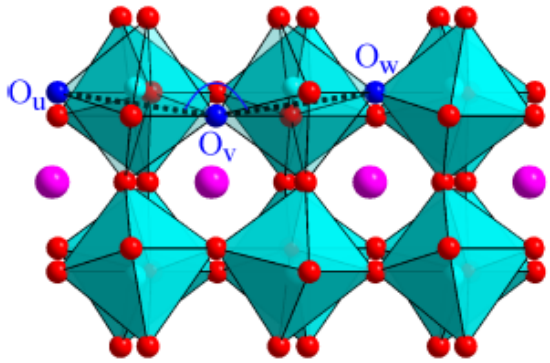


Figure 4.13. Measurement of distortion angles along a particular direction.

$NaNdNb_2O_7$		
	bond angle (°)	corresponding distortion
O1-O2-O1	173.4 (3)	*b*
O3-O4-O3	159.2 (2)	*a*

Table 4.11. Selected bond angles from the refined *Pnnm* structure of $NaNdNb_2O_7$

Table 4.11 shows that the O-O-O angle corresponding to '*a*' tilting distortion is much greater than the angle of '*b*' and the '*b*' angle is close to 180 °. Since the fitting statistics to the neutron diffraction data are also very similar, it is impossible to differentiate $P4_2/mnm$ and *Pnnm* models based on diffraction data only. DFT calculations show that $P4_2/mnm$ and *Pnnm* structures are equivalently stable within the calculation precision, which indicates the relaxed structures for both models are likely to be the same. Close inspection of the energy minimised *Pnnm* structure shows that it has exactly zero '*b*' tilting distortion, which is consistent with the $P4_2/mnm$ structure. Therefore we conclude that $NaNdNb_2O_7$ adopts the $P4_2/mnm$ structure with an $a^-b^0c^0/b^0a^-c^0$ tilting distortion. The Na^+ cations adopt an ordered arrangement between perovskite layers and the cation order will be discussed in detail later in this chapter. The observed, calculated and difference plots in space group $P4_2/mnm$ are shown in Figure 4.14 and full details of the parameters from the refinements are shown in Table 4.12. Selected bond lengths from the refined structure of $NaNdNb_2O_7$ are shown in Table 4.13. The refined structure is shown in Figure 4.15.

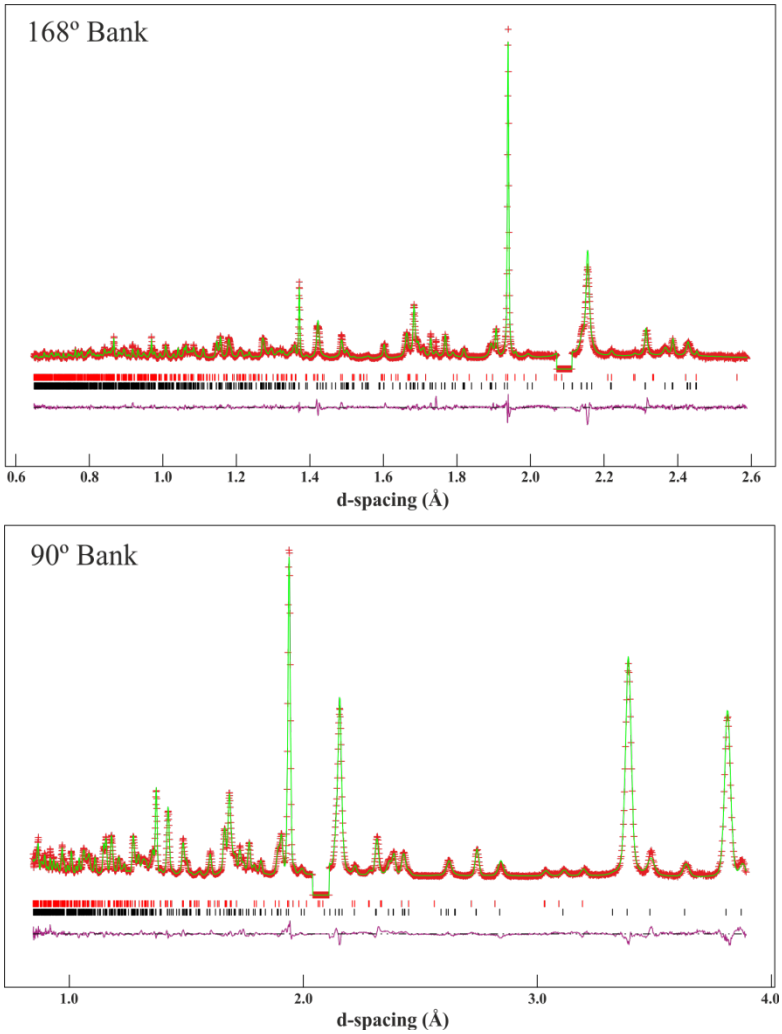


Figure 4.14. Observed, calculated and difference plots from the refinement of the *P*4$_2$/*mnm* model against high-resolution neutron diffraction data collected from $NaNdNb_2O_7$ at ambient temperature. $NdNbO_4$ was added as the secondary phase with red tick-marks. The excluded region removes the contribution from the vanadium sample holder.

Atom	site	*x*	*y*	*z*	U_{iso} (Å^3)
Na(1)	4*e*	0	0	0.2649(3)	0.0346(17)
Nd(1)	4*f*	0.2587(3)	0.2587(3)	0	0.0049(4)
Nb(1)	8*j*	0.2531(3)	0.2531(3)	0.3943(0)	0.0030(3)
O(1)	4*g*	0.8034(4)	0.8034(4)	½	0.0182(10)
O(2)	4*e*	½	½	0.5725(1)	0.0029(8)
O(3)	4*e*	0	0	0.6071(2)	0.0252(12)
O(4)	8*h*	½	0	0.4153(1)	0.0218(7)
O(5)	8*j*	0.7138(2)	0.7138(2)	0.6885(1)	0.0122(5)
$NaNdNb_2O_7$ – space group *P*4$_2$/*mnm* (#136) *a* = 5.4829(2) Å, *b* = 5.4829(2) Å, *c* = 20.9112(8) Å, volume = 628.63(6) Å^3 Formula weight: 465.04 g mol^{-1}, Z = 4 Radiation source: Neutron Time of flight Temperature: 298 K χ^2 = 8.56, wRp = 4.79%, Rp = 4.82%					

Table 4.12. Parameters from the structural refinement of $NaNdNb_2O_7$ against neutron powder diffraction data collected at 298 K.

Cation	Anion	length (Å)	BVS
Na(1)	O(5) × 2	2.303(5)	+0.88
	O(5) × 2	2.424(4)	
Nd(1)	O(1) × 2	2.413(4)	+2.96
	O(1) × 2	3.092(4)	
	O(2) × 2	2.514(3)	
	O(3) × 2	2.918(4)	
	O(4) × 4	2.627(3)	
Nb(1)	O(1)	2.253(1)	+5.15
	O(2)	2.036(2)	
	O(3)	1.963(2)	
	O(4) × 2	1.988(2)	
	O(5)	1.750(2)	

Table 4.13. Selected bond lengths from the refined structure of $NaNdNb_2O_7$.

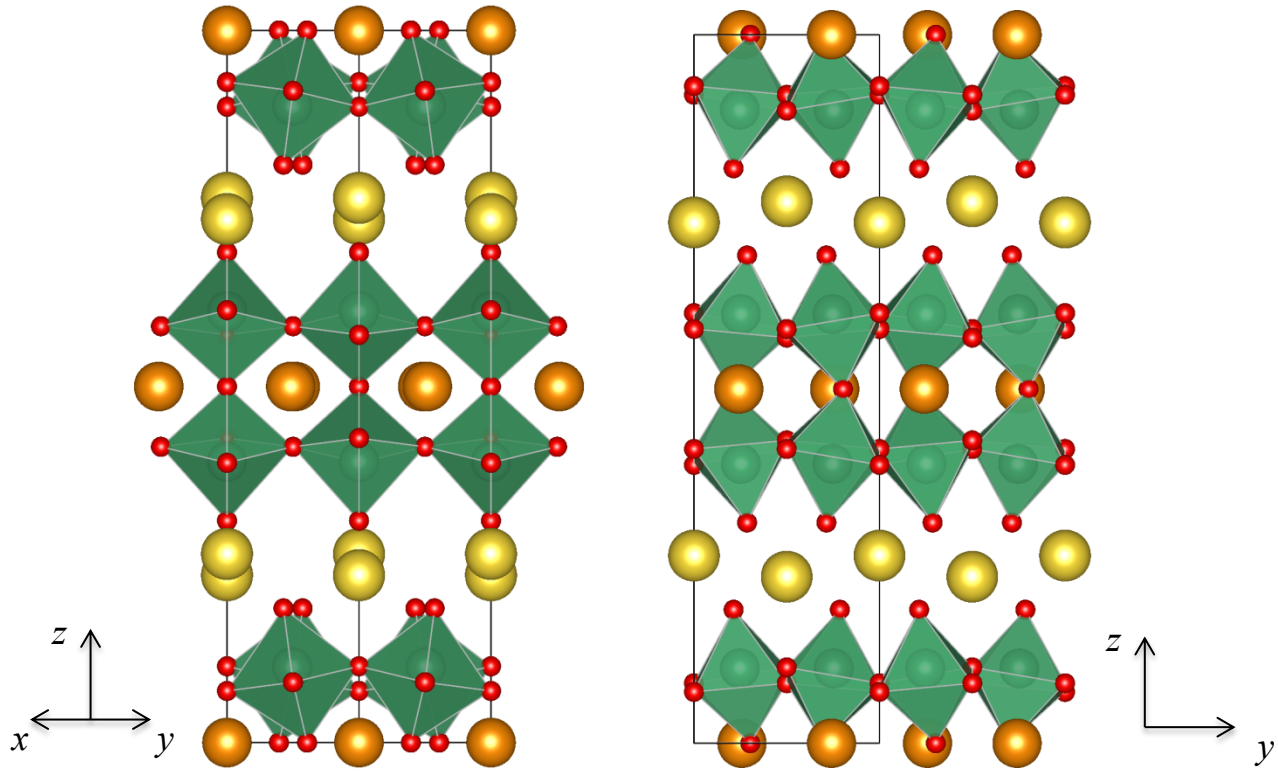


Figure 4.15. The structure of $NaNdNb_2O_7$ in space group $P4_2/mnm$, with an $a^-b^0c^0$/ $b^0a^-c^0$ distortion. The yellow and orange spheres are Na^+ and Nd^{3+} cations respectively. Nb^{5+} cations are inside the polyhedra.

4.3.6 Structure characterisation of $NaNdTa_2O_7$

4.3.6.1 Room temperature synchrotron X-ray diffraction

Synchrotron X-ray diffraction data collected from $NaNdTa_2O_7$ at ambient temperature can be indexed using a tetragonal unit cell with a $\sqrt{2} \times \sqrt{2} \times 1$ geometric expansion of the undistorted cell ($a \sim b = 5.469$ Å, $c = 21.135$ Å). Lacking SHG activity indicates it adopts a centrosymmetric structure. Similar to $NaNdNb_2O_7$, the systematic analysis (Figure 4.16) reveals that there are six structural candidates for $NaNdTa_2O_7$: *Pccm* #49, *Pbcm* #57, *Pnnm* #58, *Pnam* #62, $P4_2/mcm$ #132 and $P4_2/mnm$ #136. Structural models of *Pnnm*, *Pnam* and $P4_2/mnm$ were constructed as direct analogues to $NaNdNb_2O_7$. The *Pccm* symmetry model has one 2*e*, one 2*f*, one 2*g* and one 2*h* tetrahedral sites to accommodate the Na^+ cations. In the *Pbcm* symmetry model, there are two separate 4*e* sodium sites. In the $P4_2/mcm$ structure, there is one 4*e*, one 2*b* and one 2*d* tetrahedral site. Therefore in these three structural models, the Na^+ cations can adopt an ordered or a disordered arrangement. Refining these models against the synchrotron X-ray diffraction data gives equivalently good fits to all the models. As an example, the observed, calculated and difference plots in space group $P4_2/mnm$ are shown in Figure 4.17.

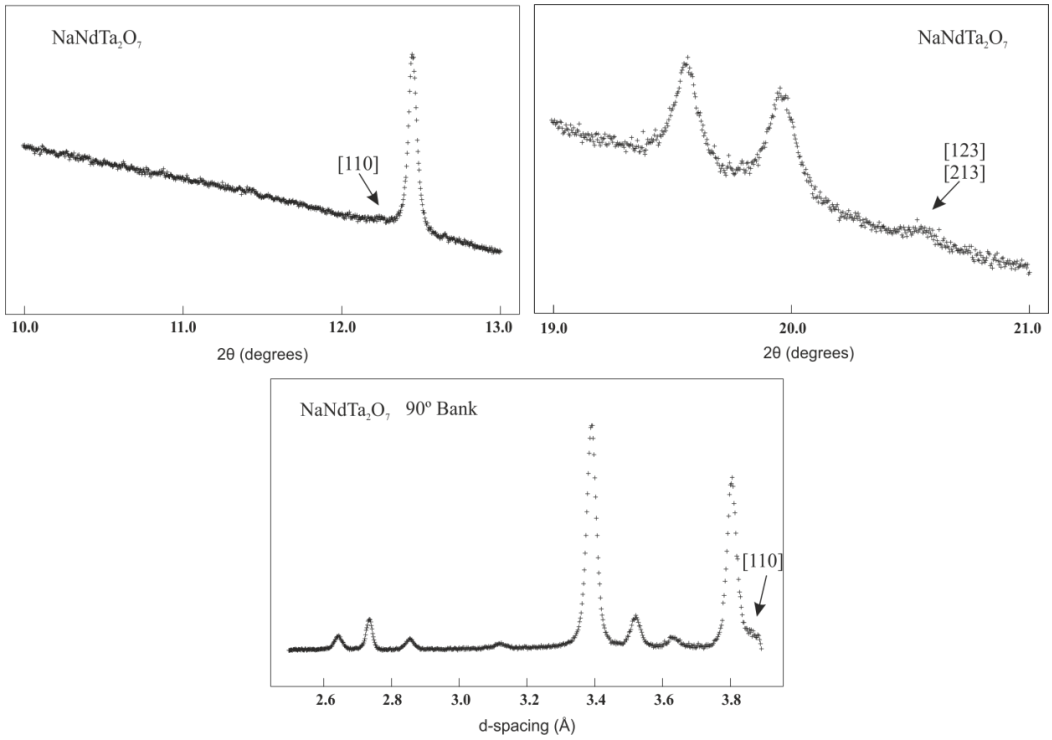


Figure 4.16. Synchrotron X-ray (top 2 panels plotted against 2θ) and neutron powder diffraction data (bottom panel plotted against d-spacing) collected from $NaNdTa_2O_7$ at ambient temperature. The [110] reflection is very weak in the synchrotron X-ray diffraction data so the neutron diffraction data is shown as a supplementary. The observations of [110], [123] and [213] peaks eliminate all *B*-centred models as well as *Pbcb* and *Pnab*.

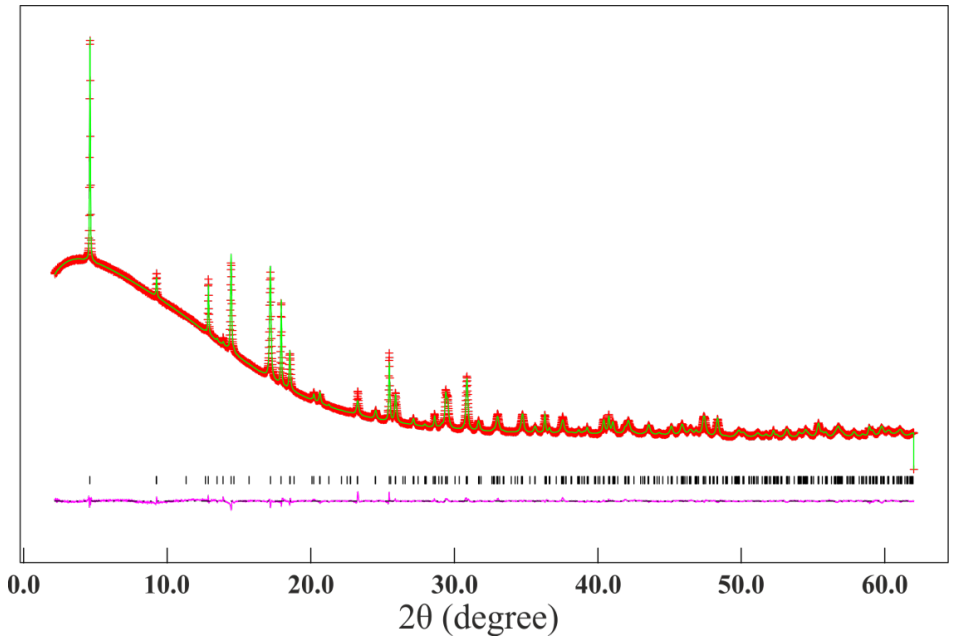


Figure 4.17. Observed, calculated and difference plots from the refinement of the $P4_2/mnm$ model against the synchrotron X-ray diffraction data collected from $NaNdTa_2O_7$ at 298 K.

4.3.6.2 Room temperature neutron powder diffraction

Neutron powder diffraction data were collected from a sample of approximately 4 g $NaNdTa_2O_7$ at ambient temperature using the HRPD instrument at ISIS. The diffraction data of $NaNdTa_2O_7$ can be indexed using a unit cell with a $\sqrt{2} \times \sqrt{2} \times 1$ geometric expansion of the undistorted cell. Models of *Pccm*, *Pbcm*, *Pnnm*, *Pnam*, $P4_2/mcm$ and $P4_2/mnm$ were refined against the neutron diffraction data. Refinements proceeded smoothly and the Na^+ cations were initially set to be disordered in all pseudo-tetrahedral sites with half occupancy. Fitting statistics suggest that models of *Pnnm*, *Pnam* and $P4_2/mnm$ achieve the best fits (Table 4.14). Refinements suggest that the Na^+ cations adopt ordered arrangements in both *Pnnm* and $P4_2/mnm$ structures while a disordered arrangement in the *Pnam* structure. However, the difference in fitting statistics is too small to unambiguously suggest the correct crystal structure.

space group	tilt system	Glazer tilt	χ^2	wRp (%)	Rp (%)
Pccm	$\Phi_1\Phi_2 0/-(\Phi_2\Phi_1)0$	$a^-b^-c^0/-(b^-a^-)c^0$	19.70	6.95	5.31
Pbcm	$\Phi\Phi\Psi_z/-(\Phi\Phi)\Psi_z$	$a^-a^-c^+/-(a^-a^-)c^+$	16.85	6.42	5.09
Pnnm	$\Phi_1\Phi_2 0/\Phi_2\Phi_1 0$	$a^-b^-c^0/b^-a^-c^0$	6.30	3.93	3.82
Pnam	$\Phi\Phi\Psi_z/\Phi\Phi\text{-}\Psi_z$	$a^-a^-c^+/a^-a^-\text{-}c^+$	5.99	3.83	3.94
$P4_2/mcm$	$\Phi 00/0\text{-}\Phi 0$	$a^-b^0c^0/b^0\text{-}a^-c^0$	21.78	7.31	5.57
$P4_2/mnm$	$\Phi 00/0\Phi 0$	$a^-b^0c^0/b^0a^-c^0$	6.96	4.13	3.98

Table 4.14. Fitting statistics from the structural refinements of different models against neutron powder diffraction data collected from $NaNdTa_2O_7$. It can clearly be seen from the fitting statistics that *Pnnm*, *Pnam* and $P4_2/mnm$ models give much superior fits than *Pccm*, *Pbcm* and $P4_2/mcm$.

A close examination of the refinements shows that there are diffraction peaks which cannot be accounted for by the *Pnam* model at high *d*-spacing regions (Figure 4.18). In addition, this model gives weak peaks which are not observed from the neutron diffraction data. This indicates the *Pnam* model is incorrect. In order to figure out whether the *Pnnm* or $P4_2/mnm$ model gives a better description of $NaNdTa_2O_7$, tilting angles were measured in the refined *Pnnm* structure to show how different '*a*' and '*b*' tilting distortions are. As demonstrated in Table 4.15, the magnitude of '*a*' tilt is significantly greater than '*b*' and the tilting angle

corresponding to the '*b*' distortion is close to 180°. As the fitting statistics of the *Pnnm* and $P4_2/mnm$ models are also very similar (Table 4.14), it is difficult to propose the final structural solution based on the diffraction data only. Again, DFT calculations show that the energy minimized *Pnnm* structure has zero '*b*' tilting distortion, which is consistent with the $P4_2/mnm$ structure ($a^-b^0c^0/b^0a^-c^0$). By combining diffraction experiments and DFT calculations, we conclude that $NaNdTa_2O_7$ is isostructural to $NaNdNb_2O_7$, in space group $P4_2/mnm$ with an $a^-b^0c^0/b^0a^-c^0$ tilting distortion. The observed, calculated and difference plots in space group $P4_2/mnm$ are shown in Figure 4.19. Full details of the parameters from the refinements are shown in Table 4.16. Selected bond lengths from the refined structure of $NaNdTa_2O_7$ are shown in Table 4.17. The refined structure is a direct analogue to $NaNdNb_2O_7$ in Figure 4.15.

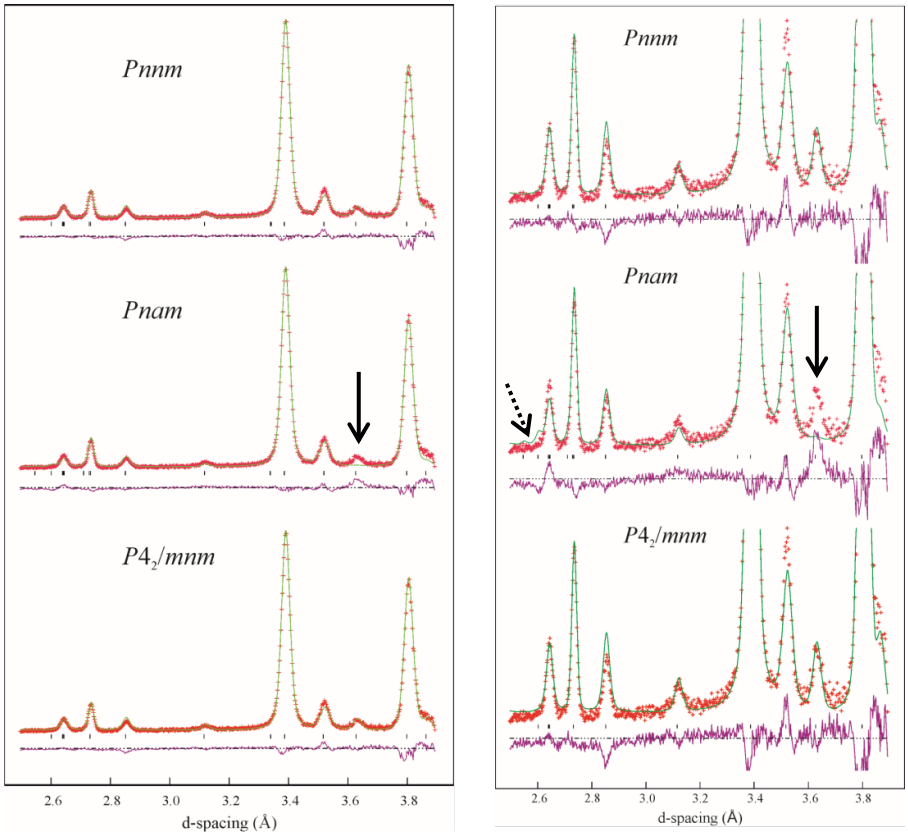


Figure 4.18. Observed, calculated and difference plots from the refinements of the *Pnnm*, *Pnam* and $P4_2/mnm$ models against neutron powder diffraction data collected from $NaNdTa_2O_7$ at 298 K. Diffraction peaks labelled with solid arrows cannot be correctly simulated by the *Pnam* model. Simulated peaks with dash arrows are not observed from the diffraction data.

$NaNdTa_2O_7$		
	bond angle (°)	corresponding distortion
O1-O2-O1	174.4(5)	*b*
O3-O4-O3	163.0(3)	*a*

Table 4.15. Selected bond angles from the refined *Pnnm* structure of $NaNdTa_2O_7$

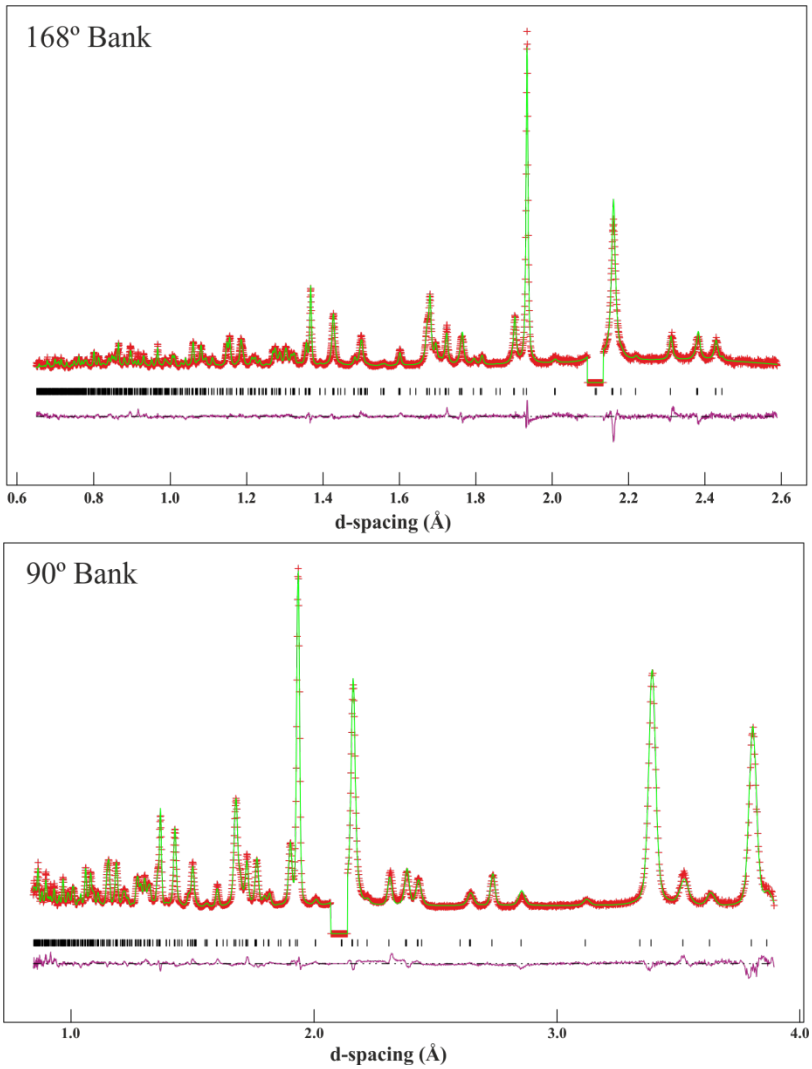


Figure 4.19. Observed, calculated and difference plots from the refinement of the *P*4$_2$/*mnm* model against high-resolution neutron diffraction data collected from $NaNdTa_2O_7$ at ambient temperature. The excluded region removes a contribution from the vanadium sample holder.

Atom	site	*x*	*y*	*z*	U_{iso} (Å^3)
Na(1)	4*e*	0	0	0.2608(4)	0.0427(17)
Nd(1)	4*f*	0.2569(3)	0.2569(3)	0	0.0043(4)
Ta(1)	8*j*	0.2543(3)	0.2543(3)	0.3957(1)	0.0050(3)
O(1)	4*g*	0.8009(4)	0.8009(4)	½	0.0130(9)
O(2)	4*e*	½	½	0.5742(2)	0.0101(9)
O(3)	4*e*	0	0	0.6020(2)	0.0352(15)
O(4)	8*h*	½	0	0.4160(1)	0.0216(7)
O(5)	8*j*	0.7181(3)	0.7181(3)	0.6883(1)	0.0099(5)
$NaNdTa_2O_7$ – space group $P4_2/mnm$ (#136) a = 5.4686(2) Å, b = 5.4686(2) Å, c = 21.1345(9) Å, volume = 632.03(7) Å^3 Formula weight: 641.12 g mol^{-1}, Z = 4 Radiation source: Neutron Time of flight Temperature: 298 K χ^2 = 6.96, wRp = 4.13%, Rp = 3.98%					

Table 4.16. Parameters from the structural refinement of $NaNdTa_2O_7$ against neutron powder diffraction data collected at 298 K.

Cation	Anion	length (Å)	BVS
Na(1)	O(5) × 2	2.279(6)	+0.91
	O(5) × 2	2.431(5)	
Nd(1)	O(1) × 2	2.430(3)	+2.95
	O(1) × 2	3.060(3)	
	O(2) × 2	2.531(3)	
	O(3) × 2	2.860(5)	
	O(4) × 4	2.625(3)	
Ta(1)	O(1)	2.245(1)	+5.21
	O(2)	2.004(3)	
	O(3)	1.967(2)	
	O(4) × 2	1.981(2)	
	O(5)	1.788(2)	

Table 4.17. Selected bond lengths from the refined structure of $NaNdTa_2O_7$.

4.4 Discussion

4.4.1 Structure differences between $LiNdM_2O_7$ and $NaNdM_2O_7$

The crystal structures of $LiNdM_2O_7$ and $NaNdM_2O_7$ are different in two main aspects: MO_6 octahedral tilting distortions and interlayer cation order. The perovskite double sheets adopt an $a^-a^-c^+$ local tilting distortion in $LiNdM_2O_7$ but an $a^-b^0c^0$ distortion in $NaNdM_2O_7$. The distorted structures in both $LiNdM_2O_7$ and $NaNdM_2O_7$ can be attributed to the size

mismatch between A-site and B-site metal cations. As demonstrated in Chapter 3, the Goldschmidt tolerance factor *t* is equal to 0.925 for the NdM_2O_7 perovskite double layer, which explains the local distortions in both the lithium and sodium phases. The remaining question is why there are different 'numbers' of tilts in these two phases.

Since the only 'chemical variables' in these two phases are the interlayer cations, it must be the difference in Li^+ and Na^+ cations, more specifically their size difference, which results in the different bulk structures. It is suggested that as the tolerance factor decreases, the perovskite framework tends to adopt a structure with more 'numbers' of tilts[69]. A tolerance factor, *t'*, is therefore formulated by considering the A' cations in the pseudo-tetrahedral sites and the B cations in the octahedral sites. Figure 4.20 shows how *t'* can be parameterized. If the A' cation sits in a perfect tetrahedron in an undistorted Ruddlesden-Popper structure, it should also fit in a cube of length *l*. It can be seen that $l = \frac{2}{\sqrt{3}}$<A'-O> = $\sqrt{2}$ <B-O>. Therefore in an undistorted Ruddlesden-Popper framework in which the A' cations reside in perfect tetrahedra, a tolerance factor can be parameterized as $t' = \frac{<A'-O>}{\sqrt{3}/\sqrt{2}<B-O>}$. Using tabulated ionic radii (Li^+ = 0.59 Å; Na^+ = 0.99 Å; Nb^{5+}/Ta^{5+} = 0.64 Å; O = 1.40 Å)[66], values of *t'* can be obtained as t'_{Li} = 0.796 and t'_{Na} = 0.956, respectively. As t'_{Li} is significantly smaller than t'_{Na}, the lithium phases tend to distort more strongly with respect to the sodium phases, which explains why the lithium phases adopt a structure with distortions along all three Cartesian axes while the sodium phases only along one. However, it should be noticed that the 'tolerance factor method' is a simplified approach and can only provide a simple qualitative explanation of the different 'numbers' of distortions adopted by the lithium and sodium phases. The calculated *t'* value cannot be used to predict if the perovskite double layer of an unknown phase would be distorted or not. This is because the tolerance factor *t'* is formulated by assuming that A' sits in a perfect tetrahedron but in

reality, the tetrahedron can be compressed and the A'-O bond lengths can be contracted by shrinking the interlayer separation of the lattice. The consequence of compression is that the cube of the length *l* is distorted to be tetragonal so the equation of *t'* is no longer valid.

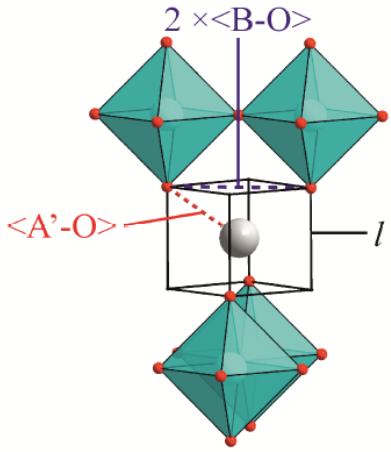


Figure 4.20. The 'tetrahedral' coordination site in the aristotype structure of A'NdB_2O_7 (A' = Li/Na; B = Nb/Ta). Grey, blue and red spheres represent A', B and O respectively.

BVS values calculated from the refined structures show that Li^+ cations are very well bonded (BVS Li_{Nb} = 0.99, Table 4.5; BVS Li_{Ta} = 0.98, Table 4.9) while Na^+ cations are slightly under-bonded (BVS Na_{Nb} = 0.88, Table 4.13; BVS Na_{Ta} = 0.91, Table 4.17). This indicates that distortions in the lithium phases have optimized the lithium coordination but the sodium coordination is not optimized in the corresponding sodium structures. Figure 4.21 shows the different ordering arrangements of the Li^+ and Na^+ cations viewing along the stacking axis, *z*. The Na^+ cations (blue spheres) are ordered in a 'checkerboard' pattern within corner-shared NaO_4 tetrahedra. Black spheres indicate the empty sites. This arrangement maximizes the Na-Na distance between the filled tetrahedral sites hence minimizes Na-Na repulsion, which agrees with Pauling's third crystallographic rule[70]. However, one feature of this ordering configuration is that shortening one Na-O bond necessarily elongates the neighbouring Na-O bonds so the average Na-O bond length remains unchanged. This means it is impossible to contract the average Na-O bond by octahedral tilting distortions only. An alternative mechanism to contract the average Na-O bond is to shrink the interlayer separation but this means the interlayer O-O bond length

will be decreased and the undesired O-O repulsion becomes stronger. Therefore the interlayer distance can only be shrunk to a limited level to avoid strong O-O repulsion. As a short conclusion, the sodium structure minimises Na-Na repulsion but Na-O bonding is slightly sacrificed.

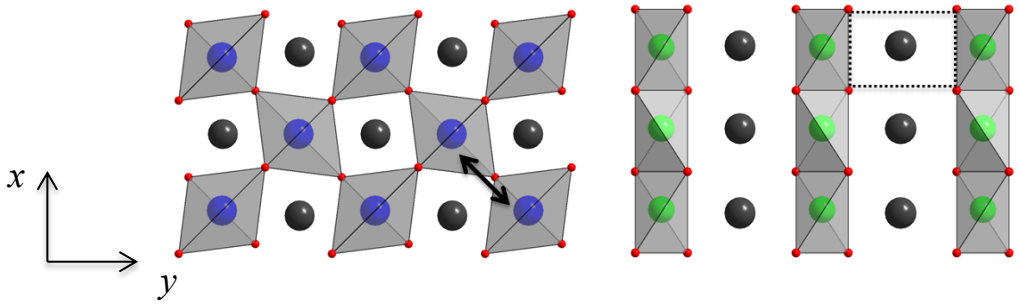


Figure 4.21. The ordering arrangements of Na^+ (left) and Li^+ (right) cations. Purple, green and red spheres represent Na, Li and O respectively. Black sphere are drawn to indicate the empty sites.

In contrast, the Li^+ cations are ordered as chains in the edge-shared LiO_4 tetrahedra (Figure 4.21). It can be immediately spotted that this arrangement is less optimal in terms of minimizing Li-Li repulsion in comparison of the corner-sharing arrangement of the Na^+ cations in the sodium structure. However, this edge-sharing configuration allows octahedral distortions to contract the average Li-O bond in the occupied tetrahedral sites. It can be observed from Figure 4.21 that the occupied sites are much smaller in size than the empty sites. The BVS values indicate that octahedral distortions do provide nearly ideal coordination environments for the Li^+ cations despite slightly stronger Li-Li repulsion.

It can be concluded from the analysis above that the structural differences in the lithium and sodium phases arise from a competition between minimizing interlayer cation repulsion and optimizing their local coordination. The sodium phases choose to minimize Na-Na repulsion, perhaps due to the relatively large size of the Na^+ cations. In the lithium phases, the lithium coordination is the dominant factor possibly because of the small size of Li^+. The small size of the Li^+ cations means Li-Li repulsion issue is not as severe as in the sodium case. In addition, the small size means Li^+ cations would be extremely under-bonded if the sodium structure was adopted.

4.4.2 DFT – A useful supplementary tool for crystal structure characterisation

It is common that refinements of different models give approximately equivalent fits, which leaves a lot of ambiguity. In such cases, DFT calculation can be a useful supplementary tool to help determine the final crystal structure.

As discussed above, the sodium structure ($P4_2/mnm$) minimizes the Na-Na repulsion while the lithium structure ($B2em$) optimizes the LiO_4 coordination. One obvious question to ask is why the lithium phases do not adopt the sodium-type, $P4_2/mnm$ structure and vice versa. In Chapter 3, hypothetical structures were constructed in order to compare the structure differences between $RbNdM_2O_7$ ($a^-a^-c^+$/-($a^-a^-c^+$)) and $CsNdM_2O_7$ ($a^-a^-c^+$). Their hypothetical structures can be constructed because the local tilting distortions and the tilting angles are very similar in the two phases. However, this is not the case for the lithium and sodium phases, in which the local tilting distortions differ significantly. Therefore it is not possible to construct hypothetical structures following a similar manner for the lithium and sodium phases. However, the DFT calculations can provide energy-minimized $P4_2/mnm$ structures and $B2em$ structures for the lithium and sodium phases respectively.

The first observation from the DFT calculation is that the energy minimized $P4_2/mnm$ structure is far less stable than the $B2em$ structure for the lithium phases. For example, the energy minimized $P4_2/mnm$ symmetry structure for $LiNdNb_2O_7$ is 289 meV/formula unit less stable than the energy minimized $B2em$ structure. On the other hand, the energy minimized $B2em$ structure for $NaNdNb_2O_7$ is 88 meV/formula unit less stable than the $P4_2/mnm$ structure. This result supports the experimental observation that lithium phases adopt the $B2em$ structure symmetry while the sodium phases adopt the $P4_2/mnm$ structure. In fact, the relaxed computational structures with the correct structural symmetries show great agreements with the experimental determined structures. Table 4.18 shows parameters from the structural refinements against the neutron diffraction data compared

to structural data extracted from DFT calculations for $LiNdNb_2O_7$ (*B*2*em*) and $NaNdNb_2O_7$ ($P4_2/mnm$)[68].

Atom	site	*x*	*y*	*z*
Li(1)	4*a*	0.5820(20) *0.56127*	0 *0*	½ *½*
Nd(1)	4*c*	0.2957(8) *0.28281*	0.2520(5) *0.24873*	¼ *¼*
Nb(1)	8*d*	0.3136(7) *0.3101*	0.7518(4) *0.75086*	0.1390(1) *0.13948*
O(1)	8*d*	0.3101(8) *0.31082*	0.8386(3) *0.84089*	0.0566(1) *0.05598*
O(2)	8*d*	0.1225(5) *0.12826*	0.4556(5) *0.44969*	0.1443(1) *0.14445*
O(3)	8*d*	0.5598(6) *0.55002*	0.0154(7) *0.03124*	0.1719(1) *0.17302*
O(4)	4*c*	0.3195(10) *0.34469*	0.6819(5) *0.67719*	¼ *¼*
$LiNdNb_2O_7$ – space group *B*2*em* (#39) *a* = 5.4498(2) Å, *b* = 5.3974(2) Å, *c* = 20.4556(8) Å, volume = 601.70(7) Å^3 DFT: *a = 5.43799* Å, *b = 5.37584* Å, *c = 20.47048* Å, volume = *598.43* Å^3				
Na(1)	4*e*	0 *0*	0 *0*	0.2649(3) *0.26413*
Nd(1)	4*f*	0.2587(3) *0.26241*	0.2587(3) *0.26241*	0 *0*
Nb(1)	8*j*	0.2531(3) *0.25345*	0.2531(3) *0.25345*	0.3943(0) *0.39445*
O(1)	4*g*	0.8034(4) *0.80966*	0.8034(4) *0.80966*	½ *½*
O(2)	4*e*	½ *½*	½ *½*	0.5725(1) *0.57197*
O(3)	4*e*	0 *0*	0 *0*	0.6071(2) *0.60810*
O(4)	8*h*	½ *½*	0 *0*	0.4153(1) *0.41723*
O(5)	8*j*	0.7138(2) *0.71507*	0.7138(2) *0.71507*	0.6885(1) *0.68983*
$NaNdNb_2O_7$ – space group $P4_2/mnm$ (#136) *a* = 5.4829(2) Å, *b* = 5.4829(2) Å, *c* = 20.9112(8) Å, volume = 628.63(6) Å^3 DFT: *a = 5.48088* Å, *b = 5.48088* Å, *c = 20.80676* Å, volume = *625.04* Å^3				

Table 4.18. Parameters from the structural refinements against neutron powder diffraction data collected from of $LiNdNb_2O_7$ and $NaNdNb_2O_7$ at 298 K, compared to parameters extracted from DFT calculations. Parameters obtained from DFT calculations are shown in *Italic*.

The second observation is that much shorter Na-Na bond distances are formed in the energy minimized *B*2*em* structure for $NaNdM_2O_7$ in comparison to the $P4_2/mnm$ structure. For

$NaNdNb_2O_7$, the shortest Na-Na bond distance is 3.93 Å in the experimentally determined $P4_2/mnm$ structure but 2.76 Å in the calculated *B*2*em* structure. The latter one indicates a much stronger Na-Na repulsion. Despite improved sodium coordination in the calculated *B*2*em* structure (BVS Na_{Nb} = +1.23), huge unfavourable cation-cation repulsion means the *B*2*em* symmetry model is not the optimal structural option for the sodium phases. In contrast, in the energy minimized $P4_2/mnm$ structures for the lithium phases, the lithium coordination sites are too big to accommodate the Li^+ cations. This is demonstrated by the very small BVS values extracted from the calculated $P4_2/mnm$ structure (BVS Li_{Nb} = +0.73). Optimizing the size of the lithium coordination has greater impact than minimizing the Li-Li repulsion. Therefore the *B*2*em* structure is the best option for the lithium phases.

4.5 Conclusion

Pure samples of $LiNdM_2O_7$ and $NaNdM_2O_7$ can be synthesized by topochemical cation exchange reactions from $RbNdM_2O_7$ (*M* = Nb/Ta). There is a structural change from the Dion-Jacobson to the Ruddlesden-Popper framework during the cation exchange reaction, which can be attributed to the size decrease of the interlayer cations. Analysis of the synchrotron X-ray and high-resolution neutron diffraction data reveals that the lithium phases adopt a polar *B*2*em* structure with an $a^-a^-c^+/-(a^-a^-c^+)$ tilting distortion while the sodium phases adopt a non-polar $P4_2/mnm$ structure with an $a^-b^0c^0/b^0a^-c^0$ tilting distortion. The Li^+ cations adopt an ordered arrangement in the small edge-shared tetrahedral sites in the polar structure while the Na^+ cations are ordered in the corner-shared tetrahedral sites between layers. The structure differences in the lithium and sodium phases arise from a competition between minimising the cation-cation repulsion and optimising the cation coordination, with the former one dominating for the sodium phases and the latter one for the lithium phases.

Our characterisation shows that interlayer cations have a great impact on the octahedral tilting distortions in the perovskite framework. This observation is consistent with the previous observations that RbNdM_2O_7 and CsNdM_2O_7 adopt another two different crystal structures. Therefore it seems likely that, by carefully choosing the interlayer cations with appropriate sizes, it is possible to tune the octahedral tilting distortions, hence preparing polar compounds.

Chapter 5 - Phase Transition Behaviours of Polar Dion-Jacobson Phases A'NdM_2O_7 (A' = Rb/Cs, M = Nb/Ta)

5.1 Introduction

In Chapters 3 and 4, it has been demonstrated that RbNdM_2O_7, CsNdM_2O_7 and LiNdM_2O_7 (M = Nb/Ta) all adopt polar structures at ambient temperature. Despite the differences in their bulk structures, locally the perovskite double sheets in all three phases adopt the same type of octahedral tilting distortion, $a^-a^-c^+$, with the differences between the structures coming from how these layers are stacked and the arrangements of interlayer cations. Recent studies have revealed that n = 2 Ruddlesden-Popper phases $Sr_3Zr_2O_7$[71] and $Sr_3Sn_2O_7$[72] are also polar at ambient temperature. Interestingly, both $Sr_3Zr_2O_7$ and $Sr_3Sn_2O_7$ also have perovskite double layers with an $a^-a^-c^+$ tilting distortion in their polar structures. This structural similarity is also observed in polar Aurivillius phases, for example $SrBi_2Ta_2O_9$, in which the $SrTa_2O_7$ perovskite layers adopt an $a^-a^-c^+$ tilting distortion[73]. These observations suggest that the $a^-a^-c^+$ tilting distortion is a stable structural option for polar layered perovskite phases. It is therefore interesting, from a crystallographic point of view, to explore if there are other common tilting distortion systems adopted by n = 2 layered perovskite compounds, especially the ones leading to polar or anti-polar structures.

Phase transition behaviours of several polar n = 2 Ruddlesden-Popper phases have been demonstrated by combining neutron diffraction, synchrotron X-ray diffraction and DFT calculations. For example, $Sr_3Zr_2O_7$ follows a phase transition sequence of $A2_1am$ ($a^-a^-c^+/a^-a^-c^+$) → $Pnab$ ($a^-a^-c^-/a^-a^--c^-$) → $Amam$ ($a^-a^-c^0/a^-a^-c^0$) → $I4/mmm$ upon heating[71]. $Sr_3Sn_2O_7$ has a slightly different transition pathway, with the third phase being $Acaa$ ($a^0a^0c^-/a^0a^0c^-$) rather than $Amam$[72].

In contrast to $n = 2$ Ruddlesden-Popper phases, phase transition behaviours of $n = 2$ Dion-Jacobson phases are not very well established. $CsBiNb_2O_7$ was found to adopt a polar $P2_1am$ structure at ambient temperature but no phase transition was observed below 1173 K, above which temperature the sample deteriorated[74]. Variable temperature neutron powder diffraction data suggest that another $n = 2$ Dion-Jacobson phase, $CsBi_{0.6}La_{0.4}Nb_2O_7$, undergoes a first-order phase transition from the polar $P2_1am$ structure to the aristotype $P4/mmm$ structure, with both tilting modes ($a^-a^-c^0$ and $a^0a^0c^+$) vanishing simultaneously at the transition temperature[75]. $CsLaNb_2O_7$ was found to have a phase transition sequence of $P2_1am \rightarrow Amm2 \rightarrow P4/mmm$ but the crystal structures at different temperatures were assigned from the analysis of the synchrotron X-ray diffraction data[63], which makes it not very convincing.

It can be seen that, remarkably, no unambiguous intermediate phase has been reported for polar $n = 2$ Dion-Jacobson phases. Therefore we have explored the phase transition behaviours of polar $RbNdM_2O_7$ and $CsNdM_2O_7$ (M = Nb/Ta) to study if there is any intermediate phase between the polar ground-state structures and the high-temperature structures. Since the rubidium and caesium phases adopt different polar structures at ambient temperature, it is also interesting to see if there is any similarity and/or difference in the transition behaviours for these two phases.

5.2 Synthesis and Measurements

Powder samples of $RbNdTa_2O_7$, $RbNdNb_2O_7$ and $CsNdTa_2O_7$ were prepared by ceramic synthesis, as described in Chapter 3. Samples of $CsNdNb_2O_7$ were prepared from Cs_2CO_3 (99.994%), Nd_2O_3 (99.99%) and Nb_2O_5 (99.9985%). The mixtures were heated at 850 °C in air for 12 hours, reground, and pressed into pellets. Samples of $CsNdNb_2O_7$ were then heated in air for four periods of 48 hours at 1000 °C. All four samples were washed with distilled water as a final step, to remove any remaining rubidium or caesium oxides, and then dried for 12 hours at 140 °C in air. Reaction progress and final sample purity for all four samples were assessed by X-ray powder diffraction data collected using a PANalytical X'pert diffractometer incorporating an X'celerator position sensitive detector (monochromatic Cu Kα1 radiation).

High-resolution synchrotron X-ray powder diffraction data were collected using instrument I11 at Diamond Light Source Ltd., UK. Samples were mixed in a 1:1 mass ratio with boron, to reduce the X-ray absorption, and sealed in 0.5 mm diameter borosilicate glass capillaries. Diffraction patterns were measured using Si-calibrated X-rays with an approximate wavelength of 0.825 Å. Data were collected as a function of temperature by heating samples with a hot-air blower in the range $300 < T / K < 1173$ K with data collected at intervals of approximately 4 K.

Time-of-flight neutron powder diffraction (NPD) data were collected using the HRPD instrument at ISIS. All four samples (approximately 4 g) were placed in cylindrical vanadium cans and loaded into a vacuum furnace. Diffraction patterns were then collected at room temperature, to confirm sample purity, and then at higher temperatures, identified by studying the synchrotron X-ray diffraction data, to characterise the structures of the high-temperature phases. Detailed temperatures for the neutron diffraction measurements will be given in the following sections.

5.3 Results

5.3.1 Symmetry analysis of n = 2 Dion-Jacobson phases

Direct crystallographic analysis of the distorted structures adopted by n = 2 Dion-Jacobson phases can be challenging. Therefore a symmetry analysis was performed by referring to an early crystallography study[76] and using the ISODISTORT software[12] to generate a series of 'chemically plausible' distorted crystal structures for n = 2 Dion-Jacobson phases. The distorted structures are generated and systematized in Table 5.1, using the same approach as described in Chapter 4 for n = 2 Ruddlesden-Popper phases.

Undistorted n = 2 Dion-Jacobson phases have a *P*4/*mmm* symmetry structure. Ten distorted structures are generated by applying a single irreducible representation on the parent *P*4/*mmm* structure. These structures only contain tilting distortions along the *x*/*y* or *z* directions. The remaining distorted structures all contain two irreducible representations therefore they are distorted along both *x*/*y* and *z* directions. It should be noticed that both in-phase and out-of-phase tilts are considered for distortions along the stacking axis, *z*, but only the out-of-phase tilts are studied along *x*/*y* directions. This is because the in-phase tilts are rarely observed along *x*/*y* directions for the layered perovskite compounds, therefore they are regarded as 'special cases' and will only be discussed when a high temperature phase adopts a structure which is not included in Table 5.1. Except for cases specifically stated in Table 5.1, all distorted structures have a geometric expansion with $a' \sim b' = \sqrt{2}\, a$ on the *x*/*y* plane where *a*' and *b*' are the lattice parameters of the expanded unit cell and *a* is the parameter of the parent *P*4/*mmm* cell.

Any intermediate phase of $RbNdM_2O_7$ and $CsNdM_2O_7$ at higher temperatures is assumed to adopt one of the structures with a 'chemically plausible' tilting distortion in Table 5.1.

Twist	Glazer Tilts	Space Group	Stacking axis in standard setting	Space Group (c-stacking)	Irrep	Centrosymmetric?
000/000	$a^0b^0c^0/a^0b^0c^0$	*P*4/*mmm* (123)	*c*	*P*4/*mmm*		Yes
00Ψ_z	$a^0b^0c^+$	*P*4/*mbm* (127)	*c*' = *c*	*P*4/*mbm*	M_2^+ (a)	Yes
00Φ_z	$a^0a^0c^-$	*P*4/*nbm* (125)	*c*' = *c*	*P*4/*nbm*	M_4^- (a)	Yes
$\Phi\Phi$0	$a^-a^-c^0$	*Pmma* (51)	*b*' = *c*	*Pmam*	M_5^- (a,0)	Yes
Φ00	$a^-b^0c^0$	*Cmmm* (65)	*c*' = 2*c*, *a*'~*b*' = 2*a*	*Cmmm*	M_5^- (a,a)	Yes
$\Phi_1\Phi_2$0	$a^-b^-c^0$	*P*2/*m* (10)	*b*' = *c*	*P*2/*m* (γ)	M_5^- (a,b)	Yes
Φ0Ψ_z	$a^-b^0c^+$	*Amm*2 (38)	*a*' = *c*, *b*'~*c*' = 2*a*	*C*2*mm*	$M_2^+ \bullet M_5^-$ (a; b,b)	No
$\Phi\Phi\Psi_z$	$a^-a^-c^+$	*Pmc*2$_1$ (26)	*a*' = *c*	*P*2$_1$*am*	$M_2^+ \bullet M_5^-$ (a; b,0)	No
$\Phi_1\Phi_2\Psi_z$	$a^-b^-c^+$	*Pm* (6)	*b*' = *c*	*Pm* (γ)	$M_2^+ \bullet M_5^-$ (a; b,c)	Yes
Φ0Φ_z	$a^-b^0c^-$	*C*2/*m* (12)	*c*' = *c*, *a*'~*b*' = 2*a*	*C*2/*m* (β)	$M_4^- \bullet M_5^-$ (a; b,b)	Yes
$\Phi\Phi\Phi_z$	$a^-a^-c^-$	*P*2/*c* (13)	*a*' = *c*	*P*2/*b* (α)	$M_4^- \bullet M_5^-$ (a; b,0)	Yes
$\Phi_1\Phi_2\Phi_z$	$a^-b^-c^-$	*P*-1 (2)	*c*' = *c*	*P*-1	$M_4^- \bullet M_5^-$ (a; b,c)	Yes
00Ψ_z/00-Ψ_z	$a^0b^0c^+/a^0b^0$-c^+	*I*4/*mcm* (140)	*c*' = 2*c*	*I*4/*mcm*	A_2^+ (a)	Yes
00Φ_z /00-Φ_z	$a^0b^0c^-/a^0b^0$-c^-	*I*4/*mcm* (140)	*c*' = 2*c*	*I*4/*mcm*	A_4^- (a)	Yes
$\Phi\Phi$0/-($\Phi\Phi$)0	$a^-a^-c^0/$-(a^-a^-)c^0	*Imma* (74)	*a*' = 2*c*	*Imcm*	A_5^- (a,0)	Yes
Φ00/-Φ00	$a^-b^0c^0/$-$a^-b^0c^0$	*Fmmm* (69)	*c*' = 2*c*, *a*'~*b*' = 2*a*	*Fmmm*	A_5^- (a,a)	Yes
$\Phi_1\Phi_2$0/-($\Phi_1\Phi_2$)0	$a^-b^-c^0/$-(a^-b^-)c^0	*C*2/*m* (12)	*b*' = 2*c*, *a*' = 2*a*	*I*2/*m* (γ)	A_5^- (a,b)	Yes
$\Phi\Phi\Psi_z$/-($\Phi\Phi\Psi_z$)	$a^-a^-c^+/$-($a^-a^-c^+$)	*Ima*2 (46)	*a*' = 2*c*	*I*2*cm*	$A_2^+ \bullet A_5^-$ (a; b,0)	No
Φ0Ψ_z/-(Φ0Ψ_z)	$a^-b^0c^+/$-($a^-b^0c^+$)	*Fmm*2 (42)	*b*' = 2*c*, *a*'~*c*' = 2*a*	*F*2*mm*	$A_2^+ \bullet A_5^-$ (a; b,b)	No
$\Phi_1\Phi_2\Psi_z$/-($\Phi_1\Phi_2\Psi_z$)	$a^-b^-c^+/$-($a^-b^-c^+$)	*Cm* (8)	*b*' = 2*c*, *a*' = 2*a*	*Im* (γ)	$A_2^+ \bullet A_5^-$ (a; b,c)	Yes
$\Phi\Phi\Phi_z$/-($\Phi\Phi\Phi_z$)	$a^-a^-c^-/$-($a^-a^-c^-$)	*C*2/*c* (15)	*a*' = 2*c*	*I*2/*a* (β)	$A_4^- \bullet A_5^-$ (a; b,0)	Yes
$\Phi_1$0Φ_z/-($\Phi_1$0Φ_z)	$a^-b^0c^-/$-($a^-b^0c^-$)	*C*2/*m* (12)	*c*' = *c*, *a*'~*b*' = 2*a*	*C*2/*m* (β)	$A_4^- \bullet A_5^-$ (a; b,b)	Yes
$\Phi_1\Phi_2\ \Phi_z$/-($\Phi_1\Phi_2\Phi_z$)	$a^-b^-c^-/$-($a^-b^-c^-$)	*P*-1 (2)	*c*' = *c*	*P*-1	$A_4^- \bullet A_5^-$ (a; b,c)	Yes
Φ0Ψ_z/Φ0-Ψ_z	$a^-b^0c^+/a^-b^0$-c^+	*Cmcm* (63)	*c*' = 2*c*, *a*'~*b*' = 2*a*	*Cmcm*	$A_2^+ \bullet M_5^-$ (a; b,b)	Yes
$\Phi\Phi\Psi_z$/$\Phi\Phi$-Ψ_z	$a^-a^-c^+/a^-a^-$-c^+	*Pbcm* (57)	*c*' = 2*c*	*Pbcm*	$A_2^+ \bullet M_5^-$ (a; b,0)	Yes
$\Phi_1\Phi_2\Psi_z$/$\Phi_1\Phi_2$-Ψ_z	$a^-b^-c^+/a^-b^-$-c^+	*P*2$_1$/*m* (11)	*b*' = 2*c*	*P*2$_1$/*m* (γ)	$A_2^+ \bullet M_5^-$ (a; b,c)	Yes
Φ0Φ_z/Φ0-Φ_z	$a^-b^0c^-/a^-b^0$-c^-	*Cmcm* (63)	*c*' = 2*c*, *a*'~*b*' = 2*a*	*Cmcm*	$A_4^- \bullet M_5^-$ (a; b,b)	Yes
$\Phi\Phi\Phi_z$/$\Phi\Phi$-Φ_z	$a^-a^-c^-/a^-a^-$-c^-	*Pbcm* (57)	*c*' = 2*c*	*Pbcm*	$A_4^- \bullet M_5^-$ (a; b,0)	Yes
$\Phi_1\Phi_2\Phi_z$/$\Phi_1\Phi_2$-Φ_z	$a^-b^-c^-/a^-b^-$-c^-	*P*2$_1$/*m* (11)	*b*' = 2*c*	*P*2$_1$/*m* (γ)	$A_4^- \bullet M_5^-$ (a; b,c)	Yes
$\Phi\Phi\Psi_z$/-($\Phi\Phi$)Ψ_z	$a^-a^-c^+/$-(a^-a^-)c^+	*Pnma* (62)	*b*' = 2*c*	*Pnam*	$M_2^+ \bullet A_5^-$ (a; b,0)	Yes
Φ0Ψ_z/-(Φ0)Ψ_z	$a^-b^0c^+/$-(a^-b^0)c^+	*Cmcm* (63)	*c*' = 2*c*, *a*'~*b*'= 2*a*	*Cmcm*	$M_2^+ \bullet A_5^-$ (a; b,b)	Yes
$\Phi_1\Phi_2\Psi_z$/-($\Phi_1\Phi_2$)Ψ_z	$a^-b^-c^+/$-(a^-b^-)c^+	*P*2$_1$/*m* (11)	*b*' = 2*c*	*P*2$_1$/*m* (γ)	$M_2^+ \bullet A_5^-$ (a; b,c)	Yes
$\Phi\Phi\Phi_z$/-($\Phi\Phi$)Φ_z	$a^-a^-c^-/$-(a^-a^-)c^-	*Pnna* (52)	*b*' = 2*c*	*Pnan*	$M_4^- \bullet A_5^-$ (a; b,0)	Yes
Φ0Φ_z/-(Φ0)Φ_z	$a^-b^0c^-/$-(a^-b^0)c^-	*Cmca* (64)	*c*' = 2*c*, *a*'~*b*' = 2*a*	*Cmca*	$M_4^- \bullet A_5^-$ (a; b,b)	Yes

Twist	Glazer Tilts	Space Group	Stacking axis in standard setting	Space Group (c-stacking)	Irrep	Centrosymmetric?
$\Phi_1\Phi_2\Phi_z$/-($\Phi_1\Phi_2$)Φ_z	$a^-b^-c^-$/-(a^-b^-)c^-	$P2_1/c$ (14)	$b' = 2c$	$P2_1/n$ (γ)	M_4^- • A_5^- (a; b,c)	Yes

Table 5.1. 'Chemically plausible' distortions of n = 2 Dion-Jacobson structures

5.3.2 Phase transition behaviours of $RbNdTa_2O_7$

5.3.2.1 The 1st phase transition of $RbNdTa_2O_7$– ferroelectric (P1) to paraelectric (P2)

As demonstrated in Chapter 3, $RbNdTa_2O_7$ adopts an *I*2*cm* structure with an $a^-a^-c^+$/-($a^-a^-c^+$) tilting distortion at ambient temperature. High-resolution neutron diffraction and synchrotron X-ray diffraction data were collected from a sample of $RbNdTa_2O_7$ at ambient temperature to identify any possible secondary phase. Refining the *I*2*cm* model against the diffraction data gives good statistical and visual fits (wRp = 3.00 %, Rp = 3.28 % for NPD data; wRp = 4.67 %, Rp = 3.35 % for SXRD data) and no secondary phase was found (Figure 5.1). Therefore any change in the diffraction patterns at higher temperatures should be attributed to the structural change of the main phase, or sample decomposition. The *I*2*cm* model was then refined against the synchrotron X-ray diffraction data collected at higher temperatures. Refinements give equivalently good fits to the diffraction data collected at the temperature range from 300 K to 500 K. Above 500 K, the refinement gives a far poorer fit. This suggests that the *I*2*cm* model cannot describe the crystal structure of $RbNdTa_2O_7$ above 500 K, indicating a possible phase transition around this temperature.

Close inspection of the diffraction data shows that the [110] peak starts to split at 500 K (Figure 5.2). Further inspection shows that superlattice peaks corresponding to doubling the *c* lattice persist above 500 K (Figure 5.3). These observations suggest that above 500 K, $RbNdTa_2O_7$ adopts a different crystal structure with a further expanded orthorhombic unit cell with $a' \sim b' = \sqrt{2}\ a = 2a_p$, $c' = 2c_p$ or a monoclinic cell with $a' \sim b' = a = \sqrt{2}\ a_p$, $c' = 2c_p$ and $\gamma \neq 90°$ (a', b' and c': lattice parameters above 500 K; a and c: lattice

parameters below 500 K; a_p and c_p: lattice parameters of the undistorted cell). Phases before and after the phase transition at approximately 500 K are assigned as P1 and P2 respectively.

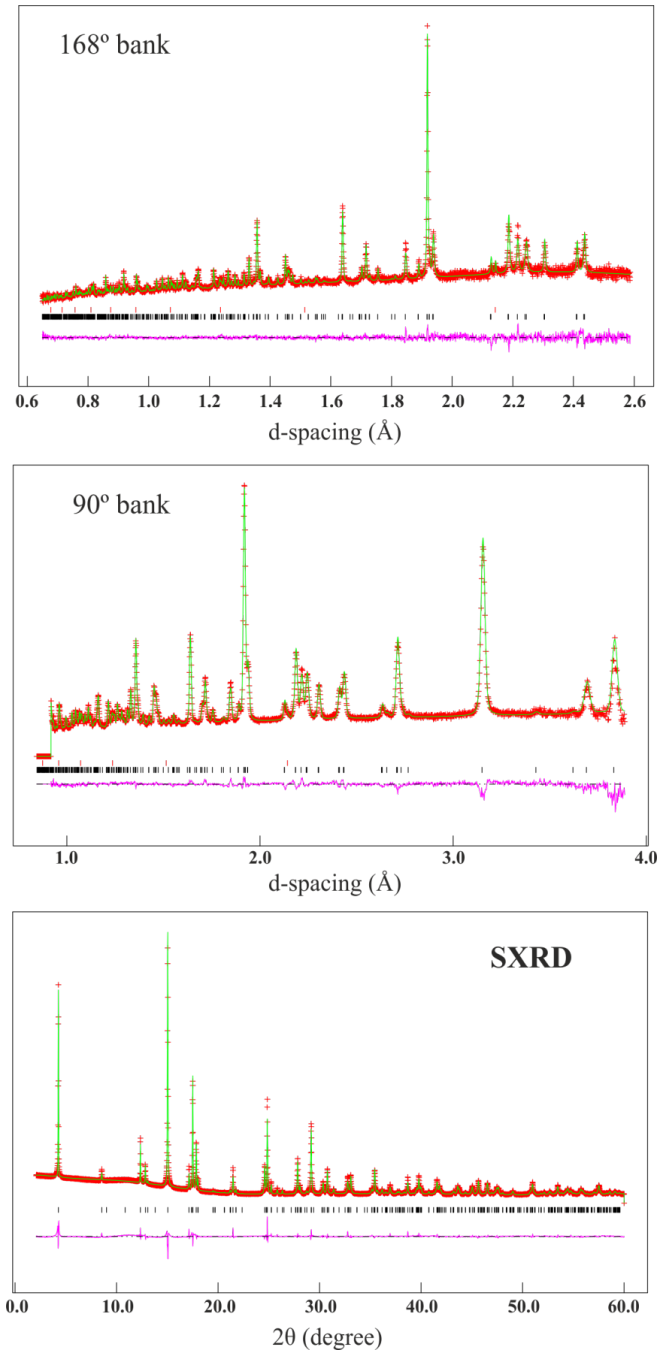


Figure 5.1. Observed, calculated and difference plots from the refinement of a structural model in space group *I2cm* against the NPD and SXRD data collected from $RbNdTa_2O_7$ at ambient temperature. Top panel shows the refinement from the NPD 168° bank, middle panel from the NPD 90° bank, bottom panel from the synchrotron X-ray diffraction data. Vanadium was added as the secondary phase with red tick-marks for the refinements against the neutron diffraction data. No secondary phase is found.

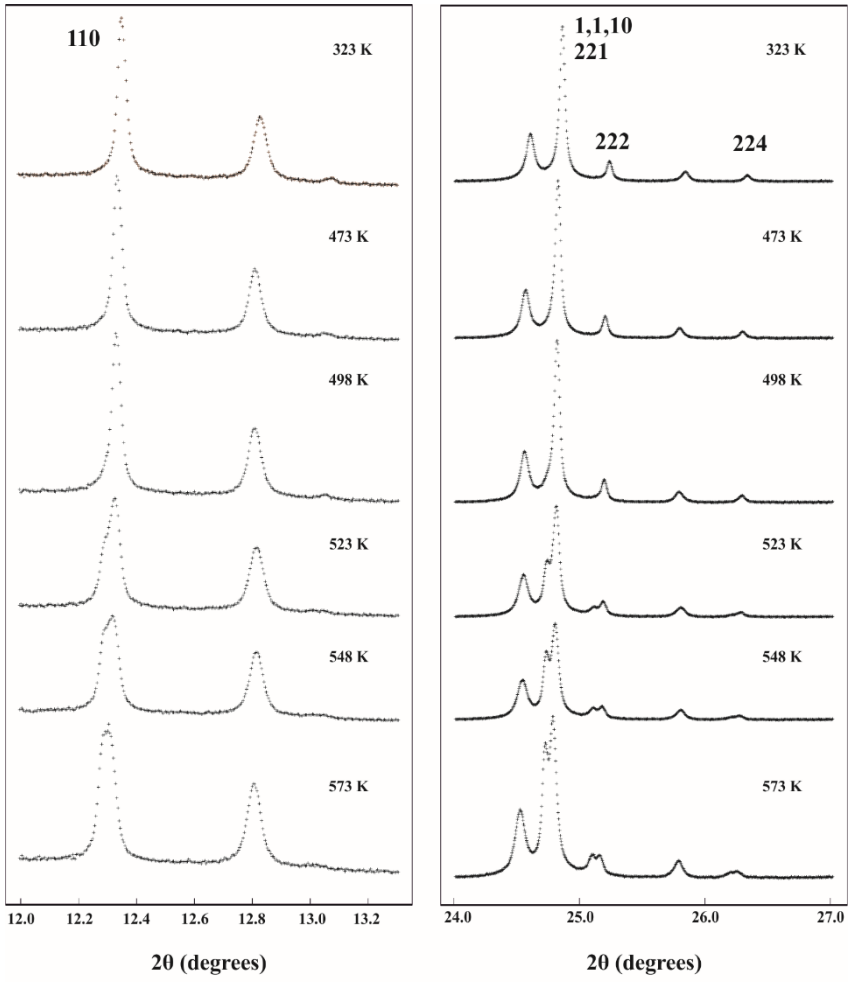


Figure 5.2. Temperature evolution of some reflections from $RbNdTa_2O_7$ upon heating. It can be observed that a set of peaks are splitting between 498 K and 523 K.

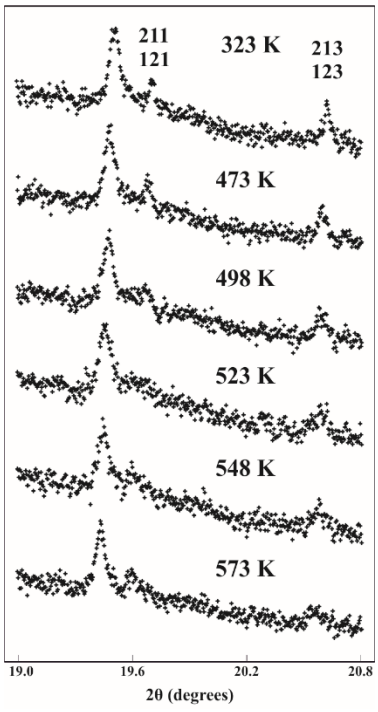


Figure 5.3. Temperature evolution of some superlattice peaks corresponding to doubling the *c* lattice.

In order to probe the crystal structure of P2, high-resolution neutron diffraction data were collected at 673 K. This particular temperature was chosen to ensure the diffraction data is corresponding to a single phase. If the neutron diffraction data was collected at a temperature close to the phase transition temperature (500 K), for example 525 K, it would be possible that the pattern was contributed from both P1 and P2. No further phase transition was observed between 500 K and 673 K, therefore 673 K was considered as an appropriate temperature to study P2.

13 symmetry models in Table 5.1 have the correct unit cell sizes for P2: *P*-1 #2, *Im* #8, three different $P2_1/m$ #11 (with different distortions), *C*2/*m* #12, *I*2/*m* #12, $P2_1/n$ #14, *F*2*mm* #42, four different *Cmcm* #63 (with different distortions), *Cmca* #64 and *Fmmm* #69. These models were constructed and refined against the neutron diffraction data collected at 673 K. Fitting statistics show that models of $P2_1/m$ ($a^-b^-c^+/-(a^-b^-)c^+$), $P2_1/n$ ($a^-b^-c^-/-(a^-b^-)c^-$) and *Cmca* ($a^-b^0c^-/-(a^-b^0)c^-$) achieve the best fits (Table 5.2).

space group	Glazer tilt	Irrep	χ^2	wRp (%)	Rp (%)
P-1 (2)	$a^-b^-c^-/-(a^-b^-c^-)$	$A_4^- \bullet A_5^-$ (a; b,c)	6.32	2.76	2.39
Im (8)	$a^-b^-c^+/-(a^-b^-c^+)$	$A_2^+ \bullet A_5^-$ (a; b,c)	6.60	2.81	2.37
$P2_1/m$ (11)	$a^-b^-c^+/a^-b^--c^+$	$A_2^+ \bullet M_5^-$ (a; b,c)	8.10	3.12	2.58
$P2_1/m$ (11)	$a^-b^-c^-/a^-b^--c^-$	$A_4^- \bullet M_5^-$ (a; b,c)	5.83	2.65	2.34
$P2_1/m$ (11)	$a^-b^-c^+/-(a^-b^-)c^+$	$M_2^+ \bullet A_5^-$ (a; b,c)	5.26	2.51	2.26
*C*2/*m* (12)	$a^-b^0c^-/-(a^-b^0c^-)$	$A_4^- \bullet A_5^-$ (a; b,b)	6.09	2.71	2.31
*I*2/*m* (12)	$a^-b^-c^0/-(a^-b^-)c^0$	A_5^- (a,b)	7.69	3.04	2.44
$P2_1/n$ (14)	$a^-b^-c^-/-(a^-b^-)c^-$	$M_4^- \bullet A_5^-$ (a; b,c)	4.67	2.37	2.20
*F*2*mm* (42)	$a^-a^0c^+/-(a^-a^0c^+)$	$A_2^+ \bullet A_5^-$ (a; b,b)	7.11	2.93	2.50
Cmcm (63)	$a^-b^0c^+/a^-b^0-c^+$	$A_2^+ \bullet M_5^-$ (a; b,b)	10.37	3.53	2.71
Cmcm (63)	$a^-b^0c^-/a^-b^0-c^-$	$A_4^- \bullet M_5^-$ (a; b,b)	6.24	2.74	2.43
Cmcm (63)	$a^-b^0c^+/-(a^-b^0)c^+$	$M_2^+ \bullet A_5^-$ (a; b,b)	5.88	2.66	2.31
Cmca (64)	$a^-b^0c^-/-(a^-b^0)c^-$	$M_4^- \bullet A_5^-$ (a; b,b)	4.85	2.42	2.25
Fmmm (69)	$a^-b^0c^0/-a^-b^0c^0$	A_5^- (a,a)	7.68	3.04	2.44

Table 5.2. Fitting statistics from the structural refinements of different symmetry models against neutron diffraction data collected from $RbNdTa_2O_7$ at 673 K

Close inspection of the refinement plots and the refined structures from the $P2_1/m$, $P2_1/n$ and *Cmca* models reveals that P2 adopts the *Cmca* structure. Figure 5.4 shows that the

$P2_1/m$ model cannot account for some peak intensities correctly. The remaining two model $P2_1/n$ ($a^-b^-c^-$/-(a^-b^-)c^-) and *Cmca* ($a^-b^0c^-$/-(a^-b^0)c^-) are very similar in terms of the tilting distortions, with *Cmca* as a special case of $P2_1/n$ in which the magnitude of the '*b*' tilt is zero. The refined $P2_1/n$ structure shows effectively zero '*b*' tilt, suggesting P2 adopts the *Cmca* structure. The observed, calculated and difference plots from the symmetry model in space group *Cmca* against the neutron diffraction data are shown in Figure 5.5. Full details of the parameters from the refinements are shown in Table 5.3. The refined structure is shown in Figure 5.12.

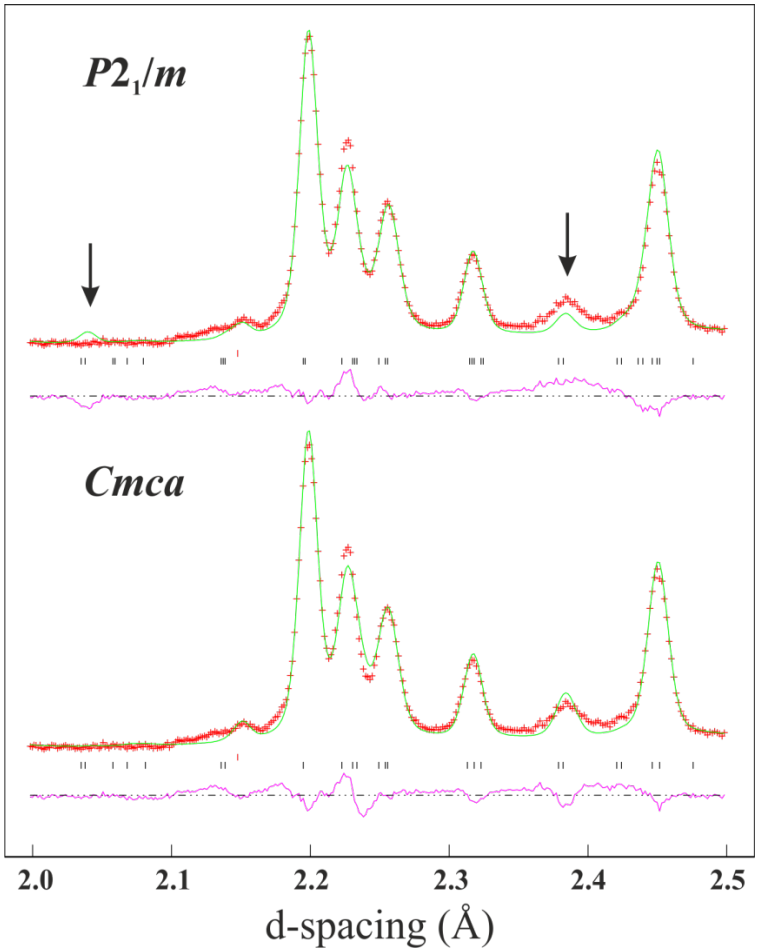


Figure 5.4. Observed, calculated and difference plots from the refinements of the $P2_1/m$ and *Cmca* models against the neutron diffraction data collected from $RbNdTa_2O_7$ at 673 K. For the $P2_1/m$ model, simulated peaks with arrows cannot fit the data correctly.

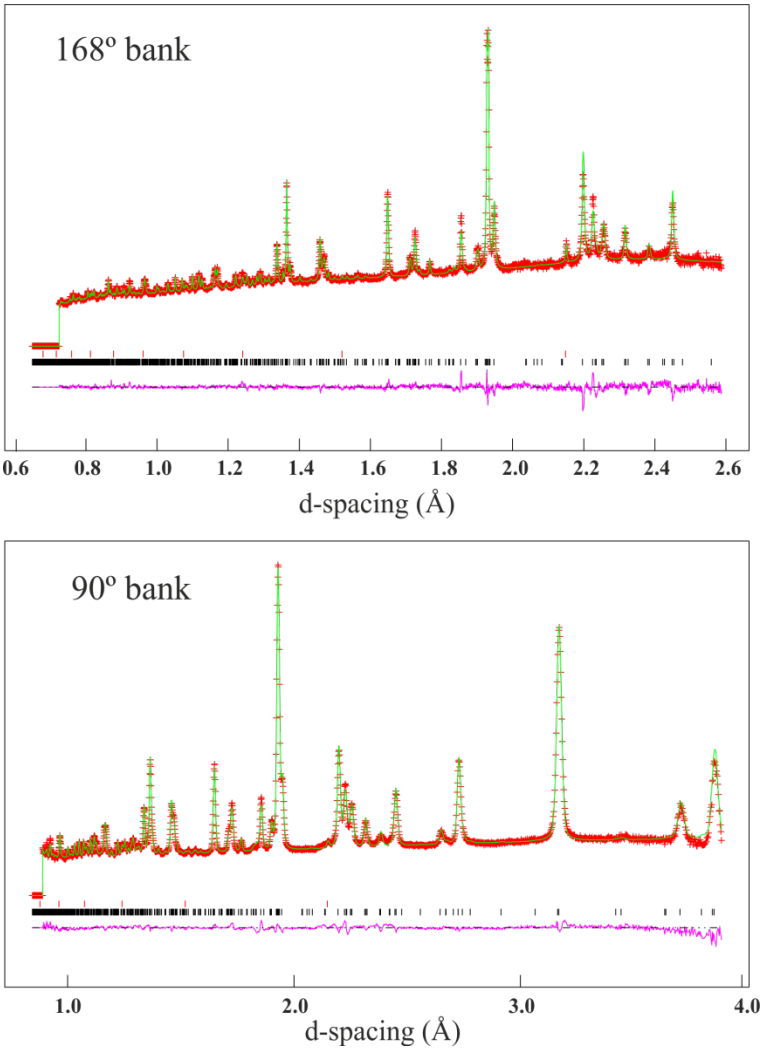


Figure 5.5. Observed, calculated and difference plots from the refinement of a structure model in space group *Cmca* against neutron diffraction data collected from $RbNdTa_2O_7$ at 673 K. Vanadium was added as the secondary phase with red tick-marks.

Atom	site	*x*	*y*	*z*	U_{iso} (Å^3)
Rb(1)	8*f*	0	0.2538(16)	0.2524(7)	0.0579(10)
Nd(1)	8*f*	0	0.2457(5)	0.0000(6)	0.0178(6)
Ta(1)	16*g*	0.7501(4)	0.0066(7)	0.1019(1)	0.0072(4)
O(1)	8*f*	0	0.4709(11)	0.5958(3)	0.0298(20)
O(2)	8*f*	0	0.4891(11)	0.0736(3)	0.0173(16)
O(3)	16*g*	0.2222(7)	0.2465(13)	0.9167(3)	0.0349(13)
O(4)	16*g*	0.7188(4)	0.0131(9)	0.1804(1)	0.0281(8)
O(5)	8*d*	0.7860(7)	0	0	0.0382(13)
$RbNdTa_2O_7$ – space group *Cmca* (#64) *a* = 7.7089(3) Å, *b* = 7.7242(3) Å, *c* = 22.2553(9) Å, volume = 1325.18(14) Å^3 Formula weight: 703.59 g mol^{-1}, Z = 8 Radiation source: Neutron Time of flight Temperature: 673 K χ^2 = 4.85, wRp = 2.42%, Rp = 2.25%					

Table 5.3. Parameters from the structural refinement of $RbNTa_2O_7$ against neutron powder diffraction data collected at 673 K.

It is then concluded that the first phase transition of $RbNdTa_2O_7$ occurs at approximately 500 K, leading to an anti-polar intermediate phase P2 in space group *Cmca* with an $a^-b^0c^-$/-$(a^-b^0)c^-$ tilting distortion. This is a first-order phase transition, which will be discussed later.

5.3.2.2 The 2nd phase transition of $RbNdTa_2O_7$ – Loss of the a^- tilts (P2 to P3)

Having established that P2 adopts a *Cmca* structure, this symmetry model was refined against the synchrotron X-ray diffraction data collected above 500 K. Sequential refinements gave equally good fits until 1025 K, at which temperature sample deterioration was observed, presumably due to a reaction with the borosilicate capillary. A careful study of the refined structural parameters reveals that *a* and *b* lattice parameters converge at approximately 950 K (Figure 5.11), which indicates a possible phase transition from an orthorhombic phase to a tetragonal phase.

Neutron diffraction data were collected at 973 K to probe if there is indeed another phase appearing above 950 K. Figure 5.6 shows a comparison of neutron diffraction data collected at 973 K and 673 K. It can be seen that some peaks vanish when the temperature was elevated from 673 K to 973 K. In addition, superlattice peaks corresponding to doubling the *a*/*b* lattice parameters coalesce. These observations together suggest that the 973 K structure has higher symmetry than the 673 K structure. Combining the information extracted from the synchrotron X-ray diffraction and neutron diffraction data, it is concluded that a tetragonal phase, P3, appears above 950 K. As shown in Figure 5.6, the superlattice peak corresponding to doubling *c* (labelled with star) persists at 973 K, which indicates P3 adopts a distorted, tetragonal structure with a doubled *c* lattice. Only two symmetry models with the correct unit cell size can be found in Table 5.1, both in space group *I*4/*mcm* but with different tilting distortions ($a^0a^0c^+/a^0a^0$-c^+ and $a^0a^0c^-/a^0a^0$-c^-).

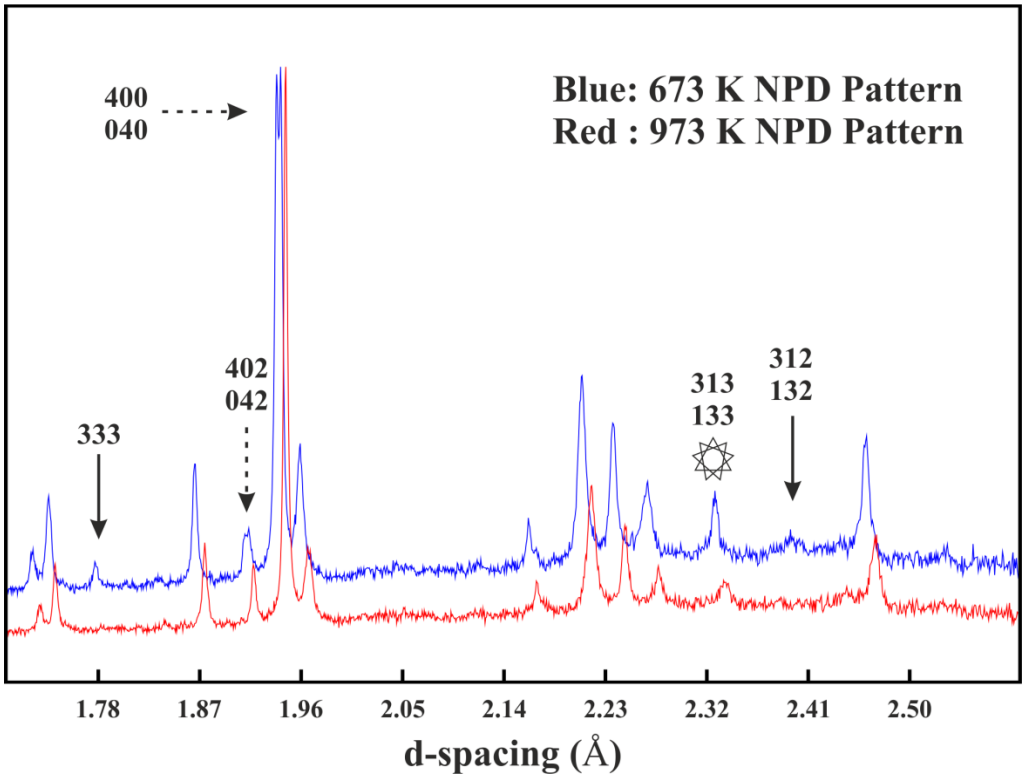


Figure 5.6. Neutron diffraction patterns collected from $RbNdTa_2O_7$ at 673 K and 973 K. Peaks labelled with solid arrows are not observed from the diffraction data at 973 K; Splitting peaks labelled with dashed arrows converge at 973 K. The peak labelled with the star corresponds to doubling the *c* lattice with respect to the undistorted cell.

Thus, two symmetry models of *I*4/*mcm* with different tilting distortions were constructed and refined against the neutron diffraction data collected at 973 K. Refinements show that the symmetry model with the out-of-phase tilt gives a much superior fit (Model with the out-of-phase tilt: $\chi^2 = 4.00$, wRp = 2.54%, Rp = 2.45%; Model with the in-phase tilt: $\chi^2 = 5.83$, wRp = 3.14%, Rp = 2.58%). In addition, as shown in Figure 5.7, only the model with the out-of-phase tilt can correctly simulate the superlattice peak at 2.33 Å. Therefore it is concluded that P3 adopts a tetragonal structure in space group *I*4/*mcm* with an $a^0a^0c^-/a^0a^0$-c^- tilting distortion. The observed, calculated and difference plots from the structural refinement in space group *I*4/*mcm* against neutron powder diffraction data are shown in Figure 5.8. Full details of the parameters from the refinements are shown in Table 5.4. The refined structure is shown in Figure 5.12.

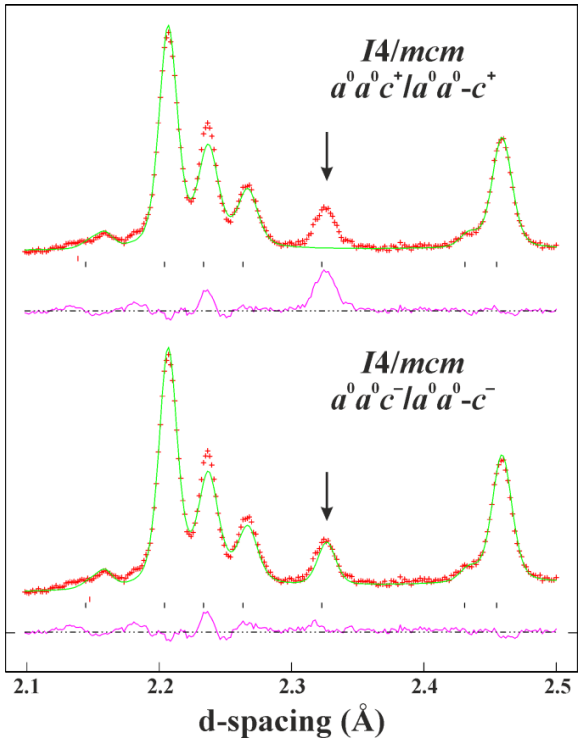


Figure 5.7. Observed, calculated and difference plots from the refinements of the *I*4/*mcm* models with $a^0a^0c^+/a^0a^0\text{-}c^+$ and $a^0a^0c^-/a^0a^0\text{-}c^-$ tilting distortions against the neutron diffraction data collected from $RbNdTa_2O_7$ at 973 K.

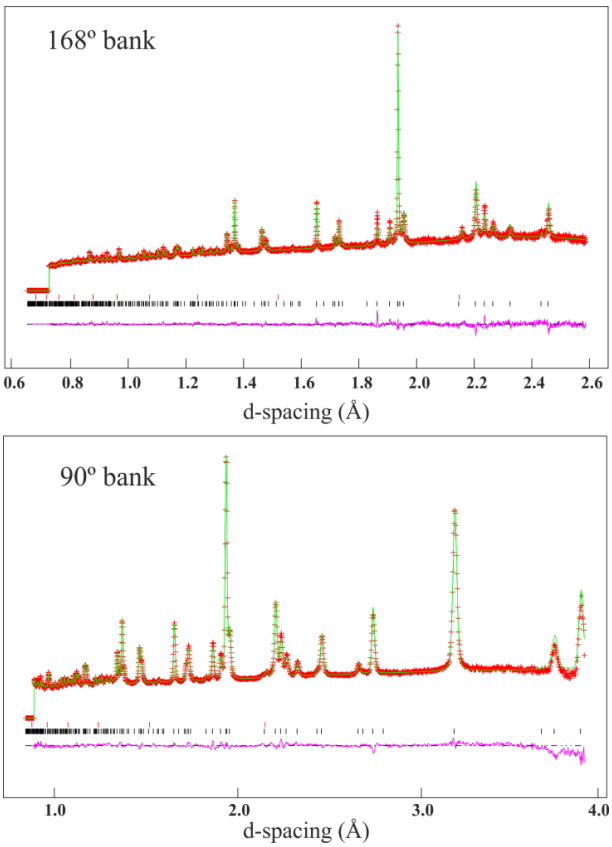


Figure 5.8. Observed, calculated and difference plots from the refinement of a structural model in space group *I*4/*mcm* against data collected from $RbNdTa_2O_7$ at 973 K. Vanadium was added as the secondary phase with red tick-marks.

Atom	site	*x*	*y*	*z*	U_{iso} (Å^3)
Rb(1)	4*d*	0	½	0	0.0840(10)
Nd(1)	4*b*	0	½	¼	0.0300(7)
Ta(1)	8*f*	0	0	0.8517(1)	0.0131(4)
O(1)	16*l*	0.7259(2)	0.2259(2)	0.3334(1)	0.0354(6)
O(2)	8*f*	0	0	0.9310(1)	0.0665(8)
O(3)	4*a*	0	0	¼	0.0872(13)
$RbNdTa_2O_7$ – space group *I*4/*mcm* (#140) *a* = 5.4730(2) Å, *b* = 5.4730(2) Å, *c* = 22.3602(10) Å, volume = 669.77(8) Å^3 Formula weight: 703.59 g mol^{-1}, Z = 4 Radiation source: Neutron Time of flight Temperature: 973 K χ^2 = 4.00, wRp = 2.54%, Rp = 2.45%					

Table 5.4. Parameters from the structural refinement of $RbNTa_2O_7$ against neutron powder diffraction data collected at 973 K.

5.3.2.3 Final phase transition of $RbNdTa_2O_7$ (P3 to P4)

A further neutron diffraction dataset was collected from $RbNdTa_2O_7$ at 1273 K and it shows that the superlattice [213] peak corresponding to doubling the *c* lattice parameter vanishes (Figure 5.9). This observation suggests that $RbNdTa_2O_7$ adopts a structure with an unexpanded *c* lattice at 1273 K, possibly an undistorted, *P*4/*mmm* structure. A model of the *P*4/*mmm* aristotype structure was then constructed and refined against the neutron diffraction data collected at 1273 K. The refinement gives good statistical and visual fits and no superlattice peak is observed (Figure 5.10). Therefore it is concluded that at 1273 K, $RbNdTa_2O_7$ adopts an undistorted, *P*4/*mmm* structure. The observed, calculated and difference plots from the structural refinement in space group *P*4/*mmm* against the neutron powder diffraction data collected at 1273 K are shown in Figure 5.10. Full details of the parameters from the refinements are shown in Table 5.5. The refined structure is shown in Figure 5.12.

Although there is a phase transition between 973 K and 1273 K, we are unable to identify the exact phase transition temperature from P3 to P4 as the sample reacted with the capillary when it was heated to approximately 973 K during the variable temperature synchrotron X-ray diffraction experiments.

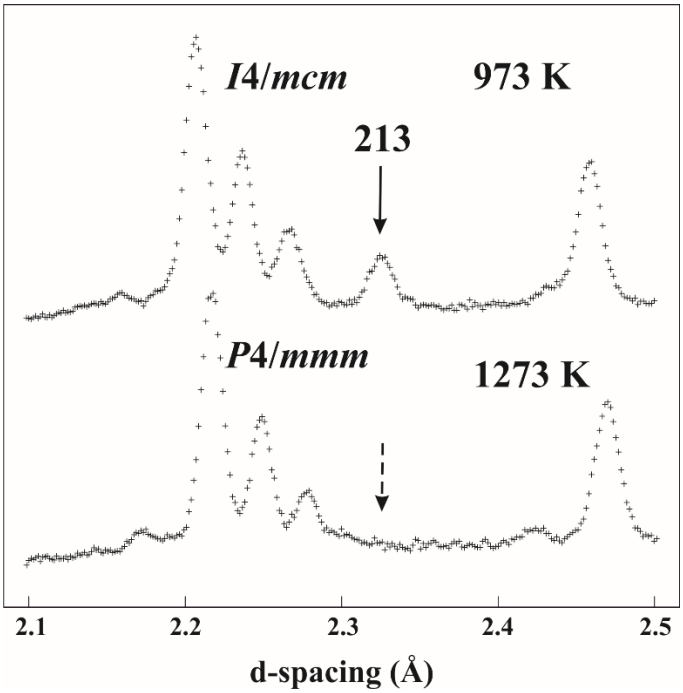


Figure 5.9. Temperature evolution of the [213] superlattice peak corresponding to the *c* lattice.

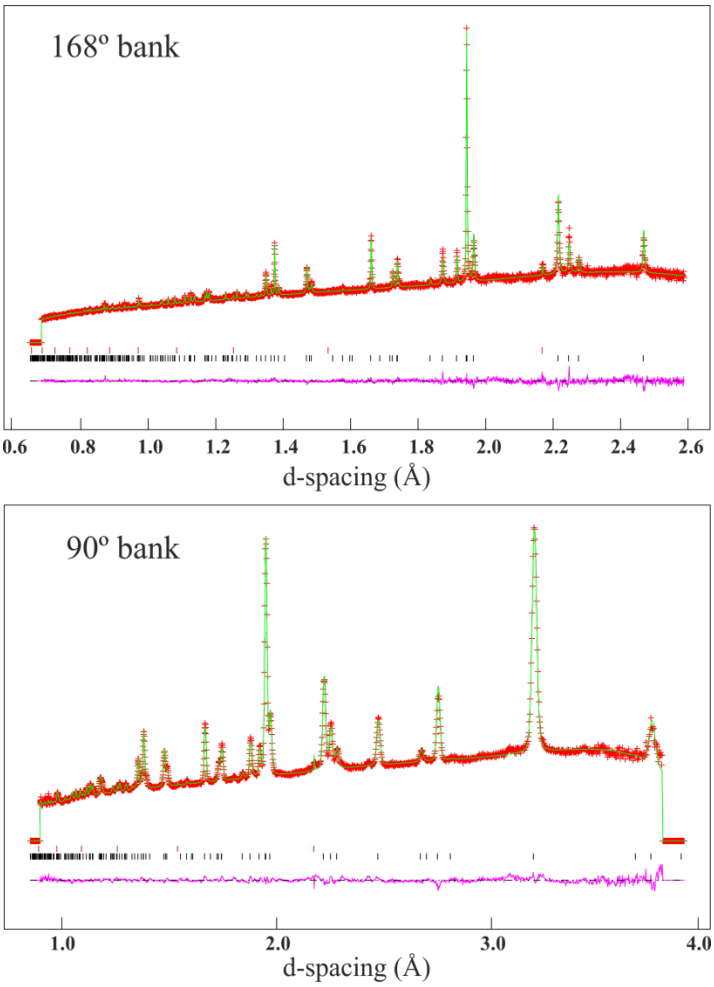


Figure 5.10. Observed, calculated and difference plots from the refinement of a structure model in space group *P*4/*mmm* against data collected from $RbNdTa_2O_7$ at 1273 K. Vanadium was added as the secondary phase with red tick-marks.

Atom	site	*x*	*y*	*z*	U_{iso} (Å^3)
Rb(1)	1*b*	0	0	½	0.1193(13)
Nd(1)	1*a*	0	0	0	0.0441(8)
Ta(1)	2*h*	½	½	0.2035(1)	0.0248(5)
O(1)	4*i*	0	½	0.1657(2)	0.0617(7)
O(2)	2*h*	½	½	0.3592(3)	0.0940(10)
O(3)	1*c*	½	½	0	0.0983(14)
$RbNdTa_2O_7$ – space group *P*4/*mmm* (#123) *a* = 3.8846(1) Å, *b* = 3.8846(1) Å, *c* = 11.2317(4) Å, volume = 169.49(2) Å^3 Formula weight: 703.59 g mol^{-1}, Z = 1 Radiation source: Neutron Time of flight Temperature: 1273 K χ^2 = 2.37, wRp = 2.08%, Rp = 2.01%					

Table 5.5. Parameters from the structural refinement of $RbNTa_2O_7$ against neutron powder diffraction data collected at 1273 K.

5.3.2.4 Summary of the phase transition behaviours of $RbNdTa_2O_7$

At ambient temperature, $RbNdTa_2O_7$ adopts a polar *I*2*cm* structure symmetry with an $a^-a^-c^+/-(a^-a^-c^+)$ tilting distortion. On heating, $RbNdTa_2O_7$ undergoes a phase transition at T ~ 500 K to adopt an $a^-b^0c^-/-(a^-b^0)c^-$ tilting distortion described in space group *Cmca* with an $a \sim b = 2a_p$, $c = 2c_p$ expanded unit cell. The intermediate *Cmca* phase is anti-polar, as shown in Figure 5.12. Although the Rb^+ and Ta^{5+} cations in the *Cmca* structure are displaced in a way to generate local electric dipoles, they cancel across the material. This polar to anti-polar phase transition is a first-order phase transition because there is no group/subgroup symmetry relation between the *I*2*cm* and *Cmca* structures. It should be noticed that the 'continuous' variation of lattice parameters around the phase transition temperature is due to the fact that they are obtained by fitting the data using a single-phase model although both the *I*2*cm* and *Cmca* phases exist (See Appendix 2.1 for more details). Further heating of $RbNdTa_2O_7$ results in another phase transition at T ~ 950 K to adopt an $a^0a^0c^-/a^0a^0\text{-}c^-$ tilting distortion described in space group *I*4/*mcm* with an $a = b = \sqrt{2}a_p$, $c = 2c_p$ cell expansion. The temperatures of the phase transitions were determined by tracking the normalized unit cell parameters of the phase, as shown in Figure 5.11. There is a final

phase transition between 973 K and 1273 K, leading to a high temperature phase with the undistorted *P*4/*mmm* structure. A schematic of the phase transitions is shown in Figure 5.12.

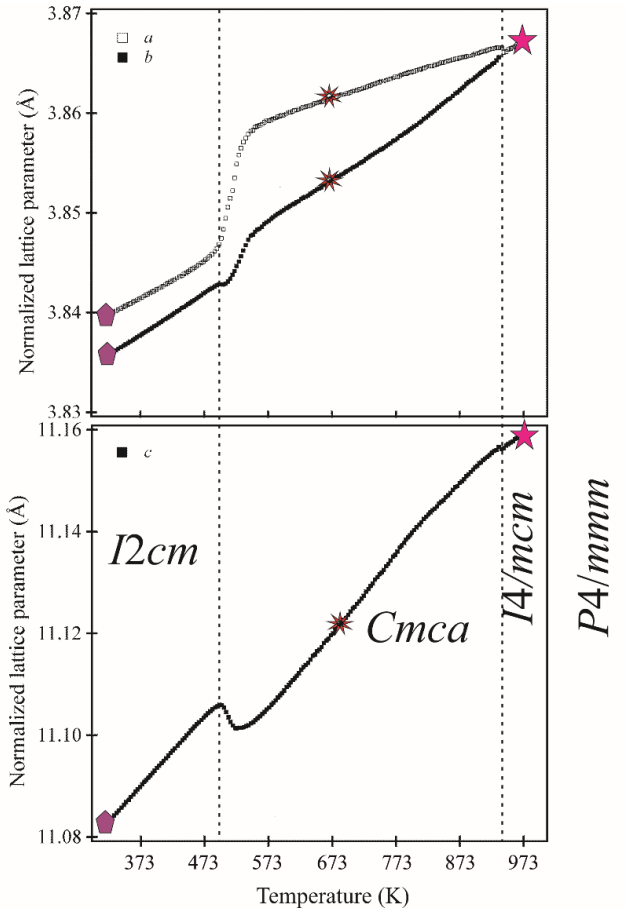


Figure 5.11. Temperature evolution of the normalised lattice parameters of $RbNdTa_2O_7$ determined from the variable temperature synchrotron X-ray diffraction experiments. Markers indicate the temperatures where neutron diffraction data were collected.

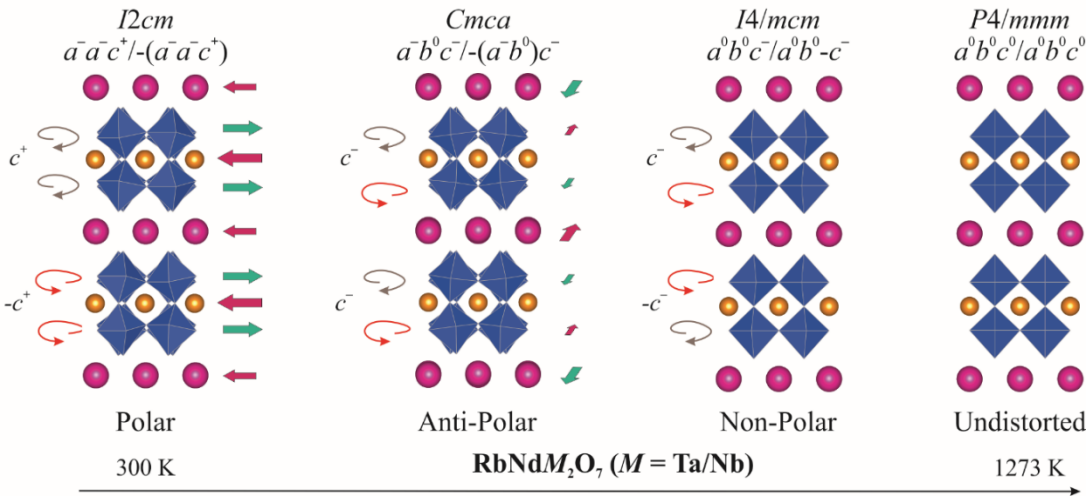


Figure 5.12. Phase transitions and the corresponding crystal structures of $RbNdTa_2O_7$ observed from high-resolution neutron powder diffraction data. Green and red arrows indicate the electric dipoles extracted from the refined cation displacements.

5.3.3 Phase transition behaviours of $RbNdNb_2O_7$

As a direct analogue, $RbNdNb_2O_7$ is expected to have a similar phase transition behaviour to $RbNdTa_2O_7$. High-resolution neutron powder diffraction and synchrotron X-ray diffraction data were collected at ambient temperature to check the sample purity. The refinement of the *I*2*cm* model against the diffraction data reveals that the sample used for variable temperature diffraction study was a single phase (Figure 5.13).

The *I*2*cm* model was then refined against the synchrotron X-ray diffraction data collected at higher temperatures. Refinements give good fits to the diffraction data collected from 300 K to 790 K. A close inspection of the synchrotron X-ray diffraction data collected between 723 K and 823 K reveals that the [110] and [112] peaks start to split at a temperature between 773 K and 798 K (Figure 5.14), indicating a phase transition from Q1 to Q2 at this temperature regime. The superlattice peaks [211], [121], [213] and [123], corresponding to the expansion of the *c* lattice parameter, persist during the phase transition. These observations are analogous to the first phase transition of $RbNdTa_2O_7$. High-resolution neutron diffraction data was collected at 823 K to probe the crystal structure of Q2. A model of *Cmca* with an $a^-b^0c^-/-(a^-b^0)c^-$ tilting distortion was constructed and refined against the neutron diffraction collected at 823 K. The refinement gives a good fit, as shown in Figure 5.15. Full details of the parameters from the refinements are shown in Table 5.6.

The *Cmca* model was then refined against the synchrotron X-ray diffraction data collected above 790 K. Sequential refinements give good statistical fits until 1025 K, at which point the sample reacted with the capillary. Figure 5.16 shows the normalized lattice parameters extracted from the refinements against the synchrotron X-ray diffraction data. It can be seen that *a* and *b* lattice parameters converge at approximately 865 K, indicating a possible transition from an orthorhombic phase (Q2) to a tetragonal phase (Q3). Another neutron diffraction dataset was collected from $RbNdNb_2O_7$ at 923 K to probe if Q3 is indeed

isostructural to P3 observed from $RbNdTa_2O_7$ (*I*4/*mcm* with an $a^0a^0c^-/a^0a^0\text{-}c^-$ tilting distortion). A model of the *I*4/*mcm* structure was constructed and refined against the neutron diffraction data collected from $RbNdNb_2O_7$ at 923 K. The refinement gives good statistical and visual fits (Figure 5.17), which confirms that Q3 adopts a distorted, *I*4/*mcm* structure with an $a^0a^0c^-/a^0a^0\text{-}c^-$ tilting distortion. Full details of the parameters from the refinements are shown in Table 5.7.

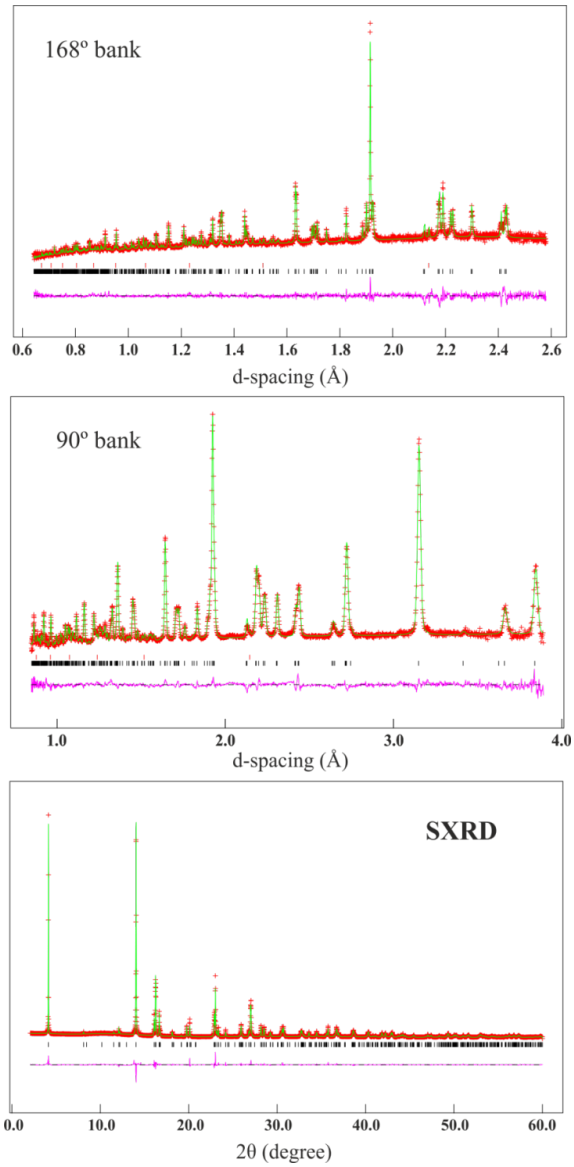


Figure 5.13. Observed, calculated and difference plots from the refinement of a structure model in space group *I*2*cm* against NPD and SXRD data collected from $RbNdNb_2O_7$ at ambient temperature. Top panel shows the refinement from NPD 168° bank, middle panel from NPD 90° bank, bottom panel from the synchrotron X-ray diffraction data. Vanadium was added as the secondary phase with red tick-marks. No secondary phase was found.

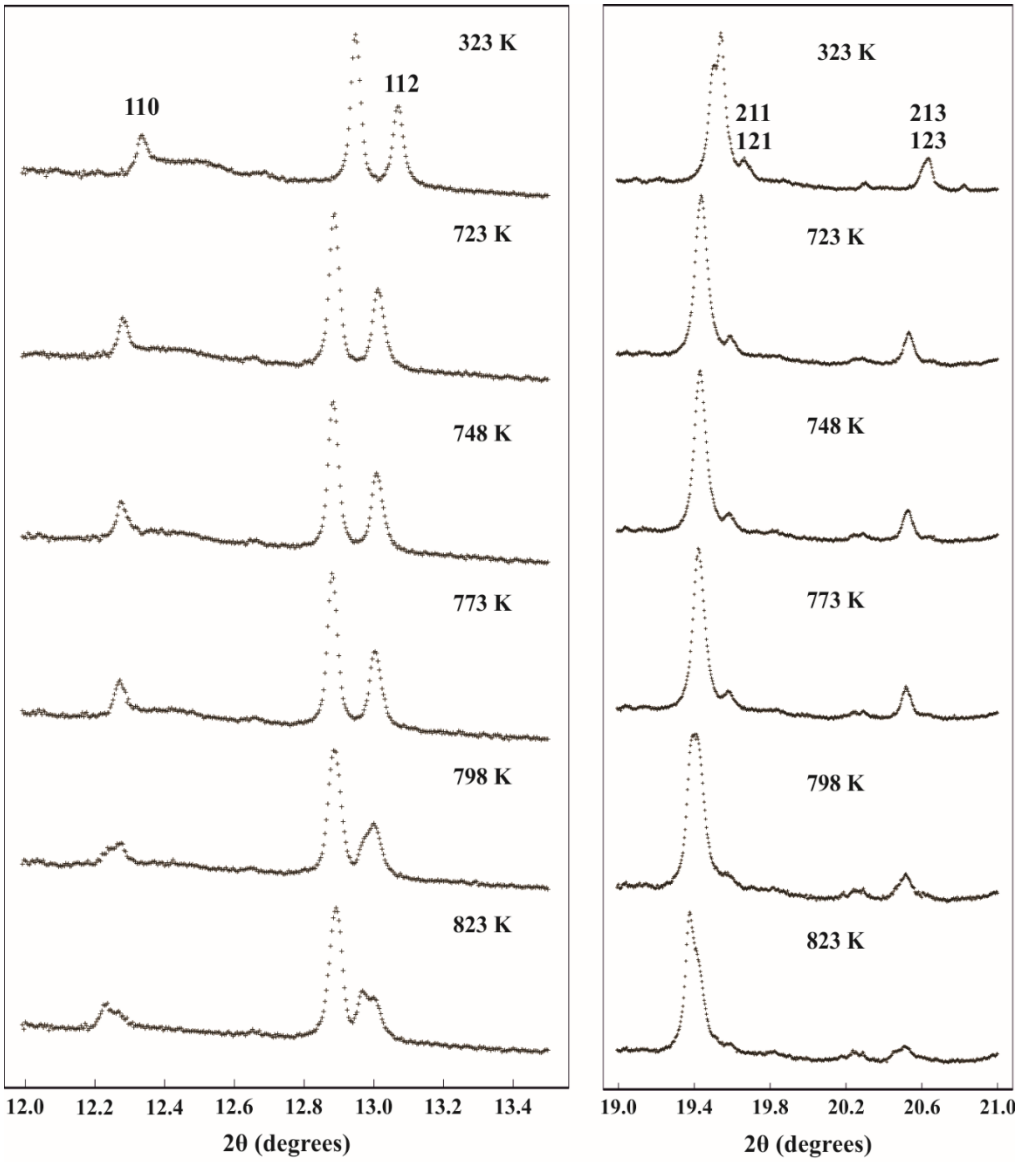


Figure 5.14. Temperature evolution of some reflections of $RbNdNb_2O_7$ upon heating. It can be observed that [110] and [112] peaks split between 773 K and 798 K. Superlattice peaks [211], [121], [213] and [123,] corresponding to doubling the *c* lattice, persist during the phase transition. These observations are consistent with the first phase transition of $RbNdTa_2O_7$ (Figure 5.2 and 5.3).

Due to the experiment time limit, no further neutron diffraction data were collected from $RbNdNb_2O_7$ at higher temperatures. However, based on the analysis of $RbNdTa_2O_7$, it is expected that there is a further phase transition of $RbNdNb_2O_7$ from *I*4/*mcm* to *P*4/*mmm*. Therefore, it is proposed that $RbNdNb_2O_7$ follows the same phase transition sequence as $RbNdTa_2O_7$: *I*2*cm* ($a^-a^-c^+$/-($a^-a^-c^+$)) → *Cmca* ($a^-b^0c^-$/-(a^-b^0)c^-) → *I*4/*mcm* ($a^0a^0c^-$/a^0a^0-c^-) → *P*4/*mmm* (Figure 5.12). Unlike the case of $RbNdTa_2O_7$, in which the coexistence of the polar and antipolar phases are clearly observed at the first phase transition temperature, the

two-phase coexistence for $RbNdNb_2O_7$ cannot be easily observed and hence not shown in Appendix 2.

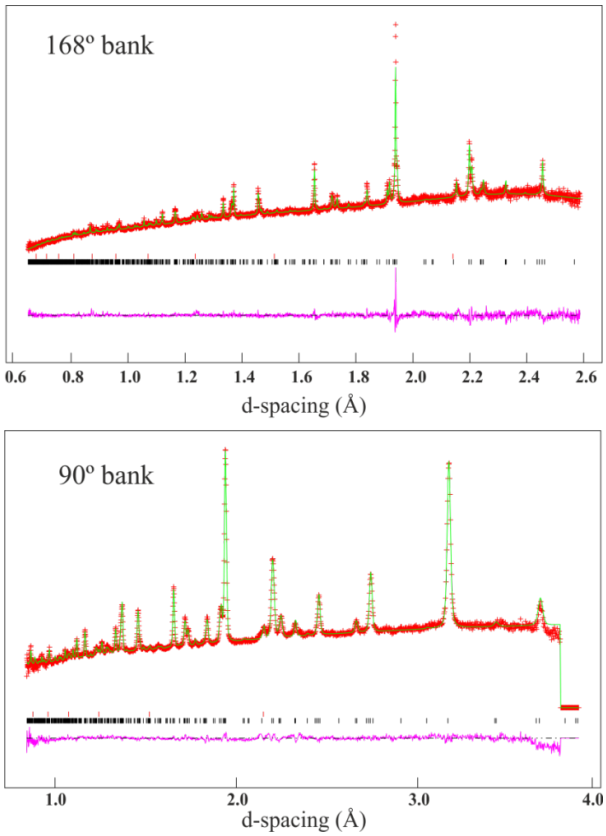


Figure 5.15. Observed, calculated and difference plots from the refinement of a structure model in space group *Cmca* against the neutron diffraction data collected from $RbNdNb_2O_7$ at 823 K. Vanadium was added as the secondary phase for the neutron refinements with red tick-marks.

Atom	site	*x*	*y*	*z*	U_{iso} (Å^3)
Rb(1)	8*f*	0	0.2384(29)	0.2560(7)	0.0575(28)
Nd(1)	8*f*	0	0.2504(11)	0.9984(6)	0.0267(13)
Nb(1)	16*g*	0.7487(7)	0.9992(13)	0.1031(1)	0.0188(9)
O(1)	8*f*	0	0.4952(35)	0.5745(5)	0.0376(42)
O(2)	8*f*	0	0.4748(35)	0.0942(11)	0.1060 (82)
O(3)	16*g*	0.2531(30)	0.2459(22)	0.9142(5)	0.0303(20)
O(4)	16*g*	0.7871(8)	0.0195(17)	0.1820(2)	0.0396(20)
O(5)	8*d*	0.7280(25)	0	0	0.1012(34)
$RbNdTa_2O_7$ – space group *Cmca* (#64) *a* = 7.7505(8) Å, *b* = 7.7523(8) Å, *c* = 22.0565(14) Å, volume = 1325.26(24) Å^3 Formula weight: 527.51 g mol^{-1}, Z = 8 Radiation source: Neutron Time of flight Temperature: 823 K χ^2 = 2.29, wRp = 2.25%, Rp = 2.19%					

Table 5.6. Parameters from the structural refinement of $RbNdNb_2O_7$ against neutron powder diffraction data collected at 823 K. The big errors of the lattice parameters and thermal parameters are attributed to the fact that it is likely there are multiple phases coexisting at 823 K.

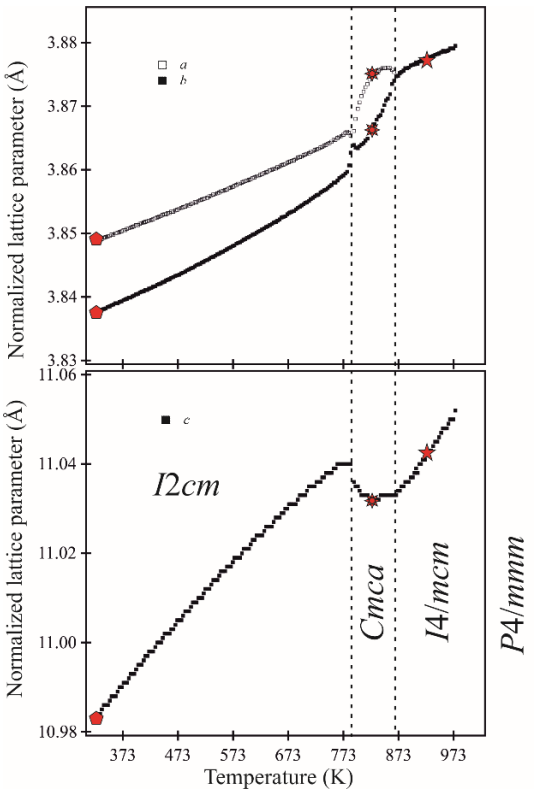


Figure 5.16. Temperature evolution of the lattice parameters of $RbNdNb_2O_7$ determined from the analysis of variable temperature synchrotron X-ray diffraction data. Markers indicate the temperatures where neutron diffraction data were collected.

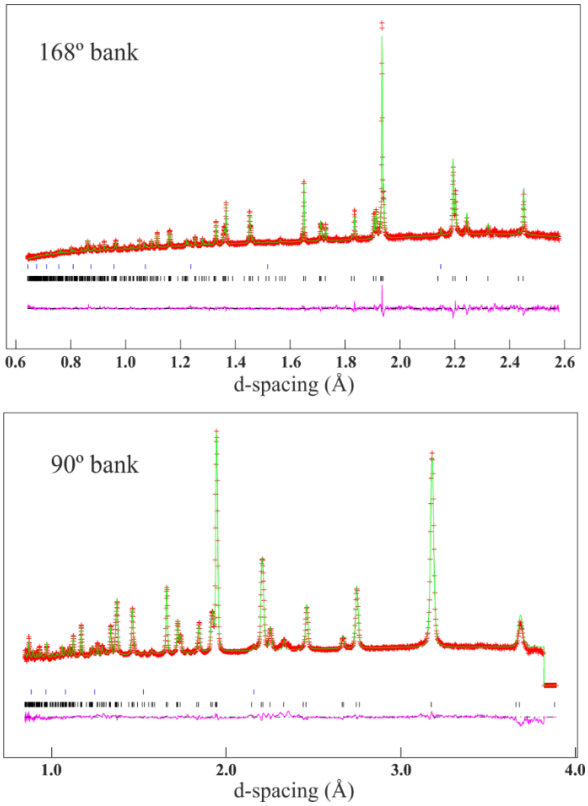


Figure 5.17. Observed, calculated and difference plots from the refinement of a structure model in space group *I*4/*mcm* against the neuron diffraction data collected from $RbNdNb_2O_7$ at 923 K. Vanadium was added as the secondary phase with blue tick-marks.

Atom	site	*x*	*y*	*z*	U_{11} (Å^2)	U_{22} (Å^2)	U_{33} (Å^2)
Rb(1)	4*d*	0	½	0	0.0700(16)	0.0700(16)	0.1111(34)
Nd(1)	4*b*	0	½	¼	0.0278(9)	0.0278(9)	0.0292(16)
Nb(1)	8*f*	0	0	0.8521(1)	0.0081(5)	0.0081(5)	0.0350(11)
O(1)	16*l*	0.7692(2)	0.2692(2)	0.3339(1)	0.0317(7)	0.0317(7)	0.0828(20)
O(2)	8*f*	0	0	0.9319(1)	0.0972(15)	0.0972(15)	0.0334(20)
O(3)	4*a*	0	0	¼	0.1083(22)	0.1083(22)	0.0826(43)
$RbNdNb_2O_7$ – space group *I*4/*mcm* (#140) *a* = 5.4893(2) Å, *c* = 22.0938(7) Å, volume = 665.73(6) Å^3 Formula weight: 527.51 g mol^{-1}, Z = 4 Radiation source: Neutron Time of flight Temperature: 923 K χ^2 = 4.40, wRp = 2.72%, Rp = 2.41%							

Table 5.7. Parameters from the structural refinement of $RbNdNb_2O_7$ against neutron powder diffraction data collected at 923 K.

5.3.4 Phase transition behaviours of $CsNdTa_2O_7$

5.3.4.1 The 1st phase transition – ferroelectric (R1) to paraelectric (R2)

As demonstrated in Chapter 3, $CsNdTa_2O_7$ adopts a polar $P2_1am$ structure with an $a^-a^-c^+$ tilting distortion at ambient temperature. High-resolution neutron powder diffraction and synchrotron X-ray diffraction data were collected from $CsNdTa_2O_7$ at ambient temperature to check the sample purity. Refinement of the $P2_1am$ symmetry model against the diffraction data gives good statistical and visual fits and no secondary phase was found (Figure 5.18). The $P2_1am$ model was then refined against the synchrotron X-ray diffraction data collected at higher temperatures. The refinements give good fits to the diffraction data collected between 300 K and 330 K, while above 330 K the refinement gives poor fits, suggesting a possible phase transition from R1 to R2.

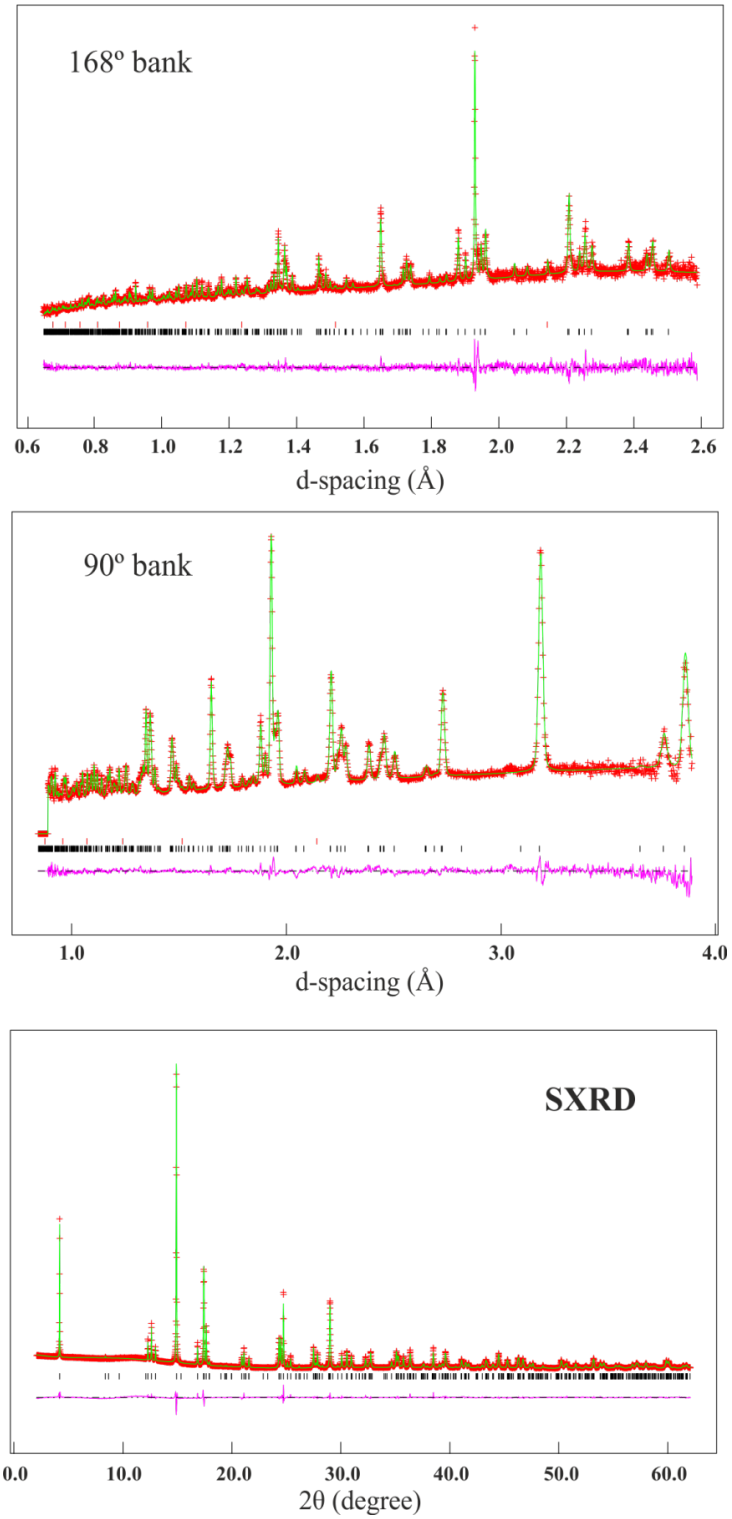


Figure 5.18. Observed, calculated and difference plots from the refinement of a structure model in space group *P*2$_1$*am* against NPD and SXRD data collected from $CsNdTa_2O_7$ at ambient temperature. Top panel shows the refinement to NPD 168° bank, middle panel to NPD 90° bank, bottom panel to the synchrotron X-ray diffraction data. Vanadium was added as the secondary phase with red tick-marks. No secondary phase was found.

Close inspection of the synchrotron X-ray diffraction data reveals that the [110] and [111] peaks split at approximately 330 K (Figure 5.19). In addition, no superlattice peak corresponding to expanding the *c* lattice is observed. Combining these observations suggests that R2 adopts a different distorted structure, with a further expanded unit cell with $a' \sim b' = \sqrt{2}\, a = 2a_p$, $c' = c_p$ or a monoclinic cell with $a' \sim b' = a = \sqrt{2}\, a_p$, $c' = c_p$ and $\gamma \neq 90°$. Five symmetry models in Table 5.1 have the correct unit cell sizes for R2: *P*-1 #2, *Pm* #6, *P*2/*m* #10, *C*2/*m* #12, *C*2*mm* #38 and *Cmmm* #65.

In order to probe the crystal structure of R2, high-resolution neutron diffraction data were collected at 473 K. This temperature was chosen to ensure the collected diffraction data were corresponding to R2 only rather than a mixture of R1 and R2. In addition, no phase transition is observed from the synchrotron X-ray diffraction data collected between 330 K and 473 K. Therefore 473 K was deemed an appropriate temperature to study R2. Symmetry models of *P*-1 #2, *Pm* #6, *P*2/*m* #10, *C*2/*m* #12, *C*2*mm* #38 and *Cmmm* #65 were constructed and refined against the neutron diffraction data. Fitting statistics show that the models of *P*-1 ($a^-b^-c^-$) and *C*2/*m* ($a^-b^0c^-$) achieve the best fits (Table 5.8). These two structures are very similar in terms of the octahedral tilting distortions. The *C*2/*m* structure can be considered as a special case of the *P*-1 structure where the magnitude of the '*b*' tilt is zero. A close look at the refined *P*-1 structure reveals that the magnitude of the '*b*' tilt is effectively zero, suggesting Q2 adopts the *C*2/*m* structure.

It is then concluded that the first phase transition of $CsNdTa_2O_7$ occurs at approximately 330 K and results in a *C*2/*m* structure with an $a^-b^0c^-$ tilting distortion. The observed, calculated and difference plots from the structural refinement in space group *C*2/*m* against neutron diffraction data are shown in Figure 5.20. Full details of the parameters from the refinements are shown in Table 5.9. The refined structure is shown in Figure 5.23.

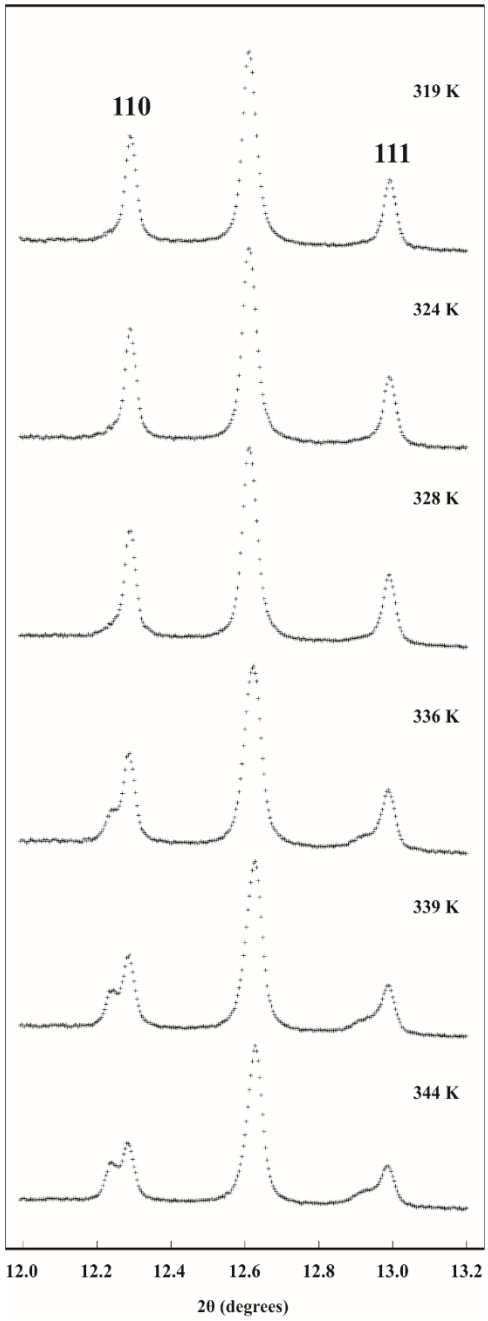


Figure 5.19. Temperature evolution of some reflections from $CsNdTa_2O_7$ upon heating. It can be observed that the [110] and [111] peaks start to split between 328 K and 336 K.

space group	Glazer tilt	Irrep	χ^2	wRp (%)	Rp (%)
P-1 (2)	$a^-b^-c^-$	$M_4^- \bullet M_5^-$ (a; b,c)	3.42	2.08	2.02
Pm (6)	$a^-b^-c^+$	$M_2^+ \bullet M_5^-$ (a; b,c)	9.07	3.39	2.84
*P*2/*m* (10)	$a^-b^-c^0$	M_5^- (a, b)	9.98	3.56	2.86
*C*2/*m* (12)	$a^-b^0c^-$	$M_4^- \bullet M_5^-$ (a; b,b)	3.61	2.14	2.05
*C*2*mm* (38)	$a^-b^0c^+$	$M_2^+ \bullet M_5^-$ (a; b,b)	9.29	3.44	2.79
Cmmm (65)	$a^-b^0c^0$	M_5^- (a,a)	10.23	3.61	2.88

Table 5.8. Fitting statistics from the structural refinement of different symmetry models against the neutron diffraction collected from $CsNdTa_2O_7$ at 473 K.

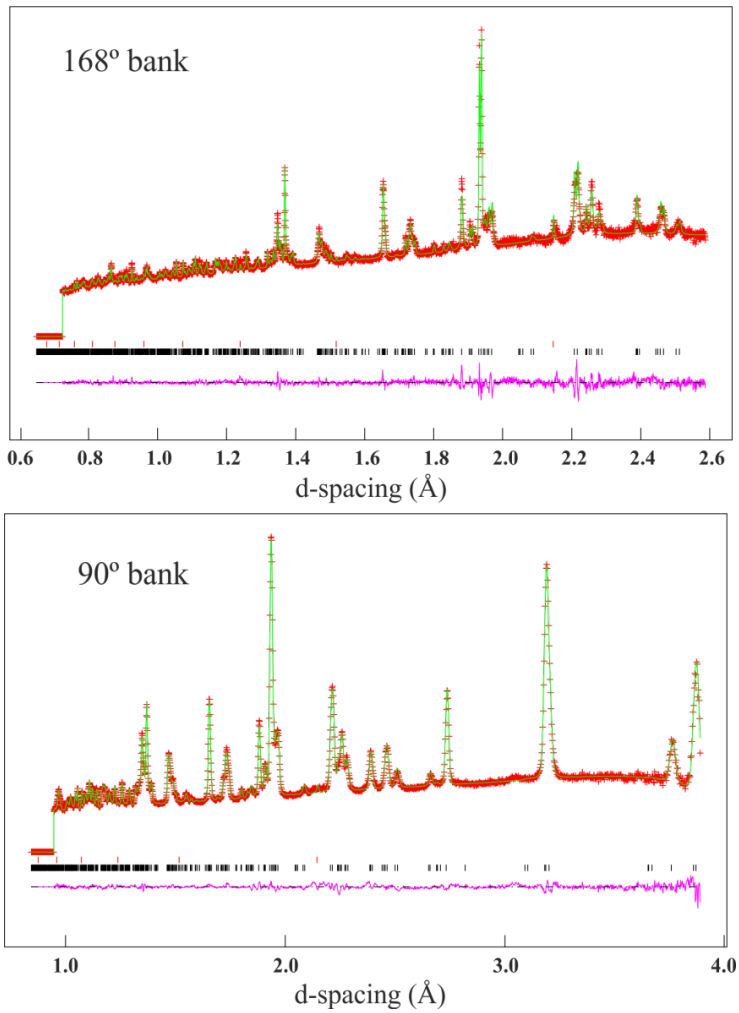


Figure 5.20. Observed, calculated and difference plots from the refinement of a structure model in space group *C*2/*m* against data collected from $CsNdTa_2O_7$ at 473 K. Vanadium was added as the secondary phase with red tick-marks.

Atom	site	*x*	*y*	*z*	U_{iso} (Å^3)
Cs(1)	4*i*	0.2594(6)	0	0.4914(7)	0.0268(8)
Nd(1)	4*i*	0.2583(5)	0	0.0009(5)	0.0133(5)
Ta(1)	8*j*	0.0049(3)	0.2501(3)	0.1989(1)	0.0034(4)
O(1)	4*i*	0.5355(6)	0	0.1878(4)	0.0169(13)
O(2)	4*i*	0.9873(6)	0	0.1428(4)	0.0171(12)
O(3)	8*j*	0.2448(4)	0.2769(4)	0.8384(3)	0.0221(9)
O(4)	8*j*	0.9990(4)	0.2239(4)	0.3550(1)	0.0248(7)
O(5)	4*g*	0	0.7077(5)	0	0.0227(10)
$CsNdTa_2O_7$ – space group *C*2/*m* (#12) *a* = 7.7513(3) Å, *b* = 7.7274(3) Å, *c* = 11.2875(4) Å, β = 90.367(2)° Volume = 676.08(7) Å^3 Formula weight: 751.03 g mol^{-1}, Z = 4 Radiation source: Neutron Time of flight Temperature: 473 K χ^2 = 3.61, wRp = 2.14%, Rp = 2.05%					

Table 5.9. Parameters from the structural refinement of $CsNTa_2O_7$ against neutron powder diffraction data collected at 473 K.

5.3.4.2 The 2nd phase transition of $CsNdTa_2O_7$ – Simultaneous loss of a^- and c^- tilts

Having established that R2 adopts the *C*2/*m* structure, the *C*2/*m* symmetry model was refined against the synchrotron X-ray diffraction data collected above 330 K. Sequential refinements give good fits until 1025 K, at which temperature the sample deteriorated due to a reaction with the capillary. A close look at the refined lattice parameters reveals that *a* and *b* lattice parameters converge at approximately 820 K, suggesting a possible phase transition to a tetragonal phase R3.

Neutron diffraction data was hence collected at 923 K to probe the crystal structure of R3. Figure 5.21 shows a comparison of the neutron diffraction data collected at 923 K and 473 K. It can be seen that a series of split peaks converge and peaks corresponding to the expansion of the *a*/*b* lattice parameters vanish when the temperature is elevated. These observations suggest that at 923 K, R3 adopts a structure with higher symmetry than R2.

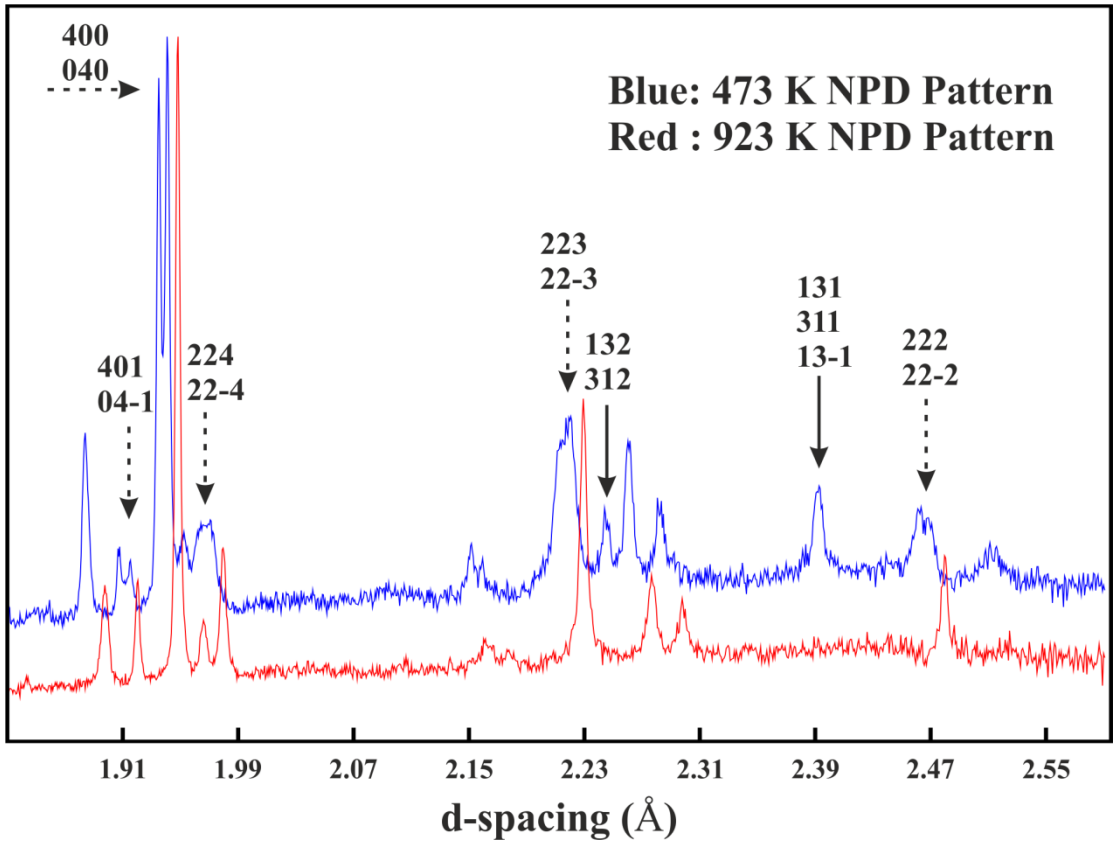


Figure 5.21. Comparison of the neutron diffraction patterns (back-scattering bank) collected at 473 K and 923 K from $CsNdTa_2O_7$. Peaks labelled with solid arrows for the 473 K data disappear when the sample was heated to 923 K; Split peaks labelled with dashed arrows converge at 923 K.

Since no superlattice peak was observed from the neutron diffraction pattern collected at 923 K, an aristotype *P*4/*mmm* symmetry model was constructed and refined against the neutron diffraction data. The refinement gives good statistical and visual fits. It is then concluded that $CsNdTa_2O_7$ adopts a *P*4/*mmm* structure at 923 K. The observed, calculated and difference plots from the structural refinement are shown in Figure 5.22. Full details of the parameters from the refinements are shown in Table 5.10. The refined structure is shown in Figure 5.23. Since the phase transition temperature is deemed to be 820 K and the neutron diffraction data was collected at 923 K, the synchrotron X-ray diffraction data collected between 820 K and 923 K were carefully examined and no evidence of the intermediate phase is spotted. The final phase transition of $CsNdTa_2O_7$ is deemed to occur at approximately 820 K, leading to a high temperature phase, R3, with an aristotype *P*4/*mmm* structure.

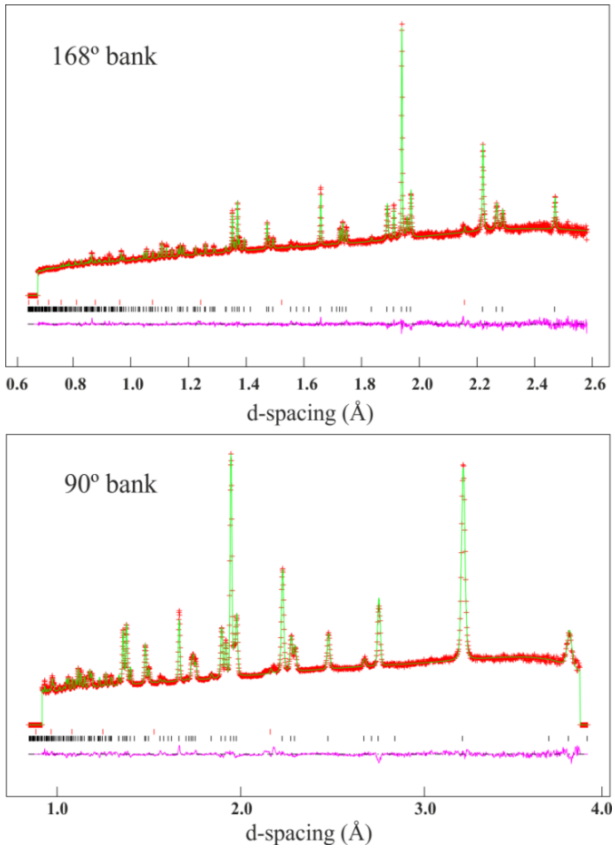


Figure 5.22. Observed, calculated and difference plots from the refinement of a structure model in space group *P*4/*mmm* against data collected from $CsNdTa_2O_7$ at 923 K. Vanadium was added as the secondary phase with red tick-marks.

Atom	site	*x*	*y*	*z*	U_{iso} (Å^3)
Cs(1)	1*b*	0	0	½	0.0655(11)
Nd(1)	1*a*	0	0	0	0.0237(6)
Ta(1)	2*h*	½	½	0.1973(1)	0.0115(4)
O(1)	4*i*	0	½	0.1619(1)	0.0452(5)
O(2)	2*h*	½	½	0.3531(2)	0.0602(8)
O(3)	1*c*	½	½	0	0.0741(11)
$CsNdTa_2O_7$ – space group *P*4/*mmm* (#123) *a* = 3.8898(1) Å, *b* = 3.8898(1) Å, *c* = 11.3665(4) Å, volume = 171.99(2) Å^3 Formula weight: 751.03 g mol^{-1}, Z = 1 Radiation source: Neutron Time of flight Temperature: 923 K χ^2 = 3.63, wRp = 2.44%, Rp = 2.02%					

Table 5.10. Parameters from the structural refinement of $CsNTa_2O_7$ against neutron powder diffraction data collected at 923 K.

5.3.4.3 Summary of the phase transition behaviours of $CsNdTa_2O_7$

$CsNdTa_2O_7$ adopts a polar *P*2$_1$*am* structure with an $a^-a^-c^+$ tilting distortion at ambient temperature. The first phase transition occurs at approximately 330 K, leading to an anti-polar phase in space group *C*2/*m* with an $a^-b^0c^-$ tilting distortion. There is a further phase transition at approximately 820 K to the aristotype, *P*4/*mmm* structure. A schematic of the phase transitions of $CsNdTa_2O_7$ is shown in Figure 5.23. The phase transition temperatures were determined by tracking the normalized lattice parameters as a function of temperature (Figure 5.24). The polar to non-polar transition is a first-order phase transition, as there is no group/subgroup symmetry relation between the *P*2$_1$*am* and *C*2/*m* structures. A close inspection of synchrotron X-ray diffraction data at around 330 K reveals the coexistence of *P*2$_1$*am* and *C*2/*m* phases (Appendix 2.2). Similar to the case of $RbNdM_2O_7$, It should be noticed that the 'continuous' variation of lattice parameters during the first phase transition is due to the fact that they are obtained by fitting the data using a single-phase model (and it is the same for the analysis of $CsNdNb_2O_7$ in Section 5.3.5 and Appendix 2.3) . Attempts of two-phase refinement never yielded stable and satisfying results.

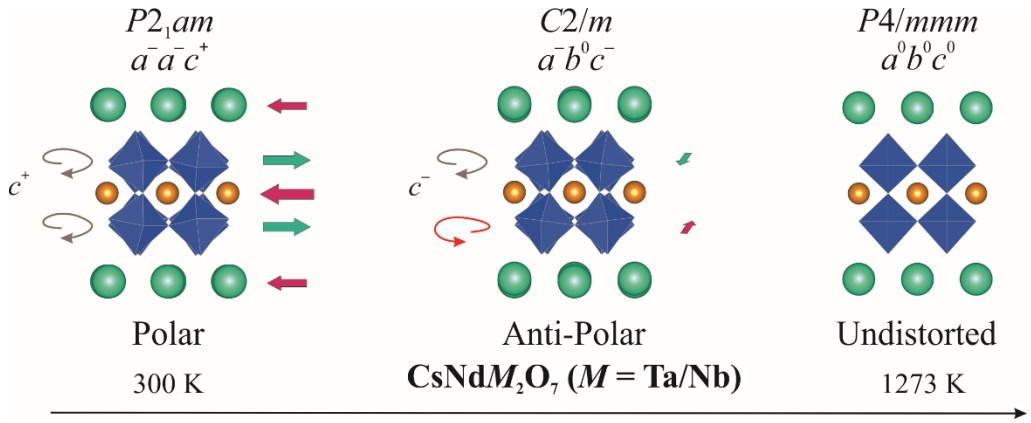


Figure 5.23. Phase transitions and the corresponding crystal structures of $CsNdTa_2O_7$ observed from high-resolution neutron powder diffraction data. Green and red arrows indicate the electric dipoles extracted from the refined cation displacements.

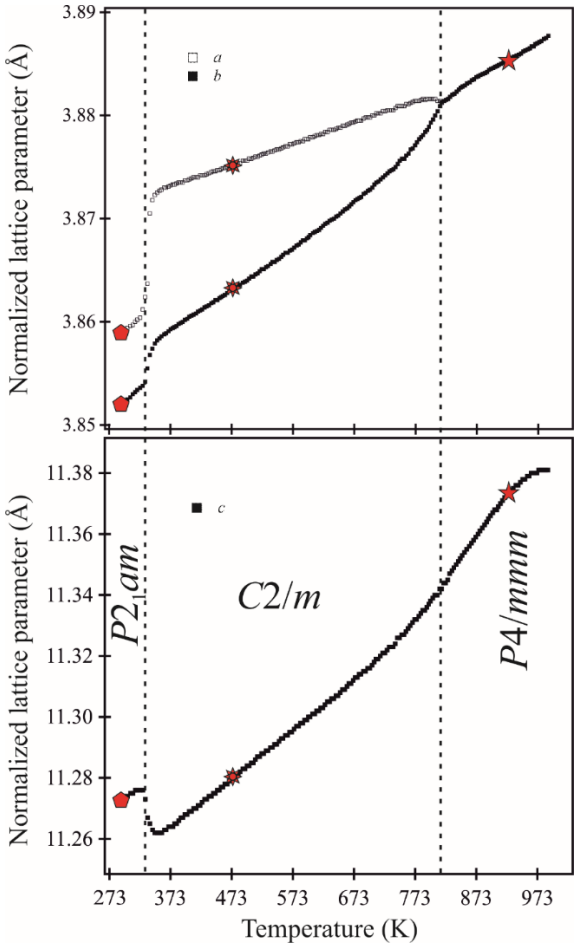


Figure 5.24. Temperature evolution of the lattice parameters for $CsNdTa_2O_7$ determined from the variable temperature synchrotron X-ray diffraction experiments. Markers indicate the temperatures where neutron diffraction data were collected.

5.3.5 Phase transition behaviours of $CsNdNb_2O_7$

As a direct analogue, $CsNdNb_2O_7$ is expected to follow a similar phase transition sequence with $CsNdTa_2O_7$. High-resolution neutron powder diffraction data and the synchrotron X-

ray diffraction data were collected from $CsNdNb_2O_7$ at ambient temperature to check the purity of the sample used for the variable temperature study. The refinement of the $P2_1am$ symmetry model reveals that the sample was a pure, single phase (Figure 5.25). Full details of the parameters from the refinements are shown in Table 5.11.

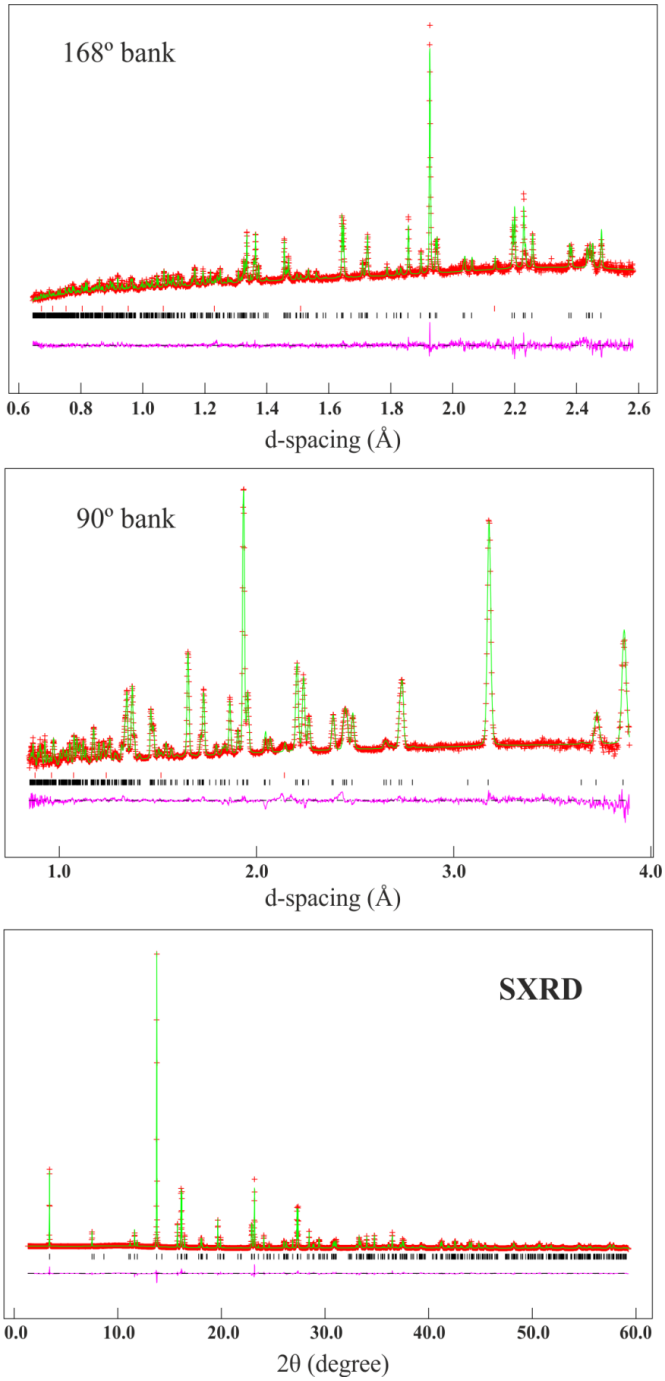


Figure 5.25. Observed, calculated and difference plots from the refinement of a structure model in space group $P2_1am$ against the NPD and SXRD data collected from $CsNdNb_2O_7$ at ambient temperature. Top panel shows the refinement plot from NPD 168° bank, middle panel from NPD 90° bank, bottom panel from t synchrotron X-ray diffraction. Vanadium was added as the secondary phase with red tick-marks. No secondary phase is found in the sample.

Atom	site	*x*	*y*	*z*	U_{iso} (Å^3)
Cs(1)	2*b*	0.2487(12)	0.2675(8)	½	0.0129(7)
Nd(1)	2*a*	0.2645(7)	0.2564(5)	0	0.0062(6)
Nb(1)	4*c*	0.2460(6)	0.7529(4)	0.2021(1)	0.0025(4)
O(1)	4*c*	0.2424(8)	0.7992(4)	0.3563(2)	0.0096(5)
O(2)	4*c*	0.0052(8)	0.0233(7)	0.1440(2)	0.0141(6)
O(3)	4*c*	0.4331(5)	0.4561(6)	0.1897(2)	0.0149(7)
O(4)	2*a*	0.2194(10)	0.6795(6)	0	0.0149(10)
$CsNdNb_2O_7$ – space group $P2_1am$ (#26) a = 5.4704(1) Å, b = 5.4464(1) Å, c = 11.1655(3) Å, volume = 332.66(2) Å^3 Formula weight: 574.95 g mol^{-1}, Z = 2 Radiation source: Neutron Time of flight Temperature: 298 K χ^2 = 2.38, wRp = 3.00%, Rp = 2.84%					

Table 5.11. Parameters from the structural refinement of $CsNdNb_2O_7$ against neutron powder diffraction data collected at ambient temperature.

Refining the $P2_1am$ model against the synchrotron X-ray diffraction data collected between 300 K and 625 K gives good fits. Figure 5.26 shows that the [110] and [111] peaks start to split above 625 K, suggesting a phase transition from S1 to S2. In addition, no superlattice peak corresponding to the expansion of the *c* lattice is observed above 625 K. These observations are analogous to the case of the first phase transition of $CsNdTa_2O_7$. High-resolution neutron diffraction data were collected from $CsNdNb_2O_7$ at 723 K to probe the crystal structure of S2. Similar structural analysis to $CsNdTa_2O_7$, as demonstrated in Section 5.4.3.1, was performed and it is concluded that S2 adopts an anti-polar *C*2/*m* structure with an $a^-b^0c^-$ tilting distortion. The observed, calculated and difference plots from the structural refinement against the neutron data collected at 723 K are shown in Figure 5.27. Full details of the parameters from the refinements are shown in Table 5.12.

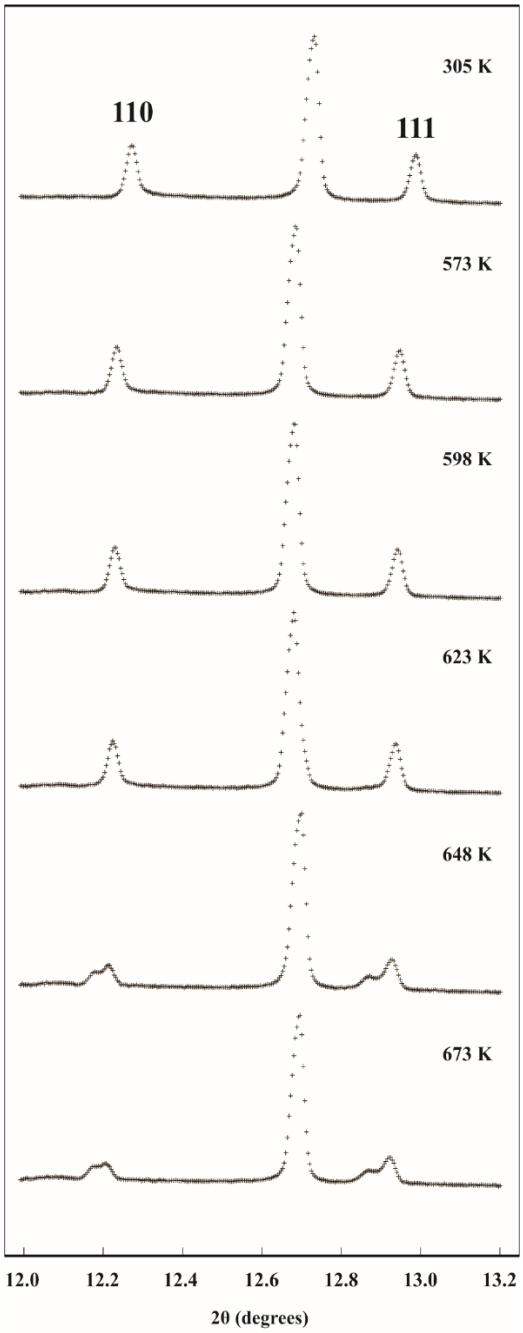


Figure 5.26. Temperature evolution of some reflections from $CsNdNb_2O_7$ upon heating. It can be observed that [110] and [111] peaks split between 623 K and 648 K.

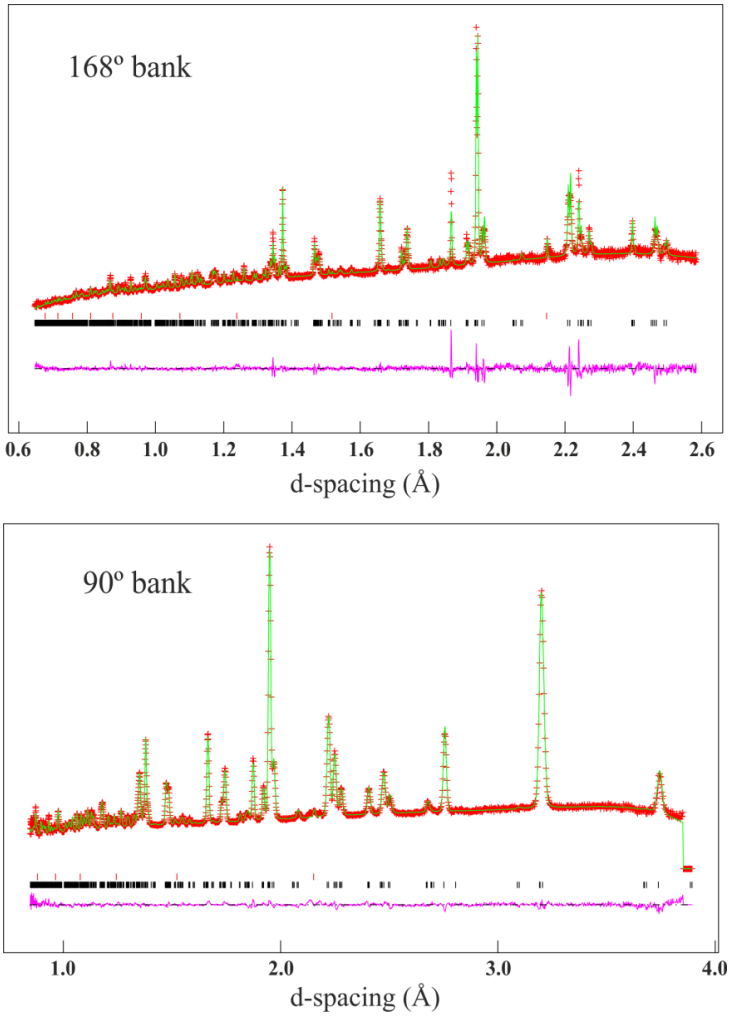


Figure 5.27. Observed, calculated and difference plots from the refinement of a structure model in space group *C*2/*m* against data collected from $CsNdNb_2O_7$ at 723 K. Vanadium was added as the secondary phase with red tick-marks.

Atom	site	*x*	*y*	*z*	U_{iso} (Å^3)
Cs(1)	4*i*	0.2585(9)	0	0.4881(8)	0.0436(11)
Nd(1)	4*i*	0.2583(6)	0	0.0028(6)	0.0178(6)
Nb(1)	8*j*	0.0033(3)	0.2504(4)	0.1994(1)	0.0075(4)
O(1)	4*i*	0.5302(8)	0	0.1893(5)	0.0258(17)
O(2)	4*i*	0.9922(8)	0	0.1437(5)	0.0186(14)
O(3)	8*j*	0.2465(6)	0.2727(7)	0.8378(4)	0.0370(14)
O(4)	8*j*	0.0003(6)	0.2244(6)	0.3555(2)	0.0398(9)
O(5)	4*g*	0	0.7125(8)	0	0.0498(15)
$CsNdTa_2O_7$ – space group *C*2/*m* (#12) *a* = 7.7873(2) Å, *b* = 7.7702(2) Å, *c* = 11.2142(4) Å, β = 90.259(2)° Volume = 678.55(6) Å^3 Formula weight: 574.95 g mol^{-1}, Z = 4 Radiation source: Neutron Time of flight Temperature: 723 K χ^2 = 3.46, wRp = 2.23%, Rp = 2.09%					

Table 5.12. Parameters from the structural refinement of $CsNdNb_2O_7$ against neutron powder diffraction data collected at 723 K.

The *C*2/*m* symmetry model was then refined against the synchrotron X-ray diffraction collected above 723 K. Tracking the refined parameters reveals that *a* and *b* lattice parameters converge at approximately 800 K, suggesting a possible phase transition towards a tetragonal phase. A further set of neutron diffraction data was collected from $CsNdNb_2O_7$ at 873 K. Refining the aristotype, *P*4/*mmm* symmetry model against the neutron diffraction data collected at 873 K gives good statistical and visual fits and no superlattice peak is found (Figure 5.29). Full details of the parameters from the refinements are shown in Table 5.13. Therefore it is concluded that the final phase transition of $CsNdNb_2O_7$ occurs at 800 K, leading to the undistorted, *P*4/*mmm* structure.

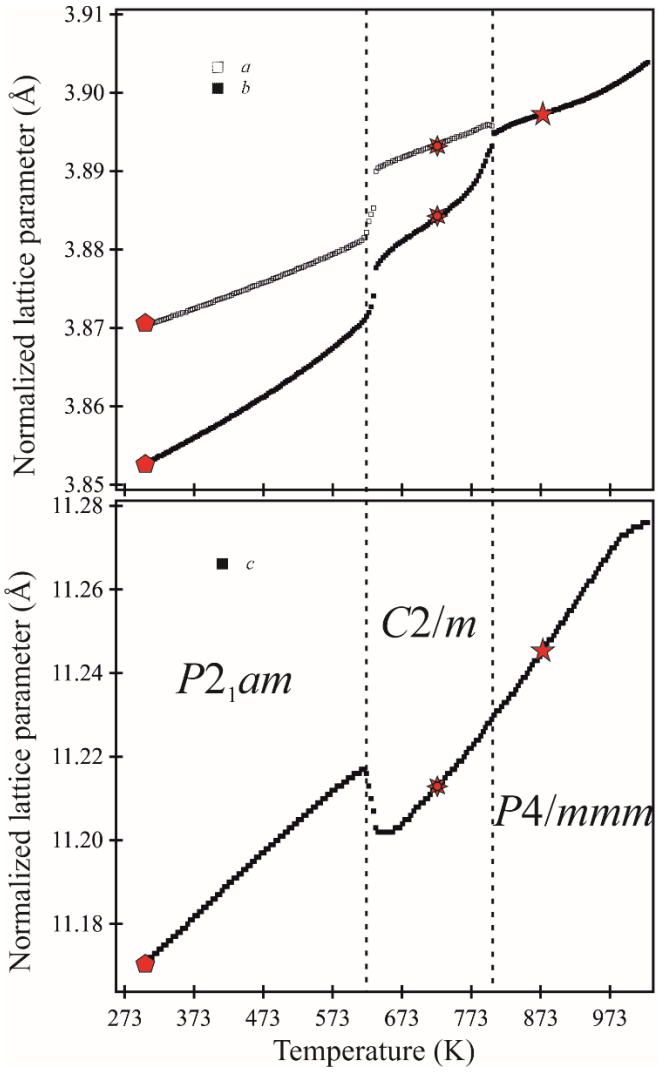


Figure 5.28. Temperature evolution of the lattice parameters for $CsNdNb_2O_7$ determined from the variable temperature synchrotron X-ray diffraction experiments. Markers indicate the temperatures where neutron diffraction data were collected.

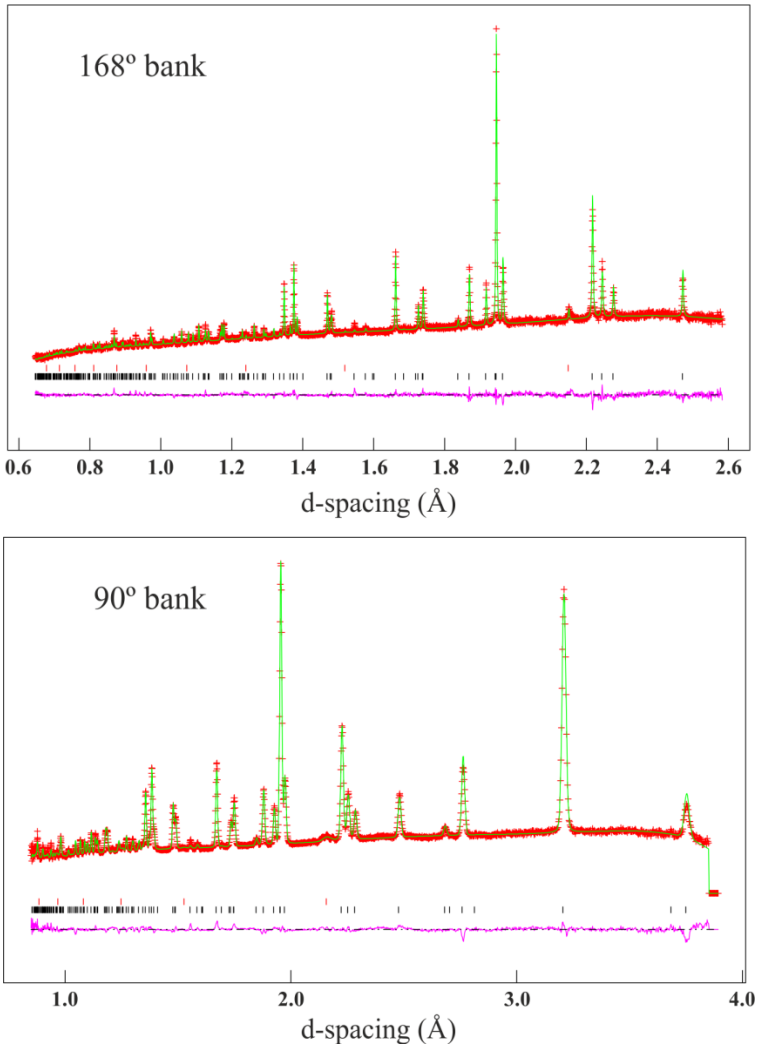


Figure 5.29. Observed, calculated and difference plots from the refinement of a structure model in space group *P*4/*mmm* against data collected from $CsNdNb_2O_7$ at 873 K. Vanadium was added as the secondary phase with red tick-marks.

Atom	site	*x*	*y*	*z*	U_{iso} (Å^3)
Cs(1)	1*b*	0	0	½	0.0670(11)
Nd(1)	1*a*	0	0	0	0.0275(6)
Nb(1)	2*h*	½	½	0.1974(1)	0.0117(4)
O(1)	4*i*	0	½	0.1635(1)	0.0482(5)
O(2)	2*h*	½	½	0.3542(2)	0.0643(7)
O(3)	1*c*	½	½	0	0.0973(13)
$CsNdNb_2O_7$ – space group *P*4/*mmm* (#123) *a* = 3.8987(1) Å, *c* = 11.2400(3) Å, volume = 170.84(1) Å^3 Formula weight: 574.95 g mol^{-1}, Z = 1 Radiation source: Neutron Time of flight Temperature: 873 K χ^2 = 4.43, wRp = 2.52%, Rp = 2.05%					

Table 5.13. Parameters from the structural refinement of $CsNdNb_2O_7$ against neutron powder diffraction data collected at 873 K.

To conclude, $CsNdNb_2O_7$ follows the same phase transition behaviour as $CsNdTa_2O_7$ (Figure 5.23). The first phase transition occurs at approximately 625 K to generate an anti-polar structure in space group *C*2/*m* with an $a^-b^0c^-$ tilting distortion. Both a^- and c^- tilts vanish at 800 K, leading to the aristotype *P*4/*mmm* structure.

5.4 Discussion

5.4.1 Comparison of the phase transition behaviours of $RbNdM_2O_7$ and $CsNdM_2O_7$

$RbNdM_2O_7$ and $CsNdM_2O_7$ are found to have different phase transition behaviours, with the rubidium phases adopting the sequence of *I*2*cm* ($a^-a^-c^+$/-($a^-a^-c^+$)) → *Cmca* ($a^-b^0c^-$/-(a^-b^0)c^-) → *I*4/*mcm* ($a^0b^0c^-$/a^0b^0-c^-) → *P*4/*mmm*, and the caesium phases adopting the sequence of $P2_1am$ ($a^-a^-c^+$) → *C*2/*m* ($a^-b^0c^-$) → *P*4/*mmm*. Despite the difference, it can be observed that the first phase transitions for $RbNdM_2O_7$ and $CsNdM_2O_7$ both lead to anti-polar structures (Figure 5.12 and Figure 5.23) and the local tilting distortions in the *Cmca* and *C*2/*m* structures are the same, both in $a^-b^0c^-$. The similarity suggests that the $a^-b^0c^-$ tilting distortion is another common tilting distortion which can be adopted by $n = 2$ Dion-Jacobson phases. The similarity in the local tilting distortion is consistent with the ground-state *I*2*cm* and $P2_1am$ structures adopted by $RbNdM_2O_7$ and $CsNdM_2O_7$ respectively, in which the local tilting distortion is the same, both in $a^-a^-c^+$. One interesting observation is that there is an extra intermediate phase for $RbNdM_2O_7$ with an $a^0b^0c^-$/a^0b^0-c^- tilting distortion. One might expect an equivalent intermediate phase with an $a^0b^0c^-$ tilting distortion for $CsNdM_2O_7$, described in space group *P*4/*nbm* (Table 5.1). However, neutron diffraction and synchrotron X-ray diffraction data show no evidence of such an intermediate phase.

As demonstrated in Chapter 3, the reason $RbNdM_2O_7$ adopts the *I*2*cm* structure, which has inverted octahedral tilting distortions in the adjacent perovskite double sheets, is because

this structural configuration can reduce the interlayer O-O repulsion. In the *Cmca* structure, a similar effect is observed. Figure 5.30 shows a comparison of the shortest interlayer O-O bonds in the refined *Cmca* and the refined *C*2/*m* structures from $RbNdNb_2O_7$ and $CsNdNb_2O_7$ respectively. It can be seen that in the *Cmca* structure, the octahedra are distorted in a way so that the interlayer oxide ions are pointing to the opposite directions, hence increasing the O-O bond length and reducing the interlayer O-O repulsion, whereas in the *C*2/*m* structure of $CsNdNb_2O_7$, interlayer oxide ions are pointing to the same direction. In Chapter 3, we discussed why $RbNdM_2O_7$ adopts the *I*2*cm* structure instead of the $P2_1am$ structure at ambient temperature and vice versa for $CsNdM_2O_7$. Unfortunately, it is not possible to have a similar discussion for the intermediate *Cmca* and *C*2/*m* structures, at least not only from the aspect of bonding. For example, it is not possible to discuss why $CsNdM_2O_7$ adopts the *C*2/*m* structure rather than the *Cmca* structure, despite the clear bonding benefit from the latter structure. The reason is when studying the crystal structure of the intermediate phases, we not only need to consider the enthalpy (the bonding), but to include the entropy change of the intermediate structures with respect to the corresponding ground-state structures and in this variable temperature case, we are not able to monitor the entropy change during the phase transitions. However, we can still confidently predict that the structural difference of the anti-polar rubidium and caesium phases arise from a competition between better interlayer metal-oxygen bonding ($CsNdM_2O_7$) and minimizing the interlayer O-O repulsion ($RbNdM_2O_7$).

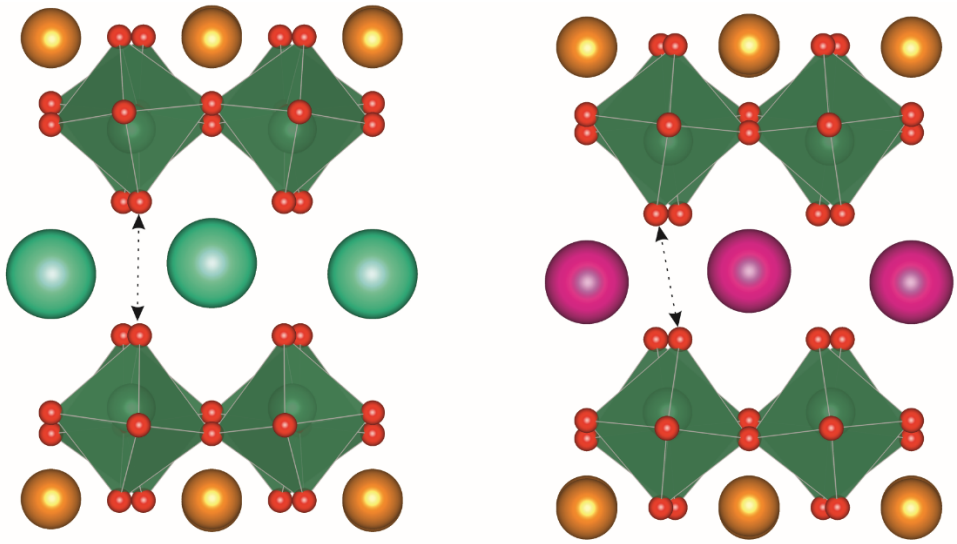


Figure 5.30. A comparison of the interlayer O-O bonds between the refined *C*2/*m* structure (left) and the refined *Cmca* structure (right) adopted by $CsNdNb_2O_7$ and $RbNdNb_2O_7$, respectively. The refined structures are obtained from the refinements against the neutron diffraction data collected from $CsNdNb_2O_7$ at 473 K and $RbNdNb_2O_7$ at 673 K.

5.4.2 Phase transition temperatures

Recent studies suggest a universal relationship between the ferroelectric transition temperature (T_C) and the tolerance factor (t) in n = 2 Ruddlesden-Popper phases (Figure 5.31)[72]. It is therefore interesting to see if T_C for n = 2 Dion-Jacobson phases also follows a similar linear relationship.

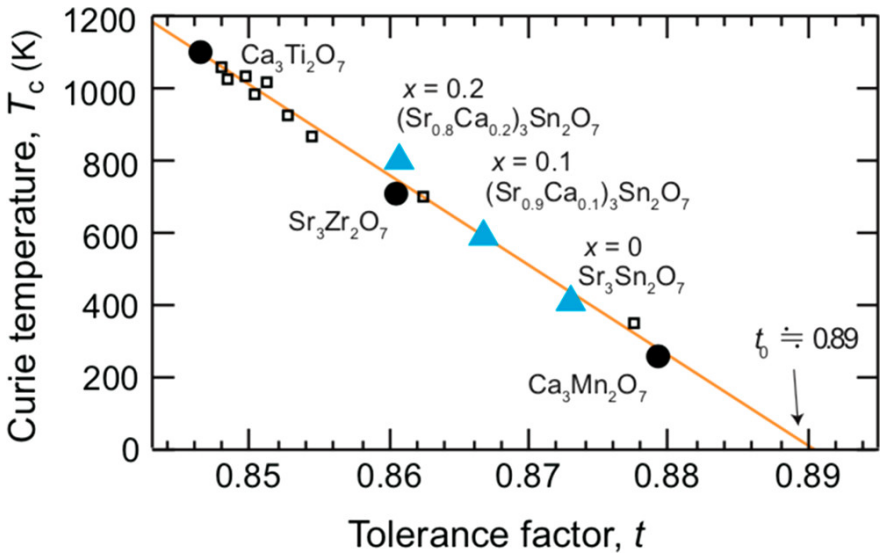


Figure 5.31. Ferroelectric transition temperatures (T_C) of a series of n = 2 Ruddlesden-Popper ferroelectrics against the tolerance factor (t) of their perovskite double layers[72].

Table 5.14 shows the phase transition temperatures of $RbNdM_2O_7$ and $CsNdM_2O_7$, determined from tracking their normalized lattice parameters (Figure 5.11, 5.16, 5.24 and 5.28). It can be immediately concluded that the linear relationship observed for n = 2 Ruddlesden-Popper phases is not reproduced by n = 2 Dion-Jacobson phases because $RbNdTa_2O_7$ has a Curie temperature of 500 K while $RbNdNb_2O_7$ has a much higher phase transition temperature at 790 K, despite that $RbNdTa_2O_7$ and $RbNdNb_2O_7$ have the same tolerance factor, due to the similar ionic radii of Ta^{5+} and Nb^{5+}.

Compound	Transition temperature (K)	
	Polar to Anti-Polar	Anti-Polar to Nonpolar
$RbNdTa_2O_7$	500	950
$RbNdNb_2O_7$	790	865
$CsNdTa_2O_7$	330	820
$CsNdNb_2O_7$	625	800

Table 5.14. Phase transition temperatures of $RbNdM_2O_7$ and $CsNdM_2O_7$. 'Nonpolar' means the *I*4/*mcm* structure for $RbNdM_2O_7$ and the *P*4/*mmm* structure for $CsNdM_2O_7$.

It can be seen from Table 5.14 that $RbNdM_2O_7$ has higher polar to anti-polar transition temperatures than $CsNdM_2O_7$ for both Ta and Nb phases. Interestingly, the Curie temperature of $RbNdTa_2O_7$ is 170 K higher than $CsNdTa_2O_7$ and the Curie temperature of $RbNdNb_2O_7$ is 165 K higher than $CsNdNb_2O_7$. The similarity in the transition temperature difference suggests that, despite the difference of the NdM_2O_7 perovskite units, change in the interlayer cation sizes may have similar impact on the change in Curie temperature. One way to test if this relationship is strictly linear is to study the Curie temperatures of $Rb_{1-x}Cs_xNdTa_2O_7$ and $Rb_{1-x}Cs_xNdNb_2O_7$ solid solutions. For example, if there is such a linear relationship, $Rb_{0.5}Cs_{0.5}NdTa_2O_7$ would have a polar to anti-polar phase transition at around 415 K and $Rb_{0.5}Cs_{0.5}NdNb_2O_7$ would have a transition at 708 K.

One question to ask is why $RbNdM_2O_7$ has a higher Curie temperature than $CsNdM_2O_7$. Table 5.15 shows the calculated bond valence sums from the refined structures against neutron diffraction data collected at different temperatures. $RbNdTa_2O_7$ and $CsNdTa_2O_7$

are used as examples. BVS values for the Rb^{+} and Nd^{3+} cations decrease significantly in the higher temperature phases of $RbNdTa_2O_7$, while for $CsNdTa_2O_7$, only the Nd^{3+} cation sees a significant decrease in the BVS values. These observations suggest that $RbNdTa_2O_7$ obtains more bonding benefit by adopting the ambient *I*2*cm* structure as both the Rb^{+} and Nd^{3+} cations are better bonded in the polar structure, while $CsNdTa_2O_7$ only has better Nd^{3+} bonding in the polar structure over the high temperature structures. Therefore $RbNdM_2O_7$ needs more entropy benefits than $CsNdM_2O_7$ to compensate for the loss in the bonding benefits, and thus a higher polar to anti-polar transition temperature.

$RbNdTa_2O_7$					
Temperature (K)	Structure	Tilts	BVS		
			Rb	Nd	Ta
298	*I*2*cm* (polar)	$a^-a^-c^+/-(a^-a^-c^+)$	0.88	3.09	5.10
673	*Cmca* (anti-polar)	$a^-b^0c^-/-(a^-b^0)c^-$	0.81	2.67	5.26
973	*I*4/*mcm*	$a^0b^0c^-/a^0b^0\text{-}c^-$	0.74	2.48	5.22
1273	*P*4/*mmm*	$a^0b^0c^0/a^0b^0c^0$	0.69	2.35	5.29
$CsNdTa_2O_7$					
Temperature (K)	Structure	Tilts	BVS		
			Cs	Nd	Ta
298	$P2_1am$ (polar)	a^-a^-c	1.04	2.91	5.14
473	*C*2/*m* (anti-polar)	$a^-b^0c^-$	1.01	2.78	5.16
923	*P*4/*mmm*	$a^0b^0c^0$	0.92	2.40	5.26

Table 5.15. BVS values from the refined structures of $RbNdTa_2O_7$ and $CsNdTa_2O_7$ from the refinements against the neutron diffraction data collected at different temperatures.

DFT calculations show that the lowest energy *I*2*cm* structure of $RbNdTa_2O_7$ is 307 meV/formula unit more stable than the aristotype *P*4/*mmm* structure. In contrast, the lowest energy $P2_1am$ structure of $CsNdTa_2O_7$ is 267 meV/formula unit more stable than the *P*4/*mmm* structure. Similarly, the lowest energy *I*2*cm* structure of $RbNdNb_2O_7$ and the $P2_1am$ structure of $CsNdNb_2O_7$ are 360 meV/formula unit and 320 meV/formula unit more stable than their corresponding *P*4/*mmm* structures respectively[10]. The energy differences between the polar structures and the aristotype *P*4/*mmm* structures are consistent with the observed Curie temperatures from the four polar Dion-Jacobson phases. The polar structure of the rubidium phases has more energy benefits compared to the caesium analogues with

respect to the aristotype structures, hence higher phase transition temperatures. In addition, the energy differences follow exactly the same sequence of the Curie temperatures for all four phases: $RbNdNb_2O_7$ has the most energy benefit (-360 meV/f.u.) and highest Curie temperature (790 K), followed by $CsNdNb_2O_7$ (-320 meV/f.u. and 625 K), then $RbNdTa_2O_7$ (-307 meV/f.u. and 500 K), and finally $CsNdTa_2O_7$ (-267 meV/f.u. and 330 K).

5.5 Conclusion

Phase transition behaviours of four polar n = 2 Dion-Jacobson phases, $RbNdTa_2O_7$, $RbNdNb_2O_7$, $CsNdTa_2O_7$ and $CsNdNb_2O_7$ have been investigated using variable temperature synchrotron X-ray and high-resolution neutron diffraction. Both rubidium phases are found to adopt a phase transition sequence of $I2cm$ ($a^-a^-c^+$/-($a^-a^-c^+$)) → $Cmca$ ($a^-b^0c^-$/-(a^-b^0)c^-) → $I4/mcm$ ($a^0b^0c^-$/a^0b^0-c^-) → $P4/mmm$ while the caesium phases have a transition sequence of $P2_1am$ ($a^-a^-c^+$) → $C2/m$ ($a^-b^0c^-$) → $P4/mmm$. Our study suggests that the $a^-b^0c^-$ tilting distortion can be another common tilting system for n = 2 Dion-Jacobson phases.

The analysis of the Curie temperatures for the four phases suggests that $CsNdM_2O_7$ have much lower polar to anti-polar transition temperatures with respect to their rubidium analogues, hence a stronger competition between the polar and the anti-polar structures. The difference in the Curie temperatures can be explained by the change in Cs^+/Rb^+ bonding during the phase transition, which is analogous to the idea in Chapter 3 and Chapter 4: the interlayer cations have great impacts on the tilting distortions and the crystal structures of layered perovskites. In addition, our study suggests that the Rb^+ cation is generally too small to sit in an undistorted Dion-Jacobson structure and hence a structural distortion is needed to facilitate the Rb^+ cation bonding. Although no simple linear

relationship between the Curie temperature and the tolerance factor is observed from $n = 2$ Dion-Jacobson phases, there is a possible correlation between the interlayer cation sizes and the Curie temperatures, which requires future studies.

Chapter 6 – $Li_2SrTa_2O_7$: A Polar Ruddlesden-Popper Phase with a Non-Trivial Crystal Structure

6.1 Introduction

As demonstrated in Chapters 3 and 5, a series of n = 2 layered perovskites with formula $A'NdM_2O_7$ (A' = Cs/Rb/Na/Li, M = Nb/Ta) adopt distorted structures, these results contrast previous reports which claimed all these phases are undistorted. These discoveries encouraged us to study another n = 2 Ruddlesden-Popper phase, $Li_2SrTa_2O_7$, which was reported to adopt a centrosymmetric structure in space group *Amam* with an $a^-a^-c^0/a^-a^-c^0$ tilting distortion[77]. This compound attracts particular interests because each formula unit of $Li_2SrTa_2O_7$ contains two Li^+ cations, which make it a good candidate for cation exchange reactions with divalent cations. Before studying the topochemical cation exchange chemistry of $Li_2SrTa_2O_7$, it is necessary to re-investigate its crystal structure.

6.2 Synthesis

Powder samples of $Li_2SrTa_2O_7$ were prepared by a ceramic synthesis method from Li_2CO_3 (99.998%), $SrCO_3$ (99.994%) and Ta_2O_5 (99.993%). Ta_2O_5 was dried at 900 °C before being used. Suitable stoichiometric ratios of $SrCO_3$ and Ta_2O_5 were ground together in an agate pestle and mortar and then combined with a 10% excess of Li_2CO_3 (to compensate for metal loss due to the volatility of Li_2CO_3 at high temperature). These mixtures were then heated at 600 °C in air for 12 hours, reground, pressed into pellets. The pellets were then heated to 1250 °C at a heating rate of 5 °C/min, then kept at 1250 °C for 12 hours, followed by a cooling at 10 °C/min to room temperature. Samples were then reground, pressed into pellets, heated at 1250 °C for 3 hours and quenched to room temperature in air. Reaction progress and final sample purity were assessed by X-ray powder diffraction

data collected using a PANalytical X'pert diffractometer incorporating an X'celerator position sensitive detector (monochromatic Cu Kα1 radiation).

6.3 Results

6.3.1 Optical SHG measurements

Particle-size dependent SHG measurements show that $Li_2SrTa_2O_7$ is SHG active, and therefore that it adopts a non-centrosymmetric structure (Figure 6.1). The observed SHG activity contrasts with the previous report in which $Li_2SrTa_2O_7$ was assigned a centrosymmetric structure in space group *Amam*[78].

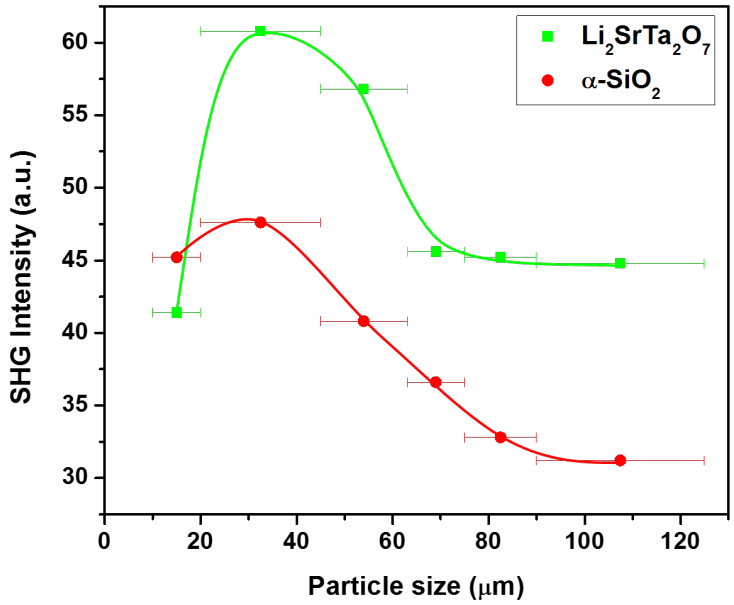


Figure 6.1. Plots of SHG activity of $Li_2SrTa_2O_7$ as a function of particle size, compared to an α-SiO_2 standard.

6.3.2 Room temperature synchrotron X-ray powder diffraction

High-resolution synchrotron X-ray powder diffraction data collected from $Li_2SrTa_2O_7$ at ambient temperature can be indexed using an orthorhombic unit cell with an approximate $\sqrt{2} \times \sqrt{2} \times 1$ geometric expansion of the aristotype *I*4/*mmm* unit cell, (a = 5.5826 Å, b = 5.5772 Å, c = 18.1874 Å) of an n = 2 Ruddlesden-Popper phase. The extinction conditions suggest an *A*-centred space group. The unit cell expansion and the extinction conditions are

consistent with the previous reported structure of $Li_2SrTa_2O_7$ in space group *Amam*, with an $a^-a^-c^0/a^-a^-c^0$ tilting distortion[78]. However, this centrosymmetric structure is not compatible with the observed SHG activity of $Li_2SrTa_2O_7$. Adding an in-phase rotation of the TaO_6 octahedra along the *z*-axis to the *Amam* structure leads to an $a^-a^-c^+/a^-a^-c^+$ tilting distortion and a non-centrosymmetric structure in space group $A2_1am$. This symmetry model was then constructed and refined against high-resolution synchrotron X-ray diffraction data. The refinement gives a reasonable fit, as shown in Figure 6.2.

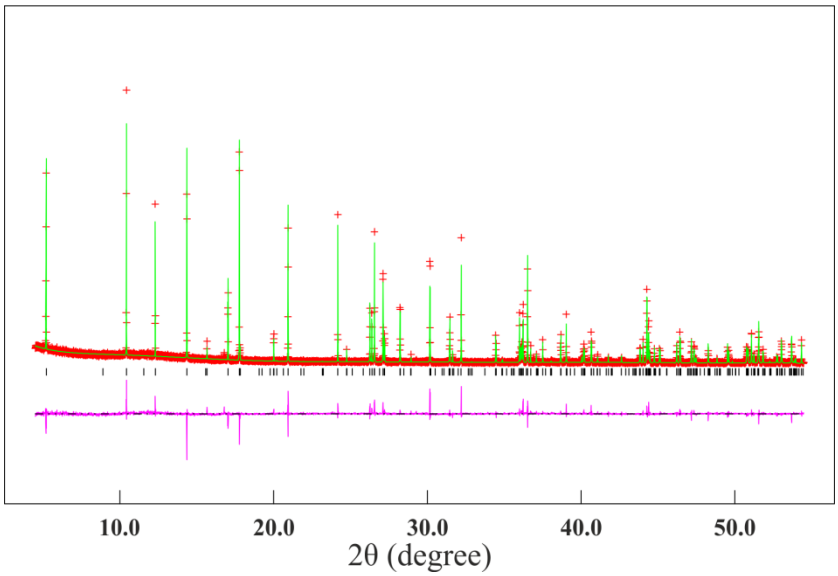


Figure 6.2. Observed, calculated and difference plots from the refinement of the $A2_1am$ model against the synchrotron X-ray diffraction data collected from $Li_2SrTa_2O_7$ at 298 K.

6.3.3 Room temperature neutron diffraction

Neutron powder diffraction data were collected from a sample of approximately 4.5 g $Li_2SrTa_2O_7$ at ambient temperature using the HRPD instrument at ISIS. In common with the synchrotron X-ray diffraction data, these neutron diffraction data can be indexed using an expanded unit cell with a $\sqrt{2} \times \sqrt{2} \times 1$ geometric expansion of the undistorted cell, with extinction conditions consistent with an *A*-centred or a primitive space group. The refinement of an $A2_1am$ symmetry model against the neutron diffraction data gives a good statistical and visual fit. The observed, calculated and difference plots from the refinement of the $A2_1am$ symmetry model are shown in Figure 6.3 and full details of the parameters

from the refinements are shown in Table 6.1. Selected bond lengths from the refined structure of $Li_2SrTa_2O_7$ are shown in Table 6.2. The refined structure is shown in Figure 6.4. This polar structure is consistent with a recent report of $Li_2SrNb_2O_7$ which also adopts a polar $A2_1am$ structure at ambient temperature[79]. The good visual fit against the neutron powder diffraction data suggests that the intensity mismatch of the refinement against the synchrotron X-ray diffraction data (Figure 6.2) is because of a strong preferred orientation of the sample in the capillary during the measurement.

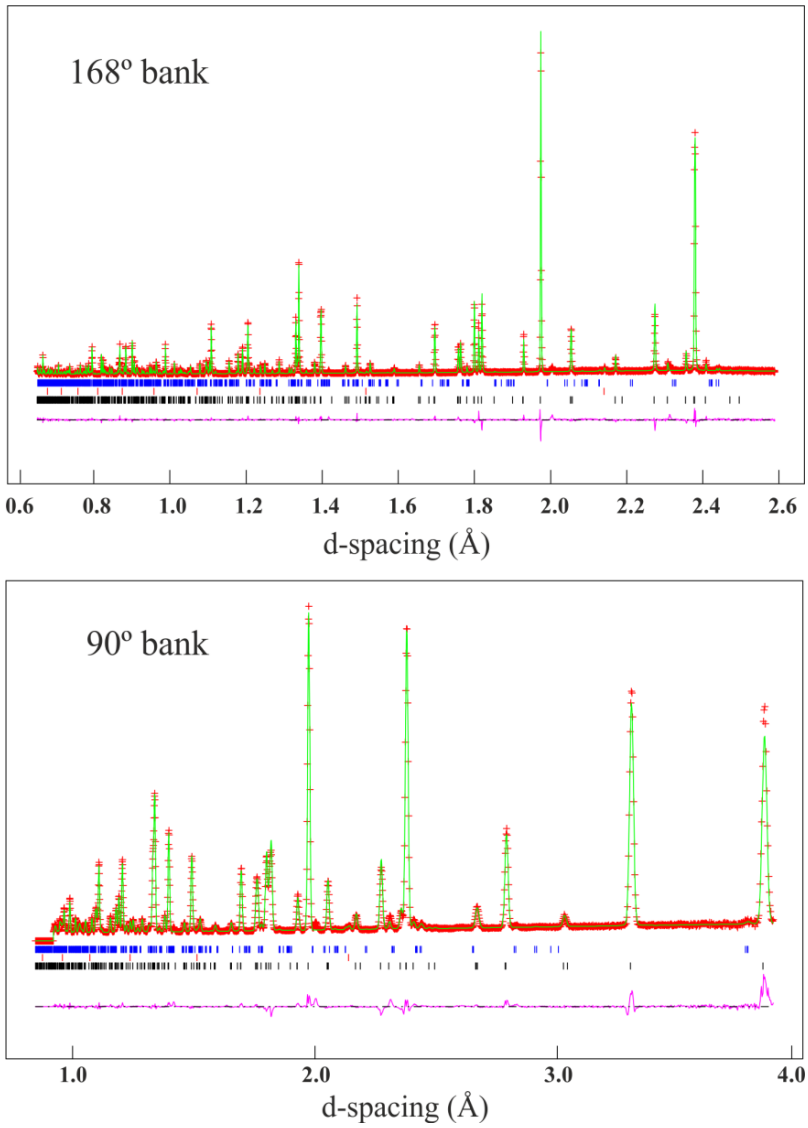


Figure 6.3. Observed, calculated and difference plots from the refinement of the $A2_1am$ model against high-resolution neutron diffraction data collected from $Li_2SrTa_2O_7$ at 298 K. Li_3TaO_4 and vanadium were added as secondary phases with blue and red tick-marks respectively.

Atom	site	*x*	*y*	*z*	U_{iso} (Å^3)
Li(1)	8*b*	0.4909(27)	0.0106(38)	0.2442(3)	0.0153(14)
Sr(1)	4*a*	0.2275(15)	0.2444(5)	0	0.0071(3)
Ta(1)	8*b*	0.2194(9)	0.7471(4)	0.1149(1)	0.0028(2)
O(1)	4*a*	0.2314(17)	0.7791(5)	0	0.0099(6)
O(2)	8*b*	0.2213(11)	0.7297(4)	0.2174(1)	0.0067(3)
O(3)	8*b*	0.9788(15)	0.4971(14)	0.0968(1)	0.0049(4)
O(4)	8*b*	0.9806(17)	0.0054(12)	0.1121(1)	0.0075(4)
$Li_2SrTa_2O_7$ – space group $A2_1am$ (#36) *a* = 5.5784(1) Å, *b* = 5.5842(1) Å, *c* = 18.1845(1) Å, volume = 566.46(1) Å^3 Formula weight: 575.39 g mol^{-1}, Z = 4 Radiation source: Neutron Time of flight Temperature: 298 K χ^2 = 10.08, wRp = 5.71%, Rp = 5.35%					

Table 6.1. Parameters from the structural refinement of $Li2SrTa_2O_7$ against neutron powder diffraction data collected at 298 K

Cation	Anion	length (Å)	BVS
Li(1)	O(2) × 1	2.060(18)	Li +0.81
	O(2) × 1	2.227(19)	
	O(2) × 1	1.984(19)	
	O(2) × 1	1.998(19)	
Sr(1)	O(1)	2.770(13)	Sr +2.21
	O(1)	2.986(5)	
	O(1)	2.599(5)	
	O(1)	2.814(13)	
	O(3) × 2	2.648(8)	
	O(3) × 2	2.673(8)	
	O(4) × 2	2.799(8)	
	O(4) × 2	2.846(8)	
Ta(1)	O(1)	2.099(1)	Ta +5.11
	O(2)	1.867(1)	
	O(3)	1.964(9)	
	O(3)	2.016(9)	
	O(4)	1.964(9)	
	O(4)	2.009(10)	

Table 6.2. Selected bond lengths from the refined structure of $Li_2SrTa_2O_7$ (300 K).

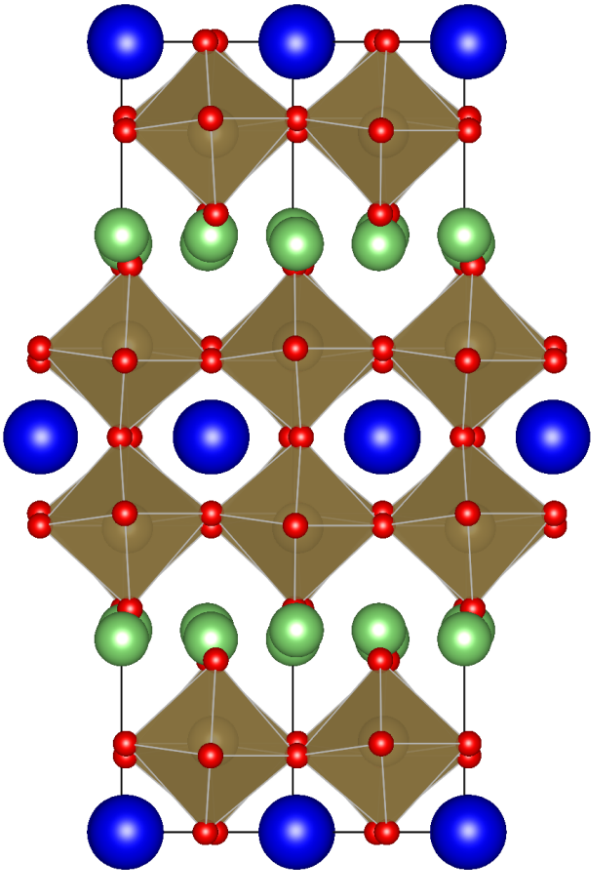


Figure 6.4. The structure of $Li_2SrTa_2O_7$ in space group $A2_1am$, with an $a^-a^-c^+/a^-a^-c^+$ tilting distortion. The green and blue spheres are the Li^+ and Sr^{2+} cations respectively, the Ta^{5+} cations are inside the polyhedra.

6.3.4 Low temperature neutron diffraction

Recent studies have suggested that $Li_2SrNb_2O_7$ undergoes a phase transition at around 210 K, observed from both temperature-dependent dielectric permittivity measurements and variable temperature synchrotron X-ray diffraction experiments[79-81]. It is therefore possible that $Li_2SrTa_2O_7$ undergoes a similar transition and adopts a different crystal instead of the $A2_1am$ structure at low temperatures. Neutron diffraction data were collected from $Li_2SrTa_2O_7$ at 5 K using the GEM instrument at ISIS. The diffraction data can be indexed using an expanded unit cell with a $\sqrt{2} \times \sqrt{2} \times 1$ geometric expansion of the undistorted cell. The extinction conditions suggest an A-centred or a primitive space group. Since $Li_2SrNb_2O_7$ was reported to adopt a $Pna2_1$ structure with roughly an $a^-a^-c^+/a^-a^--c^+$ tilting distortion at 80 K[81], both $A2_1am$ and $Pna2_1$ symmetry models of $Li_2SrTa_2O_7$ were

constructed and refined against the neutron diffraction data collected at 5 K. Refinements of the $A2_1am$ and $Pna2_1$ models reveal that both models give equally good statistical and visual fits (Table 6.3). No evidence corresponding to the loss of *A*-centring is observed from the 5 K neutron diffraction data. Therefore it is concluded that $Li_2SrTa_2O_7$ still adopts a polar $A2_1am$ structure at 5 K. Further discussion of the crystal structure of $Li_2SrTa_2O_7$ will be given later in this chapter. The observed, calculated and difference plots from the refinement of the $A2_1am$ symmetry model against the 5 K neutron diffraction data are shown in Figure 6.5 and full details of the parameters from the refinements are shown in Table 6.4. Selected bond lengths from the refined structure of $Li_2SrTa_2O_7$ are shown in Table 6.5. The refined structure is analogues to the structure shown in Figure 6.4.

space group	tilt system	Glazer tilt	χ^2	wRp (%)	Rp (%)
$A2_1am$	$\Phi\Phi\Psi_z/\Phi\Phi\Psi_z$	$a^-a^-c^+/a^-a^-c^+$	9.37	4.40	3.51
$Pna2_1$	$\Phi\Phi\Psi_z/\Phi\Phi\text{-}\Psi_z$	$a^-a^-c^+/a^-a^-\text{-}c^+$	8.74	4.30	3.45

Table 6.3. Fitting statistics from the structural refinements of the $A2_1am$ and $Pna2_1$ models against neutron powder diffraction data collected from $Li_2SrTa_2O_7$ at 5 K.

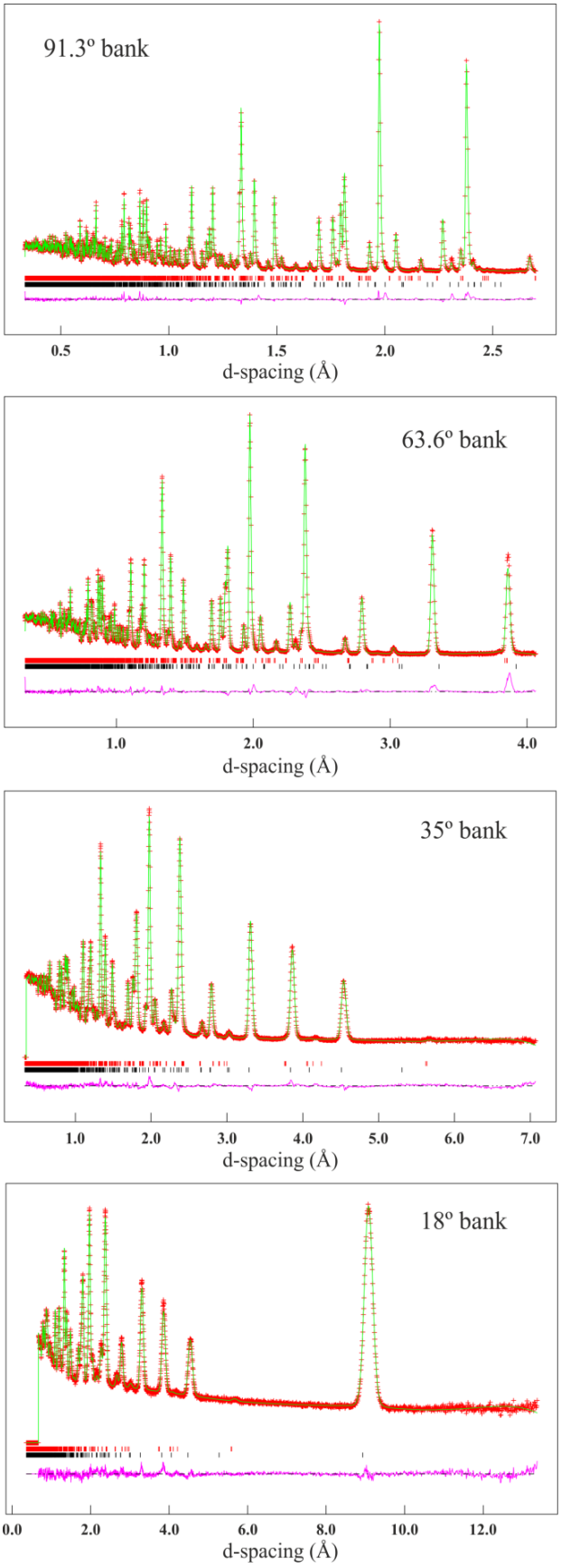


Figure 6.5. Observed, calculated and difference plots from the refinement of the $A2_1am$ model against high−resolution neutron diffraction data collected from $Li_2SrTa_2O_7$ at 5 K. Li_3TaO_4 was added as the secondary phase with red tick-marks.

Atom	site	*x*	*y*	*z*	U_{iso} (Å^3)
Li(1)	8*b*	0.4614(18)	0.9964(26)	0.2422(2)	0.0055(8)
Sr(1)	4*a*	0.1971(22)	0.2443(3)	0	0.0021(2)
Ta(1)	8*b*	0.1976(12)	0.7468(2)	0.1150(1)	0.0006(1)
O(1)	4*a*	0.1950(23)	0.7878(3)	0	0.0031(3)
O(2)	8*b*	0.1966(16)	0.7241(2)	0.2177(1)	0.0030(2)
O(3)	8*b*	0.9484(15)	0.4982(14)	0.0957(1)	0.0023(2)
O(4)	8*b*	0.9518(15)	0.0031(12)	0.1137(1)	0.0033(2)
$Li_2SrTa_2O_7$ – space group $A2_1am$ (#36) *a* = 5.5745(2) Å, *b* = 5.5842(2) Å, *c* = 18.1238(5) Å, volume = 564.18(4) Å^3 Formula weight: 575.39 g mol^{-1}, Z = 4 Radiation source: Neutron Time of flight Temperature: 5 K χ^2 = 9.37, wRp = 4.40%, Rp = 3.51%					

Table 6.4. Parameters from the structural refinement of $Li_2SrTa_2O_7$ against neutron powder diffraction data collected at 5 K.

Cation	Anion	length (Å)	BVS
Li(1)	O(2) × 1	2.166(14)	Li +0.81
	O(2) × 1	2.079(13)	
	O(2) × 1	2.086(14)	
	O(2) × 1	1.940(13)	
Sr(1)	O(1)	2.805(19)	Sr +2.26
	O(1)	3.035(3)	
	O(1)	2.549(3)	
	O(1)	2.781(19)	
	O(3) × 2	2.634(10)	
	O(3) × 2	2.653(10)	
	O(4) × 2	2.816(8)	
	O(4) × 2	2.858(9)	
Ta(1)	O(1)	2.097(1)	Ta +5.10
	O(2)	1.866(1)	
	O(3)	1.987(10)	
	O(3)	1.995(10)	
	O(4)	1.981(10)	
	O(4)	1.990(10)	

Table 6.5. Selected bond lengths from the refined structure of $Li_2SrTa_2O_7$ (5 K).

6.4 Discussion

6.4.1 Oxygen lattice

$Li_2SrTa_2O_7$ was previously assigned an *Amam* structure with an $a^-a^-c^0/a^-a^-c^0$ tilting distortion from the analysis of neutron powder diffraction and electron microscopy data[78]. However, the SHG activity clearly eliminates the possibility of this centrosymmetric structure and our analysis suggests that $Li_2SrTa_2O_7$ adopts a polar $A2_1am$ structure with an $a^-a^-c^+/a^-a^-c^+$ tilting distortion. One main difference between the polar $A2_1am$ structure and the non-polar *Amam* structure is the additional in-phase octahedral rotation along the stacking axis in the polar structure. This difference is similar to the cases of $RbNdM_2O_7$ (*M* = Nb/Ta). Figure 3.12 and 3.13 in Chapter 3 shows the refinement plots using the *Imam* ($a^-a^-c^0/-(a^-a^-)c^0$) and the *I*2*cm* ($a^-a^-c^+/-(a^-a^-c^+)$) symmetry models against the neutron diffraction data collected from $RbNdNb_2O_7$ and $RbNdTa_2O_7$, respectively. It can be seen that these two models give significantly different visual fits and it can be easily concluded that the centrosymmetric *Imam* model is incorrect and an additional in-phase tilting distortion exists. In contrast, in the case of $Li_2SrTa_2O_7$, the model of *Amam* gives a good visual fit[77]. It is therefore interesting to study why this wrong symmetry model gives a good fit, in other words, why $Li_2SrTa_2O_7$ was assigned a wrong structure in the previous study. Since a recent work proposed that $Li_2SrNb_2O_7$ adopts a $Pna2_1$ structure with roughly an $a^-a^-c^+/a^-a^--c^+$ tilting distortion at 80 K, this symmetry model will also be discussed[80, 81].

Table 6.6 shows the fitting statistics of the refinements using the $A2_1am$, *Amam* and $Pna2_1$ symmetry models against the neutron diffraction data collected from $Li_2SrTa_2O_7$ at 300 K and 5 K. It can be seen that the differences in the fitting statistics of these three models are generally too small to be significant at both temperatures. The small difference in the fitting statistics indicates that the refined structures of the three models are likely to be very similar. Figure 6.6 shows the refined $A2_1$am structure at 300 K viewing along the stacking axis. It

can be seen that compared to the out-of-phase tilts along the *x*/*y* directions, which are clear and unambiguous (Figure 6.4), the *c* tilt is negligible. An inspection of the refined $Pna2_1$ structure at 300 K reveals that the magnitude of the *c* tilt is also zero. These observations suggest that the octahedral tilting distortion of $Li_2SrTa_2O_7$ is very close to $a^-a^-c^0$, which can be described by all three structural models of $A2_1am$, *Amam* and $Pna2_1$. Since the oxygen ions contribute to approximately 70% of the total neutron scattering power, the equivalently good fits from all three models can be attributed to the oxygen lattice.

space group	tilt system	Glazer tilt	χ^2	wRp (%)	Rp (%)
300 K (HRPD)					
$Pna2_1$ #33	$\Phi\Phi\Psi_z/\Phi\Phi\text{-}\Psi_z$	$a^-a^-c^+/a^-a^-\text{-}c^+$	9.45	5.52	5.14
$A2_1am$ #36	$\Phi\Phi\Psi_z/\Phi\Phi\Psi_z$	$a^-a^-c^+/a^-a^-c^+$	10.08	5.71	5.35
Amam #67	$\Phi\Phi0/\Phi\Phi0$	$a^-a^-c^0/a^-a^-c^0$	10.22	5.75	5.40
5 K (GEM)					
$Pna2_1$ #33	$\Phi\Phi\Psi_z/\Phi\Phi\text{-}\Psi_z$	$a^-a^-c^+/a^-a^-\text{-}c^+$	8.74	4.30	3.45
$A2_1am$ #36	$\Phi\Phi\Psi_z/\Phi\Phi\Psi_z$	$a^-a^-c^+/a^-a^-c^+$	9.37	4.40	3.51
Amam #67	$\Phi\Phi0/\Phi\Phi0$	$a^-a^-c^0/a^-a^-c^0$	9.38	4.40	3.52

Table 6.6. Fitting statistics from the structural refinements of different models against neutron powder diffraction data collected from $Li_2SrTa_2O_7$ at 300 K and 5 K.

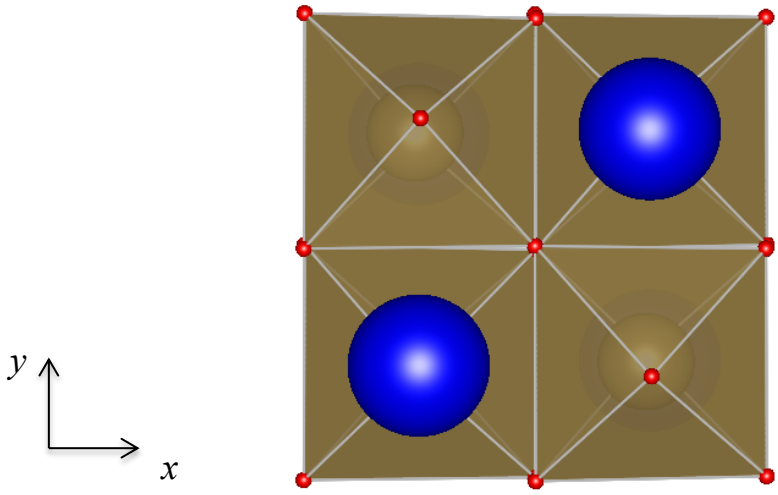


Figure 6.6. The refined $A2_1am$ structure viewing along the stacking axis. Blue and red spheres are the Sr^{2+} and O^{2-} ions respectively. The Ta^{5+} cations are inside the polyhedral. The *c* tilt is nearly negligible.

6.4.2 Cation lattice

Although the observed SHG activity eliminates the centrosymmetric *Amam* space group, the difference in the fitting statistics (Table 6.6) from the two polar structural models, $A2_1am$ and $Pna2_1$, is too small to unambiguously suggest the correct structural model. Apart from the allowed octahedral tilting distortions, another main difference between the $A2_1am$ and $Pna2_1$ symmetry models is how cations are allowed to displace. In the $A2_1am$ structural model, Sr^{2+} cations sit on a mirror plane perpendicular to the stacking *z* axis and they are allowed to move freely along both *x* and *y* directions, while the Ta^{5+} cations sit in general positions so they can move along all three Cartesian axes. These allowed cationic movements lead to the electric polarisation in the $SrTa_2O_7$ perovskite layers (Figure 6.7) and the electric dipoles are all aligned along *x*. In contrast, both the Sr^{2+} and Ta^{5+} cations sit in general positions in the $Pna2_1$ structure, meaning both cations can move freely along all three Cartesian axes. In fact, the $Pna2_1$ structure is a maximum subgroup structure of the anti-polar *Pnam* structure (Figure 6.7), meaning that the $Pna2_1$ structure possesses local electric dipoles along both *x* and *z* directions. As one can easily tell from its space group, the net polarisation in the $Pna2_1$ structure is along *z* and the local electric dipoles along *x* cancel across the material. These allowed cation displacements are useful information and the refined cation positions were hence investigated.

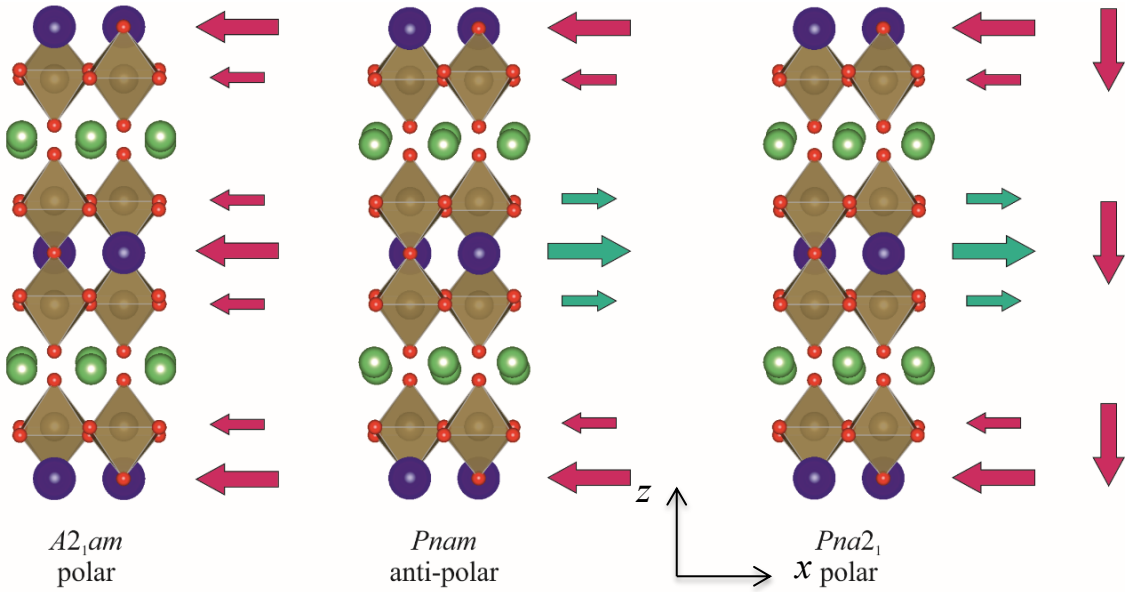


Figure 6.7. A comparison of how Sr^{2+} and Ta^{5+} cations can displace in the polar *A*2₁*am* and *Pna*2₁ as well as the anti-polar *Pnam* symmetry structures. *Pna*2₁ is a subgroup of *Pnam* with the loss of the mirror plane perpendicular to *z*. Arrows indicate the allowed displacements of the Sr^{2+} and Ta^{5+} cations.

Table 6.7 shows the refined atomic positions of the Sr^{2+} and the Ta^{5+} cations from the refinements of the *A*2₁*am*, *Pna*2₁ and *Amam* models against the neutron diffraction data collected at 300 K and 5 K, respectively. *A*2₁*am* and *Pna*2₁ space groups are both subgroups of *Amam* so they can both describe the *Amam* structure. The refined parameters from the *Amam* model are used to show the coordinates of high-symmetry special positions of metal cations. It can be seen from Table 6.7 that the refined *x* values for the Sr^{2+} and Ta^{5+} cations in the *A*2₁*am* structure at both 300 K and 5 K are far away from $x = ¼$, meaning the extra degree of freedom along *x* is necessary and the displacements of the Sr^{2+} and Ta^{5+} cations from the original, high symmetry positions are large and unambiguous. In contrast, the refined *x* values of Sr^{2+} and Ta^{5+} cations in the *Pna*2₁ structure are very close to the special value ¼, suggesting the extra degree of freedom along *x* in the *Pna*2₁ structure is not necessary. In addition, the refined *z* values for the two Ta^{5+} cations (For both HRPD (300 K) and GEM (5 K): $z(Ta1) = 0.135 = 0.25 - 0.115$; $z(Ta2) = 0.365 = 0.25 + 0.115$) indicate there is a mirror plane at (*x*, *y*, ¼) and hence the polar displacement along *z* is deemed not real.

300 K (HRPD)					
	Atom	site	*x*	*y*	*z*
$A2_1am$	Sr	4*a*	0.2275(15)	0.2444(5)	0
	Ta	8*b*	0.2194(9)	0.7471(4)	0.1149(1)
$Pna2_1$	Sr	4*b*	0.2530(18)	0.5052(6)	0.2454(2)
	Ta_1	4*b*	0.2519(18)	0.0016(16)	0.1350(3)
	Ta_2	4*b*	0.2558(22)	0.0045(16)	0.3654(2)
Amam	Sr	4*c*	¼	0.2443(5)	½
	Ta	8*g*	¼	0.2473(4)	0.1150(1)
5 K (GEM)					
	Atom	site	*x*	*y*	*z*
$A2_1am$	Sr	4*a*	0.1971(22)	0.2443(3)	0
	Ta	8*b*	0.1976(12)	0.7468(2)	0.1150(1)
$Pna2_1$	Sr	4*b*	0.2521(17)	0.5054(3)	0.2468(2)
	Ta_1	4*b*	0.2516(14)	0.0018(13)	0.1348(2)
	Ta_2	4*b*	0.2526(13)	0.0054(10)	0.3648(2)
Amam	Sr	4*c*	¼	0.2443(3)	½
	Ta	8*g*	¼	0.2469(2)	0.1150(1)

Table 6.7. Atomic positions of the selected cations from the refinements of different models against neutron powder diffraction data collected from $Li_2SrTa_2O_7$ at 300 K and 5 K.

A similar compound, $Li_2SrNb_2O_7$, was reported to have a phase transition at 210 K[79, 81]. The single crystal X-ray diffraction study clearly shows that $Li_2SrNb_2O_7$ adopts a primitive structure in space group $Pna2_1$ below 210 K. A recent study on $Li_2Sr(Nb_{2-x}Ta_x)_2O_7$ solid solutions shows that substituting Nb^{5+} with Ta^{5+} supresses the phase transition temperature[80]. Temperature dependence of dielectric permittivity suggests that there is no phase transition at the temperature range $0 < T/K < 300$ K for $Li_2SrTa_2O_7$ (Figure 6.8). This is consistent with our observations from the neutron diffraction data collected at 300 K and 5 K. The observations of the dielectric permittivity measurements suggest that at the temperature range $5 \leq T/K \leq 300$ K, $Li_2SrTa_2O_7$ is likely to be isostructural to the 300 K phase of $Li_2SrNb_2O_7$, which must be different from the low temperature phase of $Li_2SrNb_2O_7$ in space group $Pna2_1$. Combining this deduction with our crystallographic study, it is concluded that $Li_2SrTa_2O_7$ adopts a polar $A2_1am$ structure in the temperature range $5 \leq T/K \leq 300$ K.

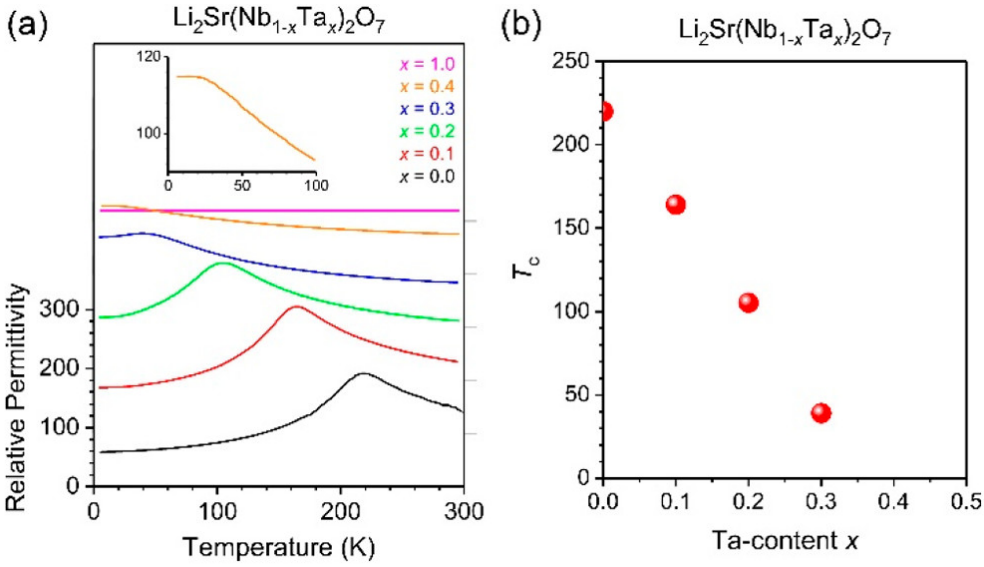


Figure 6.8. (a) Dielectric permittivity measured as a function of temperature for $Li_2Sr(Nb_{2-x}Ta_x)_2O_7$ solid solutions; (b) Phase transition temperatures as a function of Ta-content[80].

6.5 Conclusion

Optical SHG and neutron diffraction experiments show that $Li_2SrTa_2O_7$ adopts a polar $A2_1am$ structure. Although it is not possible to unambiguously conclude from the diffraction data that $Li_2SrTa_2O_7$ adopts an $A2_1am$ rather than a lower symmetry $Pna2_1$ structure, a recent study of $Li_2Sr(Nb_{2-x}Ta_x)_2O_7$ solid solutions suggests that $Li_2SrTa_2O_7$ adopts the *A*-centred structure. Further DFT study will be used to support this conclusion.

Chapter 7 – $MnSrTa_2O_7$: Retrosynthesis towards Multiferroic Materials

7.1 Introduction

Topochemical cation exchange chemistry has been widely studied for layered perovskite compounds, and wide varieties of new solids have been synthesized by these routes. For example, Chapter 4 demonstrates that metastable phases $LiNdM_2O_7$ and $NaNdM_2O_7$ (M = Nb/Ta) can be prepared by treating $RbNdM_2O_7$ with lithium nitrate or sodium nitrate and different cation ordered arrangements are found in these two types of compounds. In addition, a series of metastable layered oxyhalides, (MCl)$LaNb_2O_7$ (M = Mn, Fe, Co and Cu), were synthesized by treating $ALaNb_2O_7$ (A = Li, Na, K or Rb) with the corresponding transition metal chlorides, and magnetic properties were introduced by replacing the diamagnetic Group I cations with the transition metal halides. Similarly, an antiferromagnetic phase $FeLa_2Ti_3O_{10}$ can be prepared via the ion exchange of the diamagnetic, metastable Ruddlesden-Popper phase $Li_2La_2Ti_3O_{10}$ using anhydrous $FeCl_2$ (Figure 7.1)[82].

Chapter 6 demonstrates that $Li_2SrTa_2O_7$ adopts a polar structure in space group $A2_1am$. This discovery encourages us to search for $M^{II}SrTa_2O_7$ where M is a divalent 3d transition metal cation. Since divalent 3d transition metal cations have similar ionic radii with the Li^+ cation in a tetrahedral geometry, it is possible that $M^{II}SrTa_2O_7$ is isostructural to $Li_2SrTa_2O_7$ and adopts a polar crystal structure. However, direct ceramic synthesis towards $M^{II}SrTa_2O_7$ will lead to the formation of some thermodynamically stable binary and ternary oxides. It is therefore interesting to study if $M^{II}SrTa_2O_7$ can be synthesized via cation exchange reactions from $Li_2SrTa_2O_7$. This chapter will be focused on the synthesis and characterisation of $MnSrTa_2O_7$.

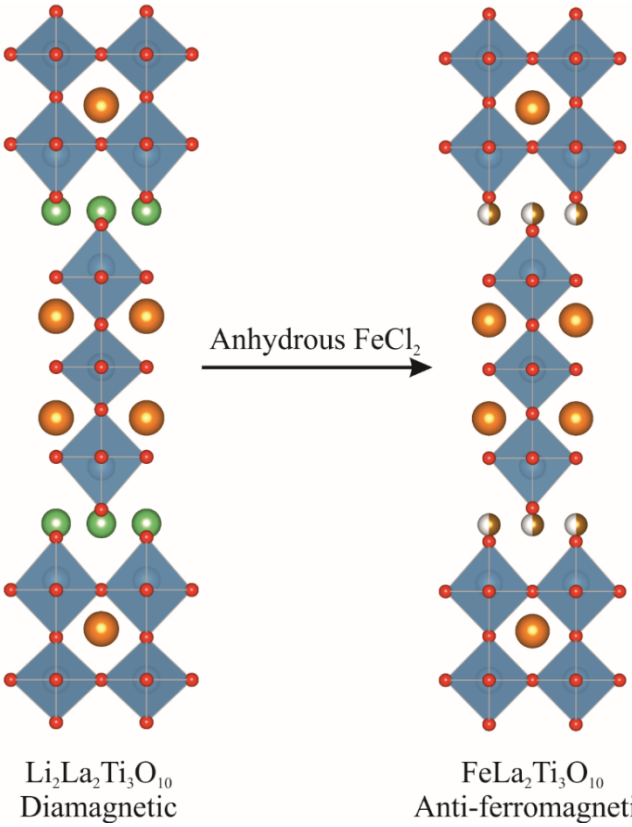


Figure 7.1. Cation exchange reaction from diamagnetic $Li_2La_2Ti_3O_{10}$ to antiferromagnetic $FeLa_2Ti_3O_{10}$. The green, gold and white/brown spheres are the Li^+, La^{3+} and Fe^{2+} cations, respectively, the Ti^{4+} cations are inside the polyhedra. The Fe^{2+} cations adopt a disordered arrangement in the interlayer tetrahedral sites[82].

7.2 Synthesis

Powder samples of $Li_2SrTa_2O_7$ were prepared by ceramic synthesis, as described in Chapter 6. $MnSrTa_2O_7$ was synthesized from $Li_2SrTa_2O_7$ and anhydrous $MnCl_2$ (98%). $Li_2SrTa_2O_7$ and anhydrous $MnCl_2$ were combined in a 1:10 molar ratio by grinding in an agate pestle and mortar in an argon-filled glovebox. The mixture was then placed in a Pyrex tube and heated at 375 °C under flowing argon for 4 days. The mixture was then washed with distilled water to remove the remaining metal chlorides, and dried for 12 hours at 140 °C. Reaction progress and final sample purity were assessed by X-ray powder diffraction data collected using a PANalytical X'pert diffractometer incorporating an X'celerator position sensitive detector (monochromatic Cu Kα1 radiation).

7.3 Results

7.3.1 Optical SHG measurements

Powder SHG measurements show that $MnSrTa_2O_7$ is SHG active, with an intensity of 0.54 times of the α-SiO_2 standard. This observation suggests that $MnSrTa_2O_7$ adopts a non-centrosymmetric crystal structure.

7.3.2 Room temperature synchrotron X-ray diffraction

High-resolution synchrotron X-ray powder diffraction data collected from $MnSrTa_2O_7$ at ambient temperature can be indexed using an orthorhombic unit cell with a $\sqrt{2} \times \sqrt{2} \times 1$ geometric expansion of the aristotype *I*4/*mmm* unit cell, (a = 5.5687 Å, b = 5.5682 Å, c = 19.0007 Å) of an n = 2 Ruddlesden-Popper phase. The extinction conditions are consistent with an *A*-centred or primitive structure. The observed SHG activity, the unit cell expansion and the extinction conditions together suggest that $MnSrTa_2O_7$ may adopt a similar polar structure to $Li_2SrTa_2O_7$ in space group $A2_1am$. Therefore an $A2_1am$ symmetry model was constructed based on the refined structure of $Li_2SrTa_2O_7$ and the Mn^{2+} cations adopt a disordered arrangement with 50% occupancy in the lithium sites between perovskite layers. The model was refined against synchrotron X-ray diffraction data and the refinement gives a reasonably good fit, as shown in Figure 7.2. The intensity mismatch is due to a strong preferred orientation effect.

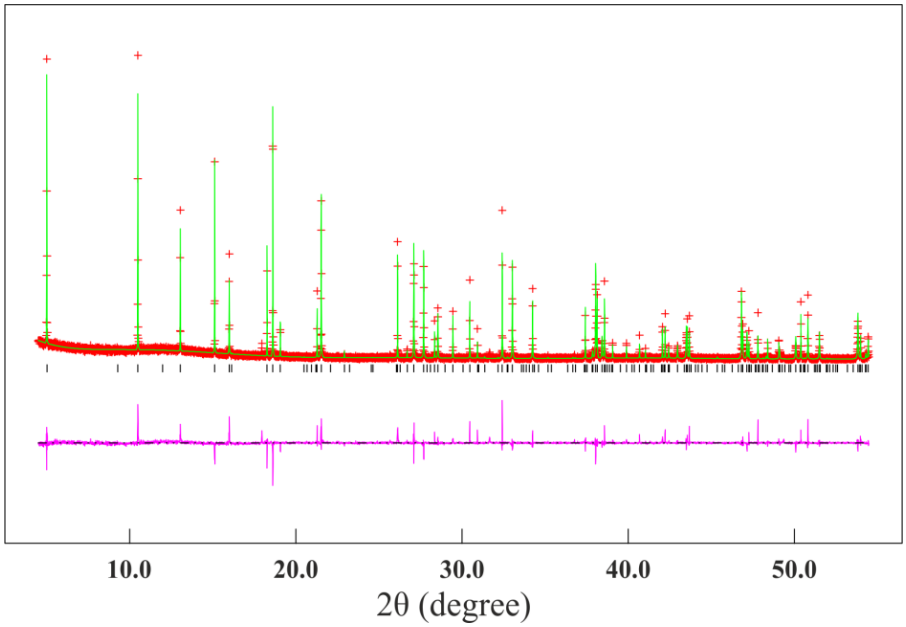


Figure 7.2. Observed, calculated and difference plots from the refinement of the *A*2$_1$*am* model against the synchrotron X-ray diffraction data collected from $MnSrTa_2O_7$ at 298 K.

7.3.3 Room temperature neutron powder diffraction

7.3.3.1 Commensurate structure

Neutron powder diffraction data were collected from a sample of approximately 4 g of $MnSrTa_2O_7$ at ambient temperature using the HRPD instrument at ISIS. In common with the analogous synchrotron X-ray diffraction data, neutron diffraction data can be indexed using an expanded unit cell with a $\sqrt{2} \times \sqrt{2} \times 1$ geometric expansion of the aristotype *I*4/*mmm* cell. The extinction conditions are consistent with an *A*-centred or a primitive structure. The *A*2$_1$*am* symmetry model obtained from the analysis of synchrotron X-ray diffraction data was refined against the neutron diffraction data. This model has a single 8*b* crystallographic site to accommodate the Mn^{2+} cations therefore the Mn^{2+} cations must adopt a disordered arrangement to follow the stoichiometry. The refinement proceeded smoothly and the manganese occupancy was refined as the last step. The refinement gives a good statistical and visual fit. The refined manganese fraction is 0.495(6), therefore it is concluded that the Mn^{2+} cations adopt a disordered arrangement with 50% occupancy and there is no lithium left to respect the stoichiometry. The observed, calculated and difference

plots from the refinement of the $A2_1am$ model are shown in Figure 7.3. A close inspection of the refinement plots reveals that there are some weak peaks which cannot be indexed by the $A2_1am$ model or any expanded cell from the current structural model. These observations lead us to suspect the possibility of an incommensurate crystal structure for $MnSrTa_2O_7$.

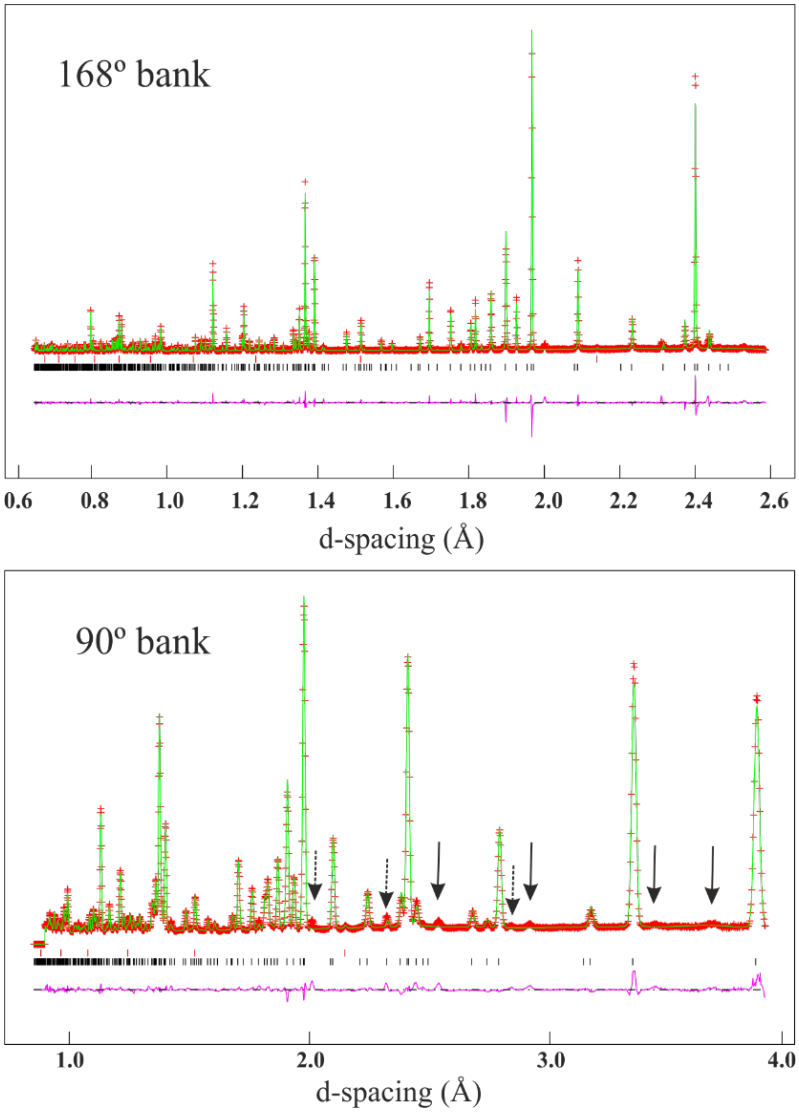


Figure 7.3. Observed, calculated and difference plots from the refinement of the $A2_1am$ model against high-resolution neutron diffraction data collected from $MnSrTa_2O_7$ at 298 K. Vanadium was as added as secondary phases with red tick-marks. Peaks with solid arrows can be indexed using a superstructure in superspace group $A2_1am(0b0)000$. Peaks with dashed arrows are attributed to impurity phases which are also seen in the precursor phase $Li_2SrTa_2O_7$ (Figure 6.3).

7.3.3.2 Incommensurate structure and the structural modulation

Peaks labelled with solid arrows in Figure 7.3 can be indexed with a superstructure in superspace group $A2_1am(0b0)000$ and the modulation vector was found to be 0.86. The following question was where the modulation comes from. The refined unmodulated crystal structure in space group $A2_1am$ is shown in Figure 7.4. In this structure, there is a single crystallographic site to accommodate Mn^{2+} cations with a disordered arrangement (Figure 7.5). This disordered cation configuration leads to short Mn-Mn bonds and hence strong cation-cation repulsion. Using Coulomb's law, $F = k_e \frac{q_1 q_2}{r^2}$ (k_e : Coulomb's constant; $q_1 q_2$: magnitudes of the charges; r: distance between the charges), the divalent charge means the nearest Mn-Mn repulsion would be as approximately four times large as the Li-Li repulsion in $Li_2SrTa_2O_7$ if Mn cations adopt a disordered arrangement. As demonstrated in $NaNdM_2O_7$ (M = Nb/Ta) in Chapter 4, a checkerboard-type order results in longer cation-cation bond distances and weaker repulsion (Figure 7.5). Therefore the modulation of Mn occupancy was refined and the refinement gives a good fit to both main peaks and satellite peaks. Figure 7.6 shows the refinement plots of the $A2_1am(0b0)000$ model using the JANA2006 software[83]. The refined structure is shown in Figure 7.7. It can be clearly observed that the refined structure contains domains of Mn^{2+} cations, which are connected by stripes or faults. Mn^{2+} cations adopt local checkerboard order in these domains and this local order reduces Mn-Mn repulsion compared to the disordered arrangement.

The dashed box shown in Figure 7.7 is not a unit cell as the translational symmetry along y is lost. The dashed box is shown to help visualize the local cation order. Full details of the parameters from the refinements are shown in Table 7.1. Selected bond lengths from the refined structure of $MnSrTa_2O_7$ are shown in Table 7.2.

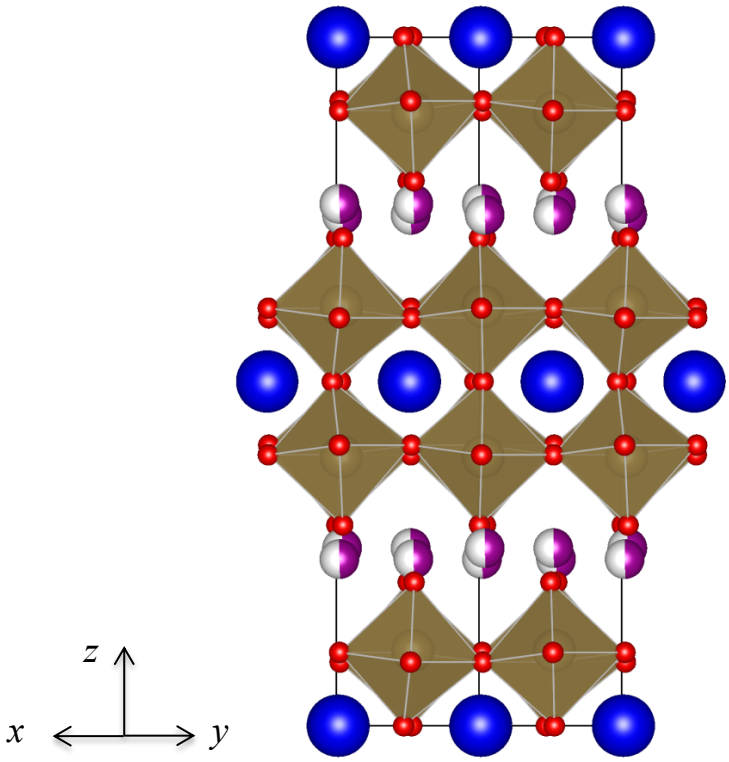


Figure 7.4. The refined unmodulated structure of $MnSrTa_2O_7$ in space group $A2_1am$. The violent/white and blue spheres are the Mn^{2+} and Sr^{2+} cations respectively, the Ta^{5+} cations are inside the polyhedra.

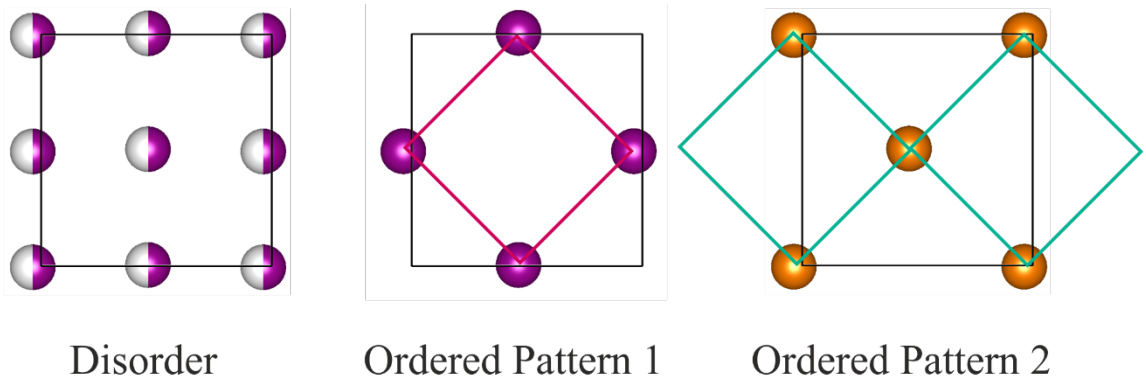


Figure 7.5. Disordered and ordered arrangements of the Mn^{2+} cations viewing along the stacking axis, solid squares show the $A2_1am$ unit cell size. There are two different types of checkerboard arrangements.

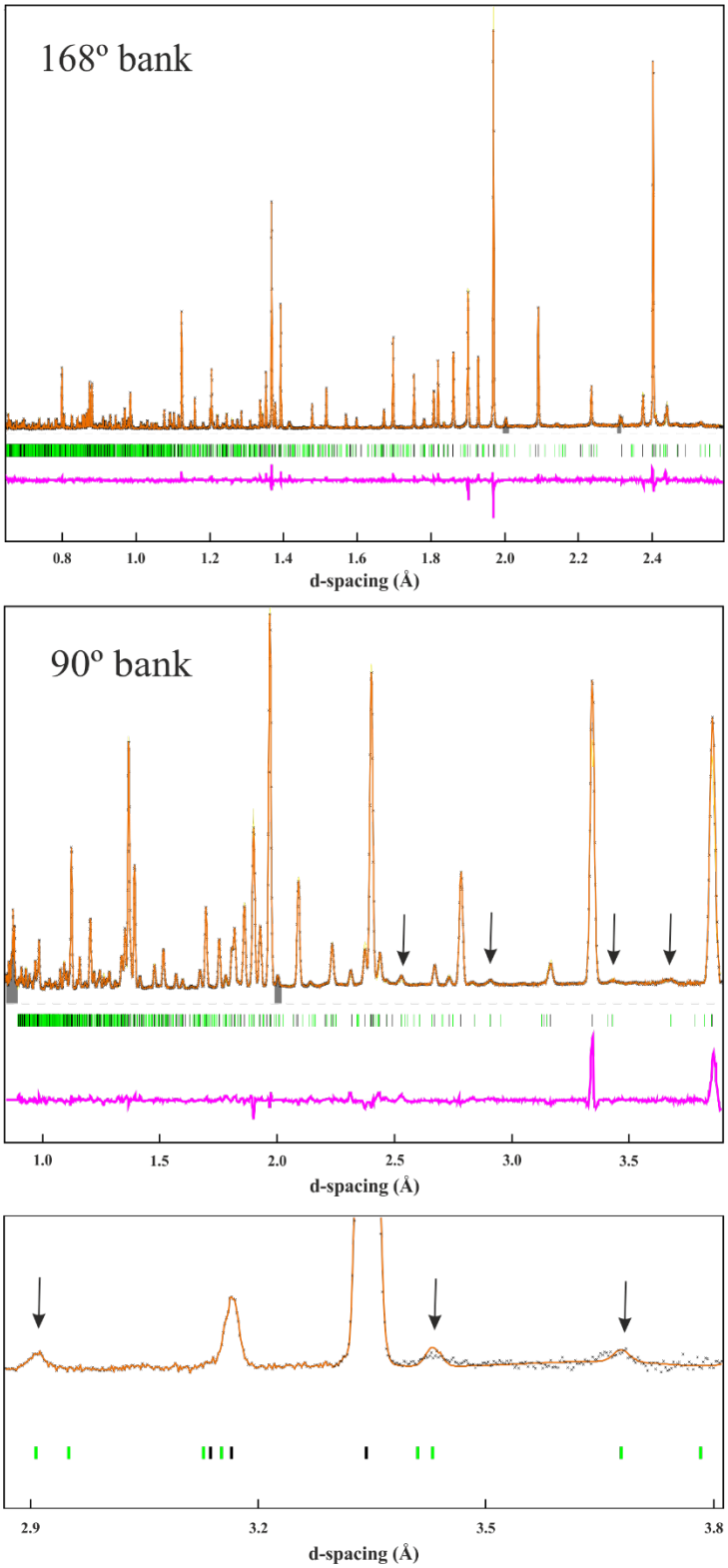


Figure 7.6. Observed, calculated and difference plots from the refinement of the *A*2$_1$*am*(0b0)000 model against high−resolution neutron diffraction data collected from $MnSrTa_2O_7$ at 298 K. Black tick marks suggest the reflection positions from the average structure; Green tick marks show the positions of the satellite reflections due to a structural modulation along *y*. Peaks with solid arrows are the strongest satellite reflections from the structure modulation. The bottom diagram shows the fits of selected satellite peaks. The shaded peak at 2.0 Å corresponds to an impurity phase which forms during the synthesis of the precursor phase $Li_2SrTa_2O_7$.

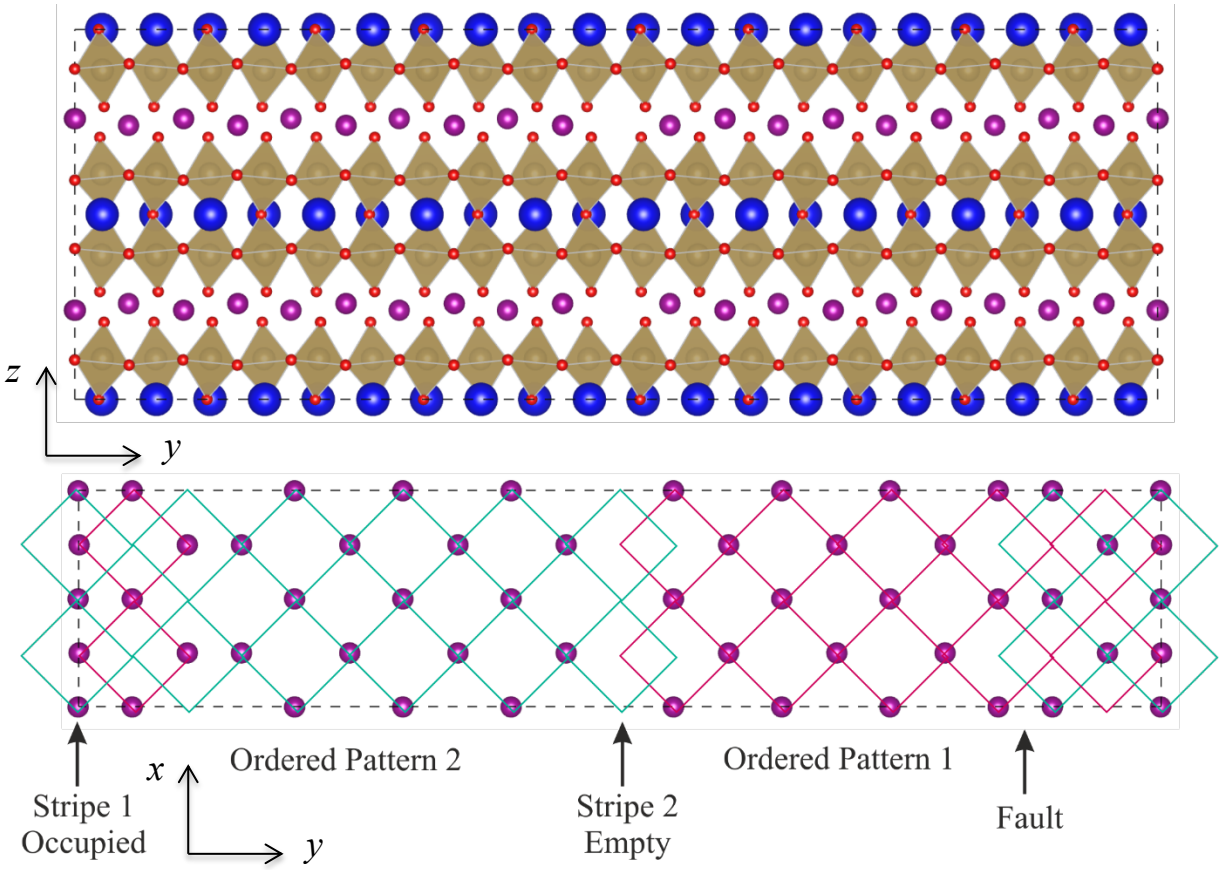


Figure 7.7. Top: Approximant incommensurate structure viewing along *x*. Bottom: Approximant distribution of Mn^{2+} cations viewing along *z*. In contrast to the commensurate $A2_1am$ structure, locally Mn^{2+} cations adopt a checkerboard type order. Local order regions are connected by either stripes (occupied or empty) or faults. It should be noticed that the dashed lines show the box size, but do not represent a unit cell.

Atom	site	*x*	*y*	*z*	Fraction	U_{iso} (Å^3)
Mn(1)	8*b*	0.4962(40)	0.4954(80)	0.2590(2)	0.5	0.0145(11)
Sr(1)	4*a*	0.2402(12)	0.2477(5)	0	1	0.0069(3)
Ta(1)	8*b*	0.7514(11)	0.2537(5)	0.1096(1)	1	0.0023(2)
O(1)	4*a*	0.7477(15)	0.2198(7)	0	1	0.0134(7)
O(2)	8*b*	0.7302(11)	0.2694(5)	0.2084(1)	1	0.0091(5)
O(3)	8*b*	0.9948(20)	0.4999(15)	0.0926(1)	1	0.0031(3)
O(4)	8*b*	0.9966(20)	0.9985(20)	0.1066(1)	1	0.0162(5)
$MnSrTa_2O_7$ – superspace group $A2_1am$(0b0)000, q2 = 0.8638 *a* = 5.5672(1) Å, *b* = 5.5673(1) Å, *c* = 18.9925(1) Å, volume = 588.65(1) Å^3 Formula weight: 615.85 g mol^{-1} Radiation source: Neutron Time of flight Temperature: 298 K GOF = 4.03, wRp = 5.22%, Rp = 5.98%						

Table 7.1. Parameters from the structural refinement of $MnSrTa_2O_7$ against neutron powder diffraction data collected at 298 K. Parameters are displayed to show the basic (average) structure.

Cation	Anion	length (Å)	BVS
Mn(1)	O(2) × 1	2.20(4)	Mn +1.61
	O(2) × 1	2.05(4)	
	O(2) × 1	2.10(4)	
	O(2) × 1	2.18(4)	
Sr(1)	O(1)	2.746(11)	Sr +2.26
	O(1)	2.603(5)	
	O(1)	2.965(5)	
	O(1)	2.830(11)	
	O(3) × 2	2.633(9)	
	O(3) × 2	2.660(9)	
	O(4) × 2	2.804(9)	
	O(4) × 2	2.831(9)	
Ta(1)	O(1)	2.090(2)	Ta +5.13
	O(2)	1.881(3)	
	O(3)	2.007(11)	
	O(3)	1.954(11)	
	O(4)	1.997(13)	
	O(4)	1.971(13)	

Table 7.2. Selected bond lengths from the refined structure of $MnSrTa_2O_7$ (300 K).

7.3.4 Magnetic characterisation of $MnSrTa_2O_7$

7.3.4.1 SQUID Magnetometry of $MnSrTa_2O_7$

Magnetisation data were collected from a sample of $MnSrTa_2O_7$ in an applied field of 100 Oe in the temperature range $5 \leq T/K \leq 300$. The zero-field cooled (ZFC) and field cooled (FC) data are shown in Figure 7.8. Both the zero-field cooled and field cooled data sets can be fitted to the Curie-Weiss law ($\chi = C / (T - \theta)$) in the temperature range $150 \leq T/K \leq 300$ to yield values of $C = 4.396(10)$ cm^3 K mol^{-1} and $\theta = -158.23(56)$ K. The observed moment (5.93 μ_B), calculated from the Curie constant, is in a good agreement with a value of 5.92 μ_B expected for the spin-only moment of one high-spin, $S = \frac{5}{2}$ Mn^{2+} center per formula unit. The zero-field cooled and field cooled data diverge below 45 K, suggesting a transition to a magnetically ordered state. Magnetization-field isotherms collected at 300 K are linear and pass through the origin, while in contrast, the analogous data collected at 5 K shows a

small hysteresis, as shown in Figure 7.9. These observations together suggest canted antiferromagnetic order (weak ferromagnetism). Therefore low temperature neutron diffraction data were collected to investigate if there is any long-range magnetic order in $MnSrTa_2O_7$.

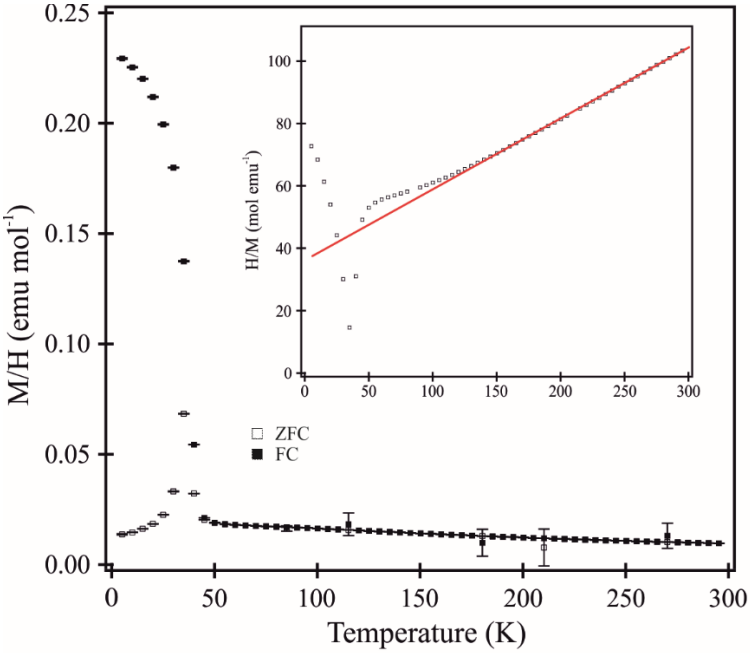


Figure 7.8. Zero-field cooled and field cooled magnetisation data collected from $MnSrTa_2O_7$. Inset shows a fit to the Curie-Weiss law to yield values of C = 4.396(10) cm^3 K mol^{-1} and θ = -158.23(56) K.

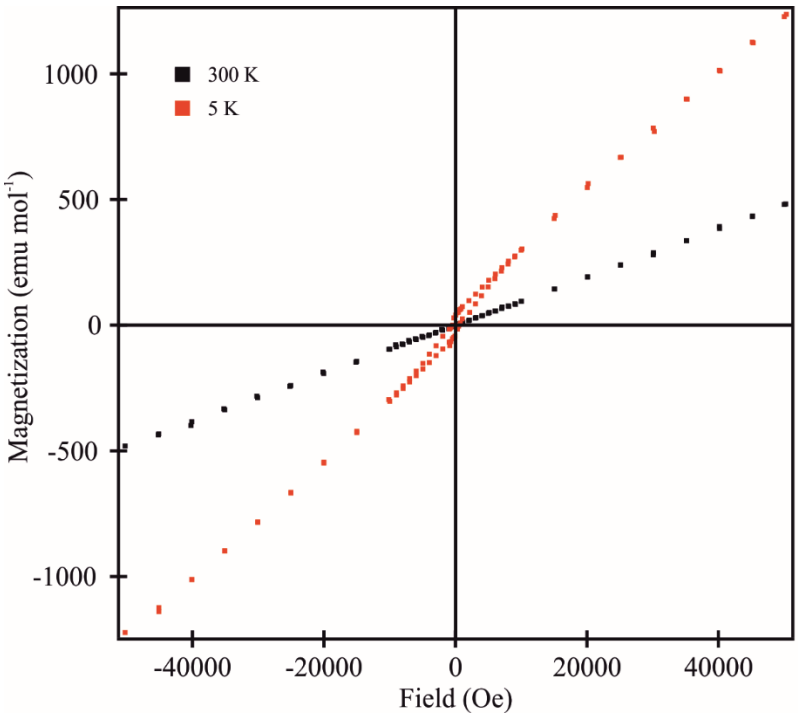


Figure 7.9. Magnetization-field isotherms collected from $MnSrTa_2O_7$ at 5 K and 300 K.

7.3.4.2 Low temperature neutron powder diffraction (1 K)

Neutron powder diffraction data were collected from a sample of 4 g $MnSrTa_2O_7$ in the temperature range $1 \leq T/K \leq 200$ using the WISH instrument at ISIS. Comparison of the neutron powder diffraction data collected at 200 K and 1 K reveals that there are a series of additional peaks in the 1 K diffraction data (Figure 7.10). The SQUID magnetization data (Figure 7.8) indicates that at around 45 K $MnSrTa_2O_7$ undergoes a magnetic transition and as such the additional diffraction peaks are attributed to a magnetically ordered state. The additional peaks can be indexed with the refined crystallographic superstructure. A series of possible magnetic models were constructed based on this superstructure. Their diffraction patterns were simulated and compared to the observed magnetic reflections in the 1 K diffraction data. The best match to the data was achieved by using the model in magnetic space group $A2_1a'm'(0b0)000$, in which the Mn lattice adopts G-type antiferromagnetic order.

The refinement in the magnetic space group $A2_1a'm'(0b0)000$ proceeded smoothly. The crystal structure was refined first, followed by the magnetic structure. The refined modulation vector is 0.86, which is consistent with the value from the refinement against the 300 K HRPD data. The refinement of the magnetic moment shows that any moment along *x* or *y* direction would give calculated intensities which are not observed from the diffraction data. Hence the moment was deemed to be only along *z* and the refined Mn moment is 4.131(8) μ_B. The refinement gives good statistical and visual fits. The observed, calculated and difference plots using the superspace group $A2_1a'm'(0b0)000$ against the 1 K neutron diffraction data are shown in Figure 7.11. It is noticed that some magnetic reflections can only be indexed and fitted as the modulated satellite peaks (with green tick marks in Figure 7.11). This observation shows that the Mn modulation is unambiguous as it is the only magnetic cation. The refined crystal structure is analogous to Figure 7.7. The

refined magnetic structure is shown in Figure 7.12. Full details of the parameters from the refinements are shown in Table 7.3. Selected bond lengths from the refined structure are shown in Table 7.4.

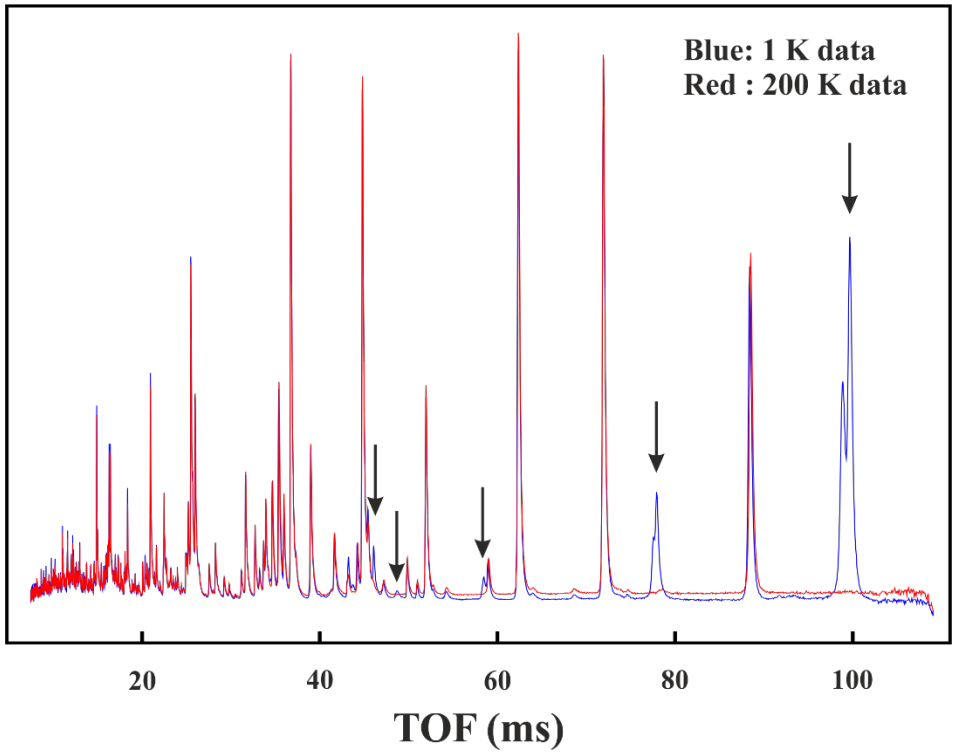


Figure 7.10. Neutron diffraction patterns collected from $MnSrTa_2O_7$ at 200 K (red) and 1 K (blue) using the WISH diffractometer (122° bank). Peaks labelled with arrows are attributed to a magnetically ordered state at 1 K.

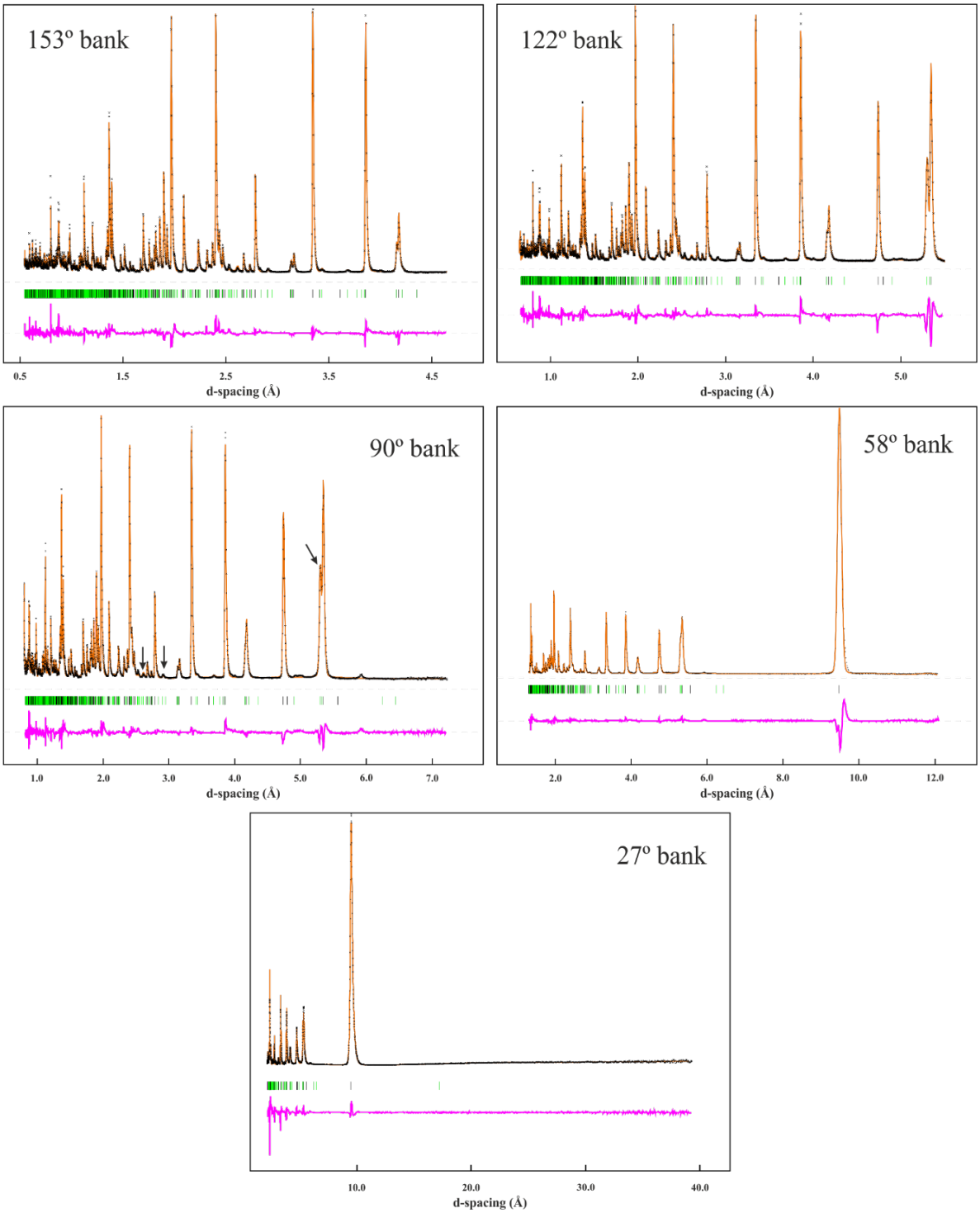


Figure 7.11. Observed, calculated and difference plots from the refinement of the $A2_1a'm'(0b0)000$ model against the neutron diffraction data collected from $MnSrTa_2O_7$ at 1 K. Black tick marks suggest the reflection positions from the average structure; Green tick marks show the positions of the satellite reflections due to the Mn modulation along *y*. The strongest magnetic peaks are found to be at 5.4 Å and 4.1 Å. Peaks labelled with solid arrows in the 90° bank are some of the satellite magnetic peaks, which shows the Mn modulation.

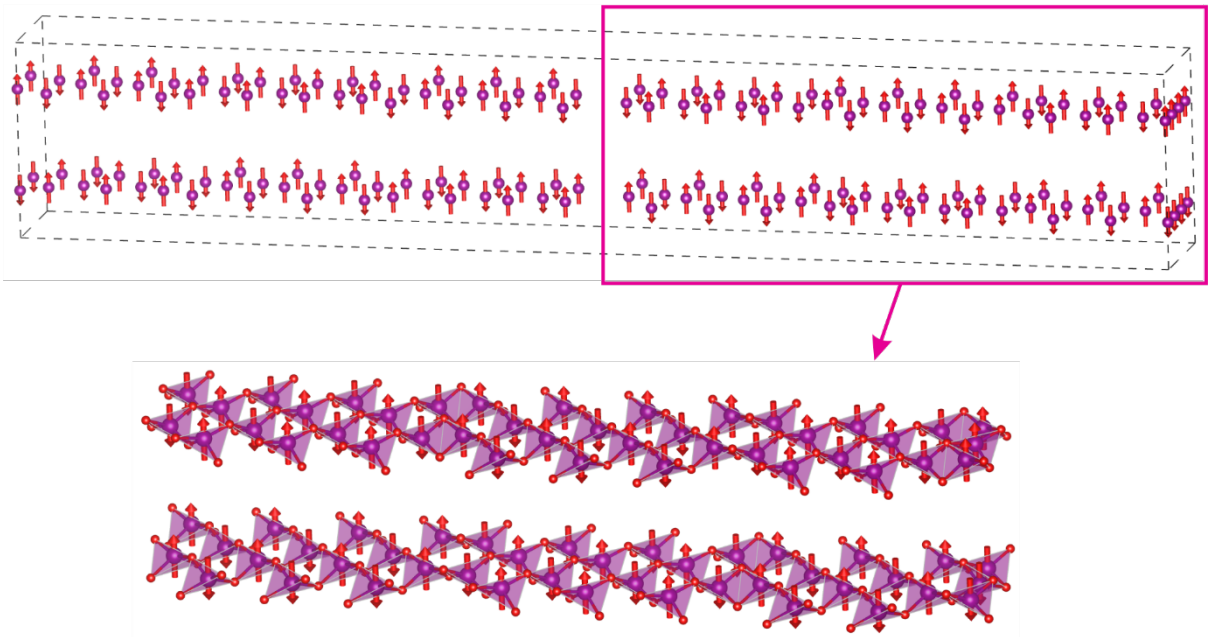


Figure 7.12. The simple G-type magnetic structure from a refinement against the neutron diffraction data collected at 1 K. Top: The refined magnetic structure with a box dimension *a* ~ 11.13 Å, *b* ~ 111.38 Å and *c* ~ 18.95 Å; Bottom: A local view of the magnetic structure, it can be seen that the bulk magnetic structure can be viewed as anti-ferromagnetic domains connected by some 'faults'. The dashed box is shown to help visualizing the structure and it is not a unit cell.

Atom	site	*x*	*y*	*z*	Fraction	U_{iso} (Å^3)
Mn(1)	8*b*	0.4694(20) $M_x = 0$	0.4964(30) $M_y = 0$	0.2602(2) $M_z = 4.131(8)$	0.5	0.0055(16)
Sr(1)	4*a*	0.2393(16)	0.2419(9)	0	1	0.0081(5)
Ta(1)	8*b*	0.7472(14)	0.2506(8)	0.1096(1)	1	0.0078(3)
O(1)	4*a*	0.7324(18)	0.2224(12)	0	1	0.0172(12)
O(2)	8*b*	0.7613(9)	0.2720(6)	0.2084(1)	1	0.0074(6)
O(3)	8*b*	0.9939(15)	0.4976(17)	0.0909(7)	1	0.0026(5)
O(4)	8*b*	0.0001(16)	0.9976(20)	0.1091(1)	1	0.0174(7)
$MnSrTa_2O_7$ – superspace group $A2_1a'm'(0b0)000$, q2 = 0.8642 *a* = 5.5671(1) Å, *b* = 5.5689(1) Å, *c* = 18.9525(1) Å, volume = 587.58(1) Å^3 Formula weight: 615.85 g mol^{-1} Radiation source: Neutron Time of flight Temperature: 1 K GOF = 8.11, wRp = 6.31%, Rp = 6.91%						

Table 7.3. Parameters from the structural refinement of $MnSrTa_2O_7$ against neutron powder diffraction data collected at 1 K. Parameters are displayed to show the basic (average) structure.

Cation	Anion	length (Å)	BVS
Mn(1)	O(2) × 1	1.983(15)	Mn +1.69
	O(2) × 1	1.992(14)	
	O(2) × 1	2.314(15)	
	O(2) × 1	2.273(14)	
Sr(1)	O(1)	2.824(14)	Sr +2.26
	O(1)	2.586(9)	
	O(1)	2.983(9)	
	O(1)	2.747(14)	
	O(3) × 2	2.620(13)	
	O(3) × 2	2.661(13)	
	O(4) × 2	2.811(9)	
	O(4) × 2	2.858(9)	
Ta(1)	O(1)	2.086(3)	Ta +5.13
	O(2)	1.877(3)	
	O(3)	2.020(12)	
	O(3)	1.976(12)	
	O(4)	1.950(12)	
	O(4)	1.992(12)	

Table 7.4. Selected bond lengths from the refined structure of $MnSrTa_2O_7$ (1 K).

7.3.4.3 Variable temperature neutron powder diffraction

Further neutron powder diffraction data were collected from $MnSrTa_2O_7$ at 5 K, 10 K, 15 K, 20 K, 25 K, 27.5 K, 30 K, 32.5 K, 35 K, 36 K, (every 1 K until 50 K), 52.5 K, 55 K, 60 K and 100 K using the same WISH instrument. The refined 1 K model was used for the refinements against the variable temperature neutron diffraction data to extract the ordered moments and the lattice parameters at these temperatures. In order to avoid a strong competition between different parameters, only the lattice parameters, the modulation vector, the magnetic moments and the background parameters were refined.

The modulation vector remains 0.86 at all temperatures. Figure 7.13 shows the evolution of the refined magnetic moments as a function of temperature in the temperature range $1 \leq T/\mathrm{K} \leq 43$. These data can be fitted to a power law, $M = M_0(1 - \frac{T}{T_N})^{\beta}$, to give following parameters: M_0 = 4.30(4) μ_B, T_N = 43.2(2) K, and β = 0.230(9). Combining this with the

ZFC/FC measurement (Figure 7.8), the magnetic transition temperature (T_N) is deemed to be approximately 43 K.

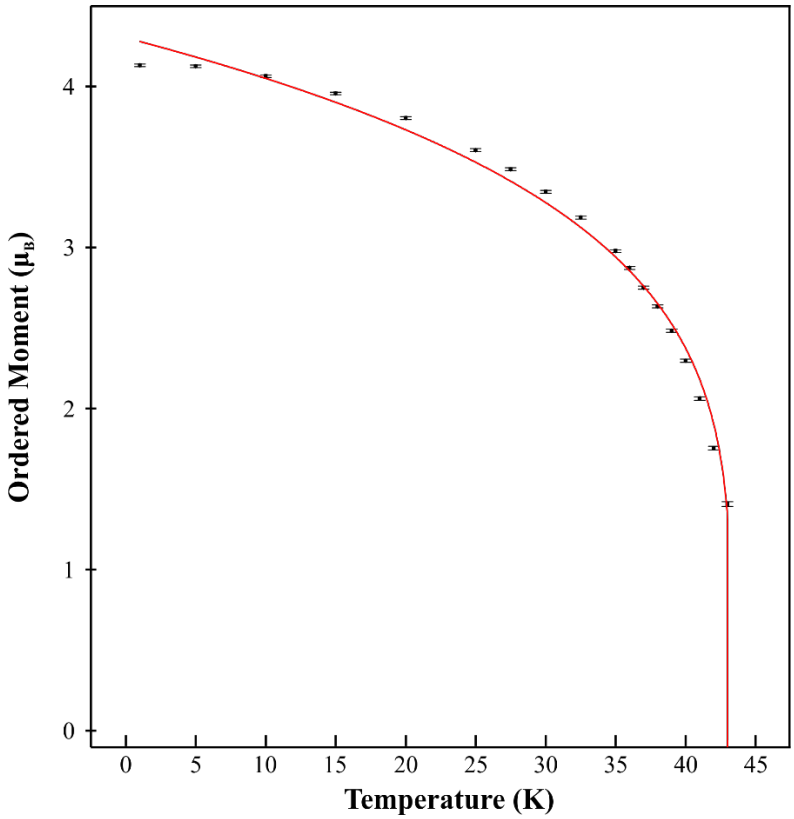


Figure 7.13. The ordered magnetic moment extracted from fits to variable temperature neutron powder diffraction data collected from $MnSrTa_2O_7$ in the temperature range $1 \leq T/K \leq 43$.

Figure 7.14 shows the evolution of the neutron powder diffraction patterns of $MnSrTa_2O_7$ measured as a function of temperature. It is noticed that some magnetic peak 'residuals' can still be observed in the 44 K and 50 K data but they are significantly broader than the magnetic peaks observed below 40 K. In addition, high backgrounds are observed around these residual peaks. These observations are attributed to the fact that the magnetic transition is a continuous, second-order transition and there is a temperature window in which magnetic moments are in a 'middle-range' ordered state. In this 'middle-range' ordered state, there is a correlation between the magnetic moments but this correlation is not strong enough to be considered as a standard long-range order. This 'middle-range' ordered state results in broad magnetic peaks in a neutron diffraction pattern. Cooling the

system down to a lower temperature would lead to sharper magnetic peaks and warming the system would lead to a complete disappearance of the magnetic peaks.

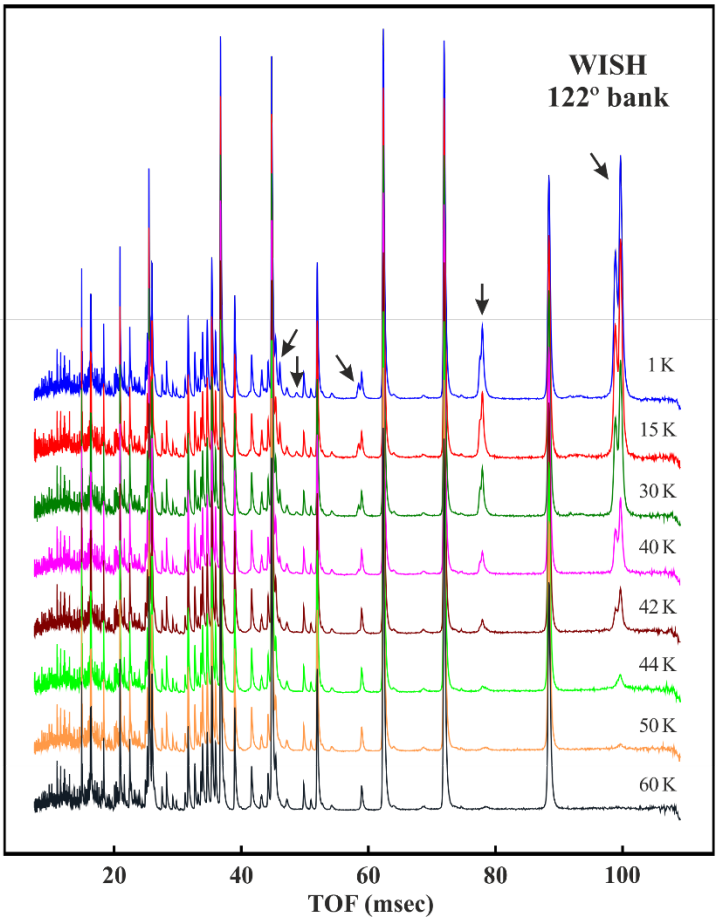


Figure 7.14. Evolution of the neutron diffraction patterns measured as a function of temperature. Magnetic peaks are labelled with the solid arrows.

The refined lattice parameters and cell volumes of the average structure are plotted as a function of temperature in Figure 7.15. A clear transition can be observed at approximately 38 K. The change in the cell parameters, especially the expansion of the average volume, is not a common behaviour one would expect when cooling a system down through the magnetic transition temperature. Another noticeable observation is that both *b* and *c* lattice parameters increase with a decreasing temperature during the transition while the *a* lattice parameter is very steady. Combining this observation with the fact that the electric polarisation is along *x*, it is concluded that this unusual magneto-lattice coupling is likely to be resulted from a magnetoelectric effect.

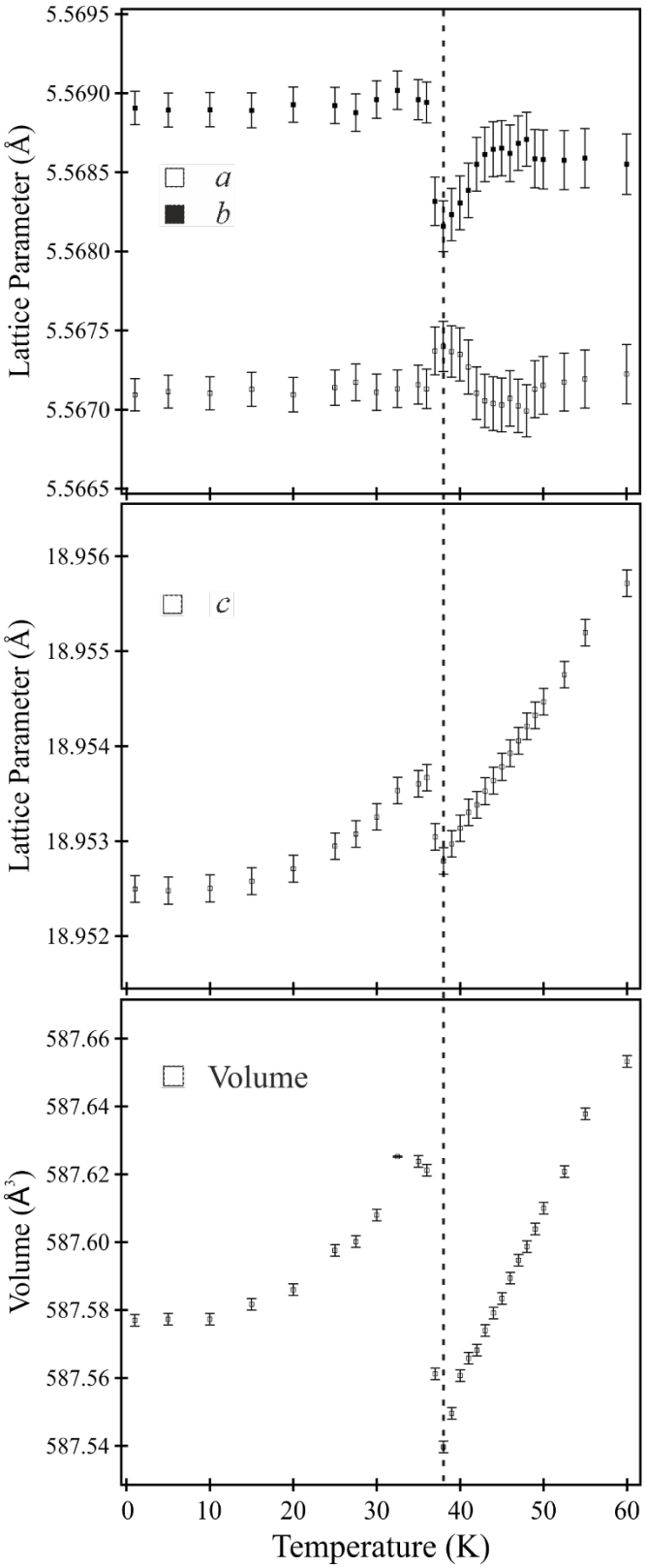


Figure 7.15. Temperature evolution of the average cell parameters for $MnSrTa_2O_7$ determined from the analysis of variable temperature neutron diffraction data.

7.4 Discussion

7.4.1 From $Li_2SrTa_2O_7$ to $MnSrTa_2O_7$: introducing magnetism into a polar phase

Most multiferroic materials are prepared by a single-step, ceramic synthesis approach which requires a high reaction temperature. One limitation of this 'heat and beat' approach is that it is difficult for chemists to predict the structures (hence the properties) of the reaction products. On the other hand, the successful synthesis of polar, magnetically ordered $MnSrTa_2O_7$ reveals a new approach, topochemical cation exchange, to synthesize novel multiferroic materials. Although there is a structural modulation in $MnSrTa_2O_7$, its average structure is the same as its precursor phase $Li_2SrTa_2O_7$. The structural similarity is attributed to the fact that Li^+ and Mn^{2+} cations have similar ionic radii. As discussed in previous chapters, the interlayer cation sizes have an influence on the tilting distortions, hence the bulk structures of layered perovskites. The similar ionic radii of Li^+ and Mn^{2+} cations mean replacing Li^+ with Mn^{2+} will not change the local structure of the $SrTa_2O_7$ perovskite sheets.

The cation exchange approach is widely applicable and can be used to synthesize other multiferroic materials. For example, both $Li_2SrNb_2O_7$ and $Li_2CaTa_2O_7$ have been reported to adopt polar structures[79, 84]. Similar cation exchange reactions with Mn^{2+} cations are expected to produce polar, magnetically ordered $MnSrNb_2O_7$ and $MnCaTa_2O_7$ (Figure 7.16). An obvious and subsequent question is if other divalent 3*d* transition metal cations, such Co^{2+} and Cu^{2+}, can be intercalated into a polar precursor in a similar manner to make more 'multiferroic' materials. This will be discussed in Chapter 8.

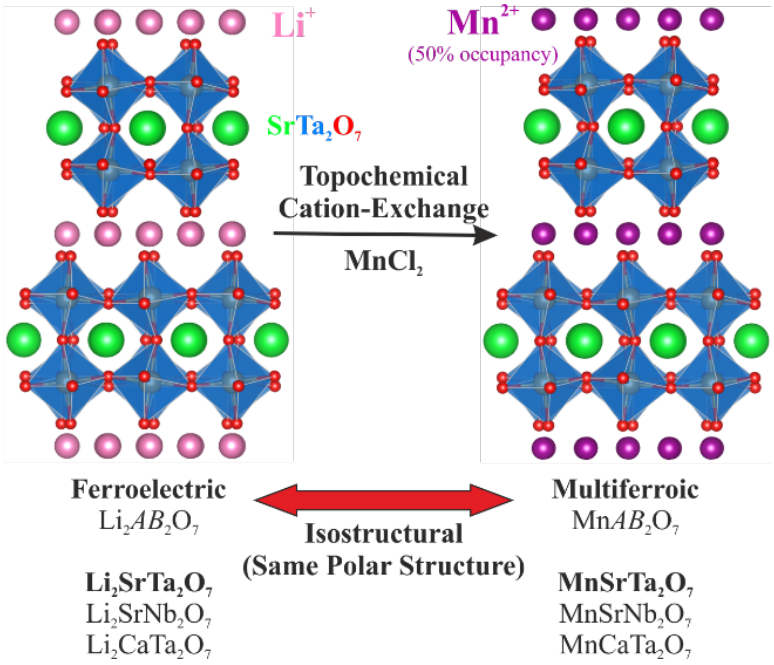


Figure 7.16. Using cation exchange chemistry to prepare novel multiferroic materials.

7.4.2 Structural modulation in $MnSrTa_2O_7$

A local checkerboard order of Mn^{2+} cations means longer Mn-Mn bonds and weaker Mn-Mn repulsion. It is noticed that Mn^{2+} cations are slightly under-bonded (BVS = 1.61, Table 7.2). As demonstrated in Chapter 4, a combination of stripe order and an $a^-a^-c^+$/-($a^-a^-c^+$) type tilting distortion can improve the interlayer cation bonding but also results in short metal-metal bond and hence strong repulsion. The fact that Mn^{2+} cations do not adopt the stripe order to benefit Mn-O bonding suggests that the priority for the structure is to minimize the unfavourable cation-cation repulsion.

One following question regarding the Mn order and the structural modulation is why $MnSrTa_2O_7$ does not adopt a simple unmodulated structure with long-range checkerboard order in space group $P4_2/mnm$ like $NaNdM_2O_7$ (M = Nb/Ta) (Chapter 4). One possible explanation is that this tetragonal structure has a higher symmetry and cations have fewer degrees of freedom to move compared to the incommensurate $A2_1am(0b0)000$ superstructure. The extra degrees of freedom in the superstructure is necessary in order to facilitate metal-oxide bonding despite the formation of small numbers of short Mn-Mn

bonds (Figure 7.7). Therefore it is concluded that the superstructure arises from a competition between minimising Mn-Mn repulsion and optimising metal-oxide bonding. The incommensurate $A2_1am(0b0)000$ structure can be considered as a 'hybrid' structure of the $A2_1am$ structure which provides good metal-oxide bonding, and the sodium-type $P4_2/mnm$ structure which minimises interlayer cation-cation repulsion.

One should be aware that although only Mn modulation is analysed in this thesis, a similar oxygen modulation is expected. The oxygen modulation and a possible correlation between Mn and oxygen modulation is currently under investigation.

7.5 Conclusion

Topochemical cation exchange from $Li_2SrTa_2O_7$ using anhydrous $MnCl_2$ leads to $MnSrTa_2O_7$ with a polar $A2_1am(0b0)000$ superstructure. SQUID magnetometry data suggest that there is a magnetic transition at approximately 45 K and the Mn^{2+} centers are antiferromagnetically ordered with a small canted moment at 5 K. Low temperature neutron diffraction experiments reveal that there is a long-range magnetic order and the Mn modulation is unambiguous, demonstrated by the observation of satellite magnetic peaks. The superstructure arises from a requirement of simultaneously facilitating metal-oxide bonding and minimising Mn-Mn repulsion.

The novel magneto-lattice coupling indicates a possible magnetoelectric effect in $MnSrTa_2O_7$. The successful synthesis of $MnSrTa_2O_7$ from $Li_2SrTa_2O_7$ suggests that topochemical cation exchange chemistry is a plausible 'retrosynthetic' method to prepare novel functional materials.

Chapter 8 – Topochemical Cation Exchange of $Li_2SrTa_2O_7$ Using Other Divalent 3*d* Transition Metal Cations

8.1 Introduction

As demonstrated in Chapter 7, a polar, magnetically ordered phase $MnSrTa_2O_7$ can be prepared by a cation exchange reaction from a thermodynamically stable precursor $Li_2SrTa_2O_7$ and anhydrous $MnCl_2$. It is therefore interesting to investigate if other divalent 3*d* transition metal cations can also be intercalated in a similar manner. The study is motivated by the fact that a series of divalent 3*d* transition metal cations have similar ionic radii with the Li^+ cation in a tetrahedral geometry (Table 8.1).

Ion	Li^+	Mn^{2+}	Fe^{2+}	Co^{2+}	Ni^{2+}	Cu^{2+}
Ionic radius (Å)	0.59	0.66	0.63	0.58	0.55	0.57

Figure 8.1. Ionic radii of selected divalent 3*d* transition metal cations in the tetrahedral geometry[85].

8.2 Synthesis

Powder samples of $Li_2SrTa_2O_7$ were prepared by a ceramic synthesis method, as described in Chapter 6. Synthesis of $M^{II}SrTa_2O_7$ (*M* = Fe, Co, Ni or Cu) was attempted by grinding $Li_2SrTa_2O_7$ and the corresponding anhydrous MCl_2 in a 1:10 molar ratio in an agate pestle and mortar in an argon-filled glovebox. The mixture was then placed in a Pyrex tube and heated at temperatures in a range $250 \leq T/°C \leq 450$ under flowing argon for several days. Reaction temperatures and reaction times were varied in order to find the optimal conditions. Samples of $CoSrTa_2O_7$ were prepared by heating mixtures at 375 °C under flowing argon for two periods of 3 days. Between heating cycles, samples of $CoSrTa_2O_7$ were reground in the glovebox. Samples of $CuSrTa_2O_7$ were prepared by heating mixtures at 400 °C under flowing argon for 4 days. Synthesis of $FeSrTa_2O_7$ and $NiSrTa_2O_7$ were deemed to be unsuccessful as no formation of $FeSrTa_2O_7$ was observed and the synthesis

of $NiSrTa_2O_7$ did not result in a single phase despite multiple attempts. After the final heating cycle, both samples of $CuSrTa_2O_7$ and $CoSrTa_2O_7$ were washed with distilled water to remove the remaining chlorides, and dried for 12 hours at 140 °C in air. $CuSrTa_2O_7$ and $CoSrTa_2O_7$ were further annealed at 300 °C for 12 hours under flowing oxygen and air respectively, as a final step. Reaction progress and final sample purity for both $CuSrTa_2O_7$ and $CoSrTa_2O_7$ were assessed by X-ray powder diffraction data collected using a PANalytical X'pert diffractometer incorporating an X'celerator position sensitive detector (monochromatic Cu Kα1 radiation).

The Cu content of samples was determined by a complexometric titration. Approximately 1 g $CuSrTa_2O_7$ was weighed and combined with LiOH in a 1:10 molar ratio. The mixture was then ground, loaded into a boat crucible and heated at 350 °C in air for 12 hours. The mixture was then dissolved in diluted sulfuric acid (~ 2M) and heated to 80 °C to give a pale-blue solution and white precipitates. The solute was collected by filtration and neutralized using a NaOH solution. This Cu^{2+} solution was titrated using a standard EDTA solution. The Co-containing compounds are insoluble in acid, therefore we were unable to determine the Co content using a complexometric titration approach.

8.3 Results

8.3.1 Structural characterisation of $Cu_xLi_{2x-2}SrTa_2O_7$

8.3.1.1 Optical SHG measurements and complexometric titration

Optical SHG measurements show $Cu_xLi_{2x-2}SrTa_2O_7$ has no detectable SHG intensity, suggesting that it adopts a centrosymmetric structure. The chemical formula determined from the complexometric titration is $Cu_{0.875}Li_{0.25}SrTa_2O_7$. This composition is used for the diffraction data analysis.

8.3.1.2 Room temperature synchrotron X-ray powder diffraction

High-resolution synchrotron X-ray powder diffraction data collected from $Cu_xLi_{2x-2}SrTa_2O_7$ at ambient temperature can be readily indexed with a metrically tetragonal unit cell (a = 3.9415 Å, c = 18.3025 Å) of an n = 2 Ruddlesden-Popper phase. The Cu^{2+}/Li^+ cations can adopt different ordered or disordered arrangements in the tetrahedral sites which lie between the perovskite layers. Since X-ray diffraction is reasonably sensitive to copper, synchrotron X-ray diffraction can be used to determine if there exists any long-range copper order even if the oxygen structure is not known exactly. Several models with different copper-ordered arrangements were constructed and refined against the synchrotron X-ray diffraction data.

In the aristotype *I*4/*mmm* model, there is only one crystallographic site to accommodate the Cu^{2+}/Li^+ cations and hence they must adopt a disordered arrangement. As demonstrated in Chapter 4, the structures of $NaNdM_2O_7$ ($P4_2/mnm$) and $LiNdM_2O_7$ ($B2em$) have different cation-ordered arrangements, with the Na^+ cations ordered as checkerboards while the Li^+ cations ordered as stripes. Therefore two analogous models were constructed to describe these two possible types of order for the Cu^{2+} cations (Figure 8.1).

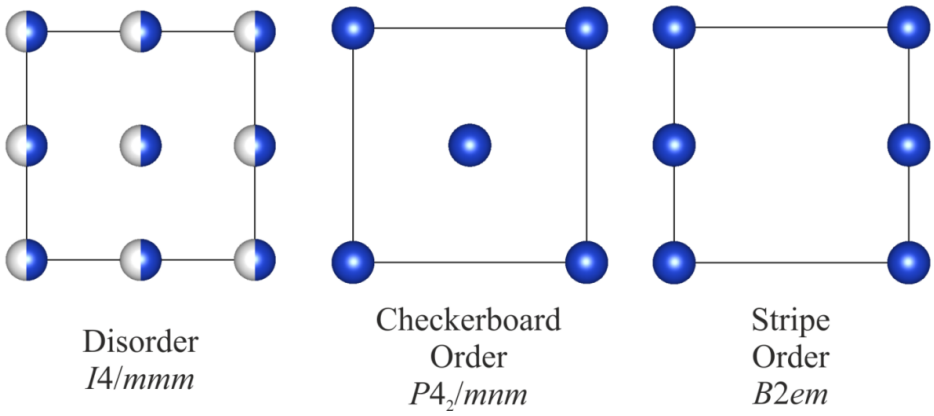


Figure 8.1. Disordered, checkerboard and stripe ordering of Cu^{2+}.

The *I*4/*mmm*, $P4_2/mnm$ and *B*2*em* models were refined against the synchrotron X-ray diffraction data. The refinements show that the two cation-ordered models give extra-simulated peaks which are not observed from the diffraction data while the *I*4/*mmm* model

does not give these extra peaks (Figure 8.2). When the Cu^{2+} cations are forced to adopt a disordered arrangement in the $P4_2/mnm$ and $B2em$ models, the extra-simulated peaks disappear, confirming that these extra peaks arise from the Cu order. Therefore it can be concluded that the Cu^{2+} cations possibly adopt either a disordered or a more complicated cation-ordered arrangement. Another possibility is that the Cu^{2+} cations adopt a short-range order which cannot be observed from X-ray diffraction data. The large intensity mismatch in the difference plots is attributed to a strong preferred orientation of the sample during the measurement.

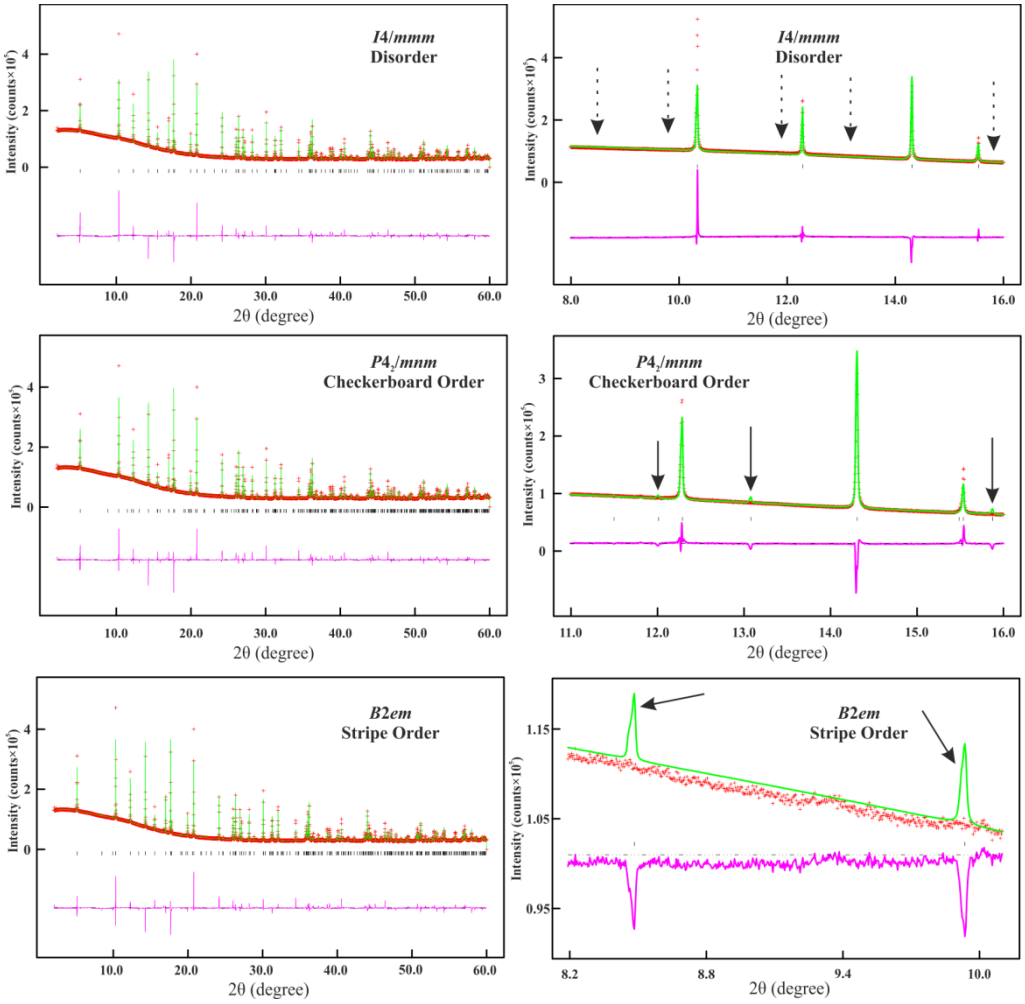


Figure 8.2. Observed, calculated and difference plots from the refinements of the *I*4/*mmm*, *P*4$_2$/*mnm* and *B*2*em* models against the synchrotron X-ray diffraction data collected from $Cu_xLi_{2-2x}SrTa_2O_7$. Regions of interests are zoomed in and shown in the right-hand-side. Solid arrows show the Cu ordering peaks which are not observed from the diffraction data. Dashed arrows show that these extra peaks are not simulated when using the *I*4/*mmm* model.

Both the checkerboard-order and stripe-order patterns in Figure 8.1 are periodic and the adjacent Cu layers adopt a primitive stacking arrangement. However, there are other types of ordering arrangements in which all Cu layers have the same type of order but the adjacent Cu layers are no longer stacked primitively. Figure 8.3 shows another three types of cation-ordered arrangements derived from the checkerboard and stripe arrangements in Figure 8.1. Three corresponding symmetry models describing these three arrangements were constructed by lowering the symmetry of the $P4_2/mnm$ and $B2em$ models using the ISODISTORT software[12]. It was found that both the 'Checkerboard Order2' and the 'Stripe Order2' arrangements can be described by a $P2_1$ space group while the 'Stripe Order3' can be described by a $P2$ space group.

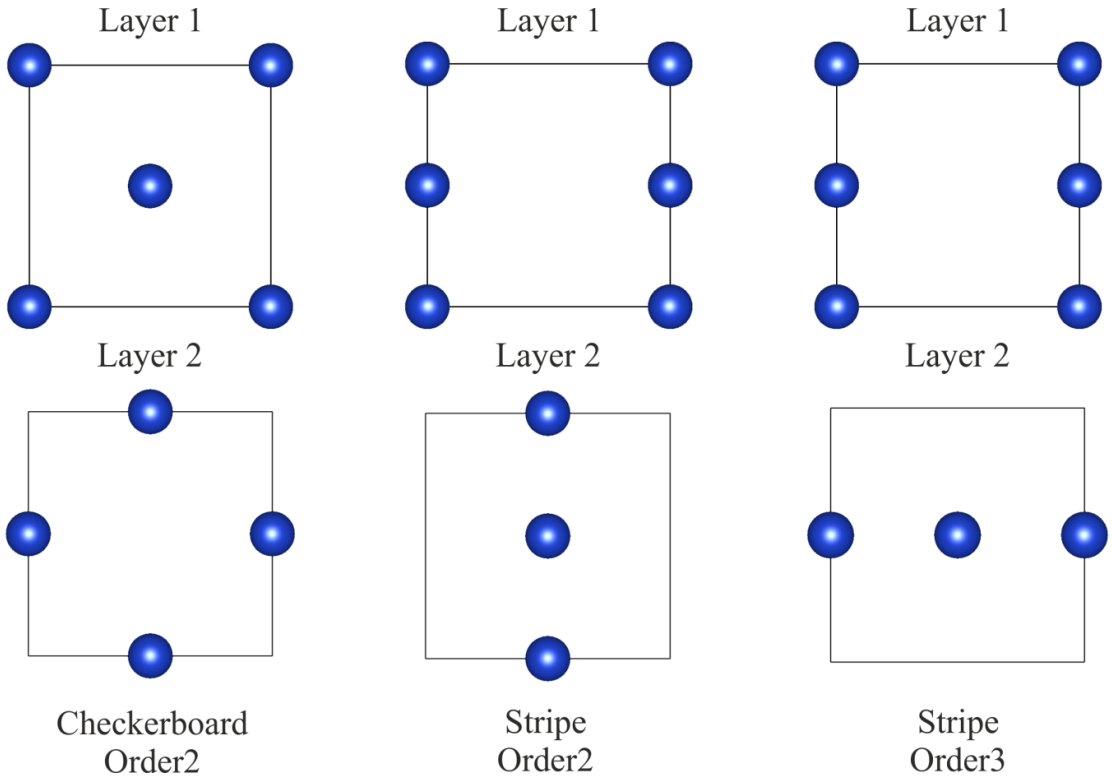


Figure 8.3. The 'modified' checkerboard and stripe ordering arrangements of the Cu^{2+} cations.

These models with different types of cation order were refined against the synchrotron X-ray diffraction data. No attempt was made to refine the atomic positions due to the large number of atoms in the asymmetric unit. The refinements show that all three cation-ordered

models in Figure 8.3 give extra diffraction peaks which are not seen from the data (Figure 8.4). Therefore it can be concluded from the analysis of the synchrotron X-ray diffraction data that Cu^{2+} cations adopt either a disordered arrangement between the perovskite layers, or they adopt a more complex ordering arrangement which is not included in Figure 8.2 or Figure 8.3. It is also possible that there is a short-range order of the Cu^{2+} cations, which cannot be observed from synchrotron X-ray diffraction data.

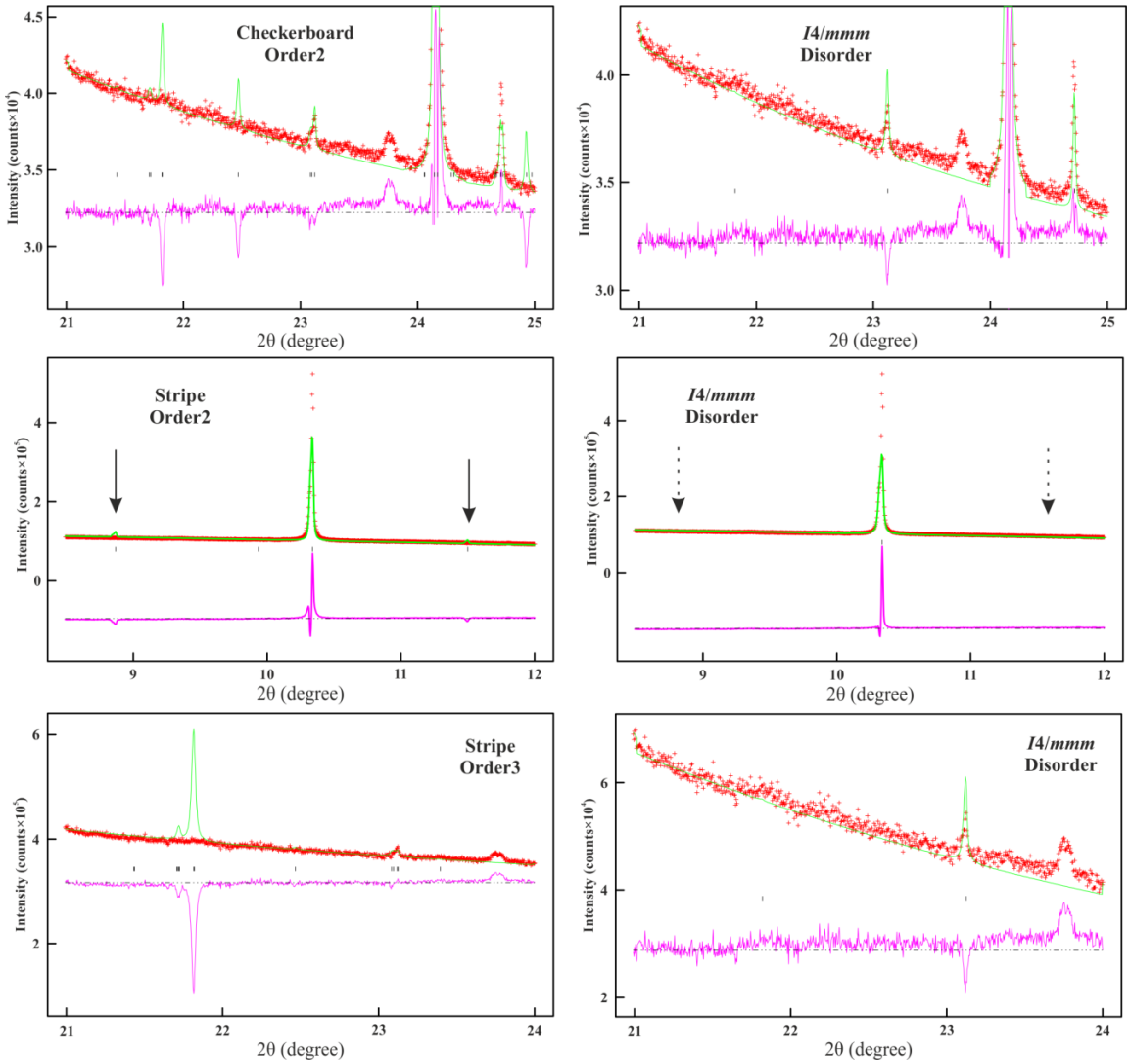


Figure 8.4. Observed, calculated and difference plots from the refinements of the cation-ordered models against the synchrotron X-ray diffraction data collected from $Cu_xLi_{2-2x}SrTa_2O_7$. The right-hand-side panels are the refinement plots using the *I*4/*mmm* model. Solid arrows show the Cu ordering peaks which are not observed from the diffraction data. Dashed arrows clearly show the corresponding extra peaks are not seen from the refinement of an *I*4/*mmm* model.

8.3.1.3 Neutron powder diffraction (HRPD)

Neutron powder diffraction data were collected from a sample of 3.7 g $Cu_xLi_{2-2x}SrTa_2O_7$ at ambient temperature using the HRPD instrument at ISIS. In common with the synchrotron X-ray diffraction data, the neutron diffraction data was initially indexed using a tetragonal, undistorted cell, and an *I*4/*mmm* symmetry model was constructed and refined against the neutron diffraction data. The observed, calculated and difference plots from the refinement are shown in Figure 8.5. It can be seen from the refinement plots that the simulated [200] reflection needs to split and some peak intensities are not accurately fitted. In addition, several weak reflections in the 90° bank cannot be indexed by the *I*4/*mmm* symmetry model and they can be attributed to either a bigger unit cell or impurity phases.

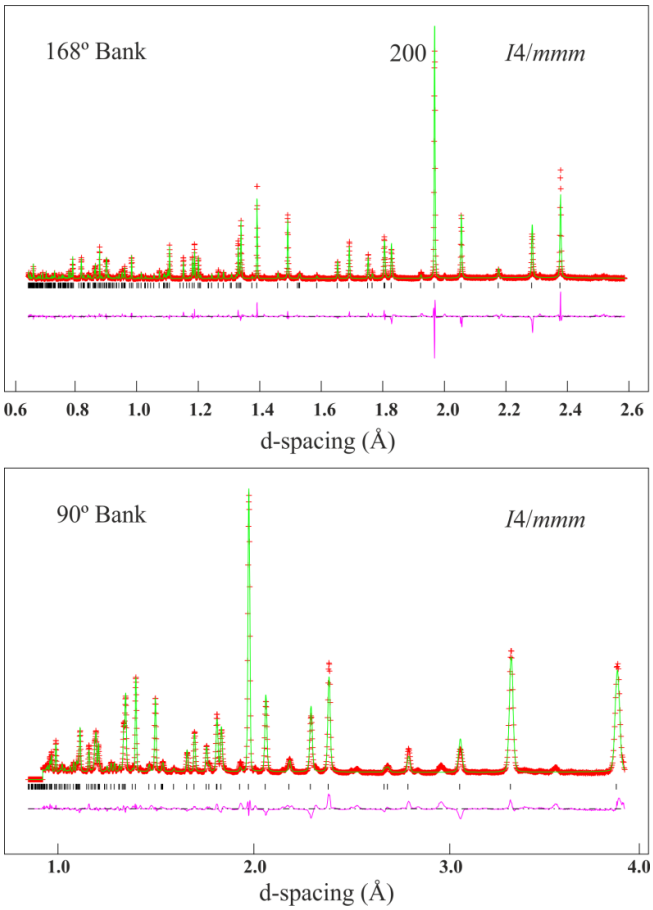


Figure 8.5. Observed, calculated and difference plots from the refinements of the *I*4/*mmm* model against the neutron powder diffraction data collected from $Cu_xLi_{2-2x}SrTa_2O_7$ (wRp = 9.29%, Rp = 8.77%).

The split [200] peak shown in Figure 8.5 cannot be indexed by a simple $\sqrt{2} \times \sqrt{2} \times 1$ geometric expansion of the *I*4/*mmm* cell to a bigger tetragonal or orthorhombic cell, but it can be indexed if the expanded cell is monoclinic with the stacking axis as the unique axis. The split peaks in this monoclinic cell can be indexed as [202] and [20-2]. The geometrical expansion and the lattice system are consistent with a $P2_1/m$ space group with an $a^-b^-c^+/a^-b^-c^+$ tilting distortion. It is noticed that this tilting distortion is not in the 'chemically plausible' distortion lists of $n = 2$ Ruddlesden-Popper structures in Chapter 4 and this is because this $P2_1/m$ structure with the $a^-b^-c^+/a^-b^-c^+$ tilting distortion cannot be generated by applying two irreducible representations on the aristotype *I*4/*mmm* structure. However, this model still obeys the chemically plausible principle as adjacent perovskite layers have the same type of tilting distortion, $a^-b^-c^+$. The $P2_1/m$ symmetry model has two separate 4*f* crystallographic sites to accommodate the Cu^{2+}/Li^+ cations. Since the analysis of the synchrotron X-ray diffraction data reveals that the Cu^{2+}/Li^+ cations are likely to have a disordered arrangement, the interlayer cations were set to be evenly distributed in the two 4*f* sites. During the refinement, the Cu^{2+}/Li^+ cations in the two 4*f* sites are constrained to have the same thermal displacement parameter. The observed, calculated and difference plots in space group $P2_1/m$ are shown in Figure 8.6. Several diffraction peaks in the 90° bank (marked with arrows) are still not indexed by this $P2_1/m$ model. A further expansion of the unit cell in *x*/*y* or *z* directions ($2 \times 2 \times 1$ or $\sqrt{2} \times \sqrt{2} \times 2$ expansion of the undistorted cell) cannot index these peaks, therefore at this stage they are deemed to be attributed to an impurity phase. A close inspection of the refined structure reveals that the Uiso value for the Cu^{2+}/Li^+ cations (0.04 $Å^2$) is too big. Combining this observation with the slight intensity mismatch shown in Figure 8.6, it is concluded that the $P2_1/m$ symmetry model is unlikely to be the final structural solution. However, the good fit to the low *d*-spacing regions suggests that the $P2_1/m$ model gives a good description of the local tilting

distortions. We therefore further collected neutron powder diffraction data using the GEM instrument to obtain structural information at higher *d*-spacing regions which are not seen in the HRPD data.

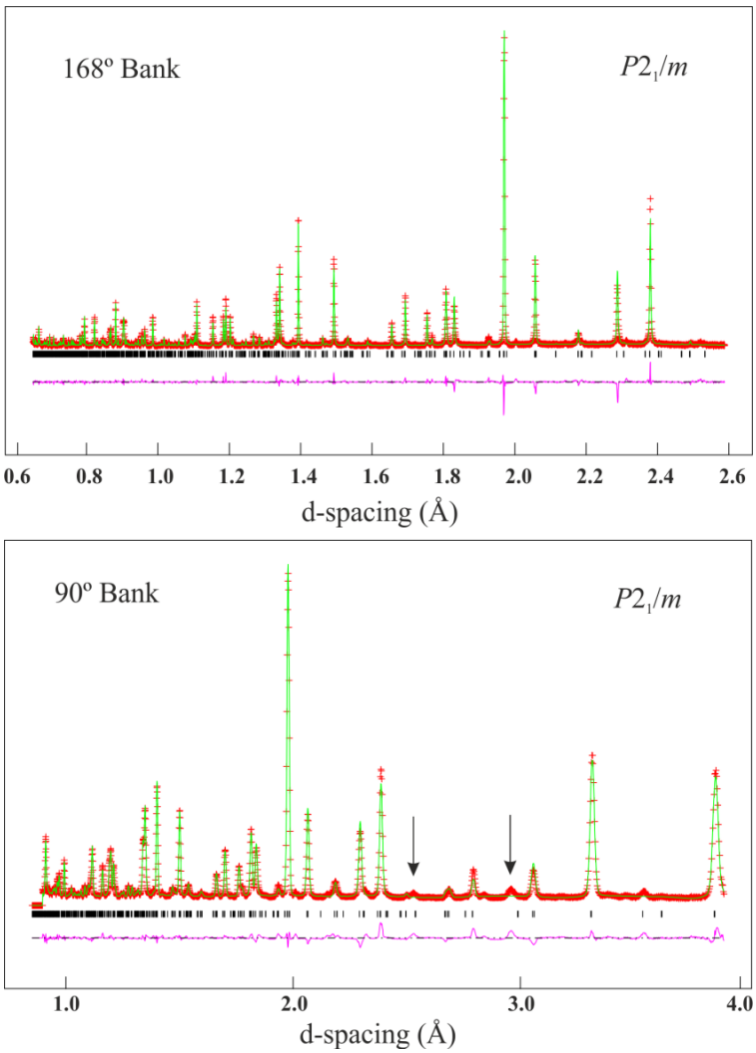


Figure 8.6. Observed, calculated and difference plots from the refinements of the $P2_1/m$ model against the neutron powder diffraction data collected from $Cu_xLi_{2-2x}SrTa_2O_7$ (wRp = 7.51%, Rp = 7.14%). Peaks labelled with arrows cannot be indexed by simple cell expansions.

8.3.1.4 Neutron powder diffraction (GEM)

Neutron powder diffraction data were collected from a sample of 3.7 g $Cu_xLi_{2-2x}SrTa_2O_7$ at both ambient temperature and 5 K using the GEM instrument at ISIS. Comparing room temperature and the 5 K diffraction data reveals that there is no phase transition and no magnetic reflection is observed from the 5 K diffraction data therefore there is no long-

range magnetic order at 5 K. Since the 5 K diffraction data have a better signal-to-noise ratio due to the longer data collection time, they were used for the structural analysis.

The $P2_1/m$ symmetry model was refined against the 5 K neutron diffraction data. The Cu^{2+}/Li^{+} cations were set to be evenly distributed in the two 4*f* sites. In common with the neutron diffraction data collected using the HRPD instrument, the refinement gives good fits to low *d*-spacing data banks but several diffraction peaks at high *d*-spacing regions are not properly fitted. The observed, calculated and difference plots in space group $P2_1/m$ with a disordered cation arrangement are shown in Figure 8.7. Peaks labelled with solid arrows cannot be indexed by doubling the unit cell size and hence they may be attributed to impurity phases. Peaks labelled with dashed arrows are indexed by the $P2_1/m$ symmetry model but the cation-disordered model gives no intensity to these peaks. Refining the atomic positions does not improve the fits but refining the Cu^{2+}/Li^{+} fractions in the two separate 4*f* sites fits these peaks better, suggesting they are likely to be attributed to some interlayer cation order (Figure 8.8). The fraction-refined $P2_1/m$ model was then used to simulate a synchrotron X-ray diffraction pattern but it gives extra peaks which are not seen from the experimental data, suggesting it is not the correct symmetry model.

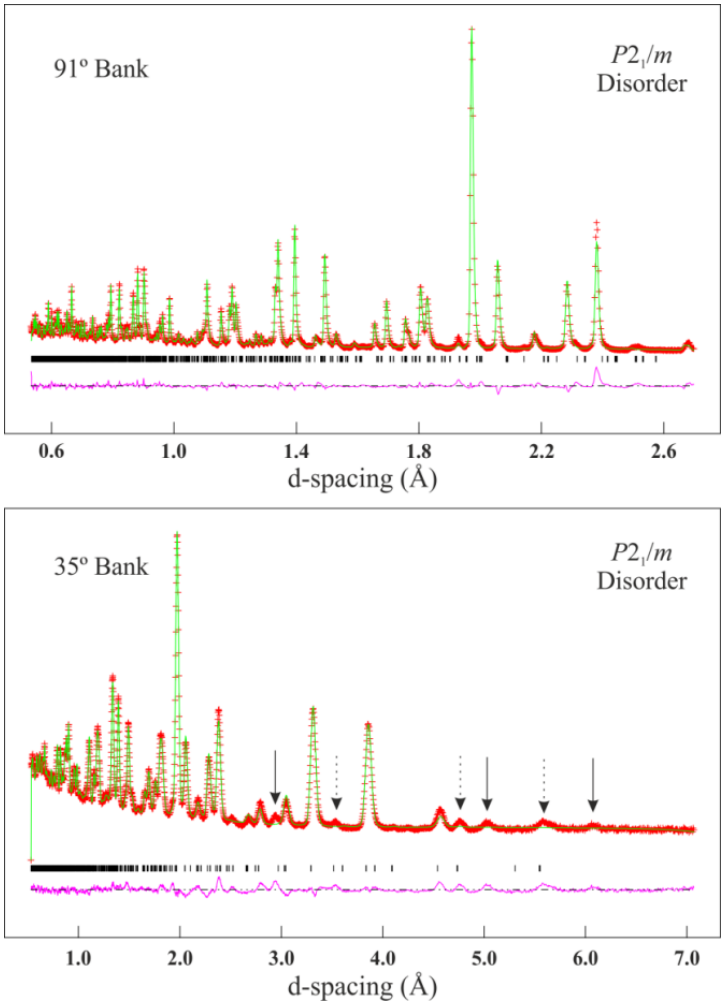


Figure 8.7. Observed, calculated and difference plots from the refinements of the *P*2$_1$/*m* model with a disordered cation arrangement against the neutron diffraction data collected from $Cu_xLi_{2-2x}SrTa_2O_7$ using the GEM instrument.

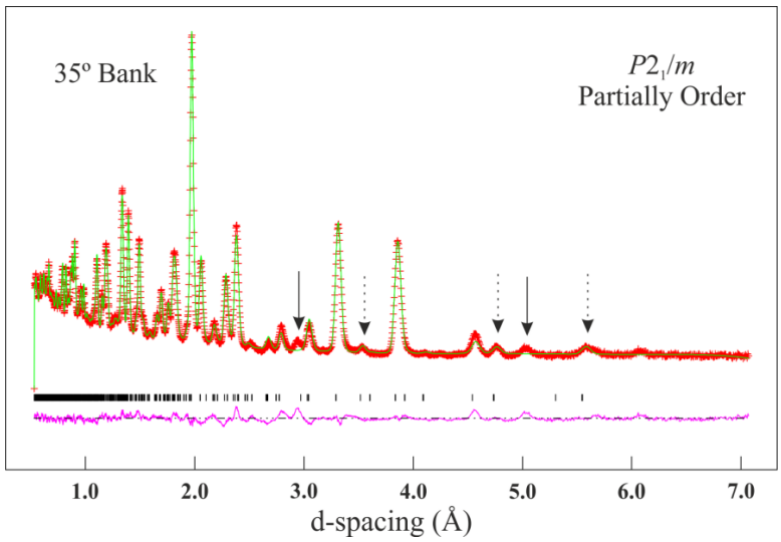


Figure 8.8. Observed, calculated and difference plots from the refinements of the *P*2$_1$/*m* model with a partially ordered cation arrangement against the neutron diffraction data (35° bank) collected from $Cu_xLi_{2-2x}SrTa_2O_7$ using the GEM instrument.

8.3.1.5 Combining the synchrotron X-ray and neutron diffraction data

The synchrotron X-ray diffraction data show no cation-ordering peak but in contrast, there is a clear evidence of cation order from the neutron diffraction data. One possible explanation is that the Cu^{2+} cations are disordered but the Li^{+} cations adopt an ordered arrangement. The thorough analysis in section 8.3.1.2 eliminates the possibility of long-range cation order from the Cu^{2+} cations. The small X-ray scattering factor (nearly zero) of lithium means the lithium order cannot be observed from the X-ray diffraction data but it can be seen by neutron diffraction (neutron scattering length for lithium: -1.90 fm).

8.3.2 Magnetic characterisation of $Cu_xLi_{2-2x}SrTa_2O_7$

8.3.2.1 SQUID Magnetometry of $Cu_xLi_{2-2x}SrTa_2O_7$

Magnetization data were collected from a sample of $Cu_xLi_{2-2x}SrTa_2O_7$ in an applied field of 100 Oe in the temperature range $5 \leq T/K \leq 300$. The ZFC and FC data are shown in Figure 8.9 and they diverge at 5 K. Fitting the FC data to the Curie-Weiss law yielded values of $C = 0.376(1)$ cm^3 K mol^{-1} and $\theta = -1.845(25)$ K. The observed moment (1.73 μ_B), calculated from the Curie constant, is larger than the theoretical value of 1.52 μ_B calculated from the spin-only moment of $S = ½$ Cu^{2+} center per formula unit from $Cu_{0.875}Li_{0.25}SrTa_2O_7$. The large observed moment can be attributed to two possibilities: 1. There is an orbital contribution to the total moment; 2. The titration underestimated the copper concentration. Magnetization-field isotherms collected at 300 K are linear. Both the 300K and 5 K data pass through the origin, as shown in Figure 8.10.

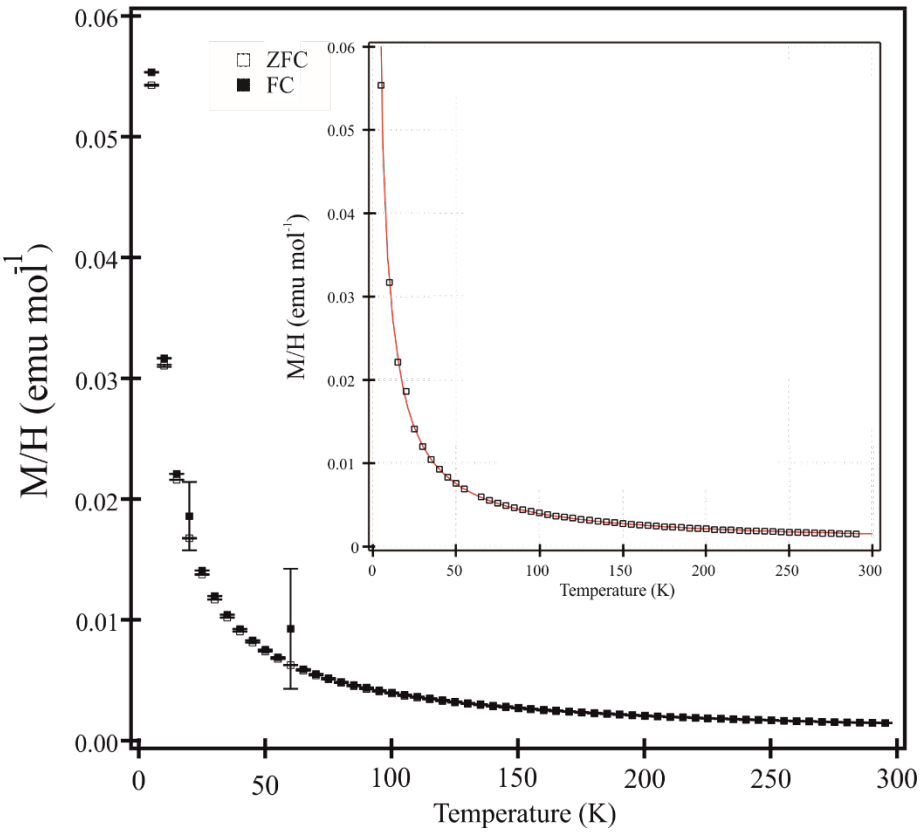


Figure 8.9. Zero-field cooled and field cooled magnetisation data collected from $Cu_xLi_{2-2x}SrTa_2O_7$. Insert shows a fit of the FC data to the Curie-Weiss law to yield values of C = 0.376(1) cm^3 K mol^{-1} and θ = -1.845(25) K.

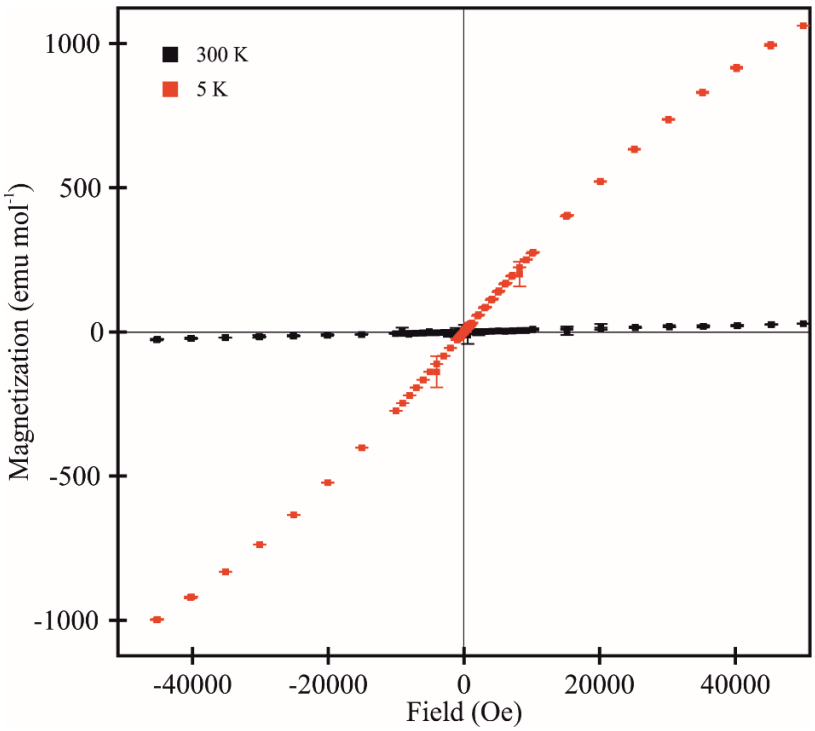


Figure 8.10. Magnetization-field isotherms collected from $Cu_xLi_{2-2x}SrTa_2O_7$.

8.3.3 Structural characterisation of $CoSrTa_2O_7$

8.3.3.1 Optical SHG measurements and titration

Powder SHG measurements show that $CoSrTa_2O_7$ is SHG active with an intensity 0.3 times of the α-SiO_2 standard. This observation suggests that $CoSrTa_2O_7$ adopts a non-centrosymmetric crystal structure. Attempts to determine the Co content by titration were unsuccessful and hence a formula of $CoSrTa_2O_7$ was used for the diffraction data analysis.

8.3.3.2 Room temperature synchrotron X-ray powder diffraction

High-resolution synchrotron X-ray powder diffraction data collected from $CoSrTa_2O_7$ at ambient temperature using the MAC detectors (Section 2.2.1.2) can be readily indexed with an orthorhombic unit cell with a $\sqrt{2} \times \sqrt{2} \times 1$ geometric expansion of the undistorted cell (a = 5.5618 Å, b = 5.5615 Å, c = 18.9160 Å) of an n = 2 Ruddlesden-Popper phase. The extinction conditions are consistent with an A-centred or primitive structure. These observations together with the observed SHG activity suggest that $CoSrTa_2O_7$ may adopt a similar polar structure to $Li_2SrTa_2O_7$ in space group $A2_1am$. Therefore an $A2_1am$ symmetry model was constructed based on the refined structure of $Li_2SrTa_2O_7$, in which the Co^{2+} cations adopt a disordered arrangement in the pseudo-tetrahedral sites. The model was refined against the synchrotron X-ray diffraction data, yielding a reasonably good fit as shown in Figure 8.11. The intensity mismatch is attributed to a strong preferred orientation of the sample. Similar to the analysis of $Cu_xLi_{2-2x}SrTa_2O_7$, different cation-ordered models were refined and there was no sign of long-range Co order with an arrangement displayed in Figure 8.1 and 8.3.

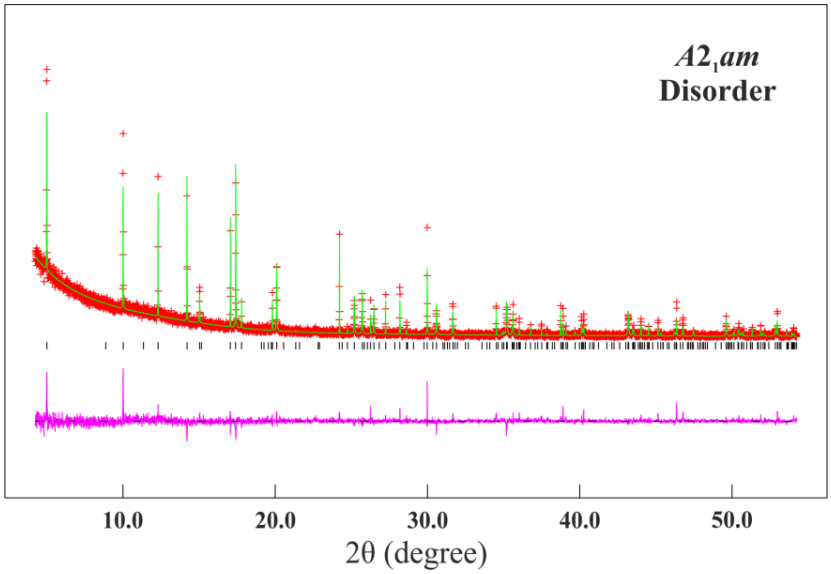


Figure 8.11. Observed, calculated and difference plots from the refinements of the *A*2$_1$*am* models against the synchrotron X-ray diffraction data collected from $CoSrTa_2O_7$.

8.3.3.3 Neutron powder diffraction (HRPD)

Neutron powder diffraction data were collected from a sample of 4.2 g $CoSrTa_2O_7$ at ambient temperature using the HRPD instrument at ISIS. The neutron diffraction data can be indexed using an expanded unit cell with a $\sqrt{2} \times \sqrt{2} \times 1$ geometric expansion of the aristotype unit cell. The extinction conditions are consistent with an *A*-centred or a primitive space group. Similar to the analysis of the synchrotron X-ray diffraction data, an *A*2$_1$*am* model was constructed and refined against the neutron diffraction data. The occupancy of Co was set to be 0.5 in order to respect the stoichiometry. The refinement proceeded smoothly and no constraint was added. It was noticed that the refined Co position was chemically unrealistic and the refined thermal displacement parameter was too big (0.1 $Å^2$) to be chemically reasonable. These observations can be attributed to a possibility that the interlayer cations are a mixture of Co^{2+} and Li^+ due to an incomplete cation exchange. The neutron scattering lengths of Co and Li are 2.49 fm and -1.90 fm respectively. A combination of Co and Li in a single site leads to the scattering power of this site to be close to zero for neutron diffraction. Considering that the neutron scattering lengths of Sr (7.02 fm), Ta×2 (6.91 fm × 2) and O×7 (5.8 fm × 7) are much larger than Co/Li, it can be

concluded that the atomic position of Co/Li cannot be precisely determined from the analysis of neutron diffraction data as the majority peak intensities come from the scattering power of Sr, Ta and O. Therefore Co was reset to a reasonable position and was not refined during the following refinement. The observed, calculated and difference plots from the refinement of the $A2_1am$ model are shown in Figure 8.12. The right-hand-side panel shows the plots with preferred orientation parameters refined and it can be seen that it gives a better visual fit.

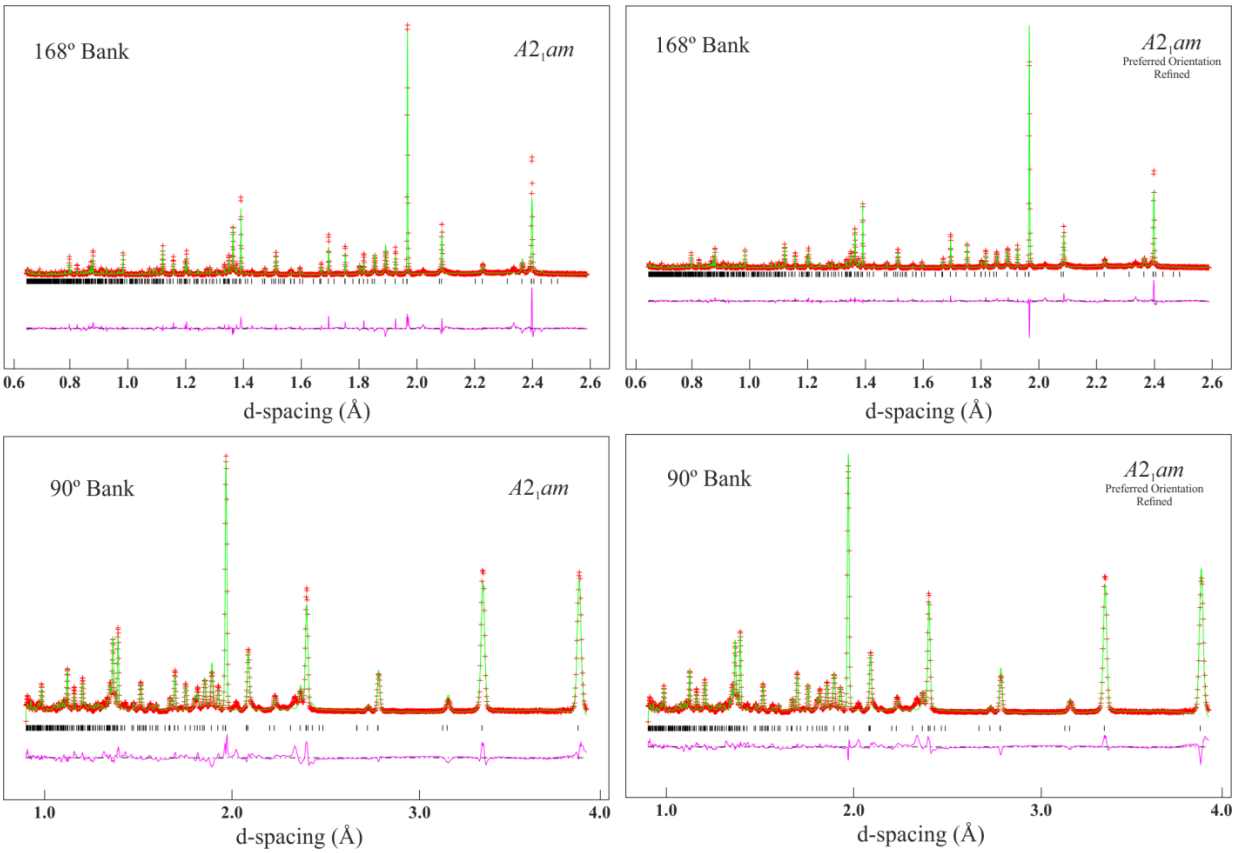


Figure 8.12. Observed, calculated and difference plots from the refinements of the $A2_1am$ models against the neutron powder diffraction data collected from $CoSrTa_2O_7$. The right-hand-side panel shows the refinement plots with an added preferred orientation term using the March-Dollase model.

8.3.4 Magnetic characterisation of $CoSrTa_2O_7$

8.3.4.1 SQUID Magnetometry of $CoSrTa_2O_7$

Magnetisation data were collected from a sample of $CoSrTa_2O_7$ in an applied field of 100 Oe in the temperature range $5 \leq T/K \leq 300$. The ZFC and FC data are shown in Figure 8.13. Both the ZFC and FC datasets can be fitted to the Curie-Weiss law ($\chi = C / (T - \theta)$) in the temperature range $75 \leq T/K \leq 300$ to yield values of $C = 1.804(5)$ cm^3 K mol^{-1} and $\theta = -50.42(60)$ K. The observed moment (3.80 μB), calculated from the Curie constant, is smaller than a value of 3.87 μB expected for the spin-only moment of one high-spin, $S = \frac{3}{2}$ Co^{2+} center per formula unit calculated from a formula $CoSrTa_2O_7$. In fact, Co^{2+}-containing compounds always have strong orbital contributions to the total moments therefore the theoretical value of $CoSrTa_2O_7$ is even higher than 3.87 μB. The small observed moment can be explained by an incomplete cation exchange which leads to a mixture of Co^{2+}/Li^+ cations between perovskite layers. The ZFC and FC data diverge below 15 K, suggesting a transition to a magnetically ordered state. Magnetization-field isotherms collected at 300 K are linear. Both 300 K and 5 K data pass through the origin, as shown in Figure 8.14.

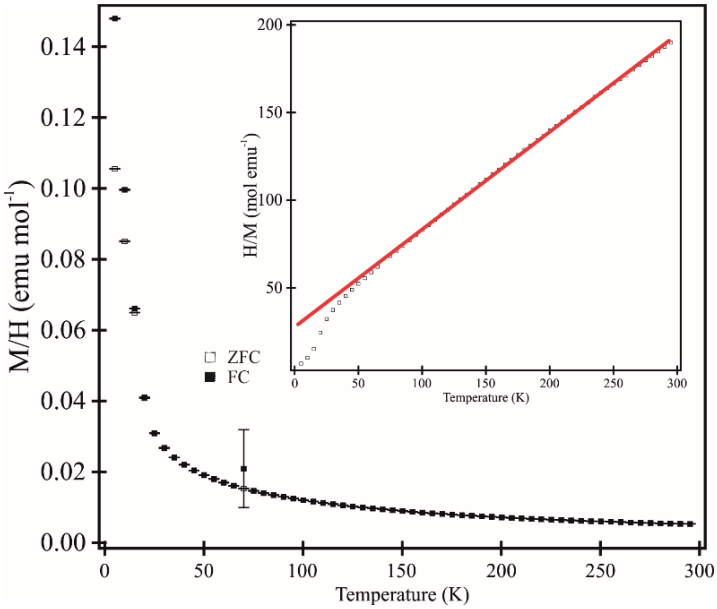


Figure 8.13. Zero-field cooled and field cooled magnetisation data collected from $CoSrTa_2O_7$. Inset shows a fit to the Curie-Weiss law to yield values of $C = 1.804(5)$ cm^3 K mol^{-1} and $\theta = -50.42(60)$ K.

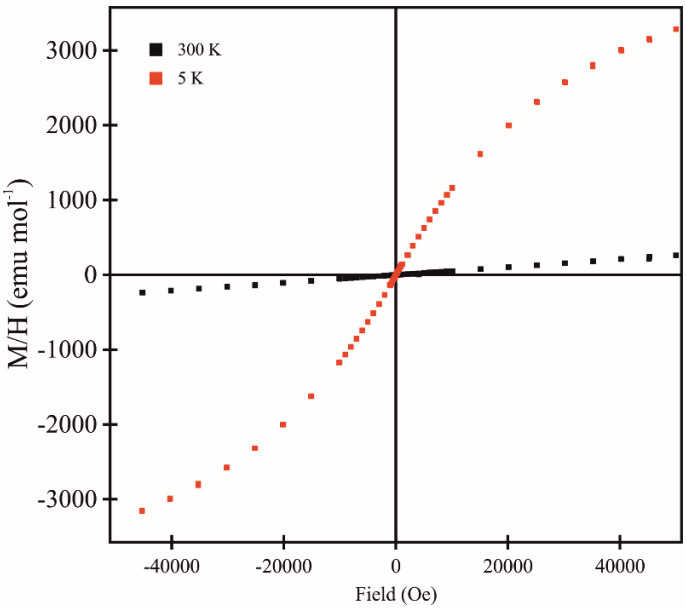


Figure 8.14. Magnetization-field isotherms collected from $CoSrTa_2O_7$ at 5 K and 300 K.

8.3.4.2 Low temperature neutron powder diffraction

Neutron powder diffraction data were collected from a sample of 4.2 g $CoSrTa_2O_7$ at both ambient temperature and 5 K using the GEM instrument at ISIS. Comparing ambient temperature and 5 K datasets reveals that there is no phase transition or long-range magnetic order at 5 K. Due to the small scattering power of the cation site with a mixture of Co/Li and the fact that the Co/Li fraction is unknown, it was not attempted to study any possible interlayer cation order from the neutron diffraction data.

8.4 Discussion

8.4.1 Structural comment on $CuSrTa_2O_7$ and $CoSrTa_2O_7$

It can be concluded from Section 8.3 that it is not possible to unambiguously characterise the crystal structures of $CuSrTa_2O_7$ or $CoSrTa_2O_7$ from the powder diffraction data only. The next step is to precisely determine the transition metal to lithium ratios. Energy-dispersive X-ray spectroscopy and neutron activation analysis can be utilized to determine the compositions of the two compounds. In addition, electron diffraction and electron

microscopy measurements will be performed to probe the existence of possible superstructure and interlayer cation order in both compounds.

Despite the fact that the exact crystal structures of the cooper and cobalt exchanged compounds are unknown, it is possible to have some reasonable hypothesis of the possible interlayer cation order. It is unlikely either Cu^{2+} or Co^{2+} cations would adopt a 'stripe'-type order (Figure 8.1 and 8.2) because this type of arrangement produces strong repulsion between the divalent transition metal cations. In addition, as demonstrated in Chapter 4, the advantage of adopting the stripe-type order is that the TaO_6 octahedral tilting distortion can make half of the interlayer tetrahedral sites very small (the other half large) to accommodate the small interlayer cations. The tilting distortion needs to be large enough to make a considerable size difference between the two distinct tetrahedral sites. However, no evidence of large tilting distortions is observed from the analysis of the neutron diffraction data. In contrast, the checkerboard order does not require a large tilting distortion, which is consistent with the observation from the neutron diffraction data. Therefore if there is any long-range or short-range cation order, it is more likely to be a checkerboard arrangement. Incomplete exchange of Li means there is an extra complexity in the structure as lithium and transition metal cations may adopt different ordering arrangements. Given the fact that $MnSrTa_2O_7$ adopts a superstructure with a local checkerboard order of Mn^{2+} cations, it is possible that $CuSrTa_2O_7$ and $CoSrTa_2O_7$ also adopt similar modulated structures.

8.4.2 Incomplete exchange of lithium

One interesting observation is that among all five M^{2+} cations (M = Mn, Fe, Co, Ni and Cu), only the Mn^{2+} cations fully replace the Li^+ cations. The main difference between Mn^{2+} and the other four transition metal cations is that the high-spin d^5 Mn^{2+} cations do not have any preferred geometric arrangement while the other four do have preferences. The Co^{2+} cation prefers an octahedral geometry while the Cu^{2+} cation prefers a square planar geometry.

However, the interlayer cations in the Ruddlesden-Popper framework can only sit in nine-coordinated or tetrahedral sites, meaning there is a crystal field energy 'penalty' when Cu^{2+} and Co^{2+} cations are intercalated into the pseudo-tetrahedral sites during the cation exchange reaction. A possible consequence of this energy 'penalty' is that the completely exchanged products are kinetically unstable. It is also possible that a higher temperature is required to fully overcome the diffusion barrier of the Cu^{2+}/Co^{2+} cations but other kinetically stable products, rather than the fully exchanged products, are forming at a lifted temperature. Other synthetic techniques such as high-pressure synthesis may be tested to see if fully cation-exchanged products can be prepared.

There are two obvious consequences from incomplete cation exchange reactions: 1. A complicated interlayer cation order may occur due to the existence of both the transition-metal and the lithium cations, which can couple with the octahedral tilting distortions and lead to a different crystal structure instead of the polar (average) $A2_1am$ structure adopted by both $Li_2SrTa_2O_7$ and $MnSrTa_2O_7$. This is demonstrated by the non-polar, monoclinic crystal structure adopted by $Cu_xLi_{2-2x}SrTa_2O_7$. 2. The remaining Li^+ cations can interrupt the long-range magnetic interactions between the magnetic cations and prevent the bulk compound from exhibiting a long-range magnetic order. Indeed, magnetic reflections are only observed from $MnSrTa_2O_7$.

8.5 Conclusion

Optical SHG measurements show that $Cu_xLi_{2-2x}SrTa_2O_7$ adopts a centrosymmetric crystal structure while $Co_xLi_{2-2x}SrTa_2O_7$ remains a non-centrosymmetric structure. The cation exchange reactions using the Cu^{2+} and Co^{2+} cations are incomplete and both products contain some lithium cations between the perovskite layers. In both cases, a complex interlayer cation order may exist, which further lowers the symmetry from an $A2_1am$

structure. Elemental analysis, electron diffraction and microscopy measurements are required to unambiguously determine the composition and crystal structures of both compounds.

Comparing the cation exchange reactions using a series of divalent 3*d* transition metal cations, it can be concluded that the Mn^{2+} cation is the most suitable candidate to prepare multiferroic materials as it is the only candidate leading to a complete exchange and exhibiting a long-range magnetic order. It is possible a complete cation exchange is one of the requirements for a long-range magnetic order. This conclusion can be used to prepare similar cation exchanged products. For example, similar precursors with slightly different compositions in the perovskite blocks, such as $Li_2SrNb_2O_7$, $Li_2CaNb_2O_7$ and $Li_2CaTa_2O_7$, can be utilized for cation exchange reactions and the Mn^{2+} cation is an obvious choice to be intercalated. Other divalent 3*d* transition metal cations should also be tested to see if a full exchange can be achieved.

Chapter 9 – More Diffraction and More Than Diffraction: Synthesis and Characterisation of Some Layered Oxynitrides

9.1 Introduction

Perovskite oxynitrides have attracted a lot of interests due to their useful electronic, optical and catalytic properties. Oxynitrides can combine the advantages of both metal oxides and nitrides. They are generally more stable in air and moisture than pure nitride phases and have smaller band gaps than pure oxides[86]. The crystal structures of 3D perovskite oxynitrides are relatively well studied and it is suggested that in 3D perovskite oxynitrides the nitride ions tend to have a complicated local order to facilitate metal-ion bonding[87-90]. In contrast, layered perovskite oxynitrides are not well studied, perhaps because of the synthetic and characterisation difficulties.

As demonstrated in Chapter 4, $NaNdM_2O_7$ (M = Nb/Ta) adopt a non-polar, tetragonal structure in space group $P4_2/mnm$. In this structure, Na^+ cations are ordered as checkerboards to minimise the undesired Na-Na repulsion (Figure 4.21), in an agreement with Pauling's third crystallographic rule[70]. This ordered arrangement produces an $a^-b^0c^0/b^0a^-c^0$ tilting distortion which is deemed as an unusual arrangement because NdM_2O_7 perovskite blocks in $CsNdM_2O_7$, $RbNdM_2O_7$ and $LiNdM_2O_7$ all adopt an $a^-a^-c^+$ tilting distortion. These observations together encourage a study to prepare oxynitrides in the form $Na_{1+x}NdM_2O_{7-x}N_x$. As more Na^+ cations are intercalated between perovskite layers, it is impossible to have a checkerboard arrangement in which only half of the tetrahedral sites are occupied and it is therefore interesting to see if the crystal structure of the oxynitrides would differ from their oxide analogues. It is also interesting to see if any oxide/nitride order can be observed.

In addition, most solid-state syntheses are 'one-pot' reactions with only a single step. There are a few two-step reactions which typically include a ceramic synthesis step followed by a topochemical reaction. It is therefore interesting to investigate, from a synthetic point view, if it is possible to perform multiple-step solid-state reactions.

9.2 Synthesis

Powder samples of $RbNdTa_2O_7$ and $RbNdNb_2O_7$ were prepared by a ceramic synthesis method, as described in Chapter 3. The cation-exchanged products, $NaNdTa_2O_7$ and $NaNdNb_2O_7$, were synthesised by reacting $RbNdTa_2O_7$ and $RbNdNb_2O_7$ with 10 molar equivalents of $NaNO_3$ (99%), as described in Chapter 4. Samples of $Na_{1+x}NdTa_2O_{7-x}N_x$ and $Na_{1+x}NdNb_2O_{7-x}N_x$ were prepared from a mixture of $NaNdTa_2O_7$ or $NaNdNb_2O_7$ with Na_2CO_3 under flowing NH_3. Powders of $NaNdTa_2O_7$ or $NaNdNb_2O_7$ were thoroughly ground with 5 molar equivalents of Na_2CO_3 (99%), loaded into a boat crucible and heated at 450 °C under flowing NH_3 for 20 hours. Both samples were washed with distilled water to remove the remaining carbonates, and dried for 12 hours at 140 °C in air. As a final step, both samples were dried under flowing argon for 12 hours at 300 °C to eliminate all absorbed water and were then transferred into an argon-filled glovebox for storage.

Powder samples of $Li_{1+x}NdTa_2O_{7-x}N_x$ were synthesized from $LiNdTa_2O_7$. Samples of $LiNdTa_2O_7$ were prepared by reacting $RbNdTa_2O_7$ with 10 molar equivalents of hydrated $LiNO_3$ (99.8%), as described in Chapter 4. $LiNdTa_2O_7$ and Li_2CO_3 were then mixed in a 1:5 molar ratio, thoroughly ground and loaded into a boat crucible. The mixture was heated at 400 °C for 20 hours under flowing NH_3. The mixture was then washed with distilled water to remove the remaining carbonates, and dried for 12 hours at 140 °C in air. Attempts to synthesize $Li_{1+x}NdNb_2O_{7-x}N_x$ under the same reaction conditions were deemed

unsuccessful as no formation of product was observed. Raising the reaction temperature leads to the decomposition of $LiNdNb_2O_7$ into some binary oxides.

Cation exchange reactions were performed on mixtures of $Na_{1+x}NdTa_2O_{7-x}N_x$ or $Na_{1+x}NdNb_2O_{7-x}N_x$ using anhydrous MCl_2 or MBr_2 (M = Mn/Fe/Co/Ni/Cu). The mixtures were heated in the temperature range $250 \leq T/°C \leq 450$ under flowing argon but no evidence of forming the cation-exchanged product was observed by X-ray powder diffraction. Similar cation exchange reactions were performed from the mixtures of $Li_{1+x}NdTa_2O_{7-x}N_x$ with anhydrous MCl_2 or MBr_2 (M = Mn/Fe/Co/Ni/Cu) at the temperature range $250 \leq T/°C \leq 450$ under flowing argon for 3 to 7 days. These reactions were deemed successful. The products were then washed with distilled water to remove the remaining chlorides or bromides, and dried for 12 hours at 140 °C.

Reaction progress and final sample purity for all products were assessed by X-ray powder diffraction data collected using a PANalytical X'pert diffractometer incorporating an X'celerator position sensitive detector (monochromatic Cu Kα1 radiation).

9.3 $Na_{1+x}NdTa_2O_{7-x}N_x$ and $Na_{1+x}NdNb_2O_{7-x}N_x$

9.3.1 Results

9.3.1.1 Optical SHG measurements

Powder SHG measurements show that both $Na_{1+x}NdTa_2O_{7-x}N_x$ and $Na_{1+x}NdNb_2O_{7-x}N_x$ are SHG active, with intensities of 0.22 and 0.23 times of the α-SiO_2 standard respectively. These observations indicate that both $Na_{1+x}NdTa_2O_{7-x}N_x$ and $Na_{1+x}NdNb_2O_{7-x}N_x$ adopt non-centrosymmetric crystal structures.

9.3.1.2 Structural characterisation of $Na_{1+x}NdTa_2O_{7-x}N_x$

9.3.1.2.1 Room temperature synchrotron X-ray powder diffraction

High-resolution synchrotron X-ray powder diffraction data collected from $Na_{1+x}NdTa_2O_{7-x}N_x$ at ambient temperature can be indexed using an orthorhombic unit cell with an approximate $\sqrt{2} \times \sqrt{2} \times 1$ geometric expansion of the aristotype $I4/mmm$ unit cell (a = 5.4759 Å, b = 5.4801 Å, c = 20.8250 Å) of an n = 2 Ruddlesden-Popper phase. The extinction conditions suggested an A-centred space group. The cell expansion, the extinction conditions and the observed SHG activity are consistent with the polar $A2_1am$ structure reported for $Li_2SrTa_2O_7$ (Chapter 6). An $A2_1am$ symmetry model was then constructed based on a molecular formula $Na_2NdTa_2O_6N$. The model was refined against the synchrotron X-ray diffraction data and the refinement gives good statistical and visual fits. During the refinement, the nitride ions were set to be evenly distributed in all four crystallographic oxide sites and no attempt was made to refine the nitride occupancy due to the similar X-ray scattering factors of oxygen and nitrogen. The observed, calculated and difference plots against the synchrotron X-ray diffraction data in space group $A2_1am$ are shown in Figure 9.1.

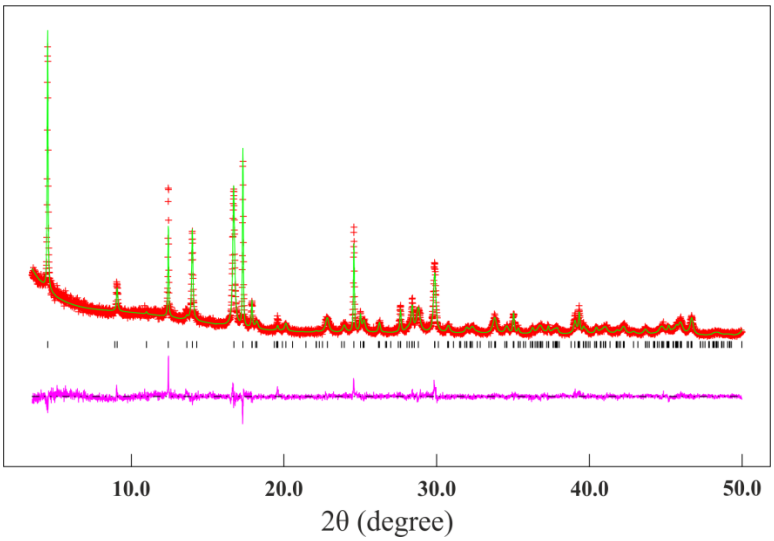


Figure 9.1. Observed, calculated and different plots from the refinement of the $A2_1am$ model against the synchrotron X-ray diffraction data collected from $Na_{1+x}NdTa_2O_{7-x}N_x$ at 298 K.

9.3.1.2.2 Room temperature neutron powder diffraction

Neutron powder diffraction data were collected from a sample of approximately 3.4 g $Na_{1+x}NdTa_2O_{7-x}N_x$ at ambient temperature using the HRPD instrument at ISIS. In common with the synchrotron X-ray diffraction data, the neutron diffraction data can be indexed using an expanded unit cell with a $\sqrt{2} \times \sqrt{2} \times 1$ geometric expansion of the undistorted cell. The extinction conditions again suggested an *A*-centred or a primitive structure. An $A2_1am$ symmetry model was then constructed and refined against the diffraction data. A molecular formula $Na_2NdTa_2O_6N$ was used to construct the model and the nitride anion was set to be evenly distributed in all four oxide sites to begin with. In this model, the Na^+ cations sit in a single crystallographic site, 8*b*, with a full occupancy. The anion sites were constrained to have the same thermal parameters. During the refinement, it was observed that the thermal parameter for Na was too large to be realistic and hence it was constrained to be the same as Nd. The refinement proceeded smoothly and it gave a good statistical fit (wRp = 5.46%, Rp = 5.13 %). The large thermal parameter of Na suggests that the occupancy of Na is likely to be smaller than 1. Consequently, the nitride to oxide ratio needs to be altered to maintain the charge neutrality of the phase. Therefore the occupancies of Na and O/N were refined with a constraint to balance the charge. The refinement achieves the best statistical fit (wRp = 4.94%, Rp = 4.78%) with a refined composition $Na_{1.2}NdTa_2O_{6.8}N_{0.2}$, which is very different from the hypothetical composition $Na_2NdTa_2O_6N$.

In the $A2_1am$ symmetry model, there are four crystallographic sites to accommodate the oxide and/or the nitride ions. As the nitrides may adopt an ordered arrangement in some anion sites, models with different nitride-ordered arrangements were constructed and refined against the neutron diffraction data. The composition was set to be $Na_2NdTa_2O_6N$ to begin with. The refinement shows that the model with the nitride ions ordered in the two apical sites (Figure 9.2) gives superior fits (wRp = 5.18%, Rp = 5.00%) than other anion

ordered models. The occupancies of Na and O/N were then refined with a constraint. During the refinement, the nitride ions were set to be evenly distributed between the two apical sites (Figure 9.2). The refinement proceeded smoothly and the best statistical fit (wRp = 4.97%, Rp = 4.80%) was achieved with a refined composition of $Na_{1.4}NdTa_2O_{6.6}N_{0.4}$.

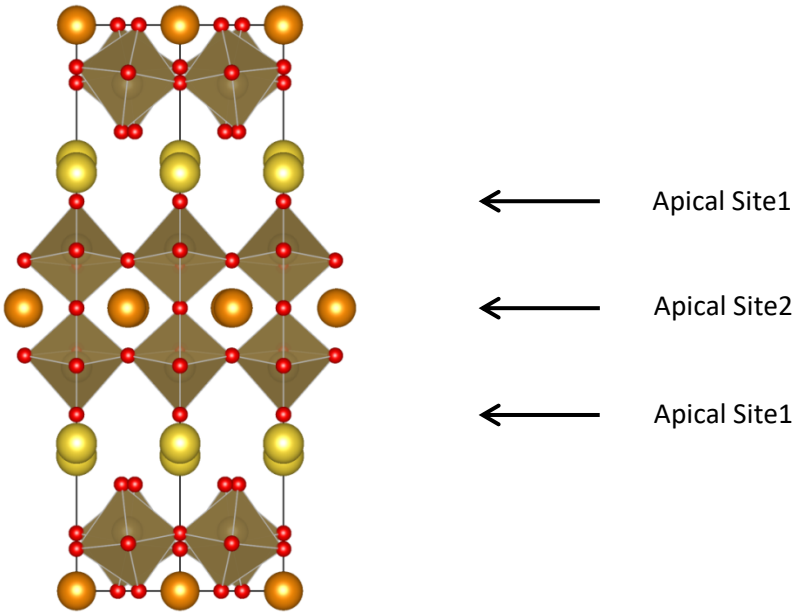


Figure 9.2. Apical anion sites which are preferred by the nitride ions.

It can be seen from the above analysis that it is not possible to unambiguously determine if the nitride ions have an ordered/disordered arrangement from the diffraction data only. As an example to show the quality of the Rietveld fits but not the final structural solution, the observed, calculated and difference plots from the refinement of the $A2_1am$ symmetry model with a disordered nitride arrangement are shown in Figure 9.3. The refined structure is shown in Figure 9.4. Full details of the parameters from the refinements are shown in Table 9.1.

Atom	site	Fraction	*x*	*y*	*z*	U_{iso} (Å^3)
Na(1)	8*b*	0.6	0.0136(32)	0.2497(22)	0.2403(9)	0.0317(12)
Nd(1)	4*a*	1	0.2640(20)	0.5768(16)	0	0.0317(12)
Ta(1)	8*b*	1	0.2417(12)	0.0958(11)	0.1020(1)	0.0049(7)
O/N(1)	4*a*	0.97/0.03	0.2226(27)	0.0548(30)	0	0.0509(10)
O/N(2)	8*b*	0.97/0.03	0.4974(21)	0.3379(20)	0.9156(2)	0.0509(10)
O/N(3)	8*b*	0.97/0.03	0.0331(15)	0.8026(16)	0.9039(4)	0.0509(10)
O/N(4)	8*b*	0.97/0.03	0.2634(18)	0.0445(0)	0.1912(2)	0.0509(10)
$Na_{1.2}NdTa_2O_{6.8}N_{0.2}$ – space group $A2_1am$ (#36) a = 5.4798(6) Å, b = 5.4769(8) Å, c = 20.8204(20) Å, volume = 624.87(16) Å^3 Formula weight: 645.32 g mol^{-1}, Z = 4 Radiation source: Neutron Time of flight Temperature: 298 K χ^2 = 8.94, wRp = 4.94%, Rp = 4.78%						

Table 9.1. Parameters from the structural refinement of $Na_{1.2}NdTa_2O_{6.8}N_{0.2}$ against neutron powder diffraction data collected at 298 K.

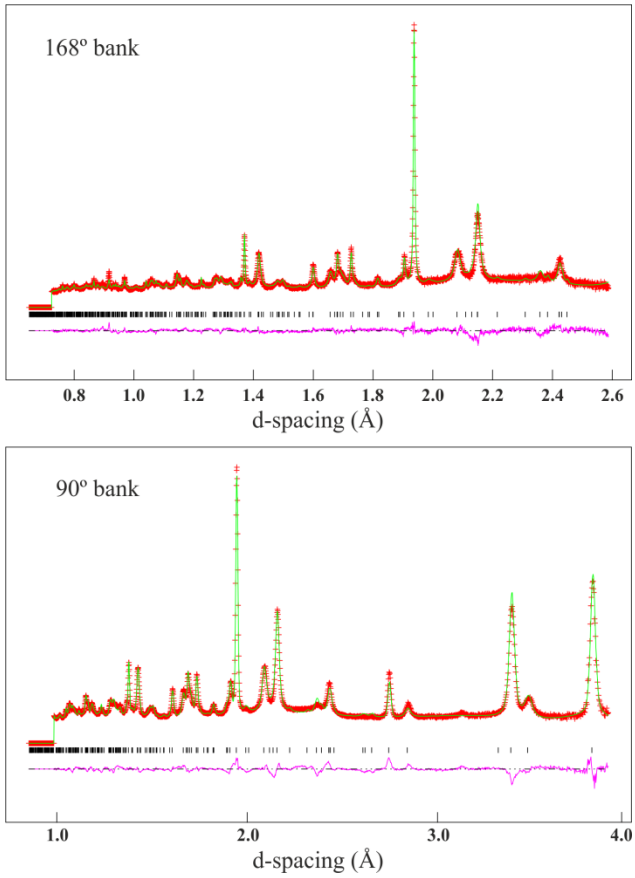


Figure 9.3. Observed, calculated and different plots from the refinement of the $A2_1am$ model with a composition $Na_{1.2}NdTa_2O_{6.8}N_{0.2}$ against the neutron powder diffraction data collected at 298K. The nitride ions were constrained to be evenly distributed in all four oxide sites.

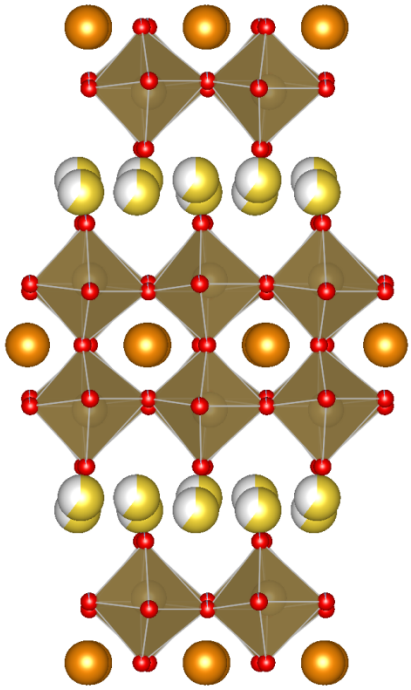


Figure 9.4. The refined structure of $Na_{1.2}NdTa_2O_{6.8}N_{0.2}$. The gold and yellow/white spheres are the Nd^{3+} and Na^{+} cations respectively, Ta^{5+} cations are inside the octahedra. Red spheres are a mixture of O^{2-} and N^{3-} ions.

9.3.1.3 Structural characterisation of $Na_{1+x}NdNb_2O_{7-x}N_x$

Synchrotron X-ray diffraction data collected from different batches of $Na_{1+x}NdNb_2O_{7-x}N_x$ reveal that the products always contain a large amount of $NaNdNb_2O_7$. Although different reaction conditions (different reaction temperatures, ammonia flowing rates and reaction time) were attempted, the reaction never yielded a pure, satisfying, single-phase product. As demonstrated in Section 9.3.1.2, the crystal structure analysis of $Na_{1+x}NdTa_2O_{7-x}N_x$ is very complicated as a result of a combination of the octahedral tilting distortion, a possible anion-site order and its unknown chemical composition, it is hence considered unrealistic to characterise the crystal structure of $Na_{1+x}NdNb_2O_{7-x}N_x$ from impure samples. However, it is likely that $Na_{1+x}NdNb_2O_{7-x}N_x$ would be isostructural to $Na_{1+x}NdTa_2O_{7-x}N_x$ based on the observation that *A*'$NdNb_2O_7$ and *A*'$NdTa_2O_7$ always adopt the same crystal structure (*A*' = Cs/Rb/Na/Li).

9.3.2 Discussion

The determination of crystal structure from powder diffraction data can be sometimes challenging, especially when the solid of interest adopts a low symmetry crystal structure. The analysis of $Na_{1+x}NdTa_2O_{7-x}N_x$ is even more complicated because not only the structural symmetry, but also the chemical composition is unknown. Although it is possible to determine the chemical composition, in this case the oxide to nitride ratio, using the neutron diffraction data as a result of the different neutron scattering lengths of O (5.8 fm) and N (9.36 fm), the O/N ratio can only be reliably refined when the crystal structure and the cation composition are both well known. However, in the case of $Na_{1+x}NdTa_2O_{7-x}N_x$, neither its crystal structure nor the cation composition is clear. In addition, previous study of $(SrO)(SrNbO_{2-x}N)n$ (n = 1, 2) reveals that the Nb^{5+} cation was reduced to a lower oxidation state during the reaction using flowing NH_3[91]. As a direct analogue, Ta^{5+} cations may also be reduced and hence there might be no linear relation between the sodium and nitrogen contents, in other words, the real composition should be described as $Na_{1+x}NdTa_2O_{7-y}N_y$, assuming there is no anion vacancy. Consequently, other techniques should be used to determine the chemical composition. Cation contents can be determined by plasma absorption analyses and/or energy-dispersive X-ray spectroscopy. The nitride content can be determined by the combustion analysis.

It can be seen in Section 9.3.1.2 and the study of previous perovskite oxynitrides[87-89] that the nitride ions may adopt an ordered arrangement. From a crystallographic point of view, the nitride order itself can lower the structure symmetry. In the analysis in Section 9.3.1.2, the low symmetry $A2_1am$ structure was constructed by considering the octahedral tilting distortions only. Despite the visually good fit in Figure 9.3, $Na_{1+x}NdTa_2O_{7-y}N_y$ may have a lower symmetry structure than $A2_1am$ due to a possible nitride order or even the interlayer

sodium order. Consequently, other techniques such as the electron diffraction should be used to help determine the space group as well as the unit cell dimension.

9.4 $Li_{1+x}NdTa_2O_{7-x}N_x$ and $M_xLi_yNdTa_2O_{7-z}N_z$ (M = Mn/Fe/Co/Ni/Cu)

9.4.1 Results

9.4.1.1 Optical SHG measurements

Powder SHG measurements show that there is no detectable SHG signal from $Li_{1+x}NdTa_2O_{7-x}N_x$, $Mn_xLi_yNdTa_2O_{7-z}N_z$, $Fe_xLi_yNdTa_2O_{7-z}N_z$, $Co_xLi_yNdTa_2O_{7-z}N_z$ or $Cu_xLi_yNdTa_2O_{7-z}N_z$, indicating these five compounds adopt centrosymmetric crystal structures. In contrast, $Ni_xLi_yNdTa_2O_{7-z}N_z$ is SHG active with the intensity 0.53 times of the α-SiO_2 standard, indicating it adopts a non-centrosymmetric crystal structure.

9.4.1.2 Structural characterisation of $Li_{1+x}NdTa_2O_{7-x}N_x$

Synchrotron X-ray diffraction data collected from $Li_{1+x}NdTa_2O_{7-x}N_x$ at ambient temperature can be indexed using a tetragonal, aristotype *I*4/*mmm* unit cell (a = 3.8756 Å, c = 19.4869 Å). No superlattice peak suggesting any cell expansion is observed. Combining this observation with its inactive SHG activity, a centrosymmetric *I*4/*mmm* symmetry model was constructed with a hypothetic composition $Li_2NdTa_2O_6N$ and refined against the synchrotron X-ray diffraction data. The nitride ions were set to be evenly distributed among all three oxide sites. The observed, calculated and difference plots against the synchrotron X-ray diffraction data in space group *I*4/*mmm* are shown in Figure 9.5.

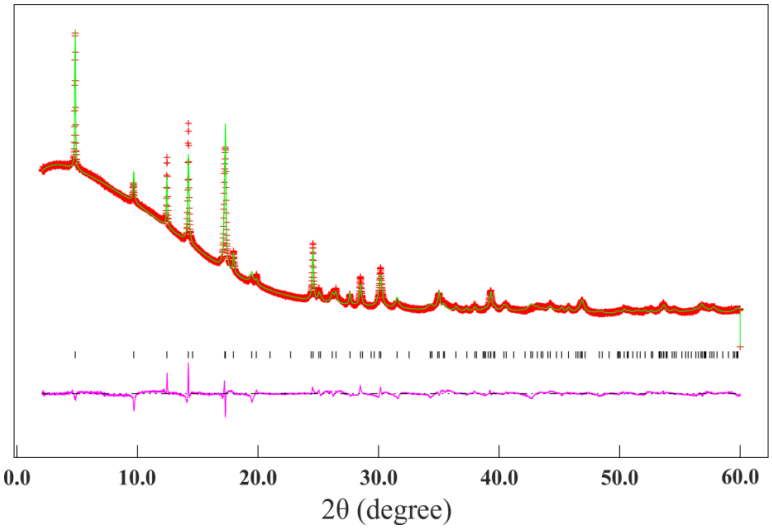


Figure 9.5. Observed, calculated and different plots from the refinement of the *I*4/*mmm* model against the synchrotron X-ray diffraction data collected from $Li_{1+x}NdTa_2O_{7-x}N_x$ at 298 K.

Neutron diffraction data collected from a sample of $Li_{1+x}NdTa_2O_{7-x}N_x$ (0.8 g) at ambient temperature using the HRPD instrument show poor quality due to the small sample size and water present in the sample. Therefore no thorough structural characterisation was performed based on the low-quality neutron diffraction data.

9.4.1.3 Cation exchange reactions of $Li_{1+x}NdTa_2O_{7-x}N_x$

$Li_{1+x}NdTa_2O_{7-x}N_x$ was used for further cation exchange reactions with divalent 3*d* transition metal salts. Since divalent 3*d* transition metal cations in the tetrahedral geometry have similar (but not the same) ionic radii with the Li^+ cation, it is expected that the cation exchange reaction would be accompanied by a subtle change in the *c* lattice. In the X-ray diffraction pattern, this subtle change is demonstrated by a small shift of the 00*l* reflections. Figure 9.6 shows the diffraction patterns collected from $Li_{1+x}NdTa_2O_{7-x}N_x$ and $M_xLi_yNdTa_2O_{7-z}N_z$ (*M* = Mn/Fe/Co/Ni/Cu) using the same X-ray diffractometer. It can be seen that although all diffraction patterns look similar, 00*l* reflections shift to the left for the cation-exchanged products and the shift of the 004 peak is emphasized by a dotted line. The shift of the 00*l* peaks suggests that the cation-exchanged products have bigger *c* lattices than the lithium precursor. This observation is consistent with the cation exchange reactions

demonstrated in Chapters 7 and 8 as reactions from $Li_2SrTa_2O_7$ to $MnSrTa_2O_7$, $Co_xLi_{2-2x}SrTa_2O_7$ and $Cu_xLi_{2-2x}SrTa_2O_7$ also lead to an expansion in the *c* lattice.

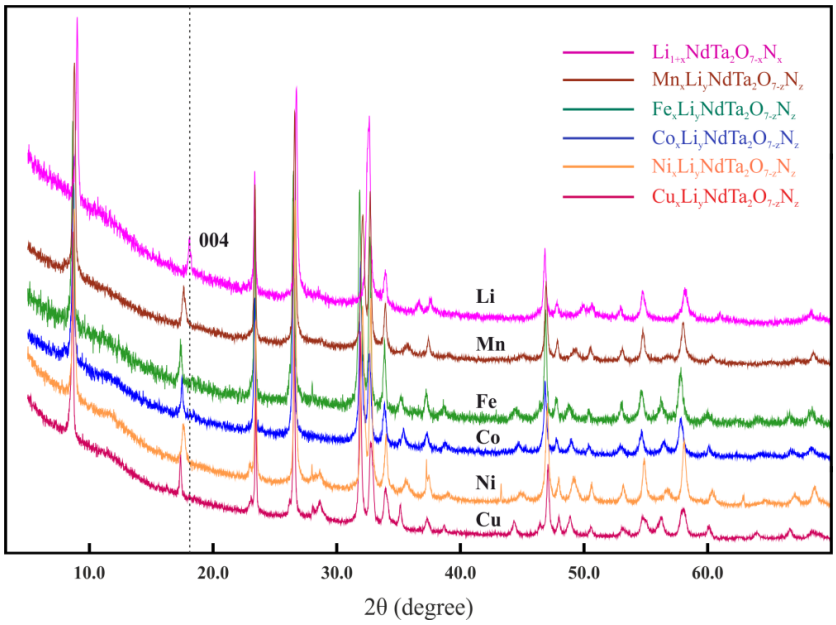


Figure 9.6. Diffraction patterns collected from $Li_{1+x}NdTa_2O_{7-x}N_x$ and $M_xLi_yNdTa_2O_{7-z}N_z$ (*M* = Mn/Fe/Co/Ni/Cu) using the same X-ray diffractometer. Shift of the 004 peak suggests there is an expansion in the *c* lattice during the cation exchange reaction.

9.4.1.4 Structural characterisation of $M_xLi_yNdTa_2O_{7-z}N_z$ (*M* = Mn/Fe/Co/Ni/Cu)

Despite the fact that it is not possible to unambiguously deduce the crystal structures of $M_xLi_yNdTa_2O_{7-z}N_z$ without knowing the transition metal to lithium ratio as well as the oxide to nitride ratio, efforts have been devoted to the analysis of the diffraction data to extract some structural information. It is observed that the cobalt-exchanged product reached the best sample quality with little impurity and high crystallinity, hence this section will focus on $Co_xLi_yNdTa_2O_{7-z}N_z$ and the polar phase $Ni_xLi_yNdTa_2O_{7-z}N_z$.

9.4.1.4.1 Structural characterisation of $Co_xLi_yNdTa_2O_{7-z}N_z$

Synchrotron X-ray diffraction data collected from $Co_xLi_yNdTa_2O_{7-z}N_z$ can be indexed using an orthorhombic unit cell with an approximate $\sqrt{2} \times \sqrt{2} \times 1$ geometric expansion of the aristotype *I*4/*mmm* unit cell, ($a = 5.4871$ Å, $b = 5.4682$ Å, $c = 20.2837$ Å). The extinction conditions suggest a *B*-centred or a primitive space group. Lacking SHG intensity suggests the compound adopt a centrosymmetric structure. Referring to the symmetry analysis of

the distorted n = 2 Ruddlesden-Popper structures in Chapter 4 (Table 4.1), several *B*-centred or primitive, centrosymmetric symmetry models were constructed and refined against the synchrotron X-ray diffraction data and they gave approximately equally good fits. As an example, the refinement plots of a *Bmcm* model against the diffraction data are shown in Figure 9.7. The insert plot shows two superlattice peaks which can only be indexed and fitted with an expanded cell.

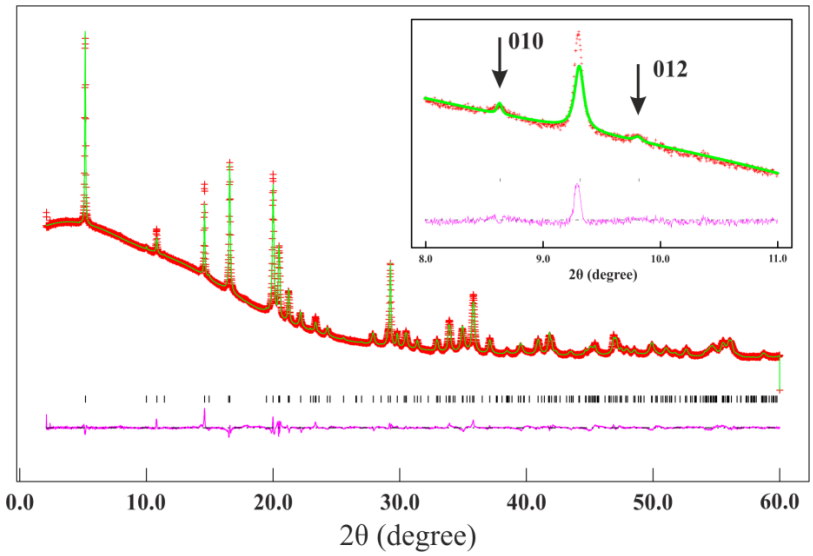


Figure 9.7. Observed, calculated and different plots from the refinement of the *Bmcm* model against the synchrotron X-ray diffraction data collected from $Co_xLi_yNdTa_2O_{7-z}N_z$ at 298 K.

High-resolution neutron powder diffraction data were collected from a sample of 2.4 g $Co_xLi_yNdTa_2O_{7-z}N_z$ at ambient temperature using the HRPD instrument at ISIS. In common with the analogous synchrotron X-ray diffraction data, the neutron diffraction data can be indexed with a $\sqrt{2} \times \sqrt{2} \times 1$ geometric expansion of the undistorted cell, with the extinction conditions consistent with a *B*-centred or primitive unit cell. The same *Bmcm* symmetry model, with an $a^-a^-c^0/-(a^-a^-)c^0$ tilting distortion, was constructed with a hypothetical composition $CoNdTa_2O_6N$ and refined against the neutron diffraction data. The nitride ions were set to be evenly distributed among all four anion sites and it was not attempted to refine the nitride/oxide ratio. The refinement gives a good visual and statistical fit (wRp = 3.30%, Rp = 3.25%), as shown in Figure 9.8. Peaks labelled with arrows are the superlattice

peaks which cannot be indexed by the aristotype *I*4/*mmm* cell. The refined structure is shown in Figure 9.9 and selected bond lengths from the refined structure are shown in Table 9.2.

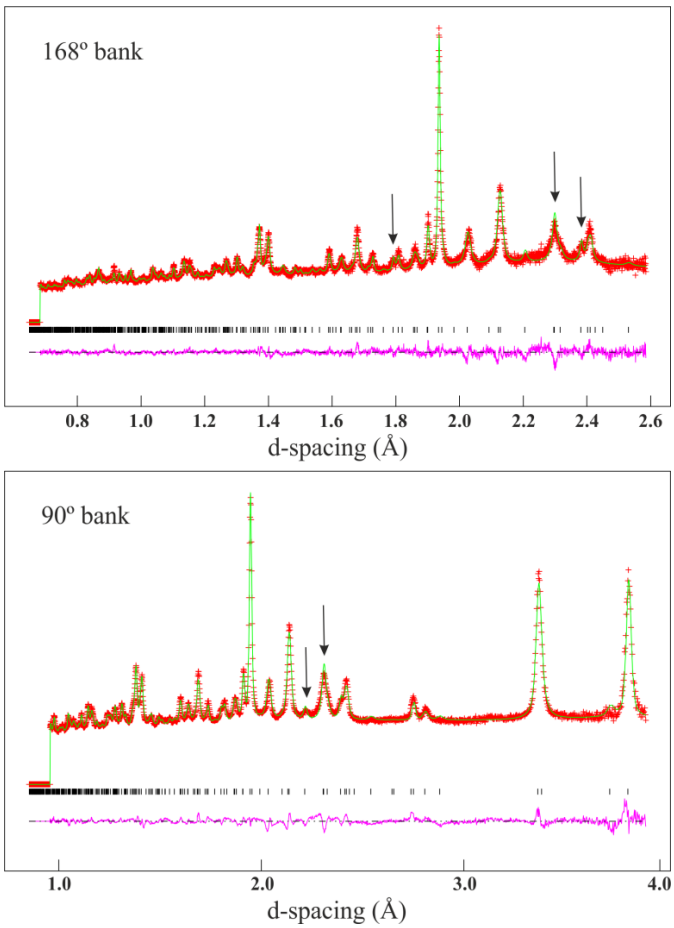


Figure 9.8. Observed, calculated and different plots from the refinement of the *Bmcm* model with a composition $Co_xLi_yNdTa_2O_{7-z}N_z$ against the neutron powder diffraction data collected at 298K. Superlattice peaks are shown with the solid arrows.

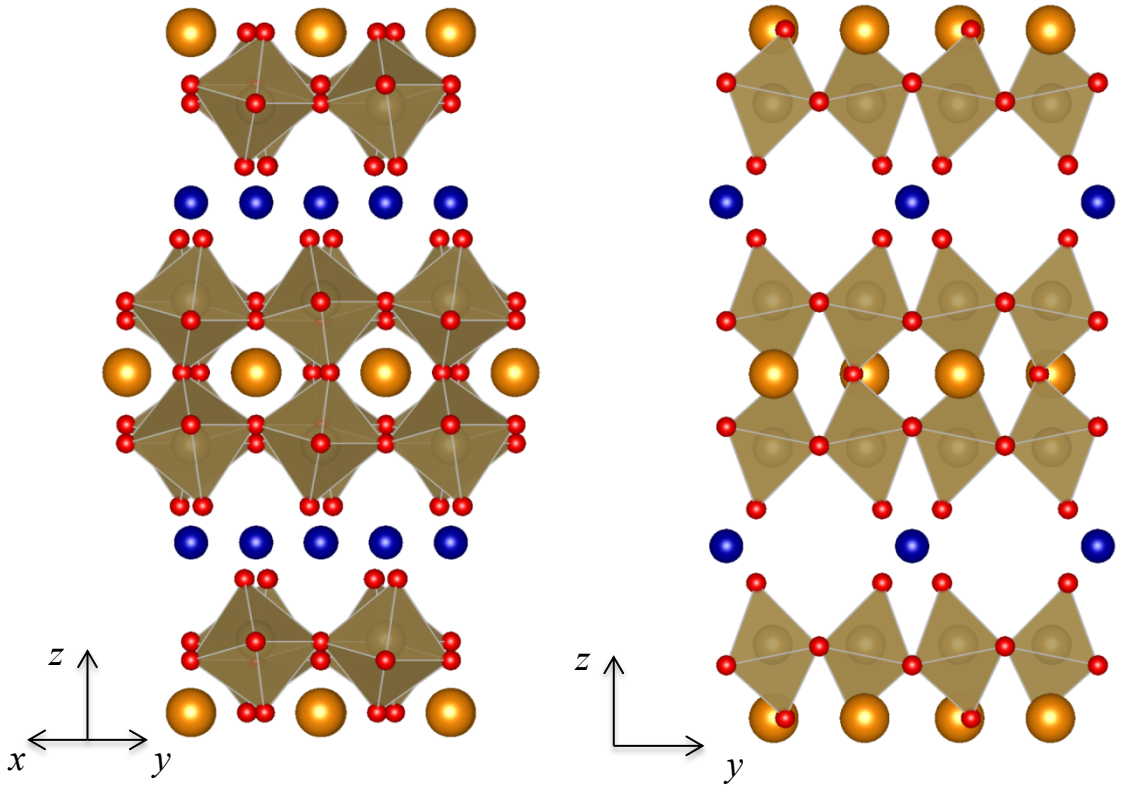


Figure 9.9. The refined *Bmcm* structure of $CoNdTa_2O_6N$, with an $a^-a^-c^0$/-(a^-a^-)c^0 tilting distortion. The blue and gold spheres are Co^{2+} and Nd^{3+} cations respectively. Ta^{5+} cations are inside the polyhedra. Red spheres are O^{2-}/N^{3-} ions.

Cation	Anion	length (Å)	BVS
Co(1)	O/N(3) × 4	1.959(3)	+1.95
Nd(1)	O/N(1) × 2	2.763(1)	+2.85
	O/N(1) × 1	3.126(7)	
	O/N(1) × 1	2.336(7)	
	O/N(2) × 4	2.499(4)	
	O/N(3) × 4	2.850(4)	
Ta(1)	O/N(1)	2.192(3)	+5.00
	O/N(2) × 2	2.025(3)	
	O/N(3) × 2	1.939(3)	
	O/N(4)	1.880(5)	

Table 9.2. Selected bond lengths from the refined structure of $CoNdTa_2O_6N$. The BVS values were calculated by assuming there are only oxide ions in the anion sites.

Although refining the *Bmcm* model gives a good fit (Figure 9.8) and the refined structure is chemically reasonable (Figure 9.9 and Table 9.2), it is not possible to confidently conclude that $Co_xLi_yNdTa_2O_{7-z}N_z$ adopts a *Bmcm* symmetry model and supplementary data is required to determine the composition and study any possible Co/Li and O/N order.

However, it can be hypothesized that the final crystal structure of $Co_xLi_yNdTa_2O_{7-z}N_z$ is likely to be a perturbation of the refined *Bmcm* structure.

9.4.1.4.2 Structural characterisation of $Ni_xLi_yNdTa_2O_{7-z}N_z$

Synchrotron X-ray diffraction data collected from $Ni_xLi_yNdTa_2O_{7-z}N_z$ can be indexed using an orthorhombic unit cell with an approximate $\sqrt{2} \times \sqrt{2} \times 1$ geometric expansion of the aristotype *I*4/*mmm* unit cell, (a = 5.4711 Å, b = 5.4576 Å, c = 20.1340 Å). The extinction conditions suggested an *A*-centred or a primitive space group. Combining these observations with its observed SHG activity, symmetry models describing non-centrosymmetric structures from Table 4.1 were constructed and refined against the synchrotron X-ray diffraction data. Refinements give similar statistical and visual fits. As an example, the refinement plots using an $A2_1am$ model against the diffraction data are shown in Figure 9.10. The model was constructed based on a composition $NiNdTa_2O_6N$ and the nitride ions were set to be evenly distributed in all anion sites.

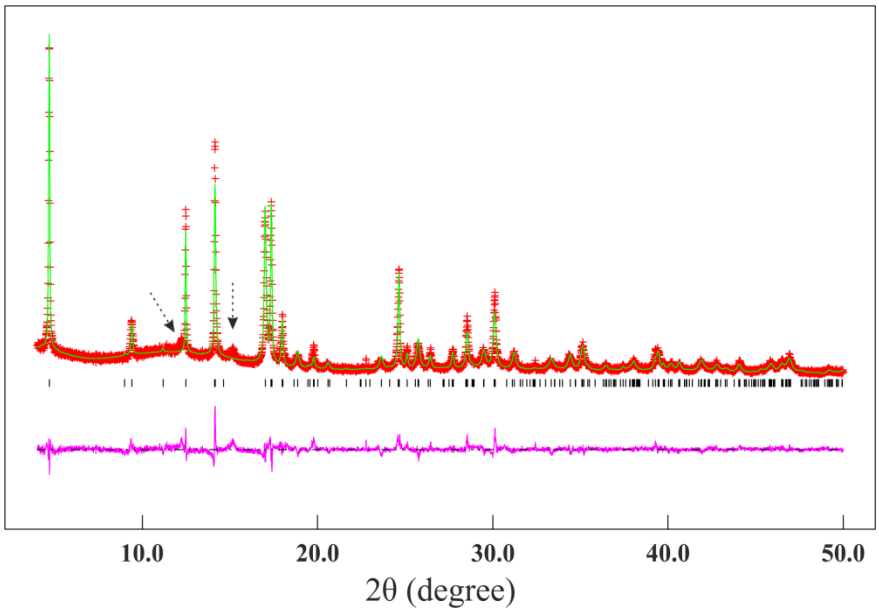


Figure 9.10. Observed, calculated and different plots from the refinement of the $A2_1am$ model against the synchrotron X-ray diffraction data collected from $Ni_xLi_yNdTa_2O_{7-z}N_z$ at 298 K. Peaks labelled with dashed arrows are attributed to unknown impurities.

High-resolution neutron powder diffraction data were collected from a sample of 2.8 g $Ni_xLi_yNdTa_2O_{7-z}N_z$ at ambient temperature using the HRPD instrument at ISIS. The diffraction data can be indexed with an orthorhombic unit cell with a $\sqrt{2} \times \sqrt{2} \times 1$ expansion of the undistorted cell. Similar to the refinements against the synchrotron X-ray diffraction data, the non-centrosymmetric structural models were refined against the neutron diffraction data but none of them gives satisfying fits, suggesting there are extra factors lowering the crystal symmetry in addition to the octahedral tilting distortions. Two obvious possibilities are the Ni/Li order and the O/N order. Consequently, supplementary measurements, such as the elemental analysis and the electron diffraction, will be used to help the structural characterisation.

9.4.1.5 Magnetic characterisation of $M_xLi_yNdTa_2O_{7-z}N_z$ (M = Mn/Fe/Co/Ni/Cu)

Magnetisation data were collected from samples of $M_xLi_yNdTa_2O_{7-z}N_z$ (M = Mn/Fe/Co/Ni/Cu) in an applied filed of 100 Oe in the temperature range $5 \leq T/K \leq 300$. The ZFC and FC data collected from $Co_xLi_yNdTa_2O_{7-z}N_z$ and $Ni_xLi_yNdTa_2O_{7-z}N_z$ diverge at 5 K and 20 K respectively (Figure 9.11), suggesting that both phases adopt magnetically ordered states at low temperatures. As shown in Figure 9.11, for both phases, magnetisation-field isotherms collected at 300 K are linear and pass through the origin, while the low temperature data collected at 5 K show small hysteresis, suggesting canted antiferromagnetic order in both $Co_xLi_yNdTa_2O_{7-z}N_z$ and $Ni_xLi_yNdTa_2O_{7-z}N_z$. The low temperature magnetic order observed from $Ni_xLi_yNdTa_2O_{7-z}N_z$, together with its polar crystal structure, indicates this oxynitride phase can be multiferroic. However, neutron diffraction data collected from $Ni_xLi_yNdTa_2O_{7-z}N_z$ at 5 K show no evidence of long-range magnetic order.

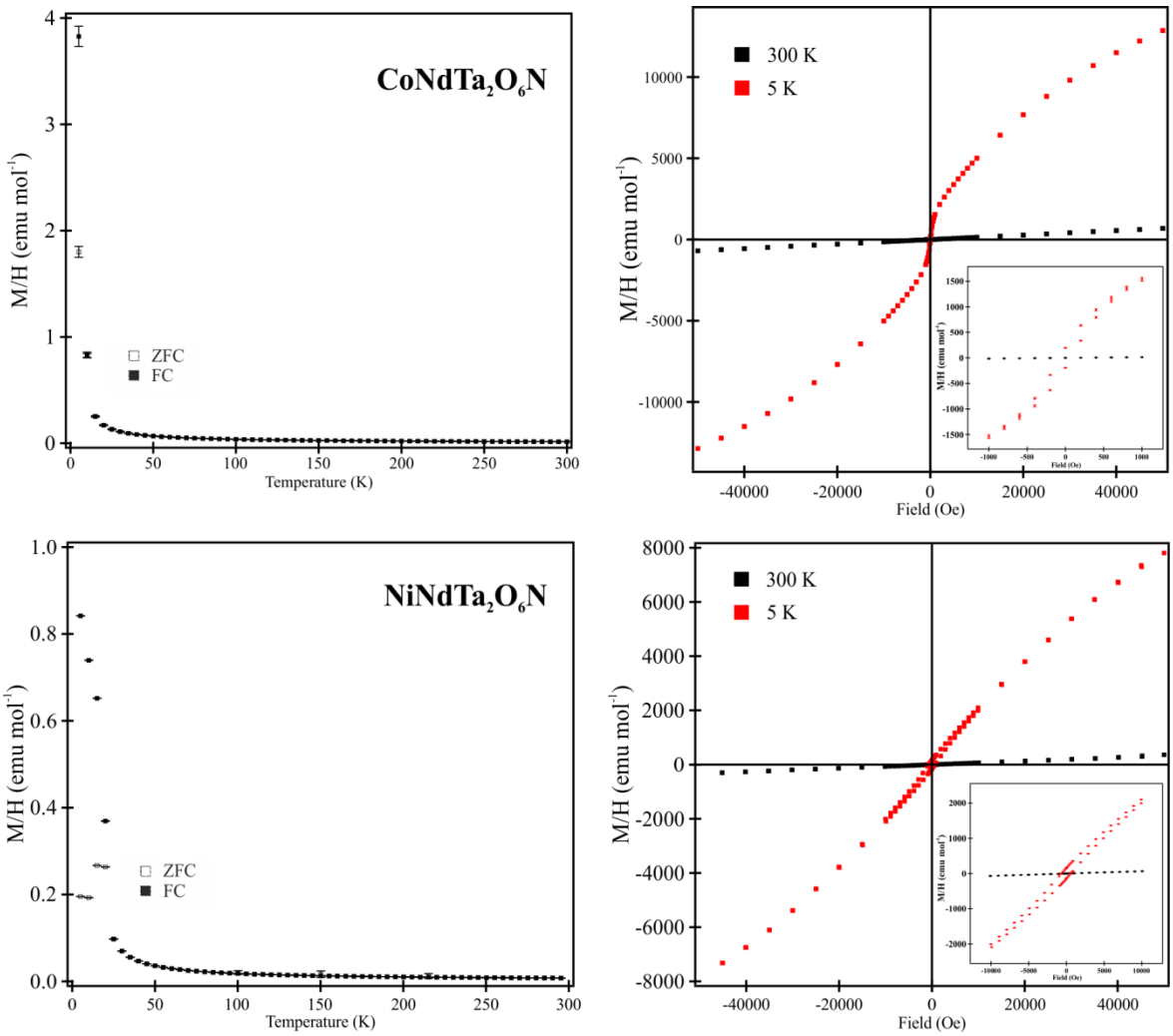


Figure 9.11. ZFC and FC magnetisation data (left) and magnetization-field isotherms (right) collected from $Co_xLi_yNdTa_2O_{7-z}N_z$ and $Ni_xLi_yNdTa_2O_{7-z}N_z$. Hypothetical formulas ($CoNdTa_2O_6N$ and $NiNdTa_2O_6N$) were used when processing the data. The insert pictures in the magnetization-field isotherms show the small hysteresis at 5 K.

As shown in Figure 9.12, ZFC and FC data collected from $Mn_xLi_yNdTa_2O_{7-z}N_z$ and $Fe_xLi_yNdTa_2O_{7-z}N_z$ show no diverge, suggesting they remain paramagnetic states down to 5 K. ZFC and FC data collected from $Cu_xLi_yNdTa_2O_{7-z}N_z$ diverge at 5 K. The magnetization-field isotherms collected at 300 K from $Cu_xLi_yNdTa_2O_{7-z}N_z$ are linear and pass the origin. The analogous data collected 5 K also pass the origin, indicating a possible antiferromagnetic state.

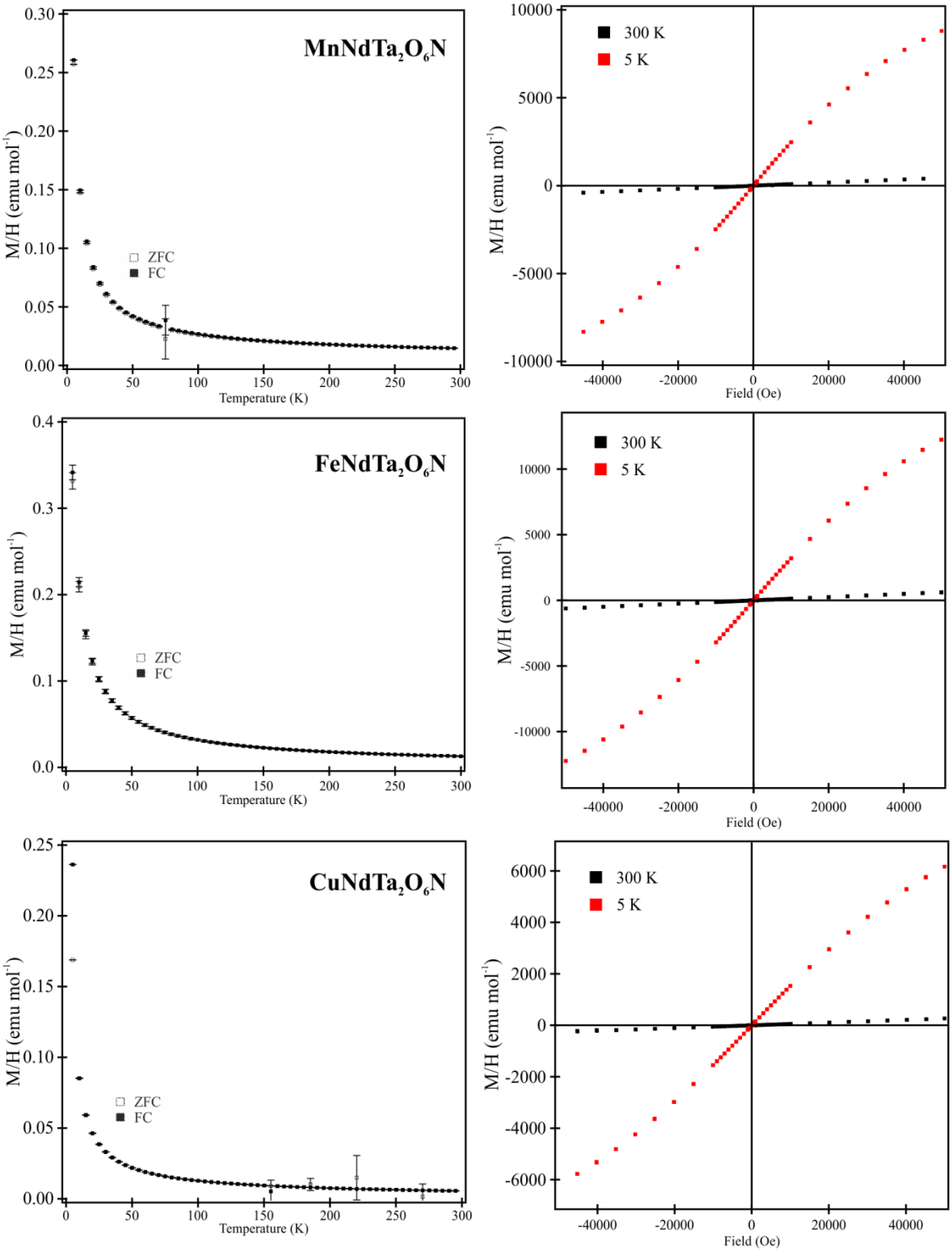


Figure 9.12. ZFC and FC magnetisation data (left) and magnetization-field isotherms (right) collected from $Mn_xLi_yNdTa_2O_{7-z}N_z$, $Fe_xLi_yNdTa_2O_{7-z}N_z$ and $Cu_xLi_yNdTa_2O_{7-z}N_z$. Hypothetical formulas ($MnNdTa_2O_6N$, $FeNdTa_2O_6N$ and $CuNdTa_2O_6N$) were used when processing the data.

9.4.2 Discussion

The successful cation exchange reactions from $Li_{1+x}NdTa_2O_{7-x}N_x$ to $M_xLi_yNdTa_2O_{7-z}N_z$ (M = Mn/Fe/Co/Ni/Cu) suggest that $Li_{1+x}NdTa_2O_{7-x}N_x$ is a robust system. The formation of single phases $M_xLi_yNdTa_2O_{7-z}N_z$, as well as $MSrTa_2O_7$ in Chapter 7 and 8, shows that it is generally feasible to replace the Li^+ cations with divalent 3*d* transition metal cations which have similar ionic radii to Li^+ (Table 8.1 in Chapter 8). In addition to the neutron diffraction and X-ray diffraction, supplementary measurements are required in order to thoroughly and precisely characterise the crystal structures of these oxynitride phases. Electron diffraction can be used to probe the possible interlayer cation order and the nitride order as it is sensitive to both nuclei and charges. Other techniques, such as the energy-dispersive X-ray spectroscopy, nuclear activation analysis and combustion analysis, can be utilised to determine the compositions of these oxynitride phases.

It is concluded from the SHG measurements that $Ni_xLi_yNdTa_2O_{7-z}N_z$ adopts a non-centrosymmetric structure while the rest four $M_xLi_yNdTa_2O_{7-z}N_z$ (M = Mn/Fe/Co/Cu) adopt centrosymmetric structures. Since the compositions of the perovskite layers $NdTa_2O_{7-z}N_z$ are roughly the same, it is hypothesised that the different crystal structures are resulted from different transition metal cations. Since the reaction precursor, $Li_{1+x}NdTa_2O_{7-x}N_x$, shows zero observed SHG intensity, the positive SHG signal observed from $Ni_xLi_yNdTa_2O_{7-z}N_z$ must be from the cation-exchanged product rather than the reactants. Its clear magnetic order and canted moment indicate that $Ni_xLi_yNdTa_2O_{7-z}N_z$ can be multiferroic.

The synthesis of $M_xLi_yNdTa_2O_{7-z}N_z$ (M = Mn/Fe/Co/Ni/Cu) is a rare example of a four-step solid-state synthesis with three soft chemical steps. It includes a traditional ceramic synthetic step ($RbNdTa_2O_7$), a topochemical cation exchange reaction ($LiNdTa_2O_7$), a topochemical anion exchange reaction accompanied by a cation insertion ($Li_{1+x}NdTa_2O_{7-x}N_x$) and finally another cation exchange reaction ($M_xLi_yNdTa_2O_{7-z}N_z$). This solid-state

'total synthesis' shows that crystalline solids, at least layered perovskites, are robust systems and can be engineered through different topochemical reactions. From a chemical point of view, it demonstrates that solid-state chemists can go far beyond the thermodynamic phases and it is possible to intercalate multiple useful properties into crystalline solids by modifying solids in a topochemical manner.

A similar compound, $Li_2LaTa_2O_6N$, was reported to be a good candidate for high-performance catalysts[92]. This compound was prepared by a citrate gel method via a single step reaction and its composition was reported to be very close to the theoretical value of $Li_2LaTa_2O_6N$. It is therefore interesting to see if a similar reaction can be performed to synthesise $Li_2NdTa_2O_6N$ and if a better control of the chemical composition can be achieved. In addition, the photocatalytic performance of $Li_{1+x}NdTa_2O_{7-x}N_x$ and $M_xLi_yNdTa_2O_{7-z}N_z$ (M = Mn/Fe/Co/Ni/Cu) should also be tested.

9.5 Conclusion

Single phases $Na_{1+x}NdTa_2O_{7-x}N_x$ and $Li_{1+x}NdTa_2O_{7-x}N_x$ were successfully synthesised. A series of cation-exchanged products $M_xLi_yNdTa_2O_{7-z}N_z$ (M = Mn/Fe/Co/Ni/Cu) were prepared from $Li_{1+x}NdTa_2O_{7-x}N_x$. The optical SHG measurements show that $Na_{1+x}NdTa_2O_{7-x}N_x$ and $Ni_xLi_yNdTa_2O_{7-z}N_z$ both adopt non-centrosymmetric structures but the rests adopting centrosymmetric structures. Supplementary measurements such as electron diffraction and elemental analysis measurements will be performed to determine the chemical composition as well as to probe possible cation/anion order in these phases.

The four-step synthesis of $M_xLi_yNdTa_2O_{7-z}N_z$ suggests that solid-state chemists can carefully engineer crystalline solids and hence make novel functional materials.

Chapter 10 – Conclusion

This thesis focuses on the synthesis and characterisation of a wide range of n = 2 Dion-Jacobson phases and Ruddlesden-Popper phases. The aim is not only to make new ferroelectric and multiferroic materials but more importantly to understand what leads to the polar structures of layered perovskites. One of the key discoveries is that the interlayer cations between perovskite blocks, more specifically their sizes, have a great influence on the bulk crystal structures. This discovery encourages us to search for new multiferroic materials by performing cation exchange reactions. It is demonstrated that cation exchange chemistry is a useful method to prepare polar and magnetically ordered compounds.

It can be seen throughout this thesis that the characterisation of layered perovskites with distorted structures is challenging as it involves complicated crystallography. Combining different techniques, such as neutron diffraction, synchrotron X-ray diffraction, optical SHG measurements and DFT calculations, is essential in order to obtain a precise and unambiguous answer. Chapter 3 demonstrates that the neutron diffraction technique is necessary to determine the oxide positions and hence the tilting distortions and the crystal structures of Dion-Jacobson phases CsNdM_2O_7 and RbNdM_2O_7. In fact, the importance of using neutron diffraction can never be underestimated when studying improper ferroelectric oxides as their non-centrosymmetric structures arise from subtle displacements of oxide ions. Chapters 4 and 5 demonstrate how one can relate 'chemically plausible' distorted crystal structures of n = 2 Ruddlesden-Popper and Dion-Jacobson phases to their corresponding space groups. This symmetry analysis has been demonstrated to be very helpful as it includes the ground-state structures of LiNdM_2O_7 and NaNdM_2O_7 (Chapter 4), as well as the crystal structures of RbNdM_2O_7 and CsNdM_2O_7 at different temperatures (Chapter 5). However, this symmetry analysis is far from perfect because low symmetry models are constructed by considering the octahedral tilting distortions only. For

example, Chapters 8 and 9 show how cation order and/or anion order can further lower the symmetry from an already distorted structure.

This thesis can be divided into three stories. The first avenue of research (Chapter 3, 4 and 5) is the demonstration of the importance of interlayer cation sizes on the crystal structures (Figure 10.1). To be more specific, a series of $n = 2$ layered $A'\mathrm{Nd}M_2\mathrm{O}_7$ (A' = Li, Na, Rb or Cs; M = Nb or Ta) with distorted structures were synthesised and characterised. Close inspection of their crystal structures reveals that the tilting distortions of the perovskite layers, especially the relation between the distortions in the adjacent perovskite layers, depend on both the tolerance factor (size mismatch between the A-site and B-site cations) and the interlayer cation sizes. Different competing factors such as the metal-oxygen bonding, interlayer oxygen-oxygen repulsion and intra-layer metal-metal repulsion, exist simultaneously and the bulk structure is a compromise, considering all these factors. As a brief conclusion, with the identity of perovskite double layers unchanged, a big change in the interlayer cation size is likely to result in a change in the crystal structure.

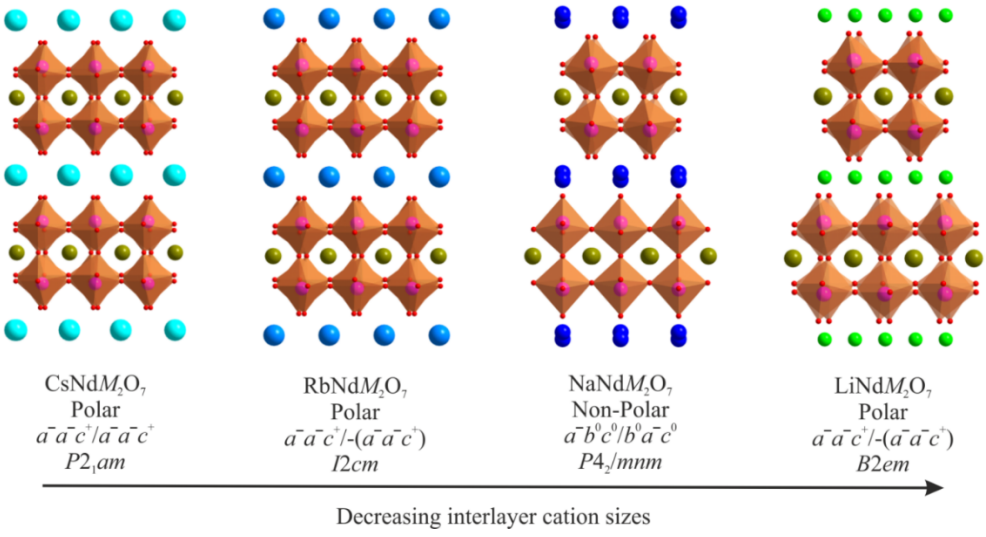


Figure 10.1. Structural evolution as a function of interlayer cation sizes (M = Ta/Nb).

The second part of this thesis (Chapters 6, 7 and 8) is inspired by the discoveries from previous three chapters. An $n = 2$ Ruddlesden-Popper phase, $Li_2SrTa_2O_7$, was demonstrated to be polar. Since the 3*d* transition metal cations M^{2+} (M = Mn/Fe/Co/Ni/Cu) have similar ionic radii with the Li^+ cation in a tetrahedral geometry, a series of cation exchange reactions were performed from $Li_2SrTa_2O_7$ in order to intercalate paramagnetic cations hence to introduce magnetic properties. The cation-exchanged products were expected to adopt the same polar structure as $Li_2SrTa_2O_7$ due to the similar ionic radii of M^{2+} and Li^+. The successful synthesis of polar, magnetically ordered $MnSrTa_2O_7$ suggests that it is feasible to make multiferroic materials via cation exchange reactions from polar precursors. The unsuccessful exchanges of Fe^{2+} and Ni^{2+}, as well as the incomplete exchanges of Co^{2+} and Cu^{2+}, indicate that the lack of crystal field energy could be the key for a complete cation exchange. All these discoveries encourage us to investigate a family of layered compounds with chemical formula $Li_2AB_2O_7$ and their cation exchange chemistry especially with the Mn^{2+} cation (Figure 10.2).

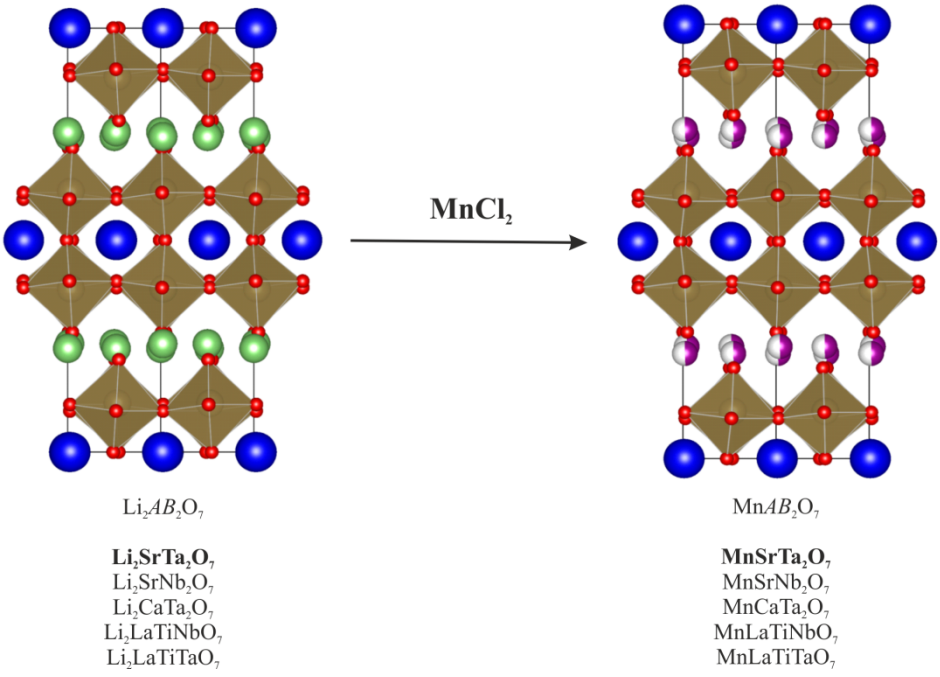


Figure 10.2. Proposed cation exchange reaction from $Li_2AB_2O_7$ to $MnAB_2O_7$.

The final part of this thesis (Chapter 9) describes the synthesis and characterisation of a series of layered perovskite oxynitrides. The discovery of polar $Na_{1+x}NdTa_2O_{7-x}N_x$ and $Ni_xLi_yNdTa_2O_{7-z}N_z$ suggests another family of materials which could adopt polar structures. As current theoretical and experimental studies of improper ferroelectric materials focus on oxides, the study in oxynitride analogues remains an exciting and unexplored area. In addition, the four-step synthesis of $M_xLi_yNdTa_2O_{7-z}N_z$ (M = Mn/Fe/Co/Ni/Cu) suggests that layered perovskites can be very robust and it is practically possible to perform different types of topochemical reactions sequentially (Figure 10.3). It can also be seen from Chapter 9 that in practise the characterisation of these layered oxynitrides is very challenging due to a combination of different complexities (tilting distortion, cation order, anion order etc.). It would be useful if a systematic method can be designed to fully characterise these materials.

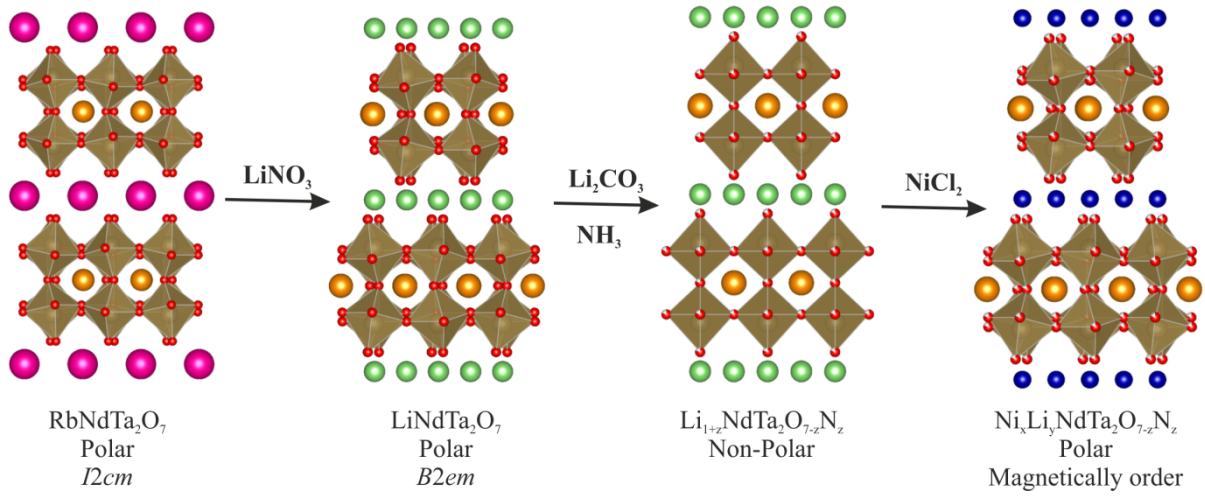


Figure 10.3. A solid-state total synthesis towards a polar, magnetically ordered phase $Ni_xLi_yNdTa_2O_{7-z}N_z$. The synthesis includes a ceramic synthetic step, two cation exchanges and an anion exchange.

Appendix 1 – Index of Figures

Figure 1.1: The simple cubic perovskite structure adopted by $SrTiO_3$……..1

Figure 1.2: The Ruddlesden-Popper structures with molecular formula A'_2BO_4 (left), $A'_2AB_2O_7$ (middle) and $Li_2La_2Ti_3O_{10}$ (right)……...…….3

Figure 1.3: The n = 2 (left) and n = 3 (right) Dion-Jacobson structures……....….4

Figure 1.4: Out-of-phase (left) and in-phase (right) tilting distortions along the *z* axis…….5

Figure 1.5: The $a^-a^-c^+$/-($a^-a^-c^+$) tilting distortion adopted by $RbNdNb_2O_7$……...6

Figure 1.6: Relationships between different physical properties in non-centrosymmetric crystal classes……...8

Figure 1.7: Room temperature *P*4*mm* structure of $BaTiO_3$……...9

Figure 1.8: Left: $CsNdTa_2O_7$ with the undistorted, high-symmetry *P*4/*mmm* structure. Middle: $CsNdTa_2O_7$ with a distorted, low-symmetry $P2_1am$ structure. Right: $CsNdTa_2O_7$ with a distorted, low-symmetry $P2_1am$ structure with extra cation displacements.....11

Figure 1.9: Left: Local electric dipoles in $SrSnO_3$ in space group *Pnam*; Right: Local electric dipoles in theoretically proposed $Ba_{0.5}Sr_{0.5}SnO_3$ in space group $P2_1am$……..…...12

Figure 1.10: Left: Polar $Ca_3Mn_2O_7$ in space group $A2_1am$ with an $a^-a^-c^+/a^-a^-c^+$ tilting distortion; Right: Anti-polar (non-polar) $La_3Ni_2O_{5.5}F_{3.5}$ in space group *Pnam* with an $a^-a^-c^+/a^-a^-c^+$ tilting distortion……13

Figure 1.11: A cation exchange reaction from $RbLaNb_2O_7$ to $(CuCl)LaNb_2O_7$……..16

Figure 2.1: Setup for a cation exchange reaction using open ended silica tubes……..18

Figure 2.2: Setup for the cation exchange reaction using a venting system…….…20

Figure 2.3: Horizontal flow system used to prepare oxynitrides……...….21

Figure 2.4: A cartoon illustration of the Bragg's Law……..……..….22

Figure 2.5 Air-sensitive sample holder used for Panalytical Empyrean and X'Pert diffractometers…….…..25

Figure 2.6: HRPD instrument at the ISIS Neutron and Muon Source…….….29

Figure 2.7: A schematic diagram of a Kurtz-Powder Laser System for SHG test……....35

Figure 3.1: The structure of $CsNdNb_2O_7$ in space group $P2_1am$, with an $a^-a^-c^+$ tilting distortion in the Glazer notation……...……...38

Figure 3.2: Plots of SHG activity of $RbNdNb_2O_7$ (top left), $RbNdTa_2O_7$ (top right) and $CsNdTa_2O_7$ (bottom) as a function of particle size, compared to KH_2PO_4 (KDP) standard……..39

Figure 3.3: Observed, calculated and difference plots from the refinement of the $P2_1am$ model against the synchrotron X-ray diffraction data collected from $CsNdTa_2O_7$ at ambient temperature……..……..…….40

Figure 3.4: Observed, calculated and difference plots from the refinement of the $P2_1am$ model against the high-resolution neutron diffraction data collected from $CsNdTa_2O_7$ at ambient temperature……..……41

Figure 3.5: Observed, calculated and difference plots from the refinement of the $I2cm$ model against the synchrotron X-ray diffraction data collected from $RbNdNb_2O_7$ at 298 K…….…43

Figure 3.6: Observed, calculated and difference plots from the refinement of the $I2cm$ model against the high-resolution neutron diffraction data collected from $RbNdNb_2O_7$ at ambient temperature……..……..……..……44

Figure 3.7: The structure of $RbNdNb_2O_7$ in space group $I2cm$, with an $a^-a^-c^+$/-($a^-a^-c^+$) distortion…….……...46

Figure 3.8: Observed, calculated and difference plots from the refinement of the $I2cm$ model against the synchrotron X-ray diffraction data collected from $RbNdTa_2O_7$ at 298 K…...…….…47

Figure 3.9: Observed, calculated and difference plots from the refinement of the $P2_1am$ model against the synchrotron X-ray diffraction data collected from $RbNdTa_2O_7$ at 298 K…….……47

Figure 3.10: Observed, calculated and difference plots from the refinement of the $I2cm$ model against the high-resolution neutron diffraction data collected from $RbNdTa_2O_7$ at ambient temperature……..……..……...48

Figure 3.11: Observed, calculated and difference plots from the refinement against the high-resolution neutron diffraction data collected from $CsNdTa_2O_7$ at ambient temperature, of structural models of $P2_1am$, $Imam$ and $I2cm$……...……...…..……...53

Figure 3.12: Observed, calculated and difference plots from the refinement against the high-resolution neutron diffraction data collected from $RbNdNb_2O_7$ at room temperature, of structural models of $P2_1am$, $Imam$ and $I2cm$…….……...……...54

Figure 3.13: Observed, calculated and difference plots from the refinement against the high-resolution neutron diffraction data collected from $RbNdTa_2O_7$ at room temperature, of structural models of $P2_1am$, $Imam$ and $I2cm$…….……...…...55

Figure 3.14: Left: Refined structure of $RbNdNb_2O_7$ in space group $I2cm$ with an $a^-a^-c^+$/-($a^-a^-c^+$) distortion. Right: Hypothetical structure of $RbNdNb_2O_7$ with an $a^-a^-c^+$ distortion…….....59

Figure 3.15: Left: A RbO_8 polyhedron in the refined $I2cm$ structure. Right: A RbO_8 polyhedron in the hypothetical, primitive stacking structure……...…...…60

Figure 3.16: Left: A CsO_8 polyhedron in the refined $P2_1am$ structure. Right: A CsO_8 polyhedron in the hypothetical, $I2cm$-type structure……...……61

Figure 4.1: Structural transformation from the n = 2 Dion-Jacobson framework to the n = 2 Ruddlesden-Popper framework……...……65

Figure 4.2: Plots of SHG activity of $LiNdNb_2O_7$ and $LiNdTa_2O_7$ as a function of particle size, compared to an α-SiO_2 standard……..…….……...67

Figure 4.3: Synchrotron X-ray powder diffraction data collected from $LiNdNb_2O_7$ and $LiNdTa_2O_7$ in the range of $7 < 2\theta/° < 11$……...……...……71

Figure 4.4: Observed, calculated and difference plots from the refinement of the *B*2*em* model against the synchrotron X-ray diffraction data collected from $LiNdNb_2O_7$ at 298 K.....71

Figure 4.5: Observed, calculated and difference plots from the refinement of the *B*2*em* model against high-resolution neutron diffraction data collected from $LiNdNb_2O_7$ at ambient temperature……...74

Figure 4.6: The structure of $LiNdNb_2O_7$ in space group *B*2*em*, with an $a^-a^-c^+$/-($a^-a^-c^+$) tilting distortion……...……...75

Figure 4.7: Observed, calculated and difference plots from the refinement of the *B*2*em* model against the synchrotron X-ray diffraction data collected from $LiNdTa_2O_7$ at 298 K……..…...76

Figure 4.8 Observed, calculated and difference plots from the refinement of the *B*2*em* model against high-resolution neutron diffraction data collected from $LiNdTa_2O_7$ at ambient temperature……...78

Figure 4.9: Synchrotron X-ray diffraction data collected from $NaNdNb_2O_7$……..…81

Figure 4.10: Observed, calculated and difference plots from the refinement of the $P4_2/mnm$ model against the synchrotron X-ray diffraction data collected from $NaNdNb_2O_7$ at 298 K…….81

Figure 4.11: Observed, calculated and difference plots from the refinement of the *Pnnm*, *Pnam* and $P4_2/mnm$ models against neutron powder diffraction data collected from $NaNdNb_2O_7$ at 298 K……..…….…...82

Figure 4.12: The refined structure of $NaNdNb_2O_7$ in space group $P4_2/mnm$, with an $a^-b^-c^0$/ $b^-a^-c^0$ distortion……..……83

Figure 4.13: Measurement of distortion angles along a particular direction……84

Figure 4.14: Observed, calculated and difference plots from the refinement of the $P4_2/mnm$ model against high-resolution neutron diffraction data collected from $NaNdNb_2O_7$ at ambient temperature……..…….85

Figure 4.15: The structure of $NaNdNb_2O_7$ in space group $P4_2/mnm$, with an $a^-b^0c^0$/ $b^0a^-c^0$ distortion……...86

Figure 4.16: Synchrotron X-ray (top 2 panels plotted against 2θ) and neutron powder diffraction data (bottom panel plotted against d-spacing) collected from $NaNdTa_2O_7$ at ambient temperature……..…….88

Figure 4.17: Observed, calculated and difference plots from the refinement of the $P4_2/mnm$ model against the synchrotron X-ray diffraction data collected from $NaNdTa_2O_7$ at 298 K…….88

Figure 4.18: Observed, calculated and difference plots from the refinements of the *Pnnm*, *Pnam* and $P4_2/mnm$ models against neutron powder diffraction data collected from $NaNdTa_2O_7$ at 298 K……..……90

Figure 4.19: Observed, calculated and difference plots from the refinement of the $P4_2/mnm$ model against high-resolution neutron diffraction data collected from $NaNdTa_2O_7$ at ambient temperature……..…….91

Figure 4.20: The 'tetrahedral' coordination site in the aristotype structure of $A'NdB_2O_7$ (A' = Li/Na; B = Nb/Ta)…….. ……94

Figure 4.21: The ordering arrangements of Na^+ (left) and Li^+ (right) cations…….…….95

Figure 5.1: Observed, calculated and difference plots from the refinement of a structural model in space group *I*2*cm* against the NPD and SXRD data collected from $RbNdTa_2O_7$ at ambient temperature……..……..…….106

Figure 5.2: Temperature evolution of some reflections from $RbNdTa_2O_7$ upon heating...107

Figure 5.3: Temperature evolution of some superlattice peaks corresponding to doubling the *c* lattice……..…….…….107

Figure 5.4: Observed, calculated and difference plots from the refinements of the $P2_1/m$ and *Cmca* models against the neutron diffraction data collected from $RbNdTa_2O_7$ at 673 K……109

Figure 5.5: Observed, calculated and difference plots from the refinement of a structure model in space group *Cmca* against neutron diffraction data collected from $RbNdTa_2O_7$ at 673 K……110

Figure 5.6: Neutron diffraction patterns collected from $RbNdTa_2O_7$ at 673 K and 973 K……112

Figure 5.7: Observed, calculated and difference plots from the refinements of the *I*4/*mcm* models with $a^0a^0c^+/a^0a^0$-c^+ and $a^0a^0c^-/a^0a^0$-c^- tilting distortions against the neutron diffraction data collected from $RbNdTa_2O_7$ at 973 K……..…..113

Figure 5.8: Observed, calculated and difference plots from the refinement of a structural model in space group *I*4/*mcm* against data collected from $RbNdTa_2O_7$ at 973 K……..113

Figure 5.9: Temperature evolution of the [213] superlattice peak corresponding to the *c* lattice……..……..115

Figure 5.10: Observed, calculated and difference plots from the refinement of a structure model in space group *P*4/*mmm* against data collected from $RbNdTa_2O_7$ at 1273 K……..115

Figure 5.11 Temperature evolution of the normalised lattice parameters of $RbNdTa_2O_7$ determined from the variable temperature synchrotron X-ray diffraction experiments....117

Figure 5.12: Phase transitions and the corresponding crystal structures of $RbNdTa_2O_7$ observed from high-resolution neutron powder diffraction data……...……117

Figure 5.13: Observed, calculated and difference plots from the refinement of a structure model in space group *I*2*cm* against NPD and SXRD data collected from $RbNdNb_2O_7$ at ambient temperature……..……...119

Figure 5.14: Temperature evolution of some reflections of $RbNdNb_2O_7$ upon heating....120

Figure 5.15: Observed, calculated and difference plots from the refinement of a structure model in space group *Cmca* against the neutron diffraction data collected from $RbNdNb_2O_7$ at 823 K……...…..121

Figure 5.16: Temperature evolution of the lattice parameters of $RbNdNb_2O_7$ determined from the analysis of variable temperature synchrotron X-ray diffraction data……..122

Figure 5.17: Observed, calculated and difference plots from the refinement of a structure model in space group *I*4/*mcm* against the neuron diffraction data collected from $RbNdNb_2O_7$ at 923 K……..……..122

Figure 5.18: Observed, calculated and difference plots from the refinement of a structure model in space group $P2_1am$ against NPD and SXRD data collected from $CsNdTa_2O_7$ at ambient temperature……..……..……..……...124

Figure 5.19: Temperature evolution of some reflections from $CsNdTa_2O_7$ upon heating……..126

Figure 5.20: Observed, calculated and difference plots from the refinement of a structure model in space group *C*2/*m* against data collected from $CsNdTa_2O_7$ at 473 K…….....….127

Figure 5.21: Comparison of the neutron diffraction patterns (back-scattering bank) collected at 473 K and 923 K from $CsNdTa_2O_7$……..…….……128

Figure 5.22: Observed, calculated and difference plots from the refinement of a structure model in space group *P*4/*mmm* against data collected from $CsNdTa_2O_7$ at 923 K……129

Figure 5.23: Phase transitions and the corresponding crystal structures of $CsNdTa_2O_7$ observed from high-resolution neutron powder diffraction data…….....…..…131

Figure 5.24: Temperature evolution of the lattice parameters for $CsNdTa_2O_7$ determined from the variable temperature synchrotron X-ray diffraction experiments…….…..…131

Figure 5.25: Observed, calculated and difference plots from the refinement of a structure model in space group $P2_1am$ against the NPD and SXRD data collected from $CsNdNb_2O_7$ at ambient temperature……..…….……..…….132

Figure 5.26: Temperature evolution of some reflections from $CsNdNb_2O_7$ upon heating……..134

Figure 5.27: Observed, calculated and difference plots from the refinement of a structure model in space group *C*2/*m* against data collected from $CsNdNb_2O_7$ at 723 K……..…135

Figure 5.28: Temperature evolution of the lattice parameters for $CsNdNb_2O_7$ determined from the variable temperature synchrotron X-ray diffraction experiments……...136

Figure 5.29: Observed, calculated and difference plots from the refinement of a structure model in space group *P*4/*mmm* against data collected from $CsNdNb_2O_7$ at 873 K……....137

Figure 5.30: A comparison of the interlayer O-O bonds between the refined *C*2/*m* structure (left) and the refined *Cmca* structure (right) adopted by $CsNdNb_2O_7$ and $RbNdNb_2O_7$, respectively……..……140

Figure 5.31: Ferroelectric transition temperatures (T_C) of a series of n = 2 Ruddlesden-Popper ferroelectrics against the tolerance factor (t) of their perovskite double layers….140

Figure 6.1: Plots of SHG activity of $Li_2SrTa_2O_7$ as a function of particle size, compared to an α-SiO_2 standard.....146

Figure 6.2: Observed, calculated and difference plots from the refinement of the $A2_1am$ model against the synchrotron X-ray diffraction data collected from $Li_2SrTa_2O_7$ at 298 K.....147

Figure 6.3: Observed, calculated and difference plots from the refinement of the $A2_1am$ model against high-resolution neutron diffraction data collected from $Li_2SrTa_2O_7$ at 298 K.....148

Figure 6.4: The structure of $Li_2SrTa_2O_7$ in space group $A2_1am$, with an $a^-a^-c^+/a^-a^-c^+$ tilting distortion.....150

Figure 6.5: Observed, calculated and difference plots from the refinement of the $A2_1am$ model against high-resolution neutron diffraction data collected from $Li_2SrTa_2O_7$ at 5 K.....152

Figure 6.6: The refined $A2_1am$ structure viewing along the stacking axis.....155

Figure 6.7: A comparison of how Sr^{2+} and Ta^{5+} cations can displace in the polar $A2_1am$ and $Pna2_1$ as well as the anti-polar $Pnam$ symmetry structures.....157

Figure 6.8: (a) Dielectric permittivity measured as a function of temperature for $Li_2Sr(Nb_{2-x}Ta_x)_2O_7$ solid solutions; (b) Phase transition temperatures as a function of Ta-content....159

Figure 7.1: Cation exchange reaction from diamagnetic $Li_2La_2Ti_3O_{10}$ to antiferromagnetic $FeLa_2Ti_3O_{10}$……...….161

Figure 7.2: Observed, calculated and difference plots from the refinement of the $A2_1am$ model against the synchrotron X-ray diffraction data collected from $MnSrTa_2O_7$ at 298 K.....163

Figure 7.3: Observed, calculated and difference plots from the refinement of the $A2_1am$ model against high-resolution neutron diffraction data collected from $MnSrTa_2O_7$ at 298 K ……...……...164

Figure 7.4: The refined unmodulated structure of $MnSrTa_2O_7$ in space group $A2_1am$….166

Figure 7.5: Disordered and ordered arrangements of the Mn^{2+} cations viewing along the stacking axis, solid squares show the $A2_1am$ unit cell size.....166

Figure 7.6: Observed, calculated and difference plots from the refinement of the $A2_1am(0b0)000$ model against high-resolution neutron diffraction data collected from $MnSrTa_2O_7$ at 298 K.....167

Figure 7.7: Top: Approximant incommensurate structure viewing along x. Bottom: Approximant distribution of Mn^{2+} cations viewing along z.....168

Figure 7.8: Zero-field cooled and field cooled magnetisation data collected from $MnSrTa_2O_7$……...170

Figure 7.9: Magnetization-field isotherms collected from $MnSrTa_2O_7$ at 5 K and 300 K.....170

Figure 7.10: Neutron diffraction patterns collected from $MnSrTa_2O_7$ at 200 K (red) and 1 K (blue) using the WISH diffractometer (122º bank).....172

Figure 7.11: Observed, calculated and difference plots from the refinement of the $A2_1a'm'(0b0)000$ model against the neutron diffraction data collected from $MnSrTa_2O_7$ at 1 K.....173

Figure 7.12: The simple G-type magnetic structure from a refinement against the neutron diffraction data collected at 1 K. Top: The refined magnetic structure with a box dimension $a \sim 11.13$ Å, $b \sim 111.38$ Å and $c \sim 18.95$ Å; Bottom: A local view of the magnetic structure.....174

Figure 7.13: The ordered magnetic moment extracted from fits to variable temperature neutron powder diffraction data collected from $MnSrTa_2O_7$ in the temperature range $1 \leq T/K \leq 43$.....176

Figure 7.14: Evolution of the neutron diffraction patterns measured as a function of temperature.....177

Figure 7.15: Temperature evolution of the average cell parameters for $MnSrTa_2O_7$ determined from the analysis of variable temperature neutron diffraction data.....178

Figure 7.16: Using cation exchange chemistry to prepare novel multiferroic materials....180

Figure 8.1: Disordered, checkerboard and stripe ordering of Cu^{2+}.....184

Figure 8.2: Observed, calculated and difference plots from the refinements of the *I*4/*mmm*, $P4_2/mnm$ and *B*2*em* models against the synchrotron X-ray diffraction data collected from $Cu_xLi_{2-2x}SrTa_2O_7$.....185

Figure 8.3: The 'modified' checkerboard and stripe ordering arrangements of the Cu^{2+} cations.....186

Figure 8.4: Observed, calculated and difference plots from the refinements of the cation-ordered models against the synchrotron X-ray diffraction data collected from $Cu_xLi_{2-2x}SrTa_2O_7$.....187

Figure 8.5: Observed, calculated and difference plots from the refinements of the *I*4/*mmm* model against the neutron powder diffraction data collected from $Cu_xLi_{2-2x}SrTa_2O_7$.....188

Figure 8.6: Observed, calculated and difference plots from the refinements of the $P2_1/m$ model against the neutron powder diffraction data collected from $Cu_xLi_{2-2x}SrTa_2O_7$.....190

Figure 8.7: Observed, calculated and difference plots from the refinements of the $P2_1/m$ model with a disordered cation arrangement against the neutron diffraction data collected from $Cu_xLi_{2-2x}SrTa_2O_7$ using the GEM instrument.....192

Figure 8.8: Observed, calculated and difference plots from the refinements of the $P2_1/m$ model with a partially ordered cation arrangement against the neutron diffraction data (35° bank) collected from $Cu_xLi_{2-2x}SrTa_2O_7$ using the GEM instrument.....192

Figure 8.9: Zero-field cooled and field cooled magnetisation data collected from $Cu_xLi_{2-2x}SrTa_2O_7$.....194

Figure 8.10: Magnetization-field isotherms collected from $Cu_xLi_{2-2x}SrTa_2O_7$.....194

Figure 8.11: Observed, calculated and difference plots from the refinements of the $A2_1am$ models against the synchrotron X-ray diffraction data collected from $CoSrTa_2O_7$……...196

Figure 8.12: Observed, calculated and difference plots from the refinements of the $A2_1am$ models against the neutron powder diffraction data collected from $CoSrTa_2O_7$.....197

Figure 8.13: Zero-field cooled and field cooled magnetisation data collected from $CoSrTa_2O_7$.....198

Figure 8.14: Magnetization-field isotherms collected from $CoSrTa_2O_7$ at 5 K and 300 K.....199

Figure 9.1: Observed, calculated and different plots from the refinement of the $A2_1am$ model against the synchrotron X-ray diffraction data collected from $Na_{1+x}NdTa_2O_{7-x}N_x$ at 298 K……...206

Figure 9.2: Apical anion sites which are preferred by the nitride ions……..……208

Figure 9.3: Observed, calculated and different plots from the refinement of the $A2_1am$ model with a composition $Na_{1.2}NdTa_2O_{6.8}N_{0.2}$ against the neutron powder diffraction data collected at 298K.....209

Figure 9.4: The refined structure of $Na_{1.2}NdTa_2O_{6.8}N_{0.2}$.....210

Figure 9.5: Observed, calculated and different plots from the refinement of the $I4/mmm$ model against the synchrotron X-ray diffraction data collected from $Li_{1+x}NdTa_2O_{7-x}N_x$ at 298 K.....213

Figure 9.6: Diffraction patterns collected from $Li_{1+x}NdTa_2O_{7-x}N_x$ and $M_xLi_yNdTa_2O_{7-z}N_z$ (M = Mn/Fe/Co/Ni/Cu) using the same X-ray diffractometer.....214

Figure 9.7: Observed, calculated and different plots from the refinement of the *Bmcm* model against the synchrotron X-ray diffraction data collected from $Co_xLi_yNdTa_2O_{7-z}N_z$ at 298 K.....215

Figure 9.8: Observed, calculated and different plots from the refinement of the *Bmcm* model with a composition $Co_xLi_yNdTa_2O_{7-z}N_z$ against the neutron powder diffraction data collected at 298K.....216

Figure 9.9: The refined *Bmcm* structure of $CoNdTa_2O_6N$, with an $a^-a^-c^0/-(a^-a^-)c^0$ tilting distortion.....217

Figure 9.10: Observed, calculated and different plots from the refinement of the $A2_1am$ model against the synchrotron X-ray diffraction data collected from $Ni_xLi_yNdTa_2O_{7-z}N_z$ at 298 K……218

Figure 9.11: ZFC and FC magnetisation data (left) and magnetization-field isotherms (right) collected from $Co_xLi_yNdTa_2O_{7-z}N_z$ and $Ni_xLi_yNdTa_2O_{7-z}N_z$.....220

Figure 9.12: ZFC and FC magnetisation data (left) and magnetization-field isotherms (right) collected from $Mn_xLi_yNdTa_2O_{7-z}N_z$, $Fe_xLi_yNdTa_2O_{7-z}N_z$ and $Cu_xLi_yNdTa_2O_{7-z}N_z$.....221

Figure 10.1: Structural evolution as a function of interlayer cation sizes (M = Ta/Nb)…..225

Figure 10.2: Proposed cation exchange reaction from $Li_2AB_2O_7$ to $MnAB_2O_7$.....226

Figure 10.3: A solid-state total synthesis towards a polar, magnetically ordered phase $Ni_xLi_yNdTa_2O_{7-z}N_z$. The synthesis includes a ceramic synthetic step, two cation exchanges and an anion exchange.....227

Appendix 2 – Additional Data for Chapter 5

Appendix 2.1 Phase coexistence at polar-antipolar phase transition ($RbNdTa_2O_7$)

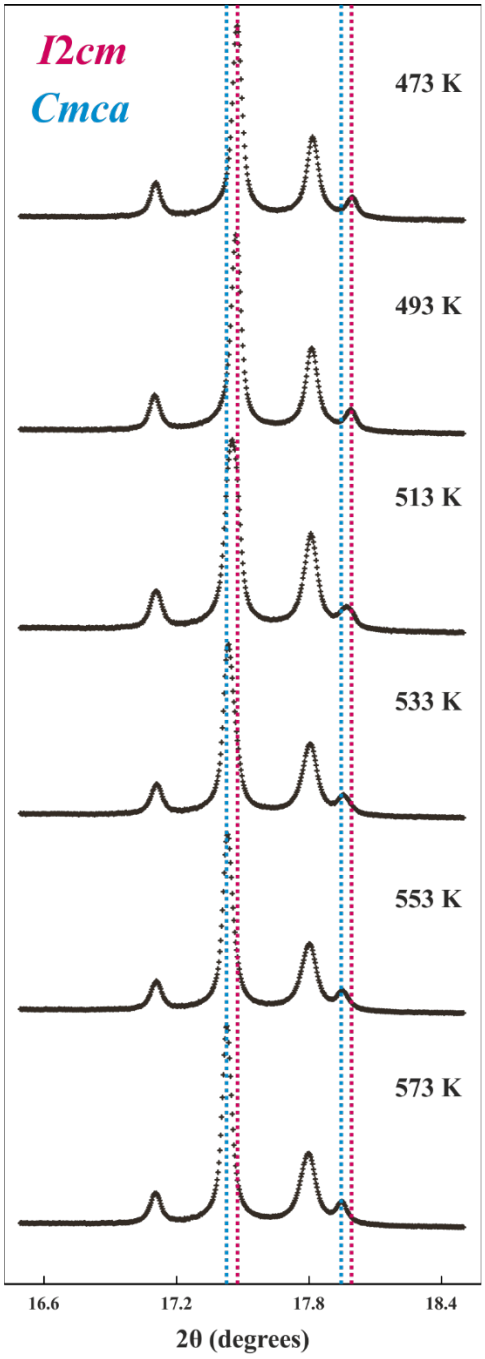


Figure A2.1: Synchrotron X-ray powder diffraction data collected as a function of temperature from $RbNdTa_2O_7$. Coexistence of *I2cm* and *Cmca* phases can be clearly observed in data collected at 513 K, consistent with a phase transition temperature of T ~ 500 K. Magenta and blue lines indicate peak positions of the *I2cm* and *Cmca* phases respectively.

Appendix 2.2 Phase coexistence at polar-antipolar phase transition ($CsNdTa_2O_7$)

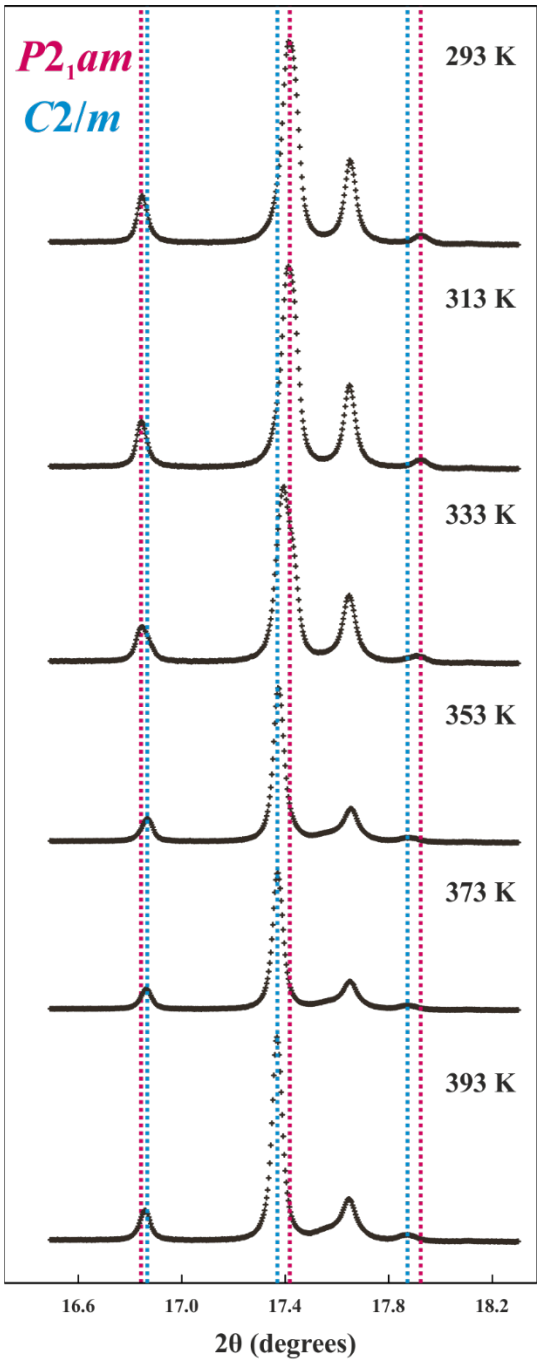


Figure A2.2: Synchrotron X-ray powder diffraction data collected as a function of temperature from $CsNdTa_2O_7$. Coexistence of $P2_1am$ and $C2/m$ phases can be clearly observed in data collected at 333 K, consistent with a phase transition temperature of T ~ 330 K. Magenta and blue lines indicate peak positions of the $P2_1am$ and $C2/m$ phases respectively.

Appendix 2.3 Phase coexistence at polar-antipolar phase transition ($CsNdNb_2O_7$)

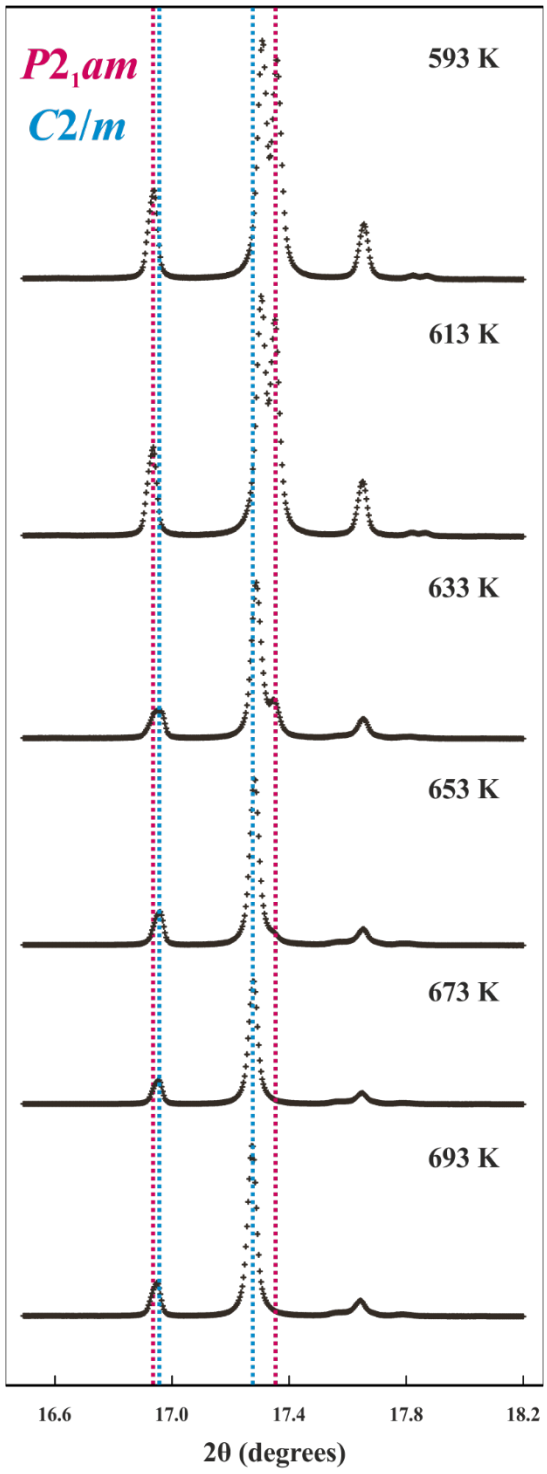


Figure A2.3: Synchrotron X-ray powder diffraction data collected as a function of temperature from $CsNdNb_2O_7$. Coexistence of $P2_1am$ and $C2/m$ phases can be clearly observed in data collected at 633 K, consistent with a phase transition temperature of T ~ 625 K. Magenta and blue lines indicate peak positions of the $P2_1am$ and $C2/m$ phases respectively.

Bibliography

1. R. J. D. Tilley, *Perovskites : structure-property relationships electronic resource*, First edn., 2016.
2. J. Hutton and R. J. Nelmes, *Journal of Physics C: Solid State Physics*, 1981, **14**, 1713-1736.
3. V. M. Goldschmidt, *Naturwissenschaften*, 1926, **14**, 477-485.
4. S. N. Ruddlesden and P. Popper, *Acta Crystallographica*, 1958, **11**, 54-55.
5. K. Toda, J. Watanabe and M. Sato, *Materials Research Bulletin*, 1996, **31**, 1427-1435.
6. M. Dion, M. Ganne and M. Tournoux, *Materials Research Bulletin*, 1981, **16**, 1429-1435.
7. A. J. Jacobson, J. W. Johnson and J. T. Lewandowski, *Inorg. Chem.*, 1985, **24**, 3727-3729.
8. *Acta Crystallographica Section B*, 1972, **28**, 3384--3392.
9. P. Woodward, *Acta Crystallographica Section B*, 1997, **53**, 32-43.
10. T. Zhu, T. Cohen, A. S. Gibbs, W. Zhang, P. S. Halasyamani, M. A. Hayward and N. A. Benedek, *Chem. Mat.*, 2017, **29**, 9489-9497.
11. K. S. Aleksandrov and J. Bartolome, *Journal of Physics: Condensed Matter*, 1994, **6**, 8219-8235.
12. B. J. Campbell, H. T. Stokes, D. E. Tanner and D. M. Hatch, *Journal of Applied Crystallography*, 2006, **39**, 607-614.
13. N. A. Hill, *The Journal of Physical Chemistry B*, 2000, **104**, 6694-6709.
14. P. S. Halasyamani and K. R. Poeppelmeier, *Chem. Mat.*, 1998, **10**, 2753-2769.
15. K. M. Ok, E. O. Chi and P. S. Halasyamani, *Chemical Society Reviews*, 2006, **35**, 710-717.
16. I. B. Bersuker, *Chemical Reviews*, 2013, **113**, 1351-1390.
17. P. S. Halasyamani, *Chem. Mat.*, 2004, **16**, 3586-3592.
18. H. Evans, Jnr, *Acta Crystallographica*, 1961, **14**, 1019-1026.
19. A. M. Glazer and S. A. Mabud, *Acta Crystallographica Section B*, 1978, **34**, 1065-1070.
20. N. A. Spaldin and R. Ramesh, *Nature Materials*, 2019, **18**, 203-212.
21. F. Kubel and H. Schmid, *Acta Crystallographica Section B*, 1990, **46**, 698-702.
22. J. Wang, J. B. Neaton, H. Zheng, V. Nagarajan, S. B. Ogale, B. Liu, D. Viehland, V. Vaithyanathan, D. G. Schlom, U. V. Waghmare, N. A. Spaldin, K. M. Rabe, M. Wuttig and R. Ramesh, *Science*, 2003, **299**, 1719.
23. N. A. Benedek and C. J. Fennie, *Physical Review Letters*, 2011, **106**, 107204.
24. N. A. Benedek, *Inorg. Chem.*, 2014, **53**, 3769-3777.
25. J. M. Rondinelli and C. J. Fennie, *Advanced Materials*, 2012, **24**, 1961-1968.

26. M. Machida, K. Miyazaki, S. Matsushima and M. Arai, *Journal of Materials Chemistry*, 2003, **13**, 1433-1437.

27. A. Vegas, M. Vallet-Regi, J. M. Gonzalez-Calbet and M. A. Alario-Franco, *Acta Crystallographica Section B*, 1986, **42**, 167-172.

28. J. Young, P. Lalkiya and J. M. Rondinelli, *Journal of Materials Chemistry C*, 2016, **4**, 4016-4027.

29. M. V. Lobanov, M. Greenblatt, E. a. N. Caspi, J. D. Jorgensen, D. V. Sheptyakov, B. H. Toby, C. E. Botez and P. W. Stephens, *Journal of Physics: Condensed Matter*, 2004, **16**, 5339-5348.

30. R. Zhang, M. S. Senn and M. A. Hayward, *Chem. Mat.*, 2016, **28**, 8399-8406.

31. A. Chauhan, S. Patel, R. Vaish and R. C. Bowen, *Materials*, 2015, **8**.

32. H. Akamatsu, K. Fujita, T. Kuge, A. Sen Gupta, A. Togo, S. Lei, F. Xue, G. Stone, J. M. Rondinelli, L.-Q. Chen, I. Tanaka, V. Gopalan and K. Tanaka, *Physical Review Letters*, 2014, **112**, 187602.

33. A. Sen Gupta, H. Akamatsu, F. G. Brown, M. A. T. Nguyen, M. E. Strayer, S. Lapidus, S. Yoshida, K. Fujita, K. Tanaka, I. Tanaka, T. E. Mallouk and V. Gopalan, *Chem. Mat.*, 2017, **29**, 656-665.

34. E. E. McCabe, E. Bousquet, C. P. J. Stockdale, C. A. Deacon, T. T. Tran, P. S. Halasyamani, M. C. Stennett and N. C. Hyatt, *Chem. Mat.*, 2015, **27**, 8298-8309.

35. R. E. Schaak and T. E. Mallouk, *Chem. Mat.*, 2002, **14**, 1455-1471.

36. M. A. Hayward, *Semiconductor Science and Technology*, 2014, **29**, 064010.

37. J. Gopalakrishnan, V. Bhat and B. Raveau, *Materials Research Bulletin*, 1987, **22**, 413-417.

38. T. A. Kodenkandath, J. N. Lalena, W. L. Zhou, E. E. Carpenter, C. Sangregorio, A. U. Falster, W. B. Simmons, C. J. O'Connor and J. B. Wiley, *Journal of the American Chemical Society*, 1999, **121**, 10743-10746.

39. P. Patnaik and Knovel, *Handbook of Inorganic Chemicals*, McGraw-Hill, 2003.

40. W. H. Bragg and W. L. Bragg, *Proceedings of the Royal Society of London. Series A, Containing Papers of a Mathematical and Physical Character*, 1913, **88**, 428-438.

41. C. Hammond and I. U. o. Crystallography, *The Basics of Crystallography and Diffraction*, Oxford University Press, 2001.

42. P. J. Brown, A. G. Fox, E. N. Maslen, M. A. O'Keefe and B. T. M. Willis, in *International Tables for Crystallography Volume C: Mathematical, physical and chemical tables*, ed. E. Prince, Springer Netherlands, Dordrecht, 2004, DOI: 10.1107/97809553602060000600, pp. 554-595.

43. S. P. Thompson, J. E. Parker, J. Potter, T. P. Hill, A. Birt, T. M. Cobb, F. Yuan and C. C. Tang, *Review of Scientific Instruments*, 2009, **80**, 075107.

44. B. Schmitt, C. Brönnimann, E. F. Eikenberry, F. Gozzo, C. Hörmann, R. Horisberger and B. Patterson, *Nuclear Instruments and Methods in Physics Research Section A: Accelerators, Spectrometers, Detectors and Associated Equipment*, 2003, **501**, 267-272.

45. J.-L. Hodeau, P. Bordet, M. Anne, A. Prat, A. N. Fitch, E. Dooryhee, G. Vaughan and A. K. Freund, *Nine-crystal multianalyzer stage for high-resolution powder diffraction between 6 keV and 40 keV*, SPIE, 1998.

46. M. T. Hutchings, P. J. Withers, T. M. Holden and T. Lorentzen, *Introduction to the Characterization of Residual Stress by Neutron Diffraction*, CRC Press, 2005.

47. E. H. Kisi, E. H. Kisi, C. J. Howard and C. J. Howard, *Applications of Neutron Powder Diffraction*, Oxford University Press, 2008.

48. R. M. Ibberson, *Nuclear Instruments and Methods in Physics Research Section A: Accelerators, Spectrometers, Detectors and Associated Equipment*, 2009, **600**, 47-49.

49. W. G. Williams, R. M. Ibberson, P. Day and J. E. Enderby, *Physica B: Condensed Matter*, 1997, **241-243**, 234-236.

50. L. C. Chapon, P. Manuel, P. G. Radaelli, C. Benson, L. Perrott, S. Ansell, N. J. Rhodes, D. Raspino, D. Duxbury, E. Spill and J. Norris, *Neutron News*, 2011, **22**, 22-25.

51. https://www.isis.stfc.ac.uk/Pages/hrpd.aspx.

52. H. Rietveld, *Journal of Applied Crystallography*, 1969, **2**, 65-71.

53. A. Larson and R. Von Dreele, *Los Almos National Laboratory, Los Almos, NM*, 2004.

54. B. D. Josephson, *Reviews of Modern Physics*, 1974, **46**, 251-254.

55. N. A. Spaldin, *Magnetic Materials: Fundamentals and Applications*, Cambridge University Press, 2010.

56. I. D. Brown, *The Chemical Bond in Inorganic Chemistry: The Bond Valence Model*, OUP Oxford, 2016.

57. N. E. Brese and M. O'Keeffe, *Acta Crystallographica Section B*, 1991, **47**, 192-197.

58. S. van Smaalen, *Incommensurate Crystallography*, OUP Oxford, 2007.

59. M. Machida, J.-i. Yabunaka and T. Kijima, *Chemical Communications*, 1999, DOI: 10.1039/A905246A, 1939-1940.

60. A. Snedden, K. S. Knight and P. Lightfoot, *Journal of Solid State Chemistry*, 2003, **173**, 309-313.

61. B.-W. Li, M. Osada, T. C. Ozawa and T. Sasaki, *Chem. Mat.*, 2012, **24**, 3111-3113.

62. C. Chen, H. Ning, S. Lepadatu, M. Cain, H. Yan and M. J. Reece, *Journal of Materials Chemistry C*, 2015, **3**, 19-22.

63. M. E. Strayer, A. S. Gupta, H. Akamatsu, S. Lei, N. A. Benedek, V. Gopalan and T. E. Mallouk, *Advanced Functional Materials*, 2016, **26**, 1930-1937.

64. H. Sim and B. G. Kim, *Physical Review B*, 2014, **89**, 144114.

65. A. R. Armstrong and P. A. Anderson, *Inorg. Chem.*, 1994, **33**, 4366-4369.

66. R. Shannon, *Acta Crystallographica Section A*, 1976, **32**, 751-767.

67. E. A. Josepha, S. Farooq, C. M. Mitchell and J. B. Wiley, *Journal of Solid State Chemistry*, 2014, **216**, 85-90.

68. T. Zhu, G. Khalsa, D. M. Havas, A. S. Gibbs, W. Zhang, P. S. Halasyamani, N. A. Benedek and M. A. Hayward, *Chem. Mat.*, 2018, **30**, 8915-8924.

69. M. J. Pitcher, P. Mandal, M. S. Dyer, J. Alaria, P. Borisov, H. Niu, J. B. Claridge and M. J. Rosseinsky, *Science*, 2015, **347**, 420.

70. L. Pauling, *Journal of the American Chemical Society*, 1929, **51**, 1010-1026.

71. S. Yoshida, K. Fujita, H. Akamatsu, O. Hernandez, A. Sen Gupta, F. G. Brown, H. Padmanabhan, A. S. Gibbs, T. Kuge, R. Tsuji, S. Murai, J. M. Rondinelli, V. Gopalan and K. Tanaka, *Advanced Functional Materials*, 2018, **28**, 1801856.

72. S. Yoshida, H. Akamatsu, R. Tsuji, O. Hernandez, H. Padmanabhan, A. Sen Gupta, A. S. Gibbs, K. Mibu, S. Murai, J. M. Rondinelli, V. Gopalan, K. Tanaka and K. Fujita, *Journal of the American Chemical Society*, 2018, **140**, 15690-15700.

73. H. Yamashita, K. Yoshio, W. Murata and A. Onodera, *Japanese Journal of Applied Physics*, 2002, **41**, 7076-7079.

74. R. J. Goff, D. Keeble, P. A. Thomas, C. Ritter, F. D. Morrison and P. Lightfoot, *Chem. Mat.*, 2009, **21**, 1296-1302.

75. C. A. L. Dixon, J. A. McNulty, K. S. Knight, A. S. Gibbs and P. Lightfoot, *Crystals*, 2017, **7**, 135.

76. K. S. Aleksandrov, *Kristallografiya*, 1995, **40**, 279-301.

77. T. Pagnier, N. Rosman, C. Galven, E. Suard, J. L. Fourquet, F. Le Berre and M. P. Crosnier-Lopez, *Journal of Solid State Chemistry*, 2009, **182**, 317-326.

78. N. Floros, C. Michel, M. Hervieu and B. Raveau, *Journal of Materials Chemistry*, 1999, **9**, 3101-3106.

79. R. Uppuluri, H. Akamatsu, A. Sen Gupta, H. Wang, C. M. Brown, K. E. Agueda Lopez, N. Alem, V. Gopalan and T. E. Mallouk, *Chem. Mat.*, 2019, **31**, 4418-4425.

80. T. Nagai, Y. Mochizuki, H. Shirakuni, A. Nakano, F. Oba, I. Terasaki and H. Taniguchi, *Chem. Mat.*, 2020, **32**, 744-750.

81. T. Nagai, H. Shirakuni, A. Nakano, H. Sawa, H. Moriwake, I. Terasaki and H. Taniguchi, *Chem. Mat.*, 2019, **31**, 6257-6261.

82. L. Gustin, Y. Hosaka, C. Tassel, T. Aharen, Y. Shimakawa, H. Kageyama and J. B. Wiley, *Inorg. Chem.*, 2016, **55**, 11529-11537.

83. V. Petříček, M. Dušek and L. Palatinus, *Journal*, 2014, **229**, 345.

84. C. Galven, D. Mounier, B. Bouchevreau, E. Suard, A. Bulou, M.-P. Crosnier-Lopez and F. L. Berre, *Inorg. Chem.*, 2016, **55**, 2309-2323.

85. R. D. Shannon and C. T. Prewitt, *Acta Crystallographica Section B*, 1969, **25**, 925-946.

86. H. Kageyama, K. Hayashi, K. Maeda, J. P. Attfield, Z. Hiroi, J. M. Rondinelli and K. R. Poeppelmeier, *Nature Communications*, 2018, **9**, 772.

87. M. Yang, J. Oró-Solé, J. A. Rodgers, A. B. Jorge, A. Fuertes and J. P. Attfield, *Nature Chemistry*, 2011, **3**, 47-52.

88. L. Clark, J. Oró-Solé, K. S. Knight, A. Fuertes and J. P. Attfield, *Chem. Mat.*, 2013, **25**, 5004-5011.

89. J. Oró-Solé, L. Clark, N. Kumar, W. Bonin, A. Sundaresan, J. P. Attfield, C. N. R. Rao and A. Fuertes, *Journal of Materials Chemistry C*, 2014, **2**, 2212-2220.

90. H. Johnston, A. P. Black, P. Kayser, J. Oró-Solé, D. A. Keen, A. Fuertes and J. P. Attfield, *Chemical Communications*, 2018, **54**, 5245-5247.

91. G. Tobías, J. Oró-Solé, D. Beltrán-Porter and A. Fuertes, *Inorg. Chem.*, 2001, **40**, 6867-6869.

92. T. Oshima, T. Ichibha, K. S. Qin, K. Muraoka, J. J. M. Vequizo, K. Hibino, R. Kuriki, S. Yamashita, K. Hongo, T. Uchiyama, K. Fujii, D. Lu, R. Maezono, A. Yamakata, H. Kato, K. Kimoto, M. Yashima, Y. Uchimoto, M. Kakihana, O. Ishitani, H. Kageyama and K. Maeda, *Angewandte Chemie International Edition*, 2018, **57**, 8154-8158.